January 2016

STRUCTURAL STUDIES ON CELL ENTRY OF RESPIRATORY ENTEROVIRUSES

Yue Liu
Purdue University

Graduate School Form
30 Updated 12/26/2015

PURDUE UNIVERSITY
GRADUATE SCHOOL
Thesis/Dissertation Acceptance

This is to certify that the thesis/dissertation prepared

By Yue Liu

Entitled

STRUCTURAL STUDIES ON CELL ENTRY OF RESPIRATORY ENTEROVIRUSES

For the degree of Doctor of Philosophy

Is approved by the final examining committee:

Wen Jiang
Chair

Michael G. Rossmann

Steven S. Broyles

Richard J. Kuhn

To the best of my knowledge and as understood by the student in the Thesis/Dissertation Agreement, Publication Delay, and Certification Disclaimer (Graduate School Form 32), this thesis/dissertation adheres to the provisions of Purdue University's "Policy of Integrity in Research" and the use of copyright material.

Approved by Major Professor(s): Michael G. Rossmann

Approved by: Stephen F. Konieczny 12/1/2016

Head of the Departmental Graduate Program Date

STRUCTURAL STUDIES ON CELL ENTRY OF RESPIRATORY ENTEROVIRUSES

A Dissertation

Submitted to the Faculty

of

Purdue University

by

Yue Liu

In Partial Fulfillment of the

Requirements for the Degree

of

Doctor of Philosophy

December 2016

Purdue University

West Lafayette, Indiana

TO MY GRANDPARENTS AND PARENTS

ACKNOWLEDGMENTS

I would like to express my deep appreciation to my advisor, Dr. Michael Rossmann. He has taught me how to be an independent scientist, that is a collection of being curious, being positive, being persistent, being critical, being enthusiastic, being self-motivated, being humble, longing for challenges, asking fundamental questions, focusing on specific problems deeply, studying questions carefully, and conveying one's ideas clearly. I thank him for allowing me to freely explore research projects, for being particularly supportive, and for his inspiration, encouragement, and guidance that have been crucial to overcome difficulties. I appreciate all his positive influences that have played an important role in my personal development and scientific career.

I am also very fortunate to have Dr. Steven Broyles, Dr. Wen Jiang, and Dr. Richard Kuhn as committee members of my graduate study. I am thankful to their invaluable support, criticisms, comments, and advice. I want to thank Dr. Jiang for making his image processing program jspr available that allowed for high resolution cryo-electron microscopic structure determination, and Dr. Kuhn for creating a favorable environment that made it possible to work on enteroviruses, for his effort in purchasing a direct electron detector, and for teaching me how to ask good scientific questions. Many thanks to Dr. Broyles, I have started to pay high attention to basic concepts and techniques.

None of my work would have been possible without collaborations with many good scientists across the globe. I would like to thank the effort of my collaborators: M. Steven Oberste (the Centers for Disease Control and Prevention, US), Claude Bernard (Monash University, Australia), Ken Fuji and Satoshi Koike (Tokyo Metropolitan Institute of Medical Science, Japan), Ian Jones (University of Reading, UK), Dante Neculai and Sergio Grinstein (University of Toronto, Canada), Kelly Watters, Marchel Hill, Yury Bochkov and Ann Palmenberg (University of Wisconsin - Madison, US),

Jane Cardosa (Universiti Malaysia Sarawak, Malaysia), Jim Baggen, Hendrik Jan Thibaut, and Frank van Kuppeveld (Utrecht University, the Netherlands) as well as Woong-Hee Shin and Daisuke Kihara (Purdue). I am grateful to the following scientists for kindly supplying me with useful reagents: Yuguang Zhao and E. Yvonne Jones (Oxford University, UK), and Jue Chen (Rockefeller University, US). I highly appreciate helpful suggestions and discussion from the following individuals: Mark McKinlay (Task Force for Global Health, US), and Roland Rueckert (University of Wisconsin - Madison, US). I thank Vukica Srajer, Robert Henning, and the other staff of the Advanced Photon Source BioCARS beamline 14 for help with X-ray diffraction data collection.

My gratitude also goes to current members of the Rossmann laboratory for their invaluable support, advice, help, and the happy, relaxing, and inspiring laboratory environment that everybody contributes to create : Vidya Magnala Prasad, Andrei Fokine, Jason Porta, Thomas Klose, Moh Lan Yap, Geeta Buda, Nick Sun, Qianglin Fang, Feng Long, Jenny Wang, S. Saif Hasan, and Sheryl Kelly. In particular, without Vidya's meticulous instruction, I would not have solved my first ever X-ray crystal structure of a protein starting from protein purification. Andrei was a good teacher who carefully explained to me many fundamental concepts in X-ray crystallography and nearly every detail of some programs. Thomas made every possible effort to establish an automated pipeline for cryo-electron microscopic data collection and data pre-processing. He is also an outstanding scientist who is knowledgeable in every aspect of structural virology. Furthermore, I would not have grasped many useful experimental skills regarding molecular biology, protein chemistry, and crystallization without Feng's consistent help. Finally, I appreciate Sheryl's help with manuscript preparation and many other aspects of my life in the Rossmann laboratory.

I want also to thank many former members of the Rossmann laboratory for their kindness, patience, and conscientiousness in helping me overcome difficulties in my research and my life: Ju Sheng, Geng Meng, Xinzheng Zhang, Long Li, Chuan Xiao, Pavel Plevka, Stefanie Becker, Anna Pallo, Zhenguo Chen, and Lei Sun. I am greatly

indebted to Ju who is a wonderful collaborator and teacher of mine, to Xinzheng who guided me through my early days of learning electron microscopy and image processing, to Zhenguo for his selfless assistance at nearly every corner of the lab, and to Geng for stimulating discussion and help with my projects on virus crystallography.

It has been an unforgettable experience being a member of the structure group at Hockmeyer Hall of Structural Biology. I thank Cynthia Stauffacher for her fascinating course on biophysical chemistry, where I learned what scientific research is about for the first time. I feel fortunate to be a teaching assistant for the introductory X-ray crystallography course by Nick Noinaj, who is an energetic scientist, a knowledgeable structural biologist, a wonderful lecturer, and a very kind teacher. I am grateful to Rushika Perera for introducing me to the mysterious jungle of virus-host interactions and for equipping me with essential experimental skills, and to Joyce Jose, Kunpeng Li, Guimei Yu, Andrew Miller, and Ampa Suksatu for very helpful discussion.

I would also like to thank Steve Wilson, Tim Schmidt, Valorie Bowman, Agustin Avila-Sakar, and Ken Kibler (FEI company, US) for training and help with technical issues as well as Rebecca Harding, Anita Robinson, Lynette Jacob, Pamela Butler, and Georgina Rupp for their administrative assistance and patience in response to my numerous questions. In addition, I very much appreciate the help from Mark Senn and Ashlee Messersmith in the process of writing my thesis.

I had very good fortune to make friends with many individuals at Purdue. I feel thankful to all of them: Yuan Ren, Longyun Guo, Ross Zhan, Yuchen Wang, Huantian Zhang, Yaowu Hu, Biaobin Jiang, Kaibo Zhang, Yi Yang, Jing Chen, Zhiping Mao, Xiangying Sun, Xiaohui Shen, Qing Zhou, Yafang Chen, Heng Wu, Tao Song, Rui Yan, Yu-Chen Yen, Chun-Liang Chen, Yoichiro Togawa, Rajdeep Bomjan, Shishir Poudyal, Ranjan Sengupta, and Matt Therkelsen. In addition, I acknowledge anybody who I talked to or met with and who unconsciously shaped my mind, influenced my life, and became part of my life in the past four years or so.

Last but not least, I am deeply indebted to my parents and grandparents for their selfless and consistent love. Their love has illuminated and will continue to illuminate the nights when I grope in the dark.

TABLE OF CONTENTS

Page

Page

Page

Page

LIST OF TABLES

LIST OF FIGURES

ABBREVIATIONS

2D	Two dimensional
3D	Three dimensional
Å	Angstrom
μg	Microgram
μL	Microliter
μM	Micromolar
°C	Celcius degree
AFM	Acute flaccid myelitis
CAR	coxsackievirus and adenovirus receptor
CC	Correlation coefficient
CCD	Charge coupled device
CDHR3	Cadherin related family member 3
CLEM	Correlative light electron microscopy
CPE	Cytopathic effect
CTF	Contrast transfer function
CV	Coxsackievirus
DAF	Decay accelerating receptor
DED	Direct electron detector
DMEM	Dulbecco's modified eagle medium
DMSO	Dimethyl sulfoixde
EDTA	Ethylenediaminetetraacetic acid
EM	Electron microscopy
ET	Electron tomography
ELISA	Enzyme-linked immunosorbent assay

EV	Enterovirus
FBS	Fetal bovine serum
Fc	Fragment crystallizable
FEG	Field emission gun
FIB	Focused ion beam
FSC	Fourier shell correlation
Gal	Galactose
Glc	Glucose
GlcNAc	N-acetylglucosamine
HFMD	Hand, foot and mouth disease
HELF	Human embryonic lung fibroblast cells
HEPES	4-(2-hydroxyethyl)-1-piperazineethanesulfonic acid
HS	Heparan sulfate
ICAM-1	Intercellular adhension molecule 1
Ig	Immunoglobulin
LDLR	Low density lipoprotein receptor
MAD	Multiple wavelength anomalous dispersion
MEM	Minimal essential medium
ML	Maximum likelihood
MIR	Multiple isomorphous replacement
mm	Millimeter
MOI	Multiplicity of infection
MR	Molecular replacement
mRNA	Messenger RNA
NCS	Non-crystallographic symmetry
NEAA	Non-essential amino acids
Neu5Ac	N-acetylneuraminic acid
ng	Nanogram
nM	Nanomolar

OD	Optical density
PEG	Polyethylene glycol
PEI	Polyethylenimine
PFU	Plaque forming unit
PNPP	Para-nitrophenyl phosphate
PSGL-1	P-selectin glycoprotein ligand 1
PV	Poliovirus
RD	Rhabdomyosacoma
rpm	Revolutions per minute
r.m.s.d.	Root mean square deviation
RNA	Ribonucleotide acid
RV	Rhinovirus
SAD	Single wavelength anomalous dispersion
SCARB2	Scavenger receptor B2
SD	Standard deviation
SIR	Single isomorphous replacement
3'SLN	Neu5Ac2-3Gal1-4GlcNAc
6'SLN	Neu5Ac2-6Gal1-4GlcNAc
6'SL	Neu5Ac2-6Gal1-4Glc
SNR	Signal-to-noise ratio
TCID50	50% Tissue Culture Infectious Dose
TEM	Transmission electron microscopy
Tris	Tris(hydroxymethyl)aminomethane
UV	Ultraviolet
VP	Viral protein
vPg	Virion protein genome linked

ABSTRACT

Liu, Yue Ph.D., Purdue University, December 2016. Structural Studies on Cell Entry of Respiratory Enteroviruses. Major Professor: Michael G. Rossmann.

Enteroviruses (EVs) represent a group of non-enveloped, positive strand RNA viruses with an icosahedral capsid shell of about 300 Å in diameter. A variety of EVs are notable for human infections, such as polioviruses, rhinoviruses, EV-A71, and EV-D68. EV-D68 causes childhood respiratory infections worldwide and has also been associated with neurological diseases. A lack of knowledge on the mechanisms of EV-D68 infection has hindered the development of antiviral interventions. Specifically, it remains obscure how the virus enters into host cells. Here, cell surface sialic acid has been identified to be indispensable for EV-D68 to attach onto and infect host cells. X-ray crystal structures of EV-D68 on its own and in complex with sialic acid receptor analogues show that binding of the sialic acid receptor to a depression on the virus outer surface destabilizes the virus. Receptor binding induces a cascade of conformational changes of the virus to eject a fatty-acid like molecule, the "pocket factor", that regulates virus stability. Furthermore, exposure of EV-D68 to an acidic environment triggers virus uncoating whereby the viral genome is released into host cell cytosol for replication and translation. In comparison with the native EV-D68 structure, the cryo-electron microscopic (cryo-EM) structure of an uncoating intermediate formed at late endosomal pH (pH 5.5) shows an expanded capsid where pores are formed at icosahedral two-fold axes and where segments of polypeptides are externalized to interact with host membranes. Because of the low stability of EV-D68, cryo-EM analyses of the virus at neutral pH indicate the involvement of multiple structural intermediates in the uncoating process. More importantly, a capsid binding compound, pleconaril, effectively inhibits EV-D68 infection by blocking

virus attachment and uncoating. Pleconaril replaces the pocket factor in occupying a hydrophobic pocket in viral protein 1. Thus these results illuminate structural rearrangements of EV-D68 during cell entry and open up an avenue for developing antiviral treatments of EV-D68 infections.

1. INTRODUCTION

Part of the text in this chapter is taken from [1–3] and is highlighted by a black, vertical line in the right margin. Macmillan Publishers Ltd: Nature Communications [3], copyright 2015. The text from [2] is reprinted with permission from AAAS.

1.1 Enterovirus Infection

The *Picornaviridae* consist of a variety of non-enveloped, icosahedral viruses with a single, positive-stranded RNA genome. The family encompasses pathogens that are notable for many human and animal diseases [4], such as poliovirus (PV) and foot-and-mouth-disease virus. Out of the 26 genera of *Picornaviridae*, the genus *Enterovirus* (EV) is classified into twelve different species, including EV-A to EV-J and rhinoviruses (RV)-A to RV-C [5, 6]. EVs that cause human infections have been primarily found in seven species, EV-A to EV-D as well as RV-A to RV-C [5]. These phylogenetically distinct species are classified according to a number of criteria concerning sequence information (e.g., amino acid sequence conservation of structural proteins and some non-structural proteins) and biological characteristics (e.g, receptor usage) [5]. Historically, EVs that belonged to a single species were typed by variation of surface antigens as determined using specific anti-sera, which is time-consuming and depends upon the availability of anti-sera [7–9]. Currently, a widely-adopted typing approach relies on complete or partial nucleotide sequence of the VP1 (viral protein 1) gene [10]. EVs are responsible for a wide range of human diseases. These include respiratory illnesses, hand, foot, and mouth disease (HFMD), myocarditis and a number of neurological diseases such as encephalitis and poliomyelitis (Table 1.1) [11]. The major transmission modes of EVs are fecal-oral route and respiratory route (e.g., airborne transmission or droplet transmission) [11].

Table 1.1
Selected EVs that infect humans and common diseases[a]

Species	Number of types	Key members	Diseases
EV-A	24	EV-A71	HFMD, neurological complications
EV-B	61	Coxsackievirus B3	Myocarditis
		Echovirus 7	Aseptic Meningitis
EV-C	23	Poliovirus 1-3	Poliomyelitis
EV-D	5	EV-D68	Respiratory illnesses
		EV-D70	Acute hemorrhagic conjunctivitis
RV-A	77	RV-A2	Respiratory illnesses
RV-B	30	RV-B14	Respiratory illnesses
RV-C	55	RV-C15	Respiratory illnesses

[a] Table content was based on [5, 11, 12] and http://www.picornaviridae.com.

1.1.1 Virion structure

Similar to many other picornaviruses, EVs have an outer diameter of approximately 300 Å [13, 14]. The atomic structures of a rhinovirus (RV-B14) and a poliovirus (PV type 1), as determined by X-ray crystallography, were the first ever three-dimensional (3D) stuctures of animal viruses [13, 14]. The determination of these virus structures represented a milestone in structural and molecular virology. Since then, extensive efforts in the past three decades have led to high resolution structures of native virions for a large number of EVs [15–32]. These viruses include members of five different species, EV-A to EV-C and RV-A to RV-B. All of these viruses exhibit pseudo T=3 icosahedral symmetry. The triangulation number T was proposed by Caspar and Klug to describe the number of structurally similar protein subunits in each icosahedral asymmetric unit [33]. Specifically, 60 copies of VP1, VP2, and VP3, each of which has a length of about 250-300 amino acids, form the capsid shell (Fig. 1.1), whereas 60 copies of VP4, a small polypeptide (about 70 amino acids), reside in the capsid interior [13]. The N-terminal glycine residue of VP4 is covalently linked to myristic acid (a fatty acid with 14 carbon atoms) [34, 35]. The N-termini of VP1, VP2, and VP3 are also located inside the virus and, together

with VP4, participate in viral RNA binding [16]. Moreover, VP1, VP2 and VP3 all possess an eight-stranded antiparallel -barrel "jelly roll" fold (Fig. 1.1), which is an evolutionarily conserved fold shared by the capsid proteins of various plant and animal viruses [36–39].

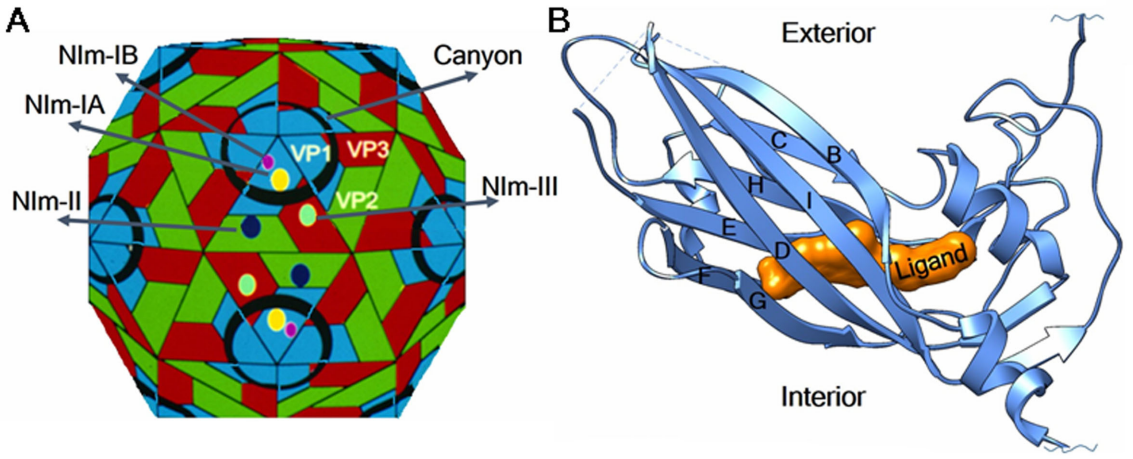

Fig. 1.1. **The structure of enteroviruses. A.** Diagrammatic representation of the virus. VP1, VP2 and VP3 are colored blue, green, and red, respectively. Each pentagonal icosahedral vertex is surrounded by a surface depression or "canyon" colored black. The epitopes for neutralizing antibodies for RV-B14 are labelled as NIm-I, NIm-II and NIm-III, where NIm is neutralizing immunogenic site. **B.** The VP1 jelly roll is shown as a ribbon diagram. If the β-strands along the polypeptide are identified sequentially as A to I, then one of the sheets is composed of the anti-parallel strands BIDG and the other by the anti-parallel strands CHEF. From [1]. Reprinted with permission from AAAS.

1.1.2 Genome organization

Enteroviruses contain a positive sense RNA genome of about 7.5 kb [40,41]. One of the unique features is that a protein, namely VPg (virion protein genome linked, about 22 amino acids long), resides at the 5' end of the genome [42]. VPg is covalently linked to the 5'-uridylylate moiety of the RNA through a tyrosine residue and acts as a primer

for viral RNA synthesis [43]. Furthermore, the 5' untranslated region (UTR) is highly structured and contains the internal ribosome entry site (IRES), which is crucial for internal ribosome binding and efficient translation of viral messenger RNA (mRNA) [44, 45]. For the 3' end, like cellular mRNAs, the viral RNA possesses a stretch of poly (A), known as poly (A) tail. The protein coding region has a single open reading frame. It is translated into a polyprotein (approximately 2200 amino acids long) [46] that is initially processed by viral protease to give three precursor proteins, P1, P2 and P3 [47]. P1 is further cleaved to produce the structural proteins VP0 (the precursor protein of VP4 and VP2), VP3, and VP1 for virus assembly [47,48], as will be discussed below. P2 and P3 are processed into a number of intermediate and final products that are functionally critical nonstructural proteins for viral replication and for virus-host interactions [4, 47]. These protein products include $2A^{pro}$, 2B, 2C (nucleoside triphosphatase), 3A, VPg, $3C^{pro}$, and $3D^{pol}$ (Fig. 1.2) (11), where pro and pol denote protease and polymerase, respectively. The proteins 3AB (the precursor to 3A and VPg), 2BC (the precursor to 2B and 2C), and $3CD^{pro}$ (the precursor to 3C and 3D) are also produced. In addition, 2B, 3A, 2BC, and 3AB contribute to membrane rearrangements, formation of membrane replication complex, and viral RNA replication [49].

1.1.3 Life cycle

Current knowledge of the infectious cycle of EVs in a host cell is largely based on studies of polioviruses over the past six decades (reviewed in [52]). As illustrated by Fig. 1.3, EV infection is initiated by viral attachment onto cell surface via specific receptor molecules [53, 54]. This step is followed by virus internalization into host cells primarily via endocytosis. EVs can utilize different endocytic pathways (e.g., clathrin-mediated endocytosis) for internalization and end up uncoating from membrane bound organelles (e.g., endosomes) within a host cell [54]. The uncoating process is facilitated by structural changes of the capsid [53]. Once the viral

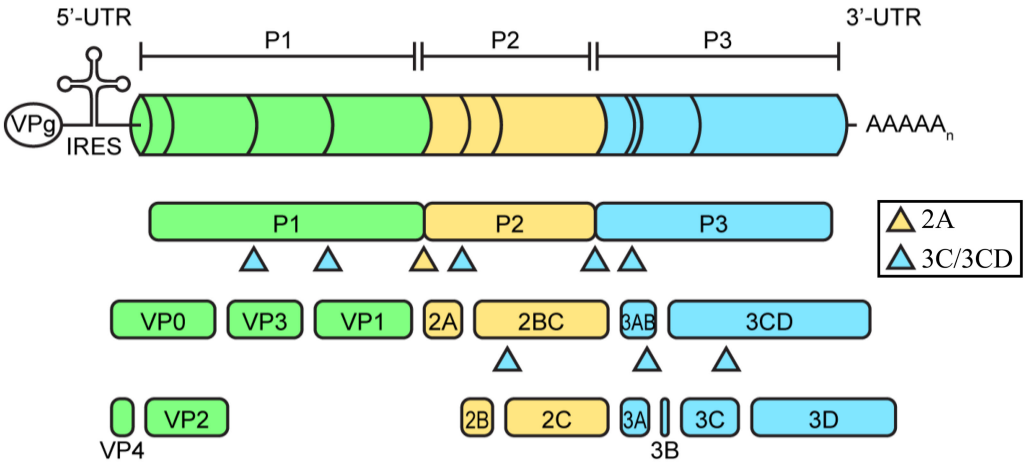

Fig. 1.2. **The genome organization of enteroviruses.** A viral protein, VPg, is covalently linked to the genome RNA. The viral RNA encodes a polyprotein, which is processed by viral proteases to form precursor proteins P1, P2, and P3. P1 is further processed into capsid proteins, whereas P2 and P3 are cleaved into non-structural proteins. The cleavage sites of viral proteases 2A and 3C (or 3CD [50]) are indicated by yellow and blue triangles. The figure was taken from [51] with some modifications.

genome is released into the cytoplasm, VPg is removed that allows for the translation of viral mRNAs. This process leads to the production of a polyprotein that is then processed by viral proteases into a number of individual viral proteins as mentioned above. The capsid P1 precursor is cleaved to form a biological protomer (VP0, VP3, and VP1). Protomers then assemble into capsid protein pentamers [48]. Viral RNA synthesis takes place inside membranous vesicles, known as membranous replication complexes [55–57], which are formed with the help of a number of viral non-structural proteins as mentioned above. The viral polymerase $3D^{pro}$ [58, 59] catalyzes the production of a full length negative strand RNA that is complementary to viral RNA in the first step [60], which serves as a template to synthesize new positive sense RNAs [61]. In the early phase of infection, these positive sense RNAs are translated into viral proteins [62]. At the late stage of infection, these viral RNA molecules become associated with capsid protein pentamers to assemble into infectious, progeny

virions [48]. In this process, VP0 is autocleaved into VP4 and VP2 when the viral RNA is present [63, 64]. Native empty particles containing uncleaved VP0 have also been found in infected cells, which might be abortive products during viral assembly [48]. The progeny virions are usually released upon the lysis of host cells [4]. Alternatively, these virions can exit from infected cells in a non-lytic manner [65]. In essence, they are released through secreted vesicles that encapsulates a cluster of viral particles [65]. The ratio of particle number to plaque forming unit for EVs is about 100 - 1000 [4], which is high. It indicates that a large portion of virus particles might not successfully undergo a complete cycle of infection.

1.1.4 Prevention and control

The first EV, poliovirus, was discovered more than a century ago [66]. The mechanisms of EV replication have been studied for more than 50 years [67]. The only vaccines that have been approved are those for PVs and for EV-A71. Vaccines for PVs, including the inactivated PV vaccine [68] and the oral PV vaccine [69, 70], have been available since 1955 and have played an instrumental role in a significant decrease of cases of PV infections. The oral PV vaccine utilizes live attenuated PVs and is currently the major cause of vaccine associated acquisition of PV infections, which prevents the global eradication of PVs [71]. Furthermore, two inactivated vaccines for EV-A71 were recently licensed in China [72, 73]. Nevertheless, a major challenge of developing vaccines against all EVs is the presence of a diversity of EVs [11]. For instance, there are more than 160 types of rhinoviruses that exhibit distinct surface immunogenecity [12]. A very recent breakthrough was the development of an effective polyvalent inactivated RV vaccine against infections of a range of RVs in animal models [74]. This vaccine was a cocktail of multiple types of inactivated RVs.

Despite some successful attempts in vaccine developments, there are still no effective antiviral therapeutics for prevention and treatments of EVs infections. In principle, it is possible to develop antiviral compounds that are directed against a

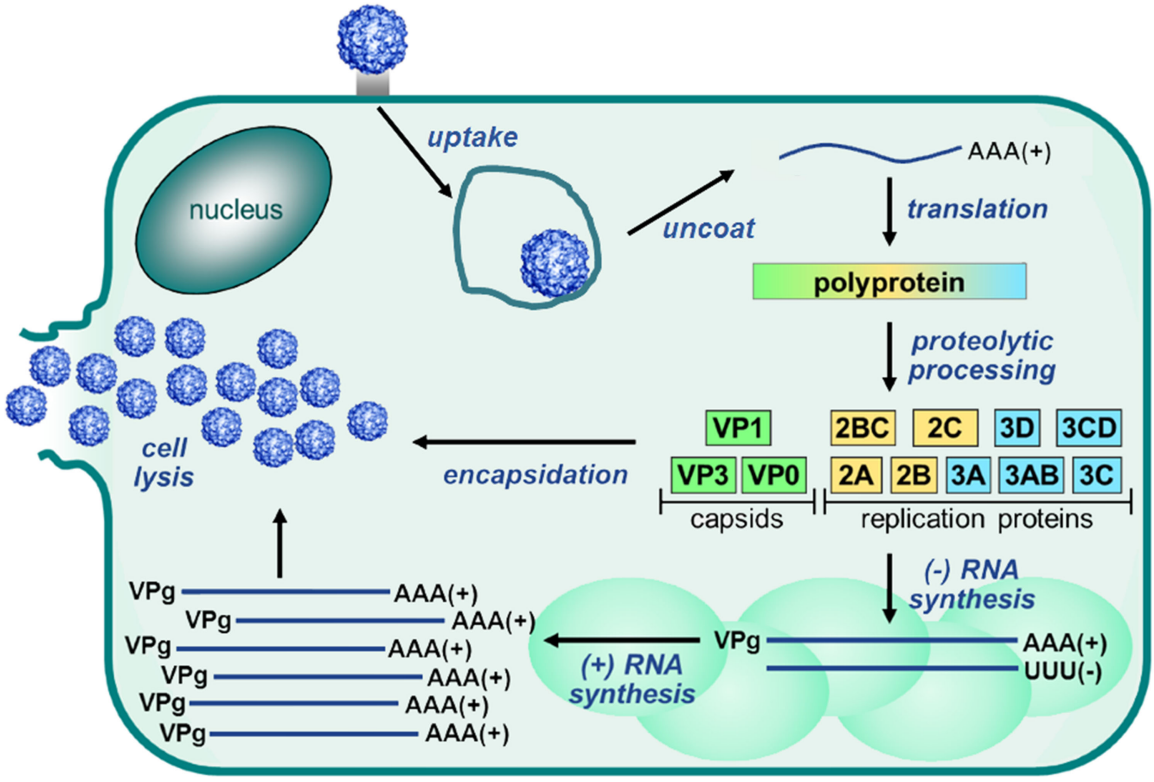

Fig. 1.3. **The life cycle of enteroviruses.** Enteroviruses attach onto a host cell via receptor binding, which is followed by virus internalization into internal membrane organelles such as endocomes. Then the positive sense viral genome is released into the cytoplasm, where translation occurs. A polyprotein is produced in the first step. It is subsequently processed by proteases into structural and non-structural proteins. Viral RNA synthesis operates via a negative sense RNA intermediate and takes place in membrane replication complexes of which the formation is facilitated by non-structural proteins. Progeny virions are then assembled from structural proteins and newly synthesized viral RNAs. These virions are mainly released upon lysis of the host cell. The figure was taken from [51] with some modifications.

conserved target or mechanism shared by a broad spectrum of EVs. In the past, two major classes of anti-EV reagents entered into at least phase II clinical trials but ended up not being approved. Pleconaril [75], a capsid binding reagent, was not approved because of side effects especially in pregnant women ([76]). An inhibitor of viral 3C

protease, rupintrivir [77], showed poor oral bio-availability and was not clinically effective against natural RV infections [78]. In addition, some other virus proteins (e.g., 2A protease and RNA-dependent RNA polymerase (reviewed in [76]) and host factors (e.g., oxysterol-binding protein that facilitates viral RNA replication [79]) have been explored as antiviral targets. Currently, the only anti-EV reagents under clinical development are two capsid binding reagents, BTA-798 (against RVs) [80] and V-073 (against PVs) [81].

1.2 Cell Entry of Enteroviruses

1.2.1 General principles of viral entry into cells

Viruses are obligate parasites of host cells in that they rely on the host for replication of viral genome, production of viral proteins, and assembly of viral particles. A general task for all viruses is the successful delivery of viral genome to sites where viral genome replication occurs within a host cell. This is true no matter whether the viral genome being released is in the form of naked nucleic acids, ribonucleoproteins or a subviral core containing nucleic acids inside. Nevertheless, in this process, there are hurdles that a virus would need to overcome. These are physical barriers presented by the host cell and energy barrier for changes of the virus structure that primes viral genome release.

The first physical barrier is the cell plasma membrane. In order to attach onto the surface of a susceptible cell, viruses have evolved to bind cellular receptors through specific physical interactions (reviewed in [82]). Recognition of viruses by host cells is frequently dependent on multivalent virus-receptor binding. There are various types of cell surface receptors, including carbohydrate molecules, lipids and proteins. Receptor specificity is largely attributed to long-term host-virus co-evolution [83]. Viral receptors are molecular determinants of the host range [84] and/or tissue tropism (i.e., preference for specific tissues) of a virus [85]. Additionally, a co-receptor [86,87] may exist that works with the primary receptor on viral entry in a synergistic manner

[88,89]. Upon receptor dependent recognition by a host cell, the virus, in many cases, triggers cell signaling so as to be internalized [90]. Alternatively, receptor binding leads to structural changes of the virus that facilitate penetration of the plasma membrane and subsequently genome release into cytosol [91]. In both ways, the virus circumvents the plasma membrane barrier.

Viruses are often internalized via endocytosis (reviewed in [92]), a process involves invagination of the plasma membrane and formation of membrane bound compartments called endosomes. In addition to endosomes, viruses can also be taken up to other internal compartments when hijacking specific endocytic pathways. Then in the process of endosome maturation, cytoplasmic transportation of endosomes by motor proteins ensures that the virus bypasses the crowding in cytoplasm [93], which is another physical barrier of the host cell. This hitchhiking mechanism also allows the virus to arrive at a destination that is close to the site of viral genome replication. With the help of endosomal acidification, many viruses can get around the intervening endosomal membrane and be primed for uncoating [92]. In the case of enveloped viruses, fusion occurs between the viral membrane and host endosomal membrane [94]. Non-enveloped viruses, instead, penetrate endosomal membrane by means of pore formation or membrane rupture using specific viral polypeptides [34, 95–98]. Additionally, many DNA viruses and some RNA viruses need to circumvent another barrier at the boundary between cytoplasma and nucleus in order to import viral genome into the nucleus (reviewed in [99]).

When a virus enters a host cell, the virus also needs to cross the energy barriers that limit structural changes of the virus. Viruses are generally stable being transmitted in between hosts, but becomes unstable during cell entry in order for genome release. Therefore, host cues, e.g., receptor binding, low pH, proteases, or redox conditions, are critical to trigger conformational changes of the virus [100]. For many enveloped viruses, an energy barrier lies in the fusion of two membranes that are distant from each other. The process requires insertion of viral fusion peptides into the host membrane upon structural rearrangements of viral enveloped proteins [94]. The

structural changes are usually triggered by low pH [101], receptor binding [102] or proteolysis [103, 104]. Non-enveloped viruses can use multiple mechanisms. Host factors can induce destabilization of the virus [105–108], release of viral components from the virions [109–113], externalization of specific regions of structural proteins [96, 114], or a series of complicated structural changes [113, 115, 116].

Therefore, viral entry is dependent on the interplay between the virus and the host cell. Determination of the role of host factors and structural changes of the virus in the entry process would open up opportunities for antiviral interventions.

1.2.2 Major approaches to study viral entry

A comprehensive view of the viral entry process often requires a variety of complementary approaches. The following are a few key aspects of studying the entry process: identification of viral receptors, analysis of virus-receptor binding, dissection of viral internalization pathways, study of structural changes of the virus necessary for penetration and uncoating, and kinetics of viral entry.

The first viral receptor, a carbohydrate moiety named sialic acid, was discovered using an enzymatic approach [117, 118]. Nevertheless, it was not until the 1980s that the field boomed with the advent of molecular cloning [119] and monoclonal antibodies [120]. Proteinaceous receptors were identified for a number of important animal viruses including human immunodeficiency virus [121–126]. In the post-genomic era, quantitative proteomics and transcriptomics approaches have become prevalent. The proteomics method utilizes mass spectrometry coupled with immunoprecipitation [127] or affinity purification [128]. It is based on specific interactions between a cellular receptor and the receptor binding components of a virus. The transcriptomics approach relies on comparison of transcription levels in susceptible over non-susceptible cell lines [129]. Most recently, genome-wide genetic screening techniques have been applied to discover viral receptors that were previously challenging. These include RNA interference (RNAi) [130], haploid screening [131], and CRISPR

(clustered regularly interspaced short palindromic repeats) [132]. The general idea is disruption of the function of individual genes by means of silencing gene expression, insertional mutagenesis or knock out of genes. All these genetic screening approaches are followed by functional validation of positive hits. Particularly, haploid screening showed that intracellular viral receptors that are present in internal compartments of a host cell can facilitate virus entry [133].

Multiple endocytic pathways for virus uptake have been found, including clathrin mediated endocytosis, macropinocytosis, caveolar/lipid raft mediated endocytosis, and some alternative mechanisms [92]. A combination of live cell imaging, genetic methods, and pharmacological inhibition can be employed. In general, there are several critical aspects concerning a specific pathway: virus induced host signaling events, the route by which viral internalization occurs, intracellular trafficking of cytoplasmic membranous compartments that carry the virus, and host factors that trigger virus penetration and uncoating. Multicolor live cell imaging using fluorescence microscopy is crucial to dissect different steps of viral entry and to track the dynamic process of each step. Due to its high sensitivity as well as good spatial (better than the diameter of a virion) and temporal resolution (often at the level of seconds), this approach provides spatiotemporal analysis of fluorescent dye-labeled single virus particles [134]. Furthermore, the other two approaches offer advantages in identification of host factors and study of molecular mechanisms. Specifically, knockdown of host genes by genetic methods (e.g., RNAi) has been utilized for discovering novel host factors that define novel pathways and for clarifying the functional role of a known factor (e.g., clathrin, caveolin, or other factors) so as to differentiate between established pathways [135]. Pharmacological inhibition takes advantage of chemical compounds that specifically target individual host factors and can be useful to determine host triggers of virus penetration and uncoating (e.g., bafilomycin is an inhibitor of endosomal acidification) [135].

Biochemical and biophysical approaches *in vitro* are suited to provide a clearer and often quantitative understanding of specific molecular events, including virus-receptor

binding, virus penetration, and genome release. Many of these molecular events have been reconstituted *in vitro* using purified macromolecules with or without artificial membrane systems (e.g., liposomes) that mimic native biological membranes [136]. General principles of the interactions of a virus with receptor molecules and of the conformational changes of viruses associated with viral entry have been illustrated by structural studies of the entire viral particles or isolated viral components at low resolution (about 30-40 Å) to near atomic resolution (4 Å or better). The major structural tools were X-ray crystallography, single particle cryo-electron microscopy (cryo-EM), cryo-electron tomography (cryo-ET), or hybrid methods (e.g., a combination of x-ray crystallography with cryo-EM [137]). One of the first examples was the crystal structure of influenza virus hemagglutinin in complex with sialic acid [138]. Studies using complementary biophysical techniques, such as surface plasmon resonance [139] and fluorescence correlation spectroscopy [140], have contributed to knowledge on the kinetics of virus-receptor binding and of genome release. Moreover, the application of mass spectrometry has been instrumental to study the stoichiometry of virus-receptor binding as well as compositional and conformational changes of viral particles [141]. Additionally, single molecule techniques have characterized the dynamics of intact viruses or viral protein structures concerning receptor binding and fusion [142, 143].

More recently, an emerging technique, namely cryo correlative light and electron microscopy (cryo-CLEM), has begun to show new details of the viral entry process by studying interactions of virus with host cells at close-to-native state [144]. CLEM combines the spatial resolution of cryo-ET (i.e., at the scale of several nanometers) with the temporal resolution (i.e., at the scale of seconds) of light microscopy and achieves spatially precise correlation using markers [145]. Although technical issues like specimen thickness await further developments, CLEM holds the promise for visualizing ultrastructural details and dynamics of virus-cell interactions that span different spatial scales.

1.2.3 Current knowledge of enterovirus entry into cells

Over the past several decades, structural and functional studies have defined some of the molecular mechanisms of EV entry into host cells. As will be discussed below, general principles underlying attachment and internalization of multiple EVs have been established, whereas the penetration and uncoating processes are less well understood.

Beginning in the 1980s, a diversity of specific cellular receptors have been identified for EVs (Table 1.2) [124–126, 146–169]. A depression on the virion surface, the "canyon", that encircles each five-fold vertex (Fig. 1.1), is frequently the binding site for EV receptors [28, 108, 170–182]. Many of these receptors belong to the immunoglobulin (Ig) superfamily (Table 1.2) [183]. This region also has limited accessibility to neutralizing antibodies [13]. In most EV structures, a hydrophobic pocket in the VP1 jelly roll is located underneath the canyon and accommodates a "pocket factor (Fig. 1.1), which is a fatty-acid like molecule that contributes to stabilize the virion [16, 184]. Many EVs interact with the N-terminal Ig-like domain of their cognate Ig-like receptors. This process proceeds via a two-step mechanism [172,185–187], which involves a competition between the pocket factor and the receptor [188]. In essence, receptor binding depresses the base of the canyon to squeeze the VP1 pocket, expelling the pocket factor [188]. Thus, binding of Ig-like receptors destabilizes the virus that primes the uncoating process. Nevertheless, receptors of some EVs, such low density lipoprotein receptor of the minor group rhinoviruses, bind to other locations on the viral surface and do not induce viral uncoating (Table 1.2) [29, 189–191].

Depending on the virus and the cell type, EVs are known to be internalized into host cells via different routes. Multiple types of distinctive endocytic pathways have been found for EV entry [54]. A large number of rhinoviruses utilize clathrin-mediated endocytosis and end up uncoating in endosomes [197]. In these cases, endosomal acidification is an important trigger for virus uncoating, of which the pH threshold is dependent on the stage of endosomal maturation (e.g., pH about 6.0 for early en-

Table 1.2
Selected enteroviruses and their cell entry characteristics[a]

Virus	Receptor	Receptor structure	Binding site on virus	Initiation of uncoating
Poliovirus 1-3	CD155	Ig-like	canyon	yes
Coxsackievirus A21	ICAM-1[b]	Ig-like	canyon	yes
Major group RVs	ICAM-1[b]	Ig-like	canyon	yes
Coxsackievirus B3	CAR[c]	Ig-like	canyon	yes
Enterovirus A71	SCARB2[d]	twisted beta barrel	?[e]	yes[f]
Echovirus 1	integrin $\alpha_2\beta_1$	V-shaped, 12 domains	canyon	?[g]
Coxsackievirus A9	integrin $\alpha_v\beta_6$	V-shaped, 12 domains	near twofold	no
Echovirus 7	CD55	scr-like[h], beta sandwich	near twofold	no
Minor group RVs	LDLR[i]	"arc" arrangement of domains	near fivefold	no

[a] Table content is according to [29, 53, 183, 191]
[b] ICAM-1: intercellular adhension molecule 1
[c] CAR: coxsackievirus and adenovirus receptor
[d] SCARB2: scavenger receptor B2
[e] Was proposed to bind to the virus canyon [192]
[f] Requires low pH [193, 194]
[g] Inconsistency between *in vitro* results [195] and cell based data [196]
[h] scr: short consensus repeat
[i] LDLR: low density lipoprotein receptor

dosomes). Many viruses from the species EV-B can follow either caveolae-dependent endocytosis or macropinocytosis [198]. Low pH is not a trigger for uncoating of these viruses. There are also known examples of EVs (e.g., EV-A71) that take two different endocytic pathways when using two separate cellular receptors [199, 200]. In addition, PV appears to be a special case, because binding of cell surface PV receptor CD155 to the virus at physiological temperature is sufficient to cause genome release directly through the plasma membrane or through vesicles near the plasma membrane shortly after internalization [201]. More importantly, binding of EVs onto host cell surface induces a series of signaling events that result in viral internalization. This is because that virus-receptor binding can lead to phosphorylation of the cytoplasmic region of receptor molecules [202] or cause clustering of receptor molecules into specific microdomains on the cell surface [203]. In both ways, downstream intracellular signaling can be activated that involves the participation of kinases, adaptor proteins, cytoskeletal proteins, and a number of other cellular proteins.

The penetration and uncoating of EVs rely on structural changes of the virus. Upon induction by host factors, the native virion (with a sedimentation coefficient of 160S) of many EVs is converted into an altered particle or subviral A-particle (135S) [105–107, 178, 182, 204, 205]. The trigger is often Ig-like receptor molecules and/or endosomal acidification. Furthermore, A-particles were also known to be formed by heating native virions *in vitro* [206–209]. A-particles are featured by expansion of the capsid shell, externalization of the N-terminal amphipathic region of VP1 (the first about 25 amino acids [114]), and release of myristoylated VP4, as compared with native virions [209–213]. A line of *in vitro* and cell-based evidence indicated that the A-particle is an intermediate during EV entry.

(1) A-particles were found in the supernatants upon increasing temperature to 37 °C after attachment of native viruses to cells at 4 °C [214–216];

(2) Pre-formed A-particles retain the ability to infect host cells despite with dramatically reduced efficiency and, more importantly, A-particles complexed with a non-neutralizing antibody infect cells in an Fc receptor-dependent manner [217, 218];

(3) A-particles were isolated from infected cells at the stage of internalization into cytoplasmic membranous compartments [114, 194, 219];

(4) Inhibition of conformational changes necessary for both thermal inactivation and uncoating correlates with the antiviral activity of capsid binding compounds [220].

Myristoylated VP4 and the N-terminal amphipathic helix of VP1 are critical for EV penetration through the membrane of intracellular vesicles, which are often endosomes. The mechanism of penetration is either pore formation (e.g., RV-A2) [221–223] or lysis of membrane (e.g., RV-B14) [224]. VP1 N-terminal amphipathic helices, which are probably externalized through the base of the canyon or two-fold axes on A-particles [209, 211, 212, 225], might act as anchors for A-particles to directly attach onto target membranes [114, 136, 226, 227]. Thus binding of A-particles to lipid membranes is independent of receptor molecules. An icosahedral two-fold axis of the A-particle appears to face the membrane [227]. Myristoylated VP4 molecules have been proposed to exit through icosahedral two-fold axes [228] or five-fold axes [229] in the transition of native virions to A-particles. The VP4 molecules are oligomerized and form channels in model membranes, as demonstrated by electrophysiological experiments and EM analysis [230, 231]. The functional importance of VP4 in virus penetration and uncoating was further confirmed by the observation that mutation of VP4 changes its ability to form pores *in vitro* and to allow RNA release during infection [232–234].

Enteroviruses uncoat from cytoplasmic membrane compartments such as endosomes. A-particles were proposed to release genomic RNA into cytosol, resulting in the formation of subviral emptied particles (80S) [114, 219]. Furthermore, emptied particles were found in isolated endosomes derived from infected cells [219]. Much like A-particles, emptied particles can be produced *in vitro* by heating and share

considerable similarity to the cell-derived equivalent in terms of composition and sedimentation coefficient [206, 229, 235–238]. Structural studies of *in vitro* produced emptied particles showed that the capsid shell of these particles is structurally similar to that of A-particles [31, 238]. They are both expanded relative to native virions. These observations support the idea that emptied particles is another intermediate (in addition to A-particles) during cell entry of EVs [53, 114, 219]. In the process of RNA release, the viral RNA is protected from RNA degrading enzymes by a shield that is possibly composed of the VP1 N-termini and perhaps VP4 molecules [226]. Using cross-linking reagents that capture the virus when releasing the genomic RNA, recent studies indicated that viral RNA exits from the virus through two-fold axes and that the exiting of genomic RNA begins with its 3'-end [239–241]. When RV-A2 was incubated at 56°C, the exiting of viral RNA 3'-end completed in about 3 min, and release of free viral RNAs into solution occurred about 7 min later. The whole process of RNA release took only around 20 min [240]. Similarly, viral RNA was first detected in the cytosol of cells infected by RV-A2 at about 10 min post infection when using a multiplicity of infection of 15 [242]. Nevertheless, the trigger for RNA release during EV infection remains unknown. It has been suggested that the disruption of viral RNA secondary structures is required for RNA release [201] and that interactions of uncoating intermediates with lipid membranes is a prerequisite [226]. In addition, negatively charged amino acid residues on the inner surface of EV capsids could expel genomic RNA from the virus via charge-charge repulsion [212]. Taken together, a wealth of information on EV penetration and uncoating has primarily been derived from work on PVs and RVs. Nevertheless, it is not clear whether other EVs, including the circulating EV-A71 and EV-D68, adopt the same molecular mechanism as what have been established for PVs and RVs.

Delineation of the mechanism of EV entry has aided the design and development of anti-EV reagents. A series of capsid-binding antiviral compounds (e.g, pleconaril) have been and are being developed to inhibit infections by a broad spectrum of EVs [76]. These inhibitors bind to the VP1 pocket of EVs often by replacement

of the pocket factor [243–246]. The major mechanisms of action are blocking of virus uncoating [246–249] and, in some cases, inhibition of receptor dependent virus attachment [249–252]. Capsid binding reagents also impede transient and reversible externalization of internal polypeptides at physiological temperature, an event named as virus "breathing" [253–255].

1.3 X-Ray Crystallography and Electron Microscopy

Two breakthrough discoveries in the 1950s ushered in a new era of biology. The double helical structure of DNA was deduced in 1953 [256]. Only several years later, the first three-dimensional structures of proteins, myoglobin [257] and hemoglobin [258], were solved. These pioneering works in structural and molecular biology provided a structural view of the functions of biological macromolecules and began to decipher the atomic secret of biological processes. Since then, nearly six decades of effort have led to the experimental determination of more than 120,000 biological macromolecular structures. These structures were made possible by three major techniques: X-ray crystallography, electron microscopy (EM), and nuclear magnetic resonance (NMR). NMR has the advantage of studying protein dynamics in solution but generally proves difficult for structure determination of biomolecules with a molecular weight of more than 50 kilodaltons (kDa). This section will focus on the other two approaches, X-ray crystallography and EM.

1.3.1 X-ray crystallography

In 1912, the phenomenon of X-ray diffraction by crystals was discovered by Max von Laue (reprinted in [259]). The diffraction pattern was subsequently interpreted by William Lawrence Bragg as being derived from the reflection of incident X-ray waves by parallel planes within a crystal [260]. This interpretation was expressed as an equation that became known as Bragg's law. These and many early crystallographic studies had dealt with crystals of inorganic compounds such as sodium chloride.

It was not until 1934 when John Bernal obtained the very first X-ray diffraction pattern of a crystalline protein (pepsin) [261]. Nevertheless, the application of X-ray crystallography to structure determination of proteins was challenging. It took more than 20 years for Max Perutz to solve the structure of hemoglobin [258]. The central problem was the phase problem. In essence, in an X-ray diffraction experiment, the phases of diffracted x-ray waves are unknown, whereas the amplitudes of diffracted X-ray waves are known according to experimentally measured reflection intensities. The aim of structure determination is to determine the electron density $\rho(xyz)$ at each point with the coordinates (x, y, z) in the crystallographic unit cell. An electron density map in real space is the inverse Fourier transform of structure factors in reciprocal (Fourier) space. Structure factor is a complex number that describes the amplitude and phase of a diffracted X-ray wave.

$$\rho(xyz) = (1/V)\sum_{h}\sum_{k}\sum_{l}|\mathbf{F}(hkl)|exp(-2\pi i(hx+ky+lz))exp(i\alpha(hkl)) \qquad (1.1)$$

where V represents the unit cell volume. $|\mathbf{F}(hkl)|$ and $\alpha(hkl)$ are the amplitude and phase of the structure factor with miller indices (hkl), respectively. i is the square root of -1.

One of the first ideas to tackle the phase problem was isomorphous replacement [262], which was crucial to structure determination of hemoglobin and myoglobin. This approach requires preparation of heavy atom derivatives, which refer to crystals of native protein complexed with heavy atoms (e.g., mercury). Heavy atoms are usually incorporated into protein crystals by means of soaking or cocrystallization with heavy atom compounds. The assumption is that the native protein crystal is isomorphous to the heavy atom derivative. It means that the two crystals have identical unit cell parameters. Depending on the number of heavy atom derivatives used for phasing, there are two variations: single isomorphous replacement (SIR) that uses one heavy atom derivative and multiple isomorphous replacement (MIR) that uses multiple heavy atom derivatives [263].

Heavy atoms diffract X-rays better than the light atoms (e.g., carbon) present in the native protein. Thus the structure factors of heavy atoms, $\mathbf{F_H}(hkl)$, have relatively large amplitudes, which contribute to the difference between the structure factors of native protein and of heavy atom derivative. Assuming that there are two heavy atom derivatives, heavy atom locations can be determined by calculation of difference Patterson maps with Fourier coefficients $(|\mathbf{F_{PH1}}(hkl)| - |\mathbf{F_P}(hkl)|)^2$, $(|\mathbf{F_{PH2}}(hkl)| - |\mathbf{F_P}(hkl)|)^2$, and $(|\mathbf{F_{PH1}}(hkl)| - |\mathbf{F_{PH2}}(hkl)|)^2$, in which $\mathbf{F_P}(hkl)$, $\mathbf{F_{PH1}}(hkl)$, and $\mathbf{F_{PH2}}(hkl)$ are the structure factors of native protein and two heavy atom derivatives, respectively [264]. The Patterson function is essentially the inverse Fourier transform of intensities and is a function of interatomic vectors in real space [265]. Information of heavy atom locations is used to compute the structure factors of heavy atoms, $\mathbf{F_{H1}}(hkl)$ and $\mathbf{F_{H2}}(hkl)$.

Structure factors are usually expressed as vectors in an Argand diagram, where the x and y axes represent the real and imaginary parts of a complex number, respectively. Thus, $\mathbf{F_{PH}}(hkl)$ is the vector sum of $\mathbf{F_P}(hkl)$ and $\mathbf{F_H}(hkl)$. The phases for native protein can be determined geometrically using a Harker construction (Fig. 1.4) [266]. There are two possible phase angles when only one heavy atom derivative is considered. This uncertainty is often resolved by the use of multiple heavy atom derivatives or by taking advantage of anomalous signals of heavy atoms (as will be descried below) [267]. However, there are experimental errors in structure factor amplitudes. Additionally, $|\mathbf{F_H}(hkl)|$ is small in many cases. These factors cause some ambiguities in determining phases using MIR. Blow and Crick developed a method where any phase angle has a probability to be the correct solution [268]. In MIR, an individual probability distribution is calculated for $\alpha(hkl)$ concerning each heavy atom derivative. The product of individual probabilities gives a joint probability for every possible phase angle, which is employed to calculate a probability-weighted average phase or the "best phase". A "figure of merit" is used as a metric to evaluate the goodness of phase determination. Nevertheless, the bottleneck of isomorphous

replacement is preparation of suitable heavy atom derivatives, which is generally difficult and time-consuming.

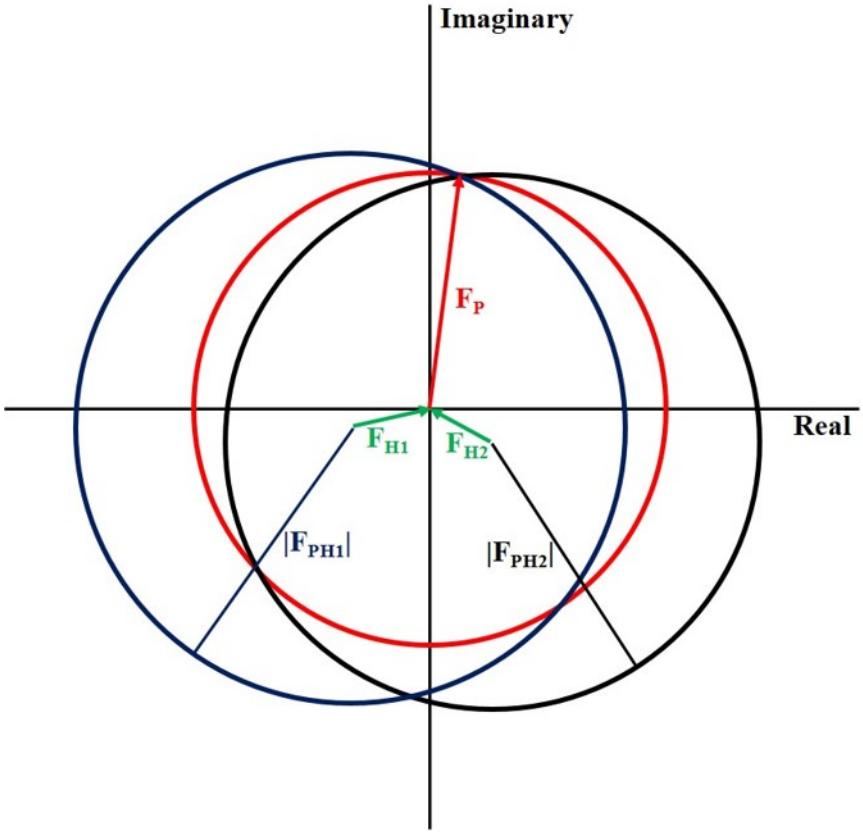

Fig. 1.4. **A Harker construction for phase determination using multiple isomorphous replacement.** The red and blue circles intersect at two positions, showing an uncertainty of phase determination when using single isomorphous replacement.

The anomalous dispersion (scattering) effect of heavy atoms offers another approach to solve the phase problem [269]. When the energy of incident X-ray beam reaches a transition energy (often referred to as absorption edge), electrons in an inner shell (e.g., K shell) of atoms become ejected due to the absorption of photon energies. This causes alterations of the amplitude and phase of the atomic scattering factor.

$$\mathbf{f} = f_0 + f^{'}(\lambda) + if^{"}(\lambda) \tag{1.2}$$

where the total atomic scattering factor $\mathbf{f}$ is a complex number, and f_0 is the normal atomic scattering factor when the energy of X-ray beam is well below the absorption edge. $f^{'}$ and $f^{"}$ are components due to anomalous scattering, which are wavelength (λ) dependent. $f^{'}$ is often negative and has the same phase as f_0, whereas $f^{"}$ is out of phase by 90° relative to f_0.

Early work had focused on combining anomalous dispersion with isomorphous replacement [267, 270–272]. Hendrickson and coworkers developed a practical approach, namely multiwavelength anomalous dispersion (MAD) [269], that has fueled structure determination of proteins without prior information about the structure. MAD is made possible by finely tunable synchrotron radiation. Selenium (Se) is a commonly used heavy atom, because its absorption edge is located within the range of usable X-ray wavelengths [273]. Se atoms are introduced into the native protein by protein expression in the presence of a surrogate of methionine named selenomethionine [273]. The aforementioned phase shift of the atomic scattering factor breaks down the Friedel's law, where the Friedel pair, $\mathbf{F}(hkl)$ and $\mathbf{F}(\overline{hkl})$, have an identical amplitude. Heavy atom locations are determined by calculation of an anomalous difference Patterson map with coefficients $(|\mathbf{F_{PH}}(hkl)| - |\mathbf{F_{PH}}(\overline{hkl})|)^2$ [274]. Thus, phases for native protein can be determined in a similar way as in isomorphous replacement. Given that the anomalous scattering components are wavelength dependent (Equation 1.2), data collection in MAD is performed at several selected X-ray wavelengths [269]. These include that of the absorption edge and of the peak absorption, which give the largest magnitudes of $f^{'}$ and $f^{"}$, respectively, and maximize anomalous signals for phasing. In most cases, a wavelength being remote from the absorption edge is also included. Nevertheless, one disadvantage of MAD is the need to produce selenomethionine substituted proteins in a large amount and suitable crytals of selenium labeled proteins. A workaround of these problems is to rely on anomalous signals of sulfur atoms in unlabeled proteins [275].

Another approach, namely molecular replacement (MR), originated from the concept of non-crystallographic symmetry (NCS) [276]. Crystallographic symmetry op-

erators are applicable to the infinite crystal lattice, whereas NCS operators are only applicable to a locally defined volume. NCS defines the rotational and translational relationship between structurally similar (or identical) subunits in one crystallographic asymmetric unit or between structurally similar subunits that are present in different crystals.

The use of NCS for determination of initial phases is described here. MR takes advantage of known structures of proteins that have a homologous amino acid sequence to the target protein for which the structure is unknown. Phases are calculated based on a properly oriented and positioned search model that is a homologous structure. Thus, the problem can be divided into two steps, rotation determination and translation determination. Rossmann and Blow worked out a rotation function that was expressed as the overlap of a Patterson function with a rotated version of the Patterson function [277]. This rotation function R has the form

$$R = (U/V^3) \sum_{\mathbf{h}} \sum_{\mathbf{p}} |\mathbf{F}(\mathbf{h})|^2 |\mathbf{F}(\mathbf{p})|^2 G_{\mathbf{h},\mathbf{h}'} \tag{1.3}$$

where $\mathbf{h}$ ($\mathbf{h} = (h, k, l)$) and $\mathbf{p}$ ($\mathbf{p} = (p, q, r)$) are vectors in reciprocal space. $\mathbf{F}(\mathbf{h})$ and $\mathbf{F}(\mathbf{p})$ are structure factors with miller indices (hkl) and (pqr), respectively. Here they can be considered as structure factors of the unknown structure and of the search model, respectively. $\mathbf{h}'$ describes the position of $\mathbf{p}$ after applying a rotation matrix $[C]$, which is specified by three Euler angles or polar angles. U is the volume of an integration sphere (by assumption) whose center is at the origin of the unit cell and whose radius is r. In such case, G is a sinc function with the argument $|\mathbf{h} + \mathbf{h}'|r$. A maximum of R would indicate that the search model is correctly rotated to match the orientation of the unknown structure. To determine the translation needed to correctly position the search model (at the determined orientation) in the unit cell, translation search can be performed to minimize the difference between the observed structure factors and the calculated structure factors (calculated using the search

model). For instance, correlation coefficient (CC) is a commonly used indicator of such difference.

$$CC = \frac{\sum_{hkl} |(\mathbf{F_o}(hkl)| - < |\mathbf{F_o}(hkl)| >)(|\mathbf{F_c}(hkl)| - < |\mathbf{F_c}(hkl)| >)}{\sqrt{\sum_{hkl} (|\mathbf{F_o}(hkl)| - < |\mathbf{F_o}(hkl)| >)^2 \sum_{hkl} (|\mathbf{F_c}(hkl)| - < |\mathbf{F_c}(hkl)| >)^2}} \quad (1.4)$$

where $\mathbf{F_o}(hkl)$ and $\mathbf{F_c}(hkl)$ are the observed and calculated structure factor amplitudes, respectively. There are also several other criteria for translation search (reviewed in [278]), e.g., the overlap of the observed Patterson map with the calculated Patterson map [279].

Averaging of NCS related identical subunits within one crystallographic asymmetric unit represents a useful method for phase improvement [36, 37, 280, 281] and for phase extension [13, 14, 282, 283]. For instance, icosahedral viruses have an NCS redundancy of at least five, where the NCS redundancy refers to the number of identical subunits in a crystallographic asymmetric unit. This redundancy leads to an effective decrease of the size of the structure to be determined. The idea is explained by the application of real space NCS averaging and phase extension to virus structure determination below [14, 284–290]. The assumption is that initial phases have been determined at a low resolution using one of the methods mentioned above. First, a molecular envelop is defined in which the NCS relationship of subunits is valid. The envelop might be a hollow spherical shell or based on a homologous atomic structure. Electron densities outside the envelop are set to low, constant value (such as zero), a procedure known as "solvent flattening" [291]. Electron densities within the envelop is averaged using the NCS operator. The averaged map is Fourier back transformed to produce more accurate phases than the original ones. A new map can be calculated when the observed structure factor amplitudes (appropriately weighted) are combined with the new phases. Iterative cycles of these procedures improve the phases until no further improvements are observed. Structure factors computed from the map (after density modifications) contain phase information at slightly higher resolution than the resolution limit used for calculating the current map. Such phase information

can be combined with the observed structure factor amplitudes to calculate a new map, thus extending the resolution limit. Phases at the current resolution limit are then improved by multiple cycles of NCS-averaging and solvent flattening. Thus, phases can be gradually extended in small incremental steps to the resolution limit that the data allow. Phase extension using large step sizes often results in erroneous phases [13]. An appropriate step size, as determined based on a similar sinc function to the G function in the rotation function mentioned above, is about one or two reciprocal space lattice units [292, 293]. In this process, better defined NCS operators and molecular envelop can be used. Convergence is usually monitored the difference between observed and calculated structure factors using correlation coefficient as an indicator.

1.3.2 Electron microscopy

The electron microscope (EM) was invented in the 1930s by Ruska [294] and initially used to characterize inorganic chemical materials. Unlike these materials, biological samples, which are made up of light elements like carbon, have intrinsically low contrast. These samples are hydrated and prone to radiation damage [295]. Sample thickness is also a concern when cells or tissues are used. Beginning in late 1950s, biological samples were negatively stained by electron dense reagents such as heavy metal salts in order to improve the image contrast [296]. The resultant samples were also tolerant to radiation damage. Nearly a decade later, DeRosier and Klug developed a general approach to computationally reconstruct the three dimensional (3D) structure of an object from two dimensional (2D) EM images that represent multiple views of the object [297]. The idea was based on the assumption that each of the 2D EM images is a projection of the 3D density distribution of the object (the effect of contrast transfer function (CTF) should be taken into account [298].) In principle, the Fourier transform of a projection is a central slice of the 3D Fourier transform of the object. Thus, a 3D density map of the object can be reconstructed

by Fourier synthesis using all available 2D slices, each of which is computed from one of the experimental images. This approach is particularly powerful when the object has screw or rotational symmetry, because different views of an asymmetric unit of the object are present in one experimental 2D image. The development of the 3D reconstruction method marked the birth of biomolecular structure determination by EM. However, the method had been applied only to images of negatively stained particles at the time. Heavy metal stains cause uneven staining and distortions of the objects present in the sample. Furthermore, the resolution of 3D reconstructions is limited by the grain size of heavy metal salts and can not go beyond about 20 Å resolution [299].

In an attempt to preserve samples at close-to-native state, to minimize radiation damage, and to keep the sample under high vacuum within the microscope, Taylor and Glaser obtained high resolution (up to 3.4 Å) electron diffraction patterns of frozen, hydrated 2D crystals (about several protein layers in thickness) of catalase [300]. This was achieved in 1974 when the field of cryo-EM began. Moreover, a general approach for producing unstained, hydrated, frozen samples was introduced by Dubochet in the 1980s [301]. Plunge freezing of a tiny volume (several nanoliters or less) of sample solution into a suitable cryogen such as liquid ethane resulted in dispersed, single molecules (or particles) being embedded within a layer of vitreous ice, which is distinct from hexagonal or cubic ice. This approach is still widely used today for a variety of samples, including cells, crystals, helical assemblies, and single particles such as icosahedral viruses and other macromolecular assemblies with or without symmetry.

Imaging of radiation sensitive, unstained biomolecules requires low electron exposures (e.g., about 16-25 e^-/A^2 for single particles [302]), because the extent of radiation damage depends on the total electron doses for imaging. For these samples, one event of elastic electron scattering is often accompanied by about three to four events of inelastic electron scattering [295]. The former does not change the energy of the incident electron and contributes to signals present in images. The latter deposits energy onto biological samples, causing ionization of the sample and formation

of radials that disrupt the chemical structures of biomolecules. This leads to a high amount of noise in experimental images and a low signal-to-noise ratio (SNR). Thus structure determination often requires averaging of multiple images. Two dimensional crystals and helical assemblies (also known as one dimensional crystals) were the first objects of which the structures were determined to 4 Å resolution or better [303–305]. These objects benefit from enhanced SNR by averaging of many repeating units. For instance, the first structure of a membrane protein, bacteriorodopsin, was determined by Unwin and Henderson in 1975 [306], whose effort subsequently yielded an atomic structure of the seven-helix protein [303]. Determination of a 1.9 Å resolution structure of aquaporin 0 using 2D crystals further showed the power of averaging in EM structure determination [307].

Icosahedral viruses represented the first samples that consist of single particles to reach subnanometer (better than 10 Å) resolution in 1997, which made it possible to assign α-helices in the structure [308, 309]. In comparison to particles with low symmetry or no symmetry, the large size (at least 260 Å in diameter) and high symmetry of icosahedral viruses are favorable to determining the orientations and centers of experimental projection images. The advantage of averaging multiple icosahedral asymmetric units reduces the number of particles needed for 3D reconstruction. Only about a decade later, determination of the first near-atomic resolution virus structures [310,311] were made possible in part because of improved transmission electron microscopes. The improvements included mechanically stable column and cryo-stage, better vacuum, and the introduction of the field emission gun (FEG). In particular, the FEG produces a much brighter beam with smaller size and better coherence than what had been conventionally used (e.g., LaB_6 crystals).

Nevertheless, it proved challenging to work with single particles that have low or no symmetry and that are smaller than icosahedral viruses. For instance, the ribosome structure was limited to about 6 Å resolution [312] before the advent of direct electron detectors (DED), as will be mentioned below. It was in part because EM images have low contrast. Unstained biomolecules in a thin (no more than 1000 Å

thick) layer of vitreous ice are essentially transparent to the electron beam. The thin specimen scatters electrons weakly and causes a slight phase shift of electron weaves. Thus such specimen is considered as a weak-phase object [298]. Images are formed due to the interference of the unscattered and scattered electron waves. In-focus (or close-to-focus) images generally have low contrast. In practice, image contrast at low resolution can be enhanced by defocusing the objective lens, which modulates the CTF of the microscope. However, a full recovery of high resolution signals by CTF correction is difficult when dealing with highly defocused images [313].

The central problem in single particle cryo-EM is the accurate determination of the orientation and center of each experimental projection image. The particle orientation is specified by three rotation angles including one in-plane rotation angle and two out-of-the-plane rotation angles, where the plane refers to the plane where the projection image lies. The particle center is specified by the position (x and y) of a point in the plane of the projection image. This is hampered by the low contrast of experimental images. Crowther and coworkers developed a common line method mainly for icosahedral viruses in the 1970s [314,315]. A common line is defined as the line shared by a pair of 2D sections in Fourier space. For a given 2D section, an icosahedral symmetry related 2D section intersects with it along one common line, and another 2D section generated using the inverse of this symmetry operator intersects with the original 2D section along another common line. These two common lines represent a pair of self-common lines. The center of a projection image can be estimated based on the cross correlation between the image and its rotational averaged derivative or by calculation of the center of mass. The orientation of a projection image is determined by searching for the best orientation in an icosahedral asymmetric unit that minimizes the sum of phase residuals for all 37 pairs of self-common lines of the icosahedral particle image. Phase residual is an indicator of the phase difference between a pair of common lines. 3D reconstruction using projection images with the determined centers and orientations produces an initial 3D model, from which a few reference projections are usually generated. The Fourier transform of an experimen-

tal image and that of a reference projection (or an experimental image for which the orientation has been determined) give rise to a pair of cross-common lines. There are 60 pairs of cross-common lines when icosahedral symmetry is considered. The sum of phase residuals for all pairs of cross-common lines is used as a criterion to determine the orientation (and subsequently the center on the basis of the determined orientation) of an experimental image. Reconstruction of all experimental images with known orientation and center produces a 3D model that serves as the initial model for the next iteration. Thus, this iterative process allows for accurate determination of particle orientations and centers. Recently, a new implementation of the common-line method in the EMAN program package has achieved simultaneous determination of all five parameters for orientation and center using a Monte Carlo optimization algorithm [316]. In addition, initial 3D models can be reconstructed using experimental images to which orientations are randomly assigned. Furthermore, the angular reconstitution method [317] developed by van Heel is essentially the real-space equivalent of the aforementioned common-line approach and has been extended to objects with other point group symmetries. This method relies on using 2D class averages for determining particle orientations and centers, because class averages have a much improved SNR compared to individual experimental images. Experimental particle images with similar orientations are clustered into a class, and they are averaged to produce a 2D class average [318].

Projection matching is a model based approach developed by Frank and coworkers [319]. The prerequisite is that an initial 3D model has been built using the aforementioned methods or other approaches that require multiple images of the same area being recorded at different tilt angles [320]. The initial 3D model is used to generate a series of reference projections that are sampled at a suitable angular step and that represent all possible different views. The centers of the experimental images are then roughly determined in a similar way as what was described above. Each experimental image is compared to every one of the reference projections. The orientation of the experimental image is determined by that of the reference projection to which it best

matches. The initially determined particle centers can also be improved in this way. Several criteria such as cross correlation can be used as an indicator of the degree of matching between images. CTF correction of the experimental images needs to be performed in the process. As in the cross-common line method, iterative cycles of projection matching and subsequently 3D reconstruction employing the current best particle orientations and centers can improve the accuracy of orientation and center determinations. This is in part because a finer angular size used to generate reference projections can potentially result in a higher resolution 3D reconstruction. There are several different implementations of the projection matching principle [302]. In these implementations, the determinations of the two out-of-the-plane rotation angles, of the in-plane rotation angle, and of particle center are generally treated separately to reduce the amount of computation. This idea is explained by the Polar Fourier Transform (PFT) method developed by Baker below [321]. For each of the experimental images and of the reference projections, the image is converted from Cartesian coordinates (x, y) to polar coordinates (γ, r), where γ and r represent angular coordinate and radial coordinate. The resultant image represents a series of annuli of data with each having a specific radius. The Fourier transform (along the direction of γ) of the image presented in polar coordinates, namely the PFT, consists of a series of one dimensional Fourier transforms, of which each is calculated from an annulus of data. The two out-of-the-plane rotation angles can be determined based on the cross correlation between the PFT of an experimental image and the PFT of each of the reference projections. Given these two rotation angles, the in-plane rotation angle is determined according to the rotational correlation of the experimental image with its best matching reference projection as determined in the previous step. Thus, the knowledge of all three rotation angles can be applied to the refinement of the initially determined particle centers.

There are three major factors that affect the contrast of cryo-EM images, including beam-induced motion, noise during detection, and the CTF of the microscope [322]. Inelastic scattering events result in emission of electrons from the sample

and a buildup of positive charges on the sample [323]. This causes deflection of electrons which increases the blurriness of EM images [324]. Translation and rotation of the sample can occur probably due to electrostatic force [324]. The sample movement is also caused by the mechanical instability of the supporting film (e.g., amorphous carbon film) [325]. Furthermore, charge coupled device (CCD) cameras convert electrons into photons, which are then transformed into electric charges. Noise can arise from scattering of electrons or photons, a large spread of electron signals over multiple pixels, and integration of electric charges [326]. These factors limits the detective quantum efficiency (DQE) of CCD cameras, where DQE reflects the performance of a detector and shows how much signal present in the original image is preserved after detection.

Recent advances in direct electron detection technologies have partially resolved the first two issues mention above [327–329]. DEDs show much reduced read-out noise via detection of single electron events and have an improved DQE (particularly at low spatial frequencies) over CCD cameras and photographic films [330]. DEDs locate single electron events at a precision of one quarter of a pixel. Because of a high frame rate (e.g., up to 400 frames per second for a K2 Summit DED), these cameras allow for recording EM data in a movie like mode. Thus computational alignments of frames lead to motion correction that deblurs experimental images [331,332]. Furthermore, because electron doses can now be fractionated into frames, images are often recorded using a high electron dose (e.g., up to 130 e^-/A^2) such that a high contrast is achieved even at low defocus [333]. These factors result in experimental images with an enhanced SNR. A direct outcome is that the number of asymmetric units needed to reach a near atomic resolution reconstruction has now been reduced from millions to tens of thousands [334]. There have also been advancements of image processing approaches [335–339] and automated data collection [340]. For instance, the application of maximum likelihood (ML) approaches [337, 341] has been instrumental to deal with noisy cryo-EM images and to classify a heterogeneous particle population into conformational (or compositional) homogenous subpopulations. Un-

like the aforementioned approaches where a single, best orientation is assigned to a particle image based on certain criteria of similarity, the idea of ML approaches is that a probability is calculated for any possible orientation with regard to each particle image. Thus ML approaches are advantageous when there is an ambiguity in assigning particle orientation based on a noisy and low resolution 3D reference. With these developments, single particle cryo-EM has become a powerful approach to determine near atomic resolution structures of macromolecular assemblies. Concerning crystallizable and conformational homogeneous samples, there have been a number of better than 3 Å resolution cryo-EM structures [333, 342–347], of which one was determined to 1.8 Å resolution [347]. Furthermore, the technique shows advantages over X-ray crystallography when the following types of samples are concerned. These include membrane proteins that can hardly be crystallized [348, 349], conformational flexible macromolecular assemblies [350–352], samples that have limited production yield [353–355], complex assemblies (e.g., many bacteriophages) where symmetry mismatch is present [356–358], as well as transient and unstable molecular assemblies or structural intermediates that are difficult to capture [359–361]. Nevertheless, in many cases, a project takes advantage of a hybrid approach. For example, available X-ray crystal structures can be fitted into cryo-EM density maps [137,362]. Mass spectrometry provides information of the interactions between components in a macromolecular assembly [363, 364], facilitating the interpretation of a cryo-EM density map.

There are new challenges that lay ahead. One of theses challenge is to break the lower limit of molecular size. The development of phase plate technologies [365] holds some promise for structure determination of biomolecules that have a molecular weight of less than about 200 kDa. Phase plates, which are situated at the back focal plane of the objective lens, cause a phase shift (e.g., 90° in the case of Zernike phase plates) of the scattered electron waves and alters the CTF to increase image contrast at low spatial frequencies that allows in-focus or close-to-focus imaging. One of the latest examples is structure determination of a 260 kDa protein to 4.4 Å resolution using a Volta phase plate [366, 367]. To overcome the hurdle, further improvements

of detectors are also needed to make detection faster and to increase the DQE (at low spatial frequencies) close to 1. The issue of beam induced motion can be further mitigated by employing mechanically stable supporting films such as graphene [368] and/or by neutralization of the positive charges on the specimen [369]. A controllable way of producing a layer of vitreous ice with a desirable thickness during sample preparation would be an additional benefit [370].

Another direction is the study of pleomorphic (i.e., variable in size and shape) molecular assemblies and organelles. These objects often contain membranes and have a large size (e.g., more than 800-1000 Å in at least one dimension). One promising technique is cryo-electron tomography (cryo-ET) developed by Baumeister and coworkers [371]. Projection images that represent multiple different views of a 3D object are acquired by tilting the sample holder. Thus cryo-ET is distinct from single particle cryo-EM that relies on randomly oriented single molecules. Without averaging, the current achievable resolution of cryo-ET is perhaps about 40 Å. Furthermore, the resolution can be improved for certain components by aligning and averaging of structurally similar 3D subvolumes that are extracted from tomograms. This process is generally referred to as subtomograpm averaging [372]. One of the most successful examples is the capsid structure of human immunodeficiency virus determined to near atomic resolution [373].

The third challenge has to do with thick samples, including large double strand DNA viruses (e.g., the mimivirus capsid has a diameter of about 5000 Å) [374], subcellular organelles [375], and cells (at the scale of μm) [376]. In these cases, dynamic scattering (i.e., electrons scatter for multiple times) is involved, making it complicated to determine the relationship between the experimental 2D image and the projection of the 3D object. The electrons also loss energy in this process, leading to images with a low SNR [377]. The idea of reducing sample thickness has long been pursued. One of the current techniques is cryo-focused ion beam (cryo-FIB) [378,379], which produces less artifacts than conventional methods such as sectioning. A high energy ion (e.g., gallium ion) beam is used to remove materials above and below a

target region in a cell, resulting in a thin section (e.g., about 2000-5000 Å thick) for imaging by EM. Gallium ions collide with atoms on the surface of the sample and remove materials in a layer-by-layer manner. A combination of complementary techniques including cryo-FIB, phase plates, direct electron detectors, and cryo-ET have now opened up a new avenue for structural studies of biomolecules in the context of cells [376, 380].

1.4 Scope of the Current Thesis

The current thesis focuses on structural rearrangements of enterovirus D68 (EV-D68) during cell entry. The major approaches are X-ray crystallography and single particle cryo-EM. Chapter 2 concerns determination of the X-ray crystal structure of EV-D68. Chapter 3 describes the discovery of sialic acid as a cellular receptor for EV-D68 and receptor induced conformational changes of the virus. Chapter 4 details the cryo-EM analysis of a rhinovirus C that helps establish a workflow of cryo-EM structure determination of similar viruses. Chapter 5 deals with structural changes of EV-D68 in the process of virus uncoating and molecular basis of the acid sensitivity of EV-D68. Chapter 6 describes the discovery of a capsid binding inhibitor against EV-D68 infections. Taken together, the present thesis defines structural mechanisms of EV-D68 entry into host cells. It also paves the way for developing antiviral compounds that interfere with virus entry.

2. X-RAY CRYSTAL STRUCTURE OF HUMAN ENTEROVIRUS D68

Part of the data and text in this chapter are taken from [2] (reprinted with permission from AAAS) and are highlighted by a black, vertical line in the right margin below.

2.1 Chapter Abstract

Enterovirus D68 (EV-D68) is a member of *Picornaviridae* and is a causative agent of recent outbreaks in the USA of respiratory illness in children. Here, the crystal structure of EV-D68 has been determined to 2.0 Å resolution. The hydrophobic drug binding pocket in viral protein 1 contained density that is consistent with a fatty acid of about 10 carbon atoms. Many rhinoviruses that cause common cold contain a similarly short fatty acid like molecule in the VP1 pocket. Thus EV-D68 shares considerable structural similarity with rhinoviruses.

2.2 Introduction

The enterovirus (EV) genus includes medically-important human pathogens, such as rhinoviruses (RV), polioviruses (PV) and coxsackieviruses (CV) [5, 6]. Many of these viruses have been characterized structurally and functionally [13, 14, 16–18, 21, 30, 31]. However, the species EV-D remains poorly characterized.

Human enterovirus D68 (EV-D68) was first isolated from children who were hospitalized due to respiratory infection in California in 1962 [381]. The virus was identified sporadically ever since until 2000s [382]. A global upsurge of EV-D68 cases since late 2000s has reminded the world of considerable threats of this human pathogen [383]. Particularly, in the summer and fall of 2014, an outbreak of mild to severe respiratory

illnesses occurred among thousands of young children in the United States of which more than 1000 cases was confirmed to be caused by EV-D68 [384]. EV-D68 mainly causes respiratory diseases among children [385]. There were also some cases of severe respiratory illnesses seen among adults [386]. In addition, this virus has been associated with occasional neurological diseases [387], including acute flaccid myelitis (AFM) [388]. To date, there are still no effective vaccines or antiviral treatments available. This is in part due to a lack of three-dimensional structural information on EV-D68.

This chapter details X-ray crystal structure determination of the prototype EV-D68 strain Fermon CA62-1.

2.3 Materials and Methods

2.3.1 Cells and viruses

HeLa cells (H1-HeLa cells, ATCC CRL-1958) were maintained in Minimum Essential Medium (Life Technologies) supplemented with 10% Fetal Bovine Serum (FBS), L-glutamine, and non-essential amino acids (NEAA). Human rhabdomyosarcoma (RD) cells (ATCC CCL-136) were maintained with Dulbecco's Modified Eagle Medium (DMEM) (Sigma-Aldrich) supplemented with 10% FBS, L-glutamine, and NEAA. Cells were grown at 37°C with 5% CO_2. EV-D68 virus (prototype strain) was kindly supplied by Dr. M. Steven Oberste at the Centers for Disease Control and Prevention (United States). EV-D68 stock was propagated in RD cells. Both the supernatant and infected cells were harvested. After multiple freeze-and-thaw cycles, the mixture was spun down. The resultant supernatant was stored at -80°C. The virus titers were determined by a plaque assay using HeLa cells.

2.3.2 Plaque assays

A series of 10-fold dilution were made for each sample. The resultant sample with a given dilution was added to confluent HeLa cells in a 6-well plate. After virus absorption at room temperature for 1h, cells were covered with an overlay of 0.9% agarose in MEM and 5% FBS per well. Plates were allowed to be incubated at 33°C for approximately 5 days. Plaques were visible and counted after neutral red or crystal violet staining.

2.3.3 Virus production and purification

The prototype strain Fermon CA62-1 of EV-D68 (GenBank: AY426531.1), which was isolated in 1962 in California [381], was grown in RD cells at 33°C using an MOI (multiplicity of infection) of approximately 0.01. When an obvious cytopathic effect was observed 3-4 days post infection, cells and supernatant were harvested at the same time. The mixture was centrifuged to separate cell debris from the supernatant. The cell debris were then thawed and frozen multiple times, and homogenized and centrifuged to remove the pellets. All supernatant was pooled up and pelleted using a Ti 50.2 rotor (277,937 x g for 2h at 4°C). The pellets were resuspended and treated sequentially with 0.01 mg/ml DNAse (Sigma-Aldrich), 7.5 mg/ml RNase (Sigma-Aldrich) and 0.8 mg/ml trypsin (Sigma-Aldrich) to remove impurities. After centrifugation and removing the pellet, the sample was further applied to a potassium tartrate gradient (10%-40%, w/v) in 250 mM HEPES, 250 mM NaCl (pH 7.5) using a SW 41 Ti rotor (221,830 x g for 2h at 4°C). The virus concentration was finally estimated by measuring the absorption at a wavelength of 260 nm (assuming a mass extinction coefficient of 7.7 ml/mg/cm because picornaviruses often consist of about 25% (mass percentage) RNA and 75% protein) using UV spectroscopy.

2.3.4 Crystallization and data collection

Because the yield of EV-D68 production was limited, crystallization conditions used for the purpose of screening were confined to a few previously reported conditions for crystallizing picornavirues in the literature. Cubic, shiny crystals with a size of approximately 0.1 mm for each dimension were grown using a hanging drop vapor diffusion technique within 2-3 days at room temperature from a drop consisting of 0.5 μl of virus (2-3 mg/mL in PBS (phosphate buffered saline): 10 mM phosphate buffer, 2.7 mM KCl, 137 mM NaCl, pH 7.4) and 0.5 μl of reservoir solution (0.1 M sodium acetate (pH 4.5) with 3.5 M sodium formate) [389]. The pH of the reservoir solution was about 6.0. When the crystals were looped out, washed twice with reservoir solution and then re-dissolved in water, the crystals contained viruses as verified by SDS-PAGE with silver staining. Crystals were soaked in reservoir solution containing glycerol by gradually increasing the concentration from 0% to 20% (v/v). The soaking time was approximately 1-2 min. They were then flash frozen in liquid nitrogen. Both glycerol and ethylene glycol were found to be effective cryoprotectants. X-ray diffraction data were collected at 100K using an ADSC Q315 CCD (charge coupled device) detector at beamline 14-BM-C of the Advanced Photon Source. The oscillation angle was 0.2 degrees.

2.3.5 Structure determination

Diffraction data were processed using the program HKL2000 [390]. The space group for native EV-D68 virus crystals was I222. Calculation of the Matthews coefficient suggested the presence of two particles per unit cell. Therefore, the particles should be sitting on 222 symmetry special position. Determination of which of the two possible orientations was accomplished with a self-rotation function using the program GLRF [391]. The correctly oriented and positioned RV-2A model (PDB accession number 1FPN) without the pocket factor was used for an initial phase calculation to 8.0 Å resolution. Phases were improved by 10 cycles of 15-fold non-

crystallographic symmetry (NCS) averaging using the program AVE [392] of the USF software package based on the convergence of the correlation between observed and calculated (from the Fourier transform of the averaged map) structure amplitudes. The mask defining the volume of the NCS was generated by selecting all grid points within a radius of 5 Å from each atom of the RV-A2 coordinate using the program MAMA [393]. Phases were then iteratively extended to 2.0 Å resolution using a step size of 1/c $Å^{-1}$. Each step was followed by 3 cycles of NCS averaging at the current resolution limit. Manual model building was performed using the program Coot [394]. The resultant structure was subjected to atomic position and B factor refinement with simulated annealing using the program CNS [395]. The quality of the averaged electron density map was judged by visual inspection. The R factor was also used as criterion to evaluate the refinement. Water molecules were finally added and checked with the program Coot [394]. The EV-D68 structure was validated by the criteria of Molprobity [396] in the program package Phenix [397]. Other calculations were done using CCP4 [398]. Pentamers were generated using VIPERdb [399]. Figures were made with Pymol (http://www.pymol.org/) and UCSF Chimera [400].

2.3.6 Cryo-electron microscopy

3.5μl of EV-D68 samples (about 1 mg/ml in PBS) was applied onto Quantifoil holey carbon grids R 2/2 (200 mesh, EMS). After manual blotting for about 1.5s, the sample was immediately plunge frozen into ethane which was pre-cooled by liquid nitrogen. The resultant grid was kept at close to liquid nitrogen temperature using a Gatan 626 cryo holder. It was then imaged under a Phillips CM200 transmission electron microscope (TEM) (FEI) with a 1K X 1K CCD camera at a nominal magnification of 38,000x. The microscope was operated at an accelerating voltage of 200 kV.

2.4 Results and Discussion

2.4.1 Virus growth and purification

The EV-D68 prototype strain Fermon CA62-1 was propagated in human rhabdomyosarcoma cells at 33°C, which had previously been shown to be the optimal growth temperature for EV-D68, indicating that EV-D68 behaves much like viruses from the RV-A and RV-B species that are responsible for common colds [401]. In the process of virus purification, density gradient centrifugation of a crude EV-D68 sample showed the presence of two major bands. Both bands were characterized by SDS-PAGE (sodium dodecyl sulfate polyacrylamide gel electrophoresis), UV spectroscopy (by analyzing the ratio of absorbance at 260 nm to that at 280 nm), and electron micrographs of the particles. The lower band corresponded to viral genome containing native virions, whereas the upper band probably represented native empty particles that contain uncleaved VP0 (Fig. 2.1).

2.4.2 Structure determination

The native virion was crystallized to yield cubic looking crystals, which had a size about 0.1 mm in each dimension. After soaking in glycerol, they were flash frozen in liquid nitrogen before data collection. The data extended to 2.0 Å resolution (Table 2.1). The crystal symmetry was I222 with two particles per unit cell, implying that the particles were located on a 222 symmetry position (Fig. 2.2). A rotation function [391] differentiated between the two orthogonal possible orientations of the icosahedron (Fig. 2.2). Initial phases were calculated based on the structure of RV-A2 (27) (PDB accession number 1FPN) after removing the pocket factor. EV-D68 and RV-A2 share about 45% amino acid sequence identity concerning the P1 capsid region. The phases were then extended in small steps to 2.0 Å resolution using 15-fold averaging and solvent flattening. A sharp drop of correlation coefficient beyond the resolution limit (2.0 Å) was observed, indicating that phase extension

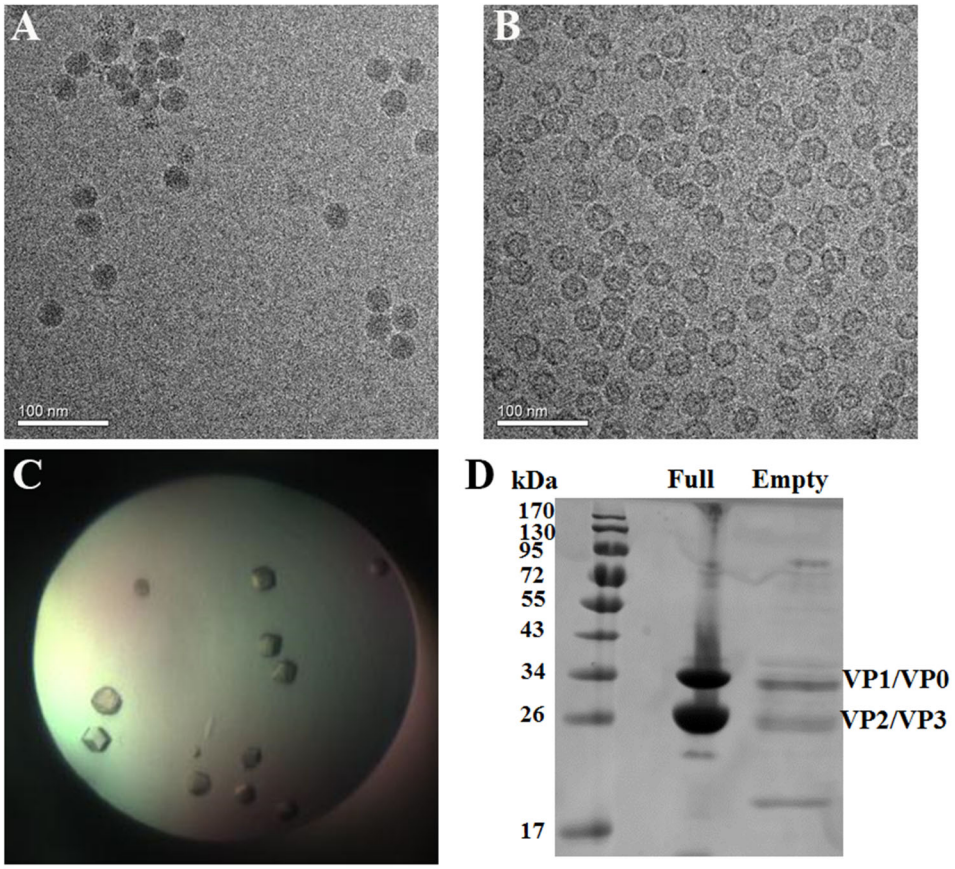

Fig. 2.1. **Chracterization of two types of EV-D68 particle.** Cryo-EM images of full (**A**) and empty (**B**) particles that were separated by gradient centrifugation. Scale bar: 100 nm. **C.** Crystals of full particles or native virions. **D.** SDS-PAGE analysis of the composition of full and empty particles. The ratio between the VP0/VP1 band and the VP2/VP3 band indicates that empty particles might have uncleaved VP0.

was successful (Fig. 2.3), where correlation coefficient is the correlation between the observed structure factor amplitudes and the calculated structure factor amplitudes. A model of the structure was built using the program Coot [394] and refined with the program CNS [395]. The final value of Rwork was 27.5%. Rfree is essentially the same as Rwork in the presence of high non-crystallographic symmetry redundancy for a randomly selected set of reflections as is the case here (Table 2.1).

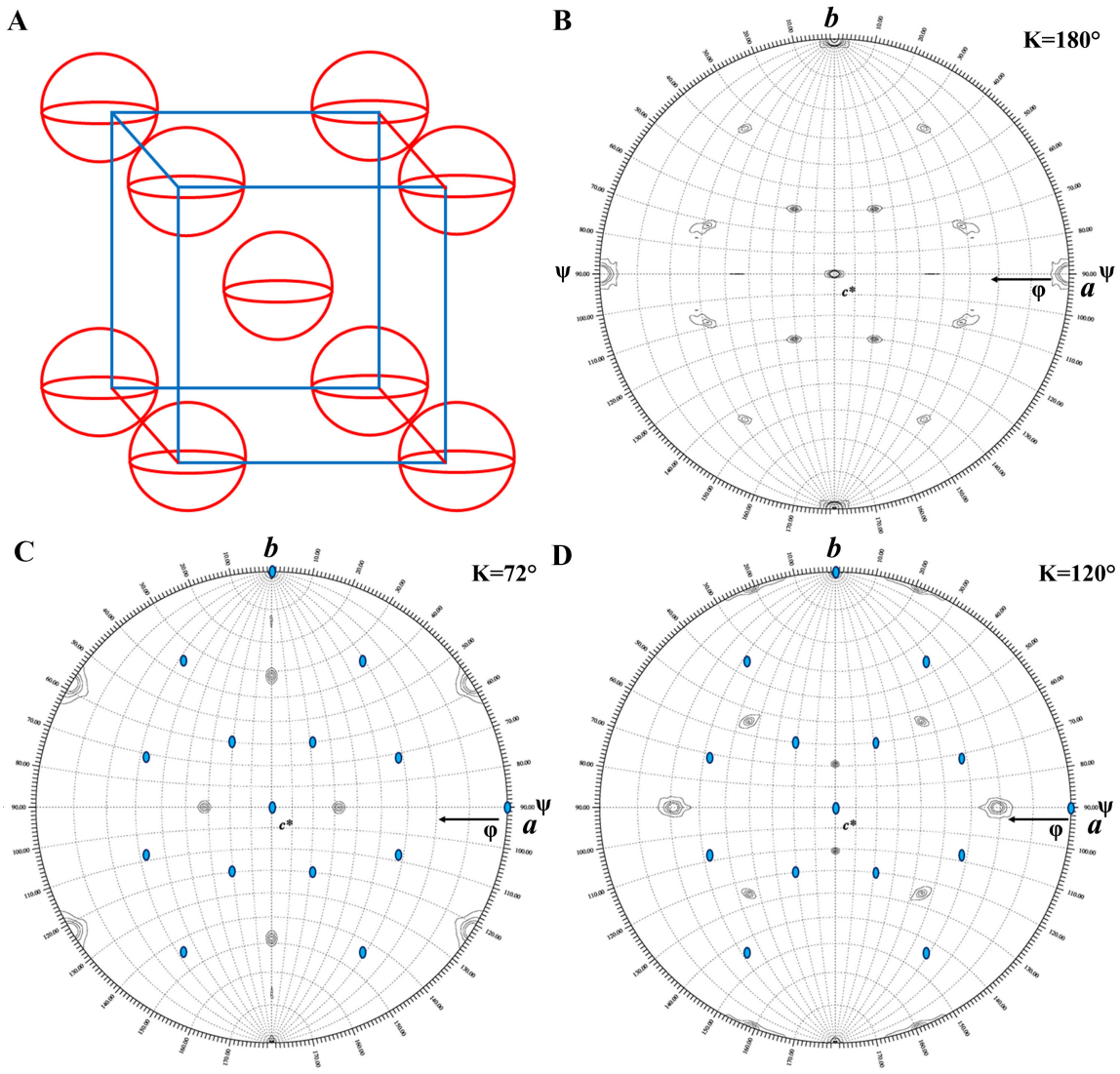

Fig. 2.2. **Packing and orientation of particles in crystallographic unit cells**. **A.** Packing of viral particles (red sphere-like object) in an orthorhombic unit cell (blue). Self-orientation function was calculated for the EV-D68 crystallographic data, where 15 Å - 8 Å resolution data and an integration radius of 150 Å were used. Shown are plots of self-rotation function peaks as a function of ψ and ϕ for the sections κ=180° (two-fold, **B**), κ=72° (five-fold, **C**), and κ=120° (three-fold, **D**). The contours start from 2.2σ with increments of 2σ.

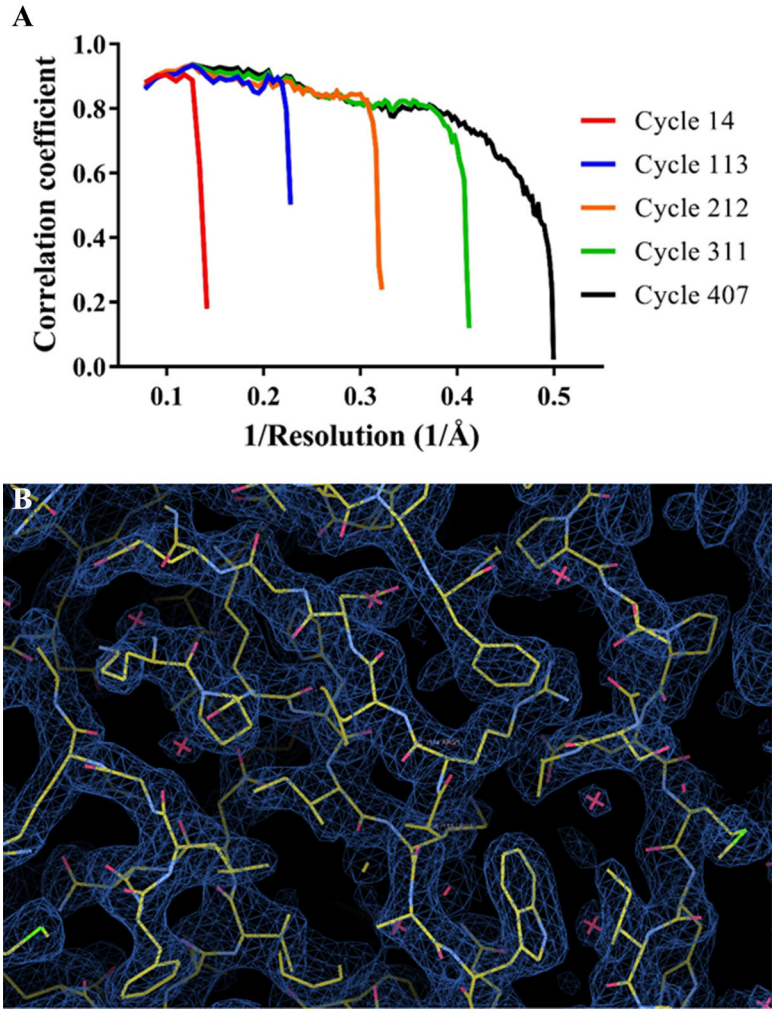

Fig. 2.3. **Phase extension and representative electron densities** **A.** A plot of correlation coefficient (CC) as a function of the inverse of resolution for selected cycles during phase extension. CC is defined as in Equation 1.4. **B.** Representative electron densities of NCS averaged $2\mathbf{F_o}$-$\mathbf{F_c}$ map at a contour level of 1.5σ. $\mathbf{F_o}$ is the observed structure factor and $\mathbf{F_c}$ is the structure factor determined after back Fourier transform of the previously NCS averaged map. Panel **B** was taken from [2] (http://science.sciencemag.org/content/347/6217/71). Reprinted with permission from AAAS.

2.4.3 Biological implications

Comparison of the amino acid sequences of EV-D68 with other enteroviruses shows that VP3 has a short, C-terminal α-helix not present in other enteroviruses (Fig.

Table 2.1
Data collection and refinement statistics[a]

	EV-D68
Data collection	
Oscillation angle (°)	0.2
No. of crystals (No. of frames)	1 (171)
Space group	I222
Cell dimensions	
a, b, c (Å)	327.0, 347.8, 357.1
α, β, γ (°)	90.0, 90.0, 90.0
Resolution (Å)	50.0-2.00 (2.07-2.00)[b]
No. of unique reflections	748623 (55656)
Completeness (%)	55.7 (41.6)
Redundancy	2.1 (2.0)
Rmerge[c]	0.105 (0.754)
$I/\sigma(I)$	8.71 (1.08)
Refinement	
Resolution (Å)	50.0-2.00 (2.07-2.00)
No. of reflections	748174 (54156)
R factor	0.275 (0.362)
Correlation coefficient	0.919
No. of atoms	
Protein	6282
Ligand	12
Water	204
RMSD bond (Å)	0.006
RMSD angle (°)	1.393
Mean B-factor (Å^2)	27.5
Mean B-factor of ligand (Å^2)	69.2
Ramachandran plot	
Favored (%)	96.5
Allowed (%)	3.4
Outliers (%)	0.1

[a] From [2]. Reprinted with permission from AAAS
[b] Values in parentheses represent the highest resolution shell
[c] $R_{merge} = \sum_{hkl} \sum_i |I_i(hkl) - < I(hkl) > | / \sum_{hkl} \sum_i I_i(hkl)$

2.4). The EV-D68 electron density map showed that this helix decorates the north side of the canyon in the neighboring, 5-fold related, icosahedral asymmetric unit.

As a result, the canyon is narrower than in other enteroviruses (Fig. 2.4) and might, therefore, not be large enough to accommodate immunoglobulin-like receptors.

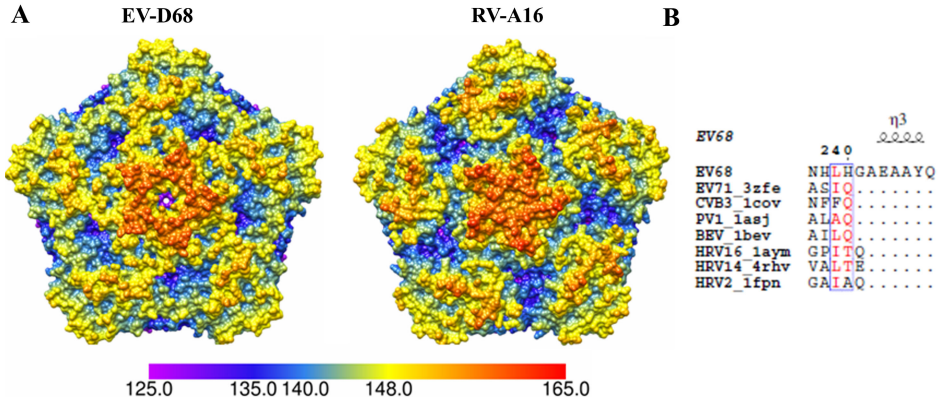

Fig. 2.4. **Surface features**. **A.** The canyon of EV-D68 is shallower and narrower than the canyon of RV-A16. Pentamers are colored by radial distance (Å) to virus center. **B.** Structure based sequence alignments of EVs with known structures. These sequences are of EV-A71 (species EV-A), CVB3 (species EV-B), PV1 (species EV-C), EV-D68 (species EV-D), bovine EV (species EV-G), RV-A16 and RV-A2 (species RV-A), and RV-B14 (species RV-B). The PDB accession numbers are given above. The secondary structural elements were based on EV-D68 native structure and the numbering of amino acids was according to EV-D68 amino acid sequence. This figure was generated using Espript [402]. Red amino acids on a white background indicate conservation only in chemical properties. From [2]. Reprinted with permission from AAAS

The BC and DE loops of VP1 are structurally the most variable among known picornaviruses. The EV-D68 VP1 has two disordered regions corresponding to residues 80-86 (EV-D68 numbering) in the BC loop and 129-136 in the DE loop, both of which are near five-fold axes. These regions harbor the neutralizing immunogen sites, NIm-IA and NIm-IB, on RV-B14, respectively [13]. Thus the flexible immunogenic regions around the five-fold axes might be an alternative mechanism for evading host humoral immune responses.

The electron density map of EV-D68 showed density in the VP1 pocket (Fig. 2.5). The height of this pocket factor density was about 3 standard deviations above the

mean of the non-crystallographic symmetry averaged map, as compared with about 5 standard deviations of most of the main chain density. As in other enteroviruses that have a pocket factor, the conformation of the GH loop of VP1, which defines the interface between the VP1 pocket and the floor of the canyon, is pushed into the pocket relative to the empty pocket in RV-B14 [13, 243] or RV-B3 [20].

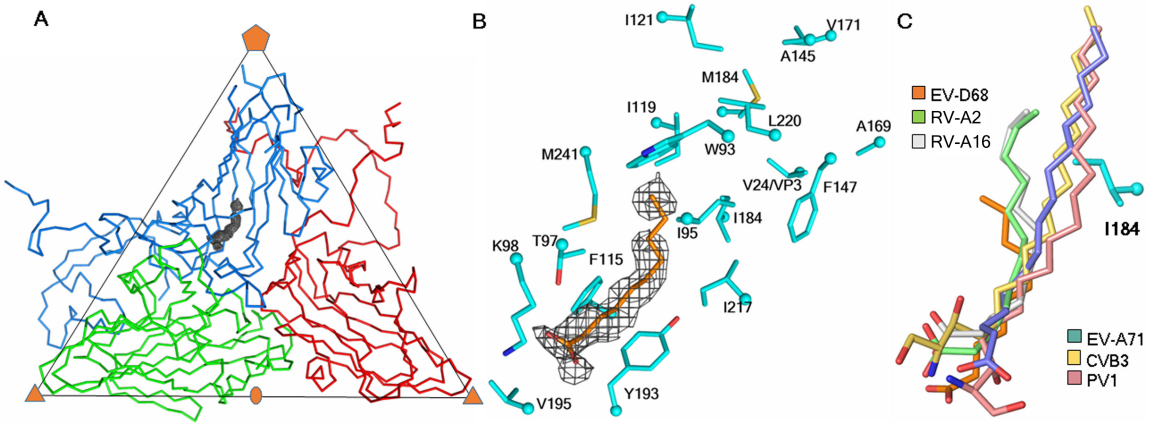

Fig. 2.5. **The pocket factor**. **A.** One icosahedral asymmetric unit of the EV-D68 structure, showing the Cα backbone for VP1, VP2, VP3 in blue, green and red, respectively. The pocket factor electron density outline is shown in grey. **B.** Enlargement of the pocket factor density with a fitted putative C10 fatty acid. Shown also are the amino acids lining the pocket. **C.** Comparison of the putative pocket factor structures in six known EV structures. Shown also is the residue I184 in EV-D68 that alters the orientation of the shorter pocket factors in some of the viruses as compared to others with longer pocket factors and a smaller residue at the equivalent position of 184. Atoms at the head of the pocket factors and of the VP1 residue side chains are colored red (oxygen), dark blue (nitrogen) and yellow (sulfur). From [2]. Reprinted with permission from AAAS

The length of the pocket factor density in the EV-D68 map corresponded to a fatty acid with an aliphatic chain of about 10 carbon atoms (Fig. 2.5). Similarly, 12 carbon atom long pocket factors were observed for RV-A16 [17] and RV-A2 [24]. In contrast, the well-formed pocket factors in PV1 [14, 16], CVB3 [18], and EV-A71 [30] corresponded to longer fatty acids with 18, 16 and 18 carbon atoms, respectively.

Furthermore, the orientation of the pocket factor tails in EV-D68, RV-A16 and RV-A2 are slightly different than that of the long pocket factors of EV-A71, PV1 and CVB3 (Fig. 2.5). The orientation is controlled in part by VP1 residue 184, which is Leu or Ile for the viruses with small, short pocket factors and Val for viruses with longer pocket factors. The larger Leu and Ile residues might push the pocket factor sideways. The similarity between the properties of the pocket factor in EV-D68 and that in the RVs might partially explain why these viruses are less stable.

These results show that EV-D68 shares considerable structural similarities to the well-studied rhinoviruses, in particular, members of the species RV-A.

3. SIALIC ACID DEPENDENT CELL ENTRY OF HUMAN ENTEROVIRUS D68

Most of the data and text in this chapter are taken from [3] and are highlighted by a black, vertical line in the right margin below. Macmillan Publishers Ltd: Nature Communications [3], copyright 2015.

3.1 Chapter Abstract

Human enterovirus D68 (EV-D68) has now emerged as a global public health threat. Nevertheless, knowledge of the tissue tropism and pathogenesis of EV-D68 has been hindered by a lack of studies on the receptor-mediated EV-D68 entry into host cells. This chapter shows that cell surface sialic acid is indispensable for EV-D68 to bind to and infect susceptible cells. Crystal structures of EV-D68 in complex with sialylated glycan receptor analogues show that they bind into the canyon on the virus surface. The sialic acid receptor induces a cascade of conformational changes of the virus to eject a fatty-acid like molecule, which regulates the stability of the virus. Thus virus binding to a sialic acid receptor and to immunoglobulin-like receptors used by most other enteroviruses share a conserved mechanism for priming viral uncoating and facilitating cell entry.

3.2 Introduction

EV-D68 is a causative agent of childhood respiratory infections [385, 401] and occasionally leads to neurological diseases [387]. Recent outbreaks of EV-D68 indicate that this virus has now emerged as a global public health threat [383, 403]. However,

the tissue tropism and pathogenesis of EV-D68 is poorly understood. Specifically, there is a lack of knowledge on the receptor-mediated EV-D68 entry into host cells.

For many EVs, binding of Ig-like receptor molecules to the virus at physiological temperatures leads to an irreversible conformational switch to an expanded A particle [105, 106], an intermediate during viral entry. Thus binding of Ig-like receptors facilitates viral genome release into the cell cytosol for successful replication. Carbohydrate receptors including sialic acid and heparin sulfate have also been identified as receptors for a number of EVs [159–164, 168, 169]. Nevertheless, it is not known whether these receptors can also initiate virus uncoating to facilitate virus infection.

EV-D68 belongs to the poorly characterized species EV-D. However it had been reported that EV-D70, a close relative of EV-D68, utilizes sialic acid as a cellular receptor [160, 404]. An early report suggested the possible usage of sialic acid as a receptor by a strain of EV-D68 [405]. Nevertheless, the complete sequence for its capsid region is currently not available, which limits further studies using this strain.Furthermore, a glycan array analysis showed that multiple EV-D68 strains can bind to synthetic glycoproteins with a terminally linked sialic acid [406]. In addition, sialic acid terminated molecules are widely distributed and abundantly expressed in the human respiratory tract [407].

3.3 Materials and Methods

3.3.1 Viruses and cells

Human embryonic lung fibroblast (HELF) cells were supplied by M. Steven Oberste at the Centers for Disease Control and Prevention (US). CMAS knockout HAP1 cells were obtained from Haplogen GmbH (Vienna, Austria). RD and HeLa cells were maintained as described in Chapter 2. HELF cells were maintained in DMEM supplemented with 10% FBS and NEAA. CMAS knockout HAP1 cells, a near-haploid human cell line that was derived from the human myeloid leukemia cell line KBM7, were grown in Iscoves Modified Dulbeccos Medium (IMDM, Life Technologies) sup-

plemented with 10% FBS. Cells were grown at 37°C with 5% CO_2 An isolate of EV-D68 from the 2014 outbreak in the United States, US/MO/14-18947 (GenBank: AIS73051.1), was also provided by M. Steven Oberste through BEI Resources, National Institute of Allergy and Infectious Diseases, National Institute of Health. All EV-D68 stock was propagated in RD cells and stored at -80°C. Procedures for Virus growth and purification was the same as that in Chapter 2. Plaque assays were performed as previously described in Chapter 2.

3.3.2 Crystallization and soaking and data collection

Cubic-looking crystals (about 0.1 mm in each dimension) were grown within 3 days at room temperature using the hanging vapor diffusion technique, as previously described in Chapter 2. Crystal soaking experiments were performed in a soaking solution that contains a given concentration of a sialylated trisaccharide in reservoir solution at room temperature for approximately 8h. The concentration used for 3'-sialyl-N-acetyl-lactosamine (3'SLN, V-Labs Inc.), 6'-sialyllactose (6'SL, V-Labs Inc.) and 6'-sialyl-N-acetyl-lactosamine (6'SLN, V-Labs Inc.) were 10 mM, 20 mM and 10 mM, respectively. Crystals were cryo-protected in the aforementioned soaking solution containing glycerol (with gradually increased concentration from 0% to 20% (v/v)) and then flash-frozen in liquid nitrogen. X-ray diffraction data on single crystals were collected at 100K at beamline 14-BM-C of the Advanced Photon Source. The detector was an ADSC Q315 CCD. The oscillation angle was 0.2°.

3.3.3 Structure determinations

Procedures for determining all three complex structures were the same, as described in Chapter 2. X-ray diffraction data were processed using the program HKL2000. The space group for all crystals was I222. Calculation of the Matthews coefficient indicated that there are two particles present in each unit cell. The particles must be sitting on 222 symmetry positions. Calculation of a self-rotation function

differentiated between the two possible 90° related orientations of the particle. The atomic model of EV-D68 (PDB accession number 4WM8) excluding the pocket factor and water molecules was employed to calculate initial phases to 8.0 Å resolution. NCS averaging and phase extension using a step size of 1/a $Å^{-1}$ were employed to determine phases up to the resolution limit of the dataset. Roadmaps were generated using the program RIVEM [408] with the help of Chuan Xiao (University of Texas at El Paso, US)

3.3.4 Virus infection assays

Each of the three cell lines, HeLa, RD and HELF cells, grown to about 90% confluency in 24-well plates were treated with either 100 mU/ml neuraminidase (NA) from *Clostridium perfringens* (Sigma) in DMEM and 1XNEAA (solution A) or solution A only at 37°C for 1h. Cells were then washed with DMEM once and infected with the EV-D68 strain Fermon CA62-1. The MOI for HeLa, RD and HELF cells were 0.3, 0.001 and 0.01, respectively. After absorption at 33°C for 1h, the inoculum was removed and cells were washed twice with DMEM. Cells were incubated at 33°C in a medium of DMEM supplemented with 5% FBS and NEAA for 0h, 24h, 48h or 72h post attachment. Samples were collected at each of these time points. These samples were freeze-thawed multiple times and then subjected to virus titer determination using plaque assays (as described in Chapter 2). For the EV-D68 strain US/MO/14-18947, infection experiments on RD cells were performed in the same way as described above for the Fermon prototype strain. All experiments were done in at least triplicate.

Experiments concerning virus infection of HAP1 cells were performed by Jim Baggen and Hendrick Jan Thibaut (Utrecht University, the Netherlands). HAP1 WT and CMAS-KO cells were seeded in a 96-wells plate at 20000 cells per well. Cells were treated with NA (from *Clostridium perfringens*, New England Biolabs) 1:50 diluted in IMDM for 30 min at 37°C. After NA was removed, EV-D68 (strain Fermon CA62-1)

was added to the cells at an MOI of 1 and incubated for 1 hour at 37°C. Virus was removed and NA (or only medium) was added again to the cells. Cells were frozen immediately (T=0) or 10h after addition of the virus. Virus titers (expressed as TCID50/ml) were determined by an end-point dilution assay using RD cells at 33°C. TCID50 (50% Tissue Culture Infectious Dose) is defined as the titer of virus that results in cytopathic effect in 50% of tissue culture cells that have been inoculated with virus.

3.3.5 Competition experiments

Cytopathic effect inhibition assays [409] were conducted in the following way. For each of the three glycans, 6'SL, 6'SLN and 3'SLN, EV-D68 (strain Fermon CA62-1) diluted in DMEM was incubated with a series of concentrations of glycans ranging from 0 mM to 4 mM at 33°C for 1h, where 0 mM was designated as the non-treated virus control. For each given concentration of glycan, a control was performed in which DMEM was incubated with glycan. The resultant mixture was added into 90% confluent RD cells in each well of a 96-well plate. The MOI was 0.001. After virus absorption at 33°C for 1h, the inoculum was removed and cells were washed twice with DMEM. Cells were allowed to be incubated in DMEM supplemented with 5% FBS and NEAA at 33°C for three days, which ensured that almost all cells became detached in the non-treated virus control. After removal of the medium, cell viability was assayed using a Quick Cell Proliferation Colorimetric Assay Kit (BioVision). The optical density for each well was recorded at a wavelength of 450 nm using a SpectraMax M5 Microplate Reader (Molecular Devices). Percent inhibition was calculated as $(OD_{cg} - OD_{vg})/(OD_c - OD_v) \times 100$, where OD_{cg} and OD_{vg} are the optical density of the uninfected and infected cell cultures treated with a given concentration of glycan, respectively. OD_c and OD_v are the optical density of the uninfected and infected cells treated with water only but no glycan, respectively. All experiments were done in triplicate.

3.3.6 Viral attachment assays

RD cells with approximately 90% confluent in 24-well plates. These were treated with 100 mU/ml NA in solution A or solution A only at 37 °C for 1h. After washing with cold DMEM once, each well was treated with 500 μl of DMEM containing 1% bovine serum album (blocking solution) at 4°C for approximately 15 min. The blocking solution was then removed and purified EV-D68 (strain Fermon CA62-1) diluted in cold DMEM was added onto cells with an MOI of 10. After incubation at 4°C for 1h, the wells were washed three times with cold DMEM to remove unbound virus.

Competition assays were performed using purified virus incubated with either 3'SLN or 6'SLN in a series of concentrations ranging from 0-3.2 mM, where 0 mM represents the virus only control in which virus was incubated with water alone. The resultant mixture was cooled down on ice and added to about 90% confluent RD cells in a 24-well plate after each well was blocked with the blocking solution as described above. The MOI was 10. After incubation at 4 °C for 1h, the wells were washed three times with cold DMEM to remove unbound virus.

For all virus attachment experiments, the RNA in each well was extracted using an RNeasy Mini Kit (Qiagen) per manufacturers protocol (RNA extraction was performed by Ju Sheng). The viral RNA of the bound virus in each sample was quantified using a quantitative real-time RT-PCR protocol. All experiments were done in triplicate.

3.3.7 Quantitative real-time RT-PCR

Quantitative real-time RT-PCR was performed (together with Ju Sheng) using a Superscript III Platinum SYBR Green One-step qRT-PCR Kit with ROX (Life Technologies) on an ABI 7300 real time PCR system. A 25 μl reaction mixture containing RNA template, SYBR green reaction mix, SuperScript III RT/Platinum Taq Mix, primers and RNAse-free water was used, where the forward and reverse primers tar-

geting the EV-D68 5'-untranslated region were EQ-1 (5'-ACATGGTGTGAAGAGT-CTATTGAGCT-3') and EQ-2 (5'-CCAAAGTAGTCGGTTCCGC-3') [410]. The thermal profile was 50°C for 3min, 95°C for 5min followed by 40 cycles at 95°C for 15s and at 60°C for 30s. Glyceraldehyde-3-phosphate dehydrogenase, a housekeeping gene, was used as an internal control for normalization purpose. The primers for GAPDH were 5'-CCCACTCCTCCACCTTTGACG-3' (forward) and 5'-CACCACC-CTGTTGCTGTAGCCA-3' (reverse). The relative levels of EV-D68 RNA in different samples were determined using a comparative $2^{-\triangle\triangle Ct}$ method [411].

3.4 Results

3.4.1 Identification of sialic acid as a receptor for EV-D68

The possible use of sialic acid as a cellular receptor by EV-D68 was examined by performing attachment and infectivity assays. Removal of cell surface sialic acid by neuraminidase (NA) treatment of HeLa cells, human rhabdomyosarcoma (RD) cells and human lung embryonic fibroblast (HELF) cells was found to significantly reduced infectivity of the EV-D68 Fermon prototype strain (Fig. 3.1). These results suggest that sialic acid might be a receptor for EV-D68 in these cell lines. To obtain further evidence that sialic acid is a functional receptor for EV-D68, human HAP1 cells were used in which the sialic acid activating enzyme cytidine monophosphate N-acetylneuraminic acid synthase (CMAS) had been knocked out. These cells are devoid of sialic acids on their surface and had previously been shown to be highly resistant to influenza A virus infection [412]. It was found that these cells were resistant to EV-D68 (Fermon strain) infection, further confirming the importance of sialic acid for EV-D68 infection (Fig. 3.1). Moreover, NA treatment of RD and HELF cells led to significantly decreased virus attachment (Fig. 3.1).

In view of these results as well as the previous glycan array analysis [407], and also because N-acetylneuraminic acid (Neu5Ac) is a frequently occurring sialic acid in humans, the sialylated trisaccharides Neu5Ac2-3Gal1-4GlcNAc (3'SLN), Neu5Ac2-

6Gal1-4GlcNAc (6'SLN), and Neu5Ac2-6Gal1-4Glc (6'SL) were used as potential receptor analogues. Preincubation of EV-D68 with these sialylated trisaccharides inhibited viral attachment and prevented killing of RD cells in a concentration-dependent manner (Fig. 3.1). Therefore, sialic acid has a crucial role in EV-D68 attachment and infection.

3.4.2 The binding site of sialylated receptor analogues

The crystal structures were determined of EV-D68 when in complex with 3'SLN, 6'SL or 6'SLN. The resolution of these structures ranged from 2.2 to 2.3 Å (Table 3.1). The procedures for the structure determination of these complexes were based on non-crystallographic symmetry averaging and step-by-step phase extension. All three receptor analogs were observed to bind near the eastern end of the canyon (Fig. 3.2). The EV-D68 canyon is unusually shallow and narrow compared to other picornaviruses that bind Ig-like receptor molecules [2, 183]. In all three structures the Neu5Ac moiety is well accommodated in a wide crater formed by VP1 and VP3 within the same protomer [13] (Fig. 3.2).

The sialic acid moiety (Neu5Ac) of these ligands is stabilized by a series of interactions provided by the surrounding residues Arg3104, Asp3232, Pro3231, Asn 1275, Pro1274, Arg1270, Asp3091, Arg3095 and Ile3233 (Fig. 3.3) (The EV-D68 amino acid numbering system is based on the Fermon strain amino acid sequence. Residues in VP1, VP2 and VP3 are defined by adding 1000, 2000 and 3000 to their sequence number). Thus, like other viral attachment proteins that bind terminal Neu5Ac [413], EV-D68 makes polar interactions with the carboxylate group and the acetamido group nitrogen atom of Neu5Ac (Fig. 3.3). The residues that interact with Neu5Ac in EV-D68 are conserved except for an Arg to Lys change at position 1270 among 51 EV-D68 isolates collected from sources on four continents between 1962 and 2014. These isolates have been classified as belonging to three lineages [383, 403, 414], although lineage 1 was the most dominant. It is, therefore, significant that these

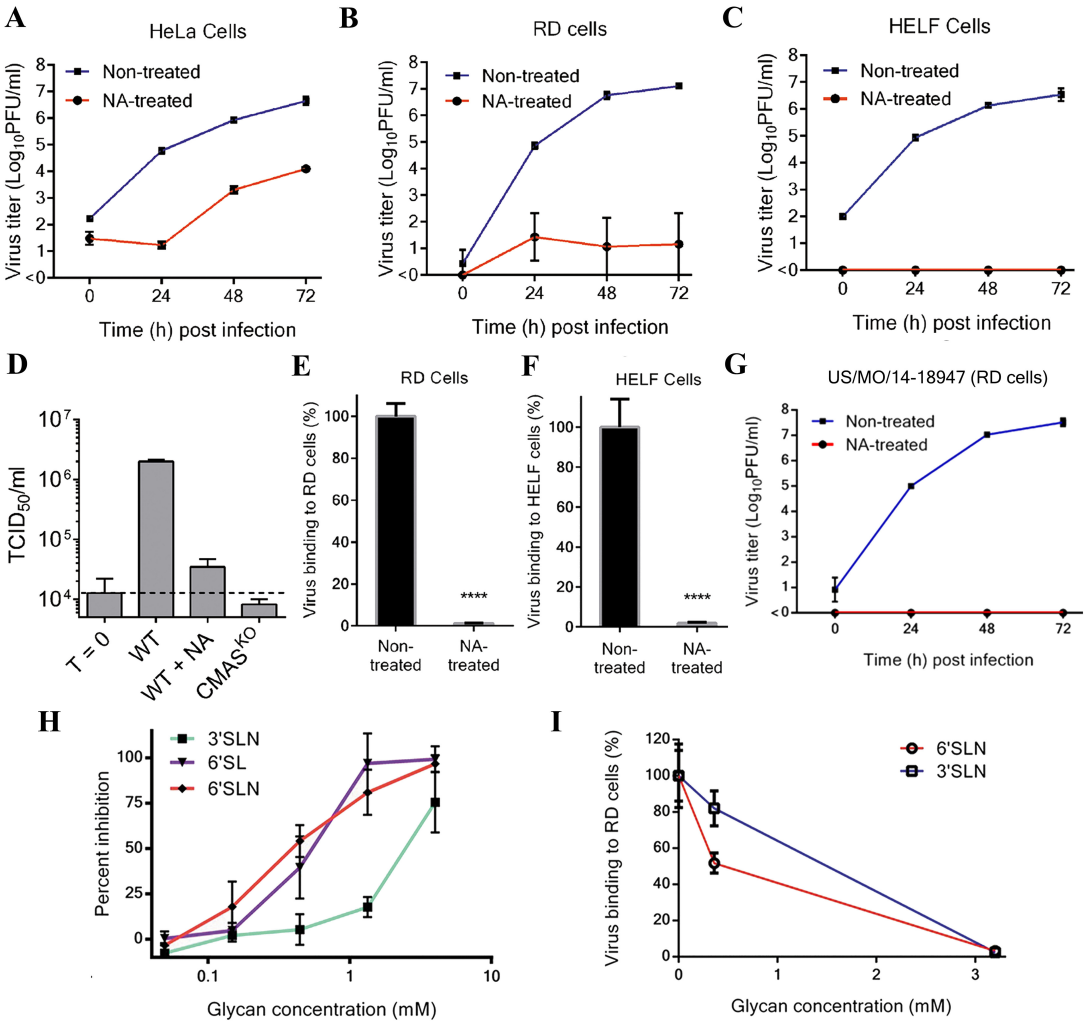

Fig. 3.1. **Cell surface sialic acid plays a crucial role in EV-D68 attachment and infection. A-C.** Growth curve of EV-D68 in susceptible cell lines cells. Neuraminidase treatment of susceptible cell lines inhibits EV-D68 (Fermon) infection. **D.** HAP1 cells (WT and CMAS KO) were infected with EV-D68 (Fermon) at an MOI of 1 and virus titers were determined at 0h (T=0) or 10h post infection. **E-F.** Histograms showing virus binding to susceptible cells. $P<0.0001$ by Student's t test. **G.** Neuraminidase treatment of RD cells inhibits the infectivity of a current EV-D68 strain (US/MO/14-18947). **H.** Preincubation of 6'SL, 6'SLN or 3'SLN with EV-D68 (Fermon) prevents killing of RD cells caused by virus infection. **I.** Preincubation of 6'SLN or 3'SLN with EV-D68 (Fermon) inhibits viral attachment to RD cells. All data are represented as mean±SD. Experiments were performed at least in triplicate.

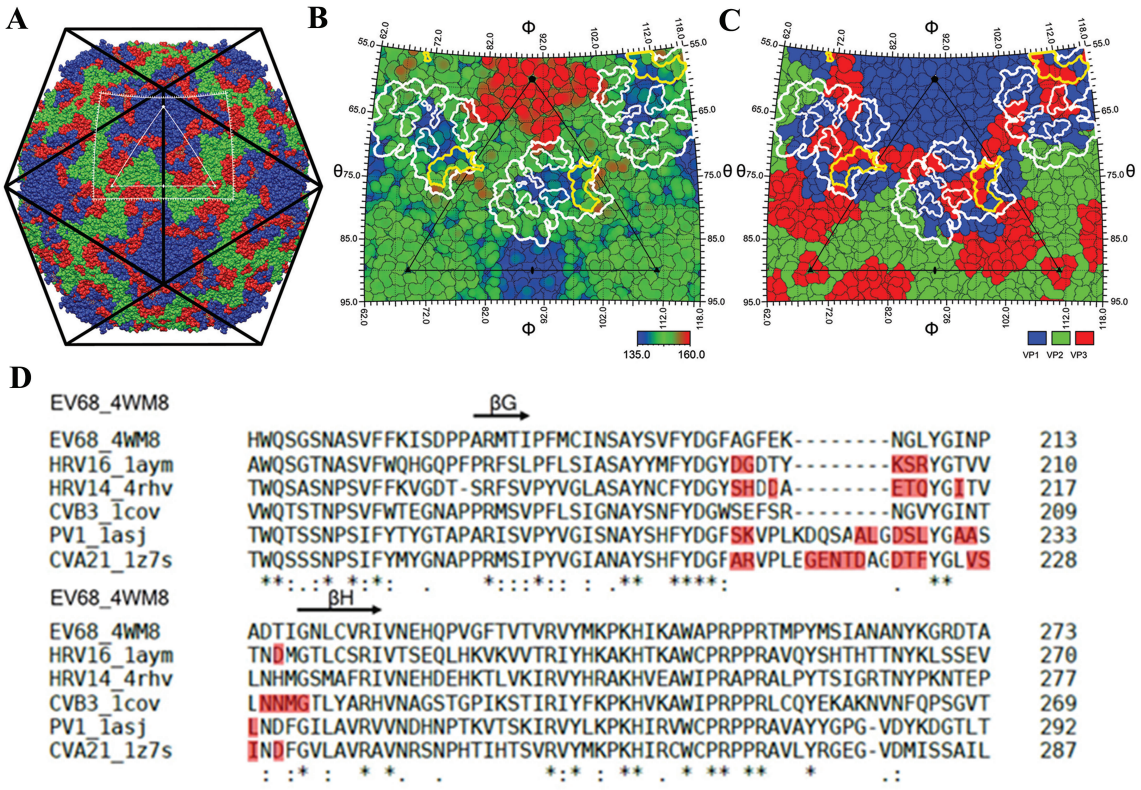

Fig. 3.2. **Sialylated receptor analogues bind to the EV-D68 canyon. A.** An EV-D68 virus particle in an icosahedral cage (black). The white triangle represents one icosahedral asymmetric unit. The surrounding white rectangular outline represents the limits of the figures shown in **B** and **C**. The thick white contour outlines the summation of five superimposed footprints of Ig-like receptors on the virus, whereas the thinner white contour represents the consensus footprint of at least four footprints. The receptors are intercellular adhension molecule-1 for human rhinovirus 14 [179], human rhinovirus 16 [179], and coxsackievirus A21 [28], CD155 for poliovirus 1 [108], and coxsackievirus and adenovirus receptor for coxsackievirus B3 [182]. Shown also is the footprint of the sialylated trisaccharides (yellow). The background is a map of the EV-D68 surface residues colored by polypeptide in **A** and **C** or colored by radial distance from the virus center in **B**. **D.** The VP1 GH loop is invariably in the footprint of Ig-like receptors used by EVs. Residues in the contact region are highlighted. Black arrows represent -strands.

Table 3.1
Data collection and refinement statistics

	EV68 – 6'SL	EV68 – 6'SLN	EV68 – 3'SLN
Data collection			
Wavelength (Å)	0.9787	0.9787	0.9787
Oscillation angle (°)	0.2	0.2	0.2
No. of frames	150	170	160
Space group	I222	I222	I222
Cell dimensions			
a, b, c (Å)	325.6, 347.1, 356.4	325.7, 347.4, 356.5	325.8, 347.2, 356.9
α, β, γ (°)	90.0, 90.0, 90.0	90.0, 90.0, 90.0	90.0, 90.0, 90.0
Resolution (Å)	50-2.32 (2.40-2.32)[a]	50-2.15 (2.23-2.15)	50-2.15 (2.23-2.15)
Unique reflections	526043 (55652)	803405 (80335)	823936 (84149)
Completeness (%)	61.4 (65.3)	74.6 (75.0)	76.3 (78.3)
Redundancy	1.9 (1.8)	1.8 (1.6)	1.7 (1.6)
Rmerge[b]	0.175 (0.722)	0.152 (0.865)	0.124 (0.529)
$I/\sigma(I)$	4.16 (1.04)	5.37 (0.89)	6.05 (1.45)
Refinement			
Resolution (Å)	50-2.32 (2.40-2.32)	50-2.15 (2.23-2.15)	50-2.15 (2.23-2.15)
No. of reflections	525999 (55490)	802817 (79585)	823388 (84396)
R factor	0.246 (0.333)	0.254 (0.327)	0.244 (0.314)
CC[c]	0.886	0.922	0.921
No. of atoms	6610	6647	6679
Protein	6296	6303	6317
Ligand	43	46	46
Water	271	298	316
RMSD bond (Å)	0.006	0.006	0.006
RMSD angle (°)	1.378	1.393	1.392
Mean B-factor/Å^2	19.3	25.1	20
Ligand B-factor/Å^2	51.6	70.6	63.7
Ramachandran plot			
Favored (%)	96.1	96.2	95.9
Allowed (%)	3.9	3.7	4.1
Outliers (%)	0	0.1	0

[a] Values in parentheses represent the highest resolution shell
[b] $R_{merge} = \sum_{hkl} \sum_i |I_i(hkl) - < I(hkl) > | / \sum_{hkl} \sum_i I_i(hkl)$
[c] Correlation coefficient

residues are also conserved in EV-D70, which is known to bind sialic acid as a cellular receptor [404]. However, enteroviruses that bind Ig-like molecules in the canyon

have quite different kinds of residues at the sialic acid binding site of EV-D68 (Table 3.2). In addition, CVA24, which utilizes sialic acid as a receptor [163], also has different kinds of residues at the EV-D68 sialic acid binding site, suggesting that sialic acid would bind to a different site on CVA24 than on EV-D68. This is consistent with the fact that Coxsackievirus A24 binds to sialic acid at a site near each five-fold axis, as shown by a previous study on the structures of CVA24 complexed with sialic acid or sialylated glycans [32]. Moreover, the infectivity of the EV-D68 strain (US/MO/14-18947) from the 2014 US outbreak (which has a lysine in position 1270) was significantly reduced in NA-treated RD cells as compared with non-treated RD cells (Fig. 3.1), suggesting that sialic acid might be a common receptor for a broad spectrum of EV-D68 strains.

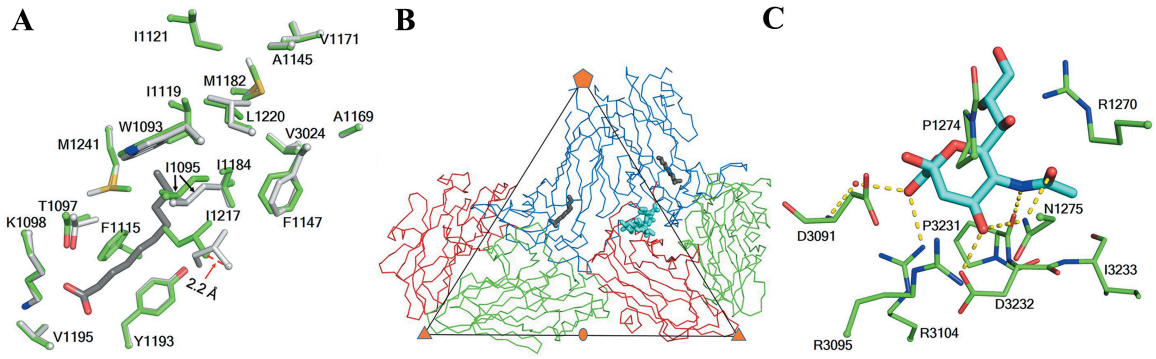

Fig. 3.3. **Binding of sialylated receptor analogues to EV-D68 displaces the pocket factor. A.** Superimposition of the amino acids lining the VP1 hydrophobic pocket in the native structure (light grey) and the receptor bound complex (green). The pocket factor in the native structure is colored grey. **B.** Two protomers of the EV-D68 capsid are represented as Cα backbones with VP1, VP2, and VP3 colored blue, green and red, respectively. The pocket factor (native structure) and the receptor analogue (receptor bound complex) are colored grey and cyan, respectively. **C.** The sialic acid moiety (Neu5Ac) (cyan carbon atoms) interacts with surrounding amino acids (green carbon atoms). A water molecule is represented by a red sphere. Dash lines indicate polar interactions. Oxygen, nitrogen and sulfur atoms in **A** and **C** are colored red, dark blue and yellow, respectively.

Table 3.2
Alignment of amino acids that interact with sialic acid in EV-D68 with the equivalent amino acids in other EVs

Receptor	Virus	Species	Amino acids[a]								
			1270	1274	1275[b]	3091	3095	3104[b]	3231[b]	3232[b]	3233
Sialic acid	EV-D68 (4WM8)[c]	EV-D	R	P	N	D	R	R	P	D	I
Sialic acid	EV-D70[d]	EV-D	R	P	N	E	R	R	P	D	I
SCARB2	EV-A71 (3ZFE)	EV-A	N	P	T	D	Q	G	S	H	I
CAR	CVB3 (1COV)[e]	EV-B	S	T	T	S	S	N	P	F	I
CD155	Poliovirus 1 (1ASJ)[e]	EV-C	-[f]	-	-	D	S	N	T	H	I
ICAM-1	CVA21 (1Z7S)[e]	EV-C	-	-	-	D	S	N	P	H	I
Sialic acid	CVA24 (4Q4W)	EV-C	-	-	-	D	Q	N	N	H	I
ICAM-1	Rhinovirus A16 (1AYM)[e]	RV-A	S	H	N	-	A	S	D	L	H
ICAM-1	Rhinovirus B14 (4RHV)[e]	RV-B	N	V	I	-	K	Q	Q	T	I

[a] Numbering based on the amino acid sequence of the EV-D68 Fermon CA 62-1 strain
[b] The amino acid provides polar interaction with the Neu5Ac moiety through side chain or main chain
[c] Virus name followed by PDB accession number in the parenthesis
[d] Strain J670/71
[e] The virus uses an Ig-like molecule as a cellular receptor
[f] This symbol represents deletion at a given position

3.4.3 Receptor specificity

Different conformations were observed between the 6'SLN and 3'SLN receptor analogues that might explain why EV-D68 preferentially recognizes sialic acid receptors with an α-2,6 linkage [406] (Fig. 3.4). These are consistent with the fact that 6'SLN prevents EV-D68 attachment and inhibits killing of RD cells more efficiently than does 3'SLN. This suggests that EV-D68 might have a tropism towards the human upper respiratory tract, where α-2,6 linked sialic acid molecules are more abundant and the temperature is optimal for EV-D68 growth than in the lower respiratory tract [401].

The receptor analogues used here are trisacchrides and presumably could be a component of the glycoconjugate on the authentic receptor that might be a glycoprotein or glycolipid. However, a previous glycan array analysis [406] used 3'SLN and 6'SLN covalently linked to bovine serum albumin (BSA) through the GlcNAc moiety. This analysis found that the Fermon strain has a limited binding affinity for 3'SLN linked to BSA compared to 6'SLN linked to BSA. In the present study, structures of EV-D68 complexed with these sialylated glycans showed that 3'SLN adopts a linear conformation such that it is lying against the eastern rim of the virus canyon (Fig. 3.4). Thus, if 3'SLN linked to BSA were to bind to the same binding site, the virus would impose a large steric hindrance that would not accommodate the BSA. In contrast, 6'SLN (as also 6'SL) adopts a bent conformation such that the GlcNAc moiety, which is furthest away from the Neu5Ac moiety, is well clear of the virus surface which, therefore, permits the presence of BSA (Fig. 3.4). Therefore, steric hindrance might limit the binding of the virus to α-2,3 but not α-2,6 linked sialic acid on the authentic sialylated receptors.

3.4.4 Sialic acid receptor binding causes the ejection of the pocket factor

The root mean square deviation (r.m.s.d.) between all the equivalent atoms of the EV-D68 native structure and the EV-D68 bound with any of the three receptor

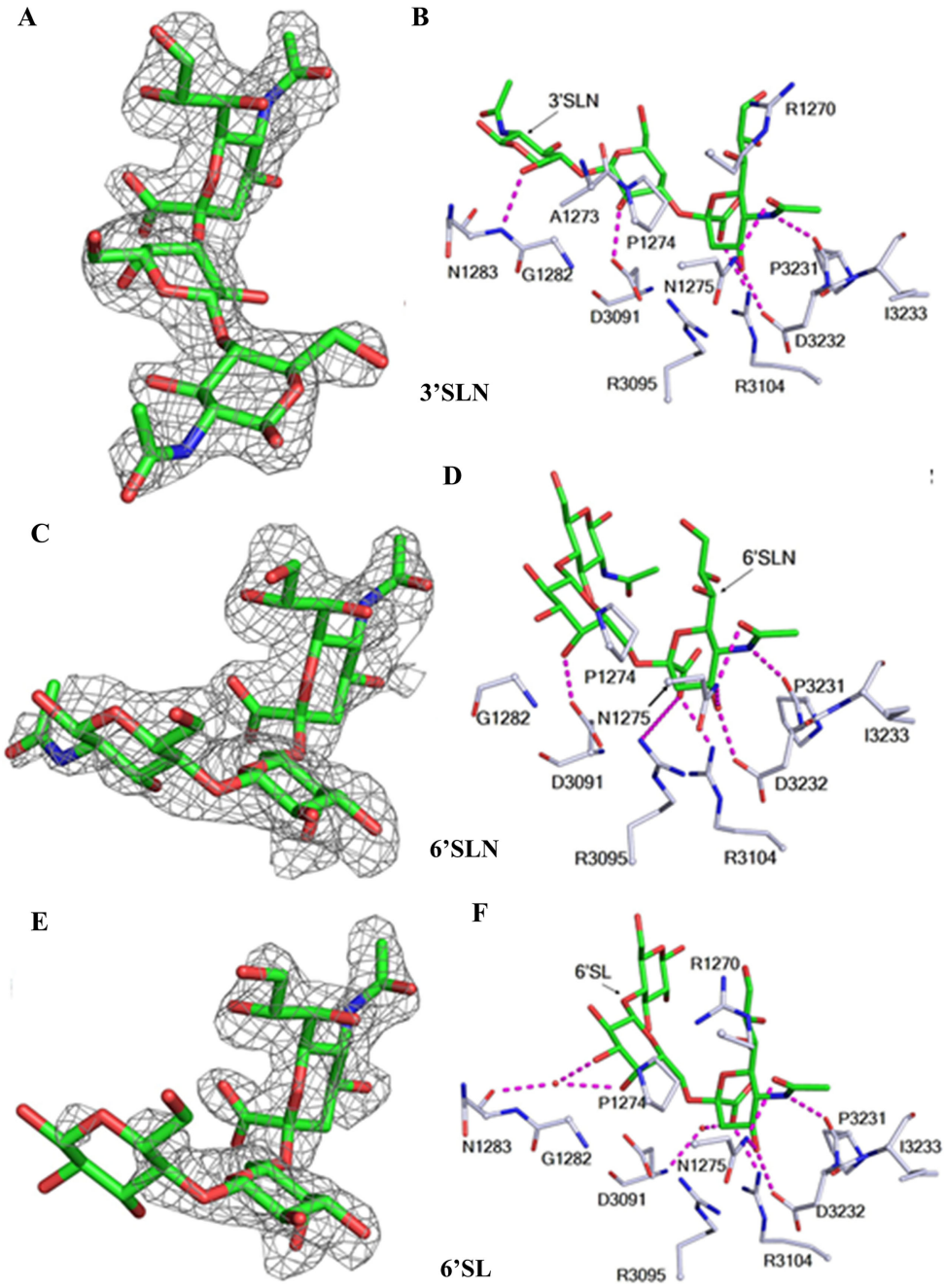

Fig. 3.4. **Receptor specificity.** Receptor analogues 6'SL (**A-B**), 6'SLN (**C-D**), and 3'SLN (**E-F**) are colored using green (carbon), red (oxygen) and blue (nitrogen). **A, C,** and **E** show these compounds in their NCS averaged difference map densities (3.0σ) all oriented to place the icosahedral two-fold axis perpendicular to the page. **B, D,** and **F** show their interaction with the virus, oriented to resolve the projected atoms. Dashed lines indicate polar interactions.

analogues is about 0.4 Å (Table 3.3). Nearly all main chain atoms that were displaced by more than four r.m.s.d. were in the loops that form the connecting region between the sialic acid binding site and the VP1 hydrophobic pocket. The same conformational changes occurred in each of the three complexes. The conformational changes included the VP1 GH loop located at the boundary between the VP1 hydrophobic pocket and the canyon. Similar changes in the VP1 GH loop occur when CD155 binds to poliovirus [108]. In particular, the Cα atom of residue Ile1217 moves 2.2 Å into the pocket (Fig. 3.3). This results in a conformation of the VP1 GH loop much like that in the RV-B14 structure where no pocket factor is present [13]. Thus binding of sialylated receptor analogues onto EV-D68 causes a partial collapse of the pocket, leading to the displacement of the pocket factor (Fig. 3.5). However, in these sialylated receptor analogue bound structures, the VP4 density is still present and the particle size is not altered, indicating that sialylated glycan binding of EV-D68 at room temperature represents an initial event of the viral entry process. In contrast to the conformational changes that occur when a sialic acid receptor binds into the canyon, binding of glycan receptors to other binding sites on picornaviruses do not cause further conformational changes [32, 415–417] (Fig. 3.6).

Table 3.3
Root mean square deviations[a] between two given structures with or without a bound receptor analogue

Structure A	Structure B	Overall	3086-91[b]	3178-79[b]	1149-53[b]	1211-19[b]
D68-6'SL	D68	0.40	1.93	2.28	2.72	1.91
D68-3'SLN	D68	0.36	1.78	2.31	2.65	1.81
D68-6'SLN	D68	0.35	1.80	2.19	2.24	1.83
D68-6'SL	D68-3'SLN	0.10	0.24	0.05	0.21	0.20
D68-6'SL	D68-6'SLN	0.11	0.21	0.48	0.48	0.21
D68-3'SLN	D68-6'SLN	0.06	0.09	0.33	0.34	0.09

[a] r.m.s.d. values (Å) were calculated using main chain atoms (N, Cα, C, O).
[b] Numbered according to the amino acid sequence of the EV-D68 strain Fermon CA 62-1.

The contact region for all three receptor analogues is the VP1 C-terminus, VP3 C-terminus and VP3 CD loop. This site is about 28 Å from the VP1 hydropho-

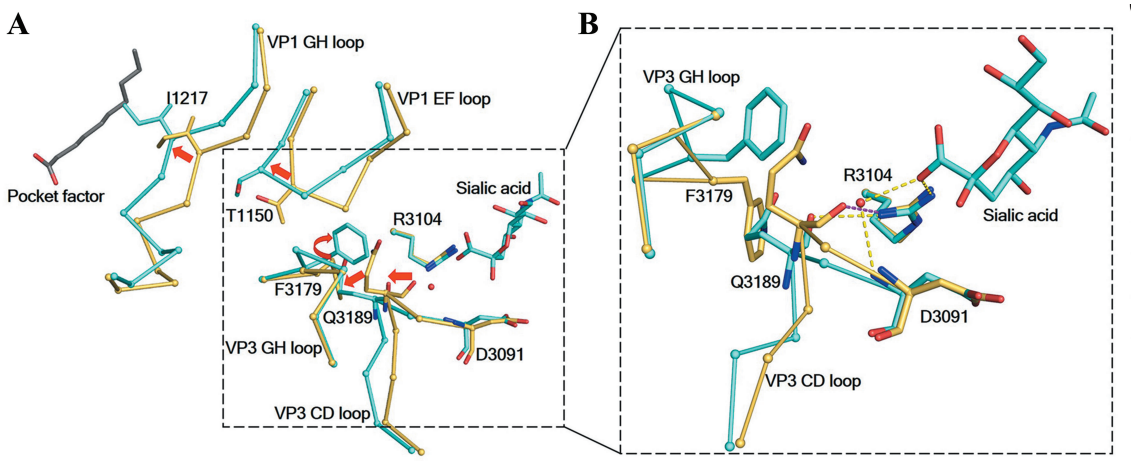

Fig. 3.5. **Competition between the sialic acid receptor and the pocket factor. A.** The conformational changes of the virus when sialylated receptor analogues bind the virus and eject the pocket factor. Amino acids in the native and in the receptor bound structures are shown in yellow and cyan, respectively. A water molecule is shown as a red sphere. Dash lines represent polar interactions. Red arrows indicate movements of the four loops. **B.** Enlarged component of marked region in a shown in a slightly different orientation.

bic pocket in the same protomer and about 30 Å away from the VP1 hydrophobic pocket in a neighboring protomer (Fig. 3.3). In contrast, all Ig-like molecules interact directly with the VP1 GH loop in the canyon (Fig. 3.2). Thus, binding of the sialylated receptor analogues displaces the pocket factor through long range structural rearrangements of the virus. The region connecting the sialic acid receptor binding site and the VP1 hydrophobic pocket is formed by the VP3 CD loop, the VP3 GH loop, the VP1 EF loop and the VP1 GH loop. These loops undergo the only significant conformational changes mentioned above (Table 3.3). Thus the signal of receptor binding must be transmitted to the hydrophobic pocket through the structural rearrangements of these loops (Fig. 3.5). These conformational changes might be initiated by charge repulsion between the negatively charged carboxylate group of Neu5Ac and the main chain carbonyl group of Gln3089. In partial agreement with this mechanism, two of the five mutations that resulted in the resistance of EV-D70 to

neuraminidase treatment of HeLa cells occur in the VP1 EF loop and GH loop [418]. Furthermore, the pocket factor was missing and the hydrophobic pocket was collapsed in A particles of other enteroviruses [212], while three of the four loops mentioned above undergo dramatic conformational changes during virus expansion to A particle in the uncoating process [209]. In summary, binding of sialic acid receptor analogues to EV-D68 ejects the pocket factor and therefore presumably destabilizes the virus to facilitate viral uncoating.

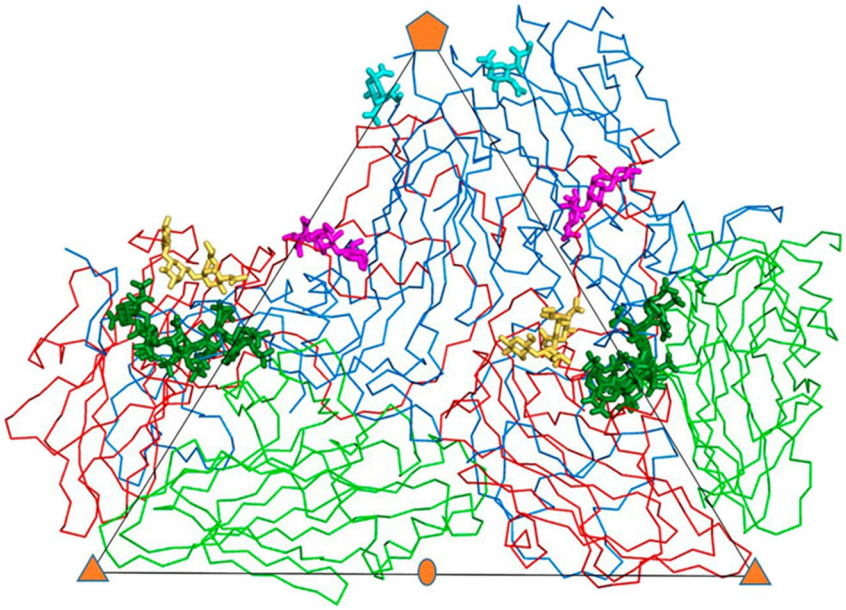

Fig. 3.6. **Comparison of carbohydrate receptor binding sites on picornaviruses.** All known picornaviruscarbohydrate receptor structures were superimposed. Two adjacent protomers of the EV-D68 capsid are represented as Cα backbones. The triangle outlines an icosahedral asymmetric unit of the virus capsid. VP1, VP2, and VP3 are colored blue, green, and red. Carbohydrate receptors are shown as sticks. Cyan, Neu5Ac (CVA24 variant, PDB 4Q4X); magenta, 3-sialyllactose (equine rhinitis A virus, PDB 2XBO); yellow, 6'-sialyllactose (EV-D68, PDB 5BNN); dark green, heparan sulfate (foot-and-mouth disease virus, PDB 1QQP).

3.5 Discussion

In the present study, a recent clinical isolate of EV-68 (US/MO/14-18947 from the 2014 US outbreak) was shown to have sialic acid dependency, as is the case for the prototype Fermon strain and another early strain isolated in the 1970s [405]. Furthermore, RD and HeLa cells were found to be susceptible to infection by both the Fermon and US/MO/14-18947 strains. In particular, these two strains exhibited similar growth kinetics when using RD cells (Fig 3.1). Thus the similarities between these two strains suggest that the results described here might be equally applicable to at least some of the recent isolates. However, the Fermon strain is likely to have undergone some changes since its isolation in 1962 due to a lengthy passage history, which may have changed its receptor binding properties and/or fitness in susceptible cell lines [419]. Therefore, it is possible that some recent strains may have potentially altered receptor usage. It is also probable that some recent strains may not replicate as efficiently as the Fermon strain in cells lines such as RD, HeLa and HELF cells examined here.

Although EV-D68 mainly causes respiratory infections, some recent isolates were associated with neurological illness such as acute flaccid myelitis (AFM) [420–425]. These recent clinical isolates are all in the same clade as US/MO/14-18947 isolated from a patient with respiratory illness but who did not have a neurological disease [421]. The amino acid sequences of the structural proteins of these isolates share approximately 99% sequence identity to that of US/MO/14-18947. Furthermore, the 51 strains used for sequence alignment, as mentioned above, include strains that were associated with neurological diseases. This suggests that these strains might also be sialic acid dependent, consistent with the fact that most EV-D68 associated AFM cases had respiratory infections [421].

Complementary to the biochemical and structural data presented here, a recent report found that host proteins involved in sialic acid biosynthesis, transport, and conjugation play crucial roles in EV-D68 infection using a haploid genetic screening

[426]. It was also discovered that three recent strains of EV-D68 did not appear to depend on cell surface sialic acid for infections [426]. These results suggested the presence of potential alternative receptors for EV-D68. Ongoing studies have shown that one of the three strains can use both sialic acid and glycoamineglycans (particularly heparan sulfate (HS)) as a receptor. The property of binding to HS has been found to be acquired in the process of virus adaptation to growth in RD cells (Personal Communications with Jim Baggen). These observations support the point that sialic acid represents a common receptor for many EV-D68 strains, while alternative receptors may be utilized by some EV-D68 strains. Nevertheless, sialic acid is only an essential moiety on the authentic cellular receptor molecules, which might be sialic acid containing glycoproteins or glycolipids. A glycoprotein, namely ICAM-5, has recently been identified as a cellular receptor for EV-D68 [427]. Both the protein component and the sialic acid terminated glycan component of ICAM-5 are important for ICAM-5 dependent EV-D68 infection. ICAM-5 is specifically expressed in neurons, which might have some relevance to the pathogenesis of EV-D68.

In summary, the structural and functional analyses showed that sialic acid is a functional cellular receptor for EV-D68. The prevalence of sialic acid in the human respiratory tract might allow efficient replication of EV-D68 that leads to human respiratory infection. Despite chemical and structural differences from the Ig-like receptors, the sialic acid receptor binds to the virus canyon and causes the expulsion of the pocket factor, suggesting that the enterovirus canyon is a sensor for receptors. Thus, the canyon transmits signals initiated by receptor binding to release the pocket factor, regulating the conformational state of EVs from being stable for virus transmission to being unstable during virus entry.

4. CRYO ELECTRON MICROSCOPIC ANALYSES OF A HUMAN RHINOVIRUS C

Most of the data and text in this chapter are taken from [428] and have been highlighted by a black, vertical line in the right margin below.

4.1 Chapter Abstract

Isolates of rhinovirus C (RV-C), a recently identified Enterovirus (EV) species, are the causative agents of severe respiratory infections among children. Moreover, the RV-C have been linked to 50-85% of hospital-level childhood asthma exacerbations that can lead to significant adult respiratory problems. Nevertheless, there are currently no effective antiviral treatments or vaccines available. The RV-C have been refractory to structure determination because they are difficult to propagate in vitro. This chapter presents the cryo-EM atomic structures of the full virion and native empty particle (NEP) of RV-C15a. The virus has 60 "fingers, on the virus outer surface that probably function as dominant immunogens. Since the NEPs also display these fingers, they may have utility as vaccine candidates. A sequence-conserved surface depression adjacent to each finger forms a likely binding site for the sialic acid on its receptor. The RV-C, unlike other EVs, are resistant to capsid-binding antiviral compounds because the hydrophobic pocket in VP1 is filled with multiple bulky residues. These results define potential molecular determinants for designing anti-viral therapeutics and vaccines. This work also provides a common work flow for cryo-EM structure determination of similar viruses.

4.2 Introduction

A number of enteroviruses have been structurally characterized by X-ray crystallography [2, 13, 14, 429], establishing the general mechanisms for virus infection and for the development of effective anti-EV therapeutics. Nevertheless, rhinovirus C (RV-C), a newly discovered species among the EVs, remains enigmatic.

RV-C viruses (55 types), together with RV-A and RV-B viruses (about 108 types), are the leading cause of common colds [12]. However, the RV-C might be associated with more severe respiratory infections among children than any other known rhinoviruses [430,431]. In contrast to other RV, the RV-C utilize cadherin related family member 3 (CDHR3) as a cellular receptor [432]. This childhood asthma susceptibility gene product is expressed in the human lower respiratory tract [433]. In line with this etiology, the RV-C cause a significantly higher rate of lower respiratory tract infections in children than in adults [434] and are directly associated with childhood asthma exacerbations [431]. Similar to influenza viruses, RV-C infections peak in winter months [435]. Currently, there are no vaccines or effective antiviral treatments available.

RV-C isolates have been refractory to structural characterization since their discovery in 2006 [436] because of an inability to infect standard tissue culture (e.g., HeLa) [437]. Only modeled structures, based on amino acid sequence comparisons, have been available to aid biological investigations [437–440]. single-particle cryo-electron microscopy (cryo-EM) has now emerged as a powerful method for determining near atomic resolution (better than 4 Å) structures of macromolecular assemblies [441]. Cryo-EM requires only limited amount of sample without intensive purification, offering advantages over X-ray crystallography in structural studies of samples that are difficult to produce.

This chapter reports atomic cryo-EM structures of the full and native empty particles (NEP) of the cell-adapted RV-C15a strain. These structures highlight novel immunogenic surfaces, a probable binding site for the glycosylated CDHR3 receptor

molecule and the requirements for antiviral compound resistance. The external surface of both types of particles is almost identical. Thus the RV-C NEPs represent potential vaccine candidates. The present findings also identify targets for designing anti-RV-C therapeutics.

4.3 Materials and Methods

4.3.1 Growth and purification of RV-C15a

The following experiments were performed by Marchel Hill at the Palmenberg laboratory (University of Winsconsin - Madison). The seed of RV-C15a was provided by Yury Bochkov from the same Institute. RV-C15a (adapted) is a virus preparation derived by serial passage (10x) of recombinant C15 virus (12), in HeLa-E8 cells, a lentivirus-transduced line expressing the full-length human CDHR3 gene (Tyr529) linked to a GFP reporter sequence [432]. To produce viruses for structure determination, HeLa-E8 cells were infected with RV-C15a at 34°C. At 40h post infection after complete cytopathic effect (CPE) was observed, infected cells (2.4 x 10^{10}) were supplemented with HEPES (to 50 mM, pH 7.2) and then subject to multiple freeze-thaw cycles (3x). Clarified supernatants were treated with RNAse A, then concentrated by pelleting through 30% sucrose, before resuspension and being assayed for titer [432, 442]. The procedure gave a sample of RV-C15a at about 1.2 x 10^{10} PFUe (by quantitative reverse transcription PCR (qRT-PCR) using HeLa-E8 cells) that is equivalent to 125 μg RNA-containing, infectious particles, assuming a particle-to-PFU ratio of 200 PFUe is the PFU-equivalent calculated based on calibrated standard curves for RV-A16/RV-B14 viruses. .

4.3.2 Characterization of two forms of RV-C15a particles

The following experiments were performed by Kelly Watters from the Palmenberg laboratory. A sample of RV-C15a, as prepared for structure determination, was sed-

imented through a 10-40% sucrose gradient (103,600 x g (Beckman SW41 Ti rotor) for 3h at 4°C). Fractions (1 ml) were collected (from the top) and then probed for VP2/VP0 content by Western blot analyses using anti-RV-C15-VP2 mouse monoclonal antibody, clone No. 517 (kindly provided by MedImmune Inc., Gaithersberg MD). The fractions were also tested for infectivity according to CPE (38), and for RNA content by qRT-PCR (8).

4.3.3 Cryo-electron microscopy

Aliquots of 2.8 μL of purified RV-C15a sample were applied onto glow-discharged holey carbon EM grids (400 mesh, Ted Pella Inc.). Grids were blotted for about 8s at a relative humidity of 80% and then plunge-frozen in liquid ethane cooled down by liquid nitrogen using a Cryoplunge 3 system (Gatan). Movies of frozen RV-C15a particles embedded in vitreous ice were collected at liquid nitrogen temperature using a Titan Krios transmission electron microscope (FEI) operated at 300 kV and equipped with a Gatan K2 Summit direct electron detector (3838 x 3710 in physical pixels). All the movies were automatically recorded in super resolution mode using Leginon [340] at a nominal magnification of 14,000x and with a defocus range of 0.7-3.5 μm. This resulted in a super resolution pixel size of 1.04 Å/pixel. The dose rate was approximately 8e^-/pixel/s. For each movie, the total electron dose was about 25.7 $e^-/Å^2$ that was fractionated into 70 frames with an exposure time of 200 ms per frame.

4.3.4 Image processing

Cryo-EM data were collected of the RV-15a particles. A total of 2,979 movies were subjected to whole-frame motion correction using a modified version of MotionCorr [331] as modified by Wen Jiang (Purdue). This process was integrated into the Appion data processing pipeline [443]. Aligned frames were subsequently summed to obtain individual micrographs. Micrographs that had ice contamination or severe drift

were discarded. The remaining micrographs were used for estimating of the contrast transfer function (CTF) parameters using CTFFIND3 [444]. For a part of the data set particles were selected semi-automatically. In this process the program e2boxer.py in the EMAN2 package [335] picked particles based on several templates (derived from manually selected particles). The selection was then confirmed by visual inspection, For the rest of the data set automatic particle selection was accomplished by using DoG picker [445]. The final number of selected particles was 24,882. Individual particle images were boxed, extracted and subjected to reference-free 2D classification into 156 classes using the program Relion [337]. Some of these classes were clearly composed of full particles, some of empty particles and some were just junk. This yielded 13,390 full particles and 5,324 empty particles. Particles were re-boxed and re-extracted from the micrographs using jspr [339,446]. CTF parameters of the particles from each micrograph were estimated using fitctf2.py [447].

Images of the full particles were divided into two half data subsets. A truly independent 3D reconstruction strategy, using the program jspr [339], was applied to each of the two subsets assuming icosahedral symmetry. For each subset, eightfold binned particle images (squares of 88 original pixels separated by 1.04 Å were averaged to represent one pixel with a spacing of 8.32 Å) were used to compute ten initial 3D reconstructions by assigning random initial angles [316] to each of 150 particle images. Refinements were performed by searching for the best orientation and particle center of each particle image relative to the ten current 3D reconstructions. Three of these structures were selected for further refinement with all the available particle images in the half subset. After multiple iterations these structures converged to roughly the same reconstruction. One of these structures was randomly chosen to extend the refinement with 4-binned, then 2-binned data and finally unbinned data. At this point, anisotropic magnification distortion remained the major resolution limiting factor. Ten images of polycrystalline gold particles were taken at a nominal magnification of 14,000x in super resolution mode. Fourier transform of these gold particle images gave powder diffraction like patterns that were used to estimate parameters

of anisotropic magnification distortion [448]. The estimated degree of distortion and angle were 2.87% and 31.3°, respectively. These parameters were then employed to correct anisotropic magnification distortion for individual particle images using jspr [449]. Subsequent refinement of particle center, orientation, defocus, astigmatism, scale and beam tilt using jspr led to the final optimal reconstructions in terms of resolution. The Fourier shell correlation (FSC) [450, 451] between the half maps independently calculated from the two subsets was used to monitor convergence. The FSC can be expressed as

$$FSC = (\sum_{r \in r_i} \mathbf{F_o}(r)\mathbf{F_e^*}(r))/\sqrt{\sum_{r \in r_i} |\mathbf{F_o}(r)|^2 \sum_{r \in r_i} |\mathbf{F_e}(r)|^2} \tag{4.1}$$

where r is spatial frequency, and $\mathbf{F_o}(r)$ and $\mathbf{F_e}(r)$ are structure factors of the two half maps. $\mathbf{F_e^*}(r)$ is the complex conjugate of $\mathbf{F_e}(r)$, and r_i represents a shell in Fourier space. The same procedures were used for determining the 3D structure of the empty particles. A 2.79 Å resolution map of the full particle was reconstructed using 8,973 particles, and a 3.16 Å resolution map of the empty particle was reconstructed using 3,614 particles. The map resolution was determined based on the FSC between the two half maps (masked with a soft mask) independently calculated using the two half data subsets following the 0.143 cut-off criterion [452, 453]. To further validate the map resolution, phase randomized (beyond 5 Å) data were refined using the same procedures as were used for the original data that were not phase randomized. A true FSC curve [454] was calculated using the FSC curve based on the original data and the FSC curve based on the phase randomized data. The full and empty particle maps were sharpened [452] using a B factor of -108.6 Å^2 and -122.2 Å^2, respectively. The pixel size of the micrographs collected at 14,000x in superresolution mode was verified in the following way. In essence, a map was calculated the homologous RV-A16 (or RV-B14) coordinates of the capsid by specifying 2.8 Å resolution. Real space correlation coefficients were calculated between the resultant RV-A16 map and the EM map of RV-C15a (full particle) by varying the pixel size of the RV-A16 map

from 0.94 Å/pixel to 1.14 Å/pixel (with an increment of 0.01 Å/pixel). This was performed using Chimera [400]. The highest correlation coeffcient was achieved when the RV-A16 map had a pixel size of 1.04, thus verifying the pixel size of the RV-C15a electron micrographes.

4.3.5 Model building and refinement

For the full particle structure, a predicted atomic structure of the RV-C15 (13) (including coordinates for a protomer, VP1-VP4) was manually fitted into a region of the final EM map that corresponds to one protomer of the capsid using Chimera [400]. Atomic positions were refined using Phenix [397] in real space. The correlation coefficient between the final EM map and a map calculated based on the coordinates was improved in this process. Model statistics including bond lengths, bond angles and all-atom clash, rotamer statistics, and Ramachandran plot statistics were also monitored. This was followed by model rebuilding with the program Coot [394]. The combination of real space refinement in Phenix and model rebuilding in Coot were repeated multiple times to achieve an optimized fit between the coordinates and the final EM map. At this point, the coordinates fit well into the densities by visual inspection.

Next, a mask, which included all grid points within a radius of 5 Å around each atom, was employed to cut out densities from the final EM map using the CCP4 [398] program suite. The resultant segment of the final EM map was placed into a pseudo crystallographic unit cell (P1 space group) and was back transformed into pseudo structure factors (including both amplitudes and phases). The coordinates were then subjected to refinement of individual B factors, atom positions and occupancy against the pseudo structure factors using standard reciprocal space refinement procedures in Phenix [397]. R factors were monitored during the refinement cycles. Only the coordinates were refined, whereas the map was kept constant. Subsequently, the coordinates were refined in real space against the final EM map by applying non-

crystallographic symmetry (60-fold) constraints using Phenix [397]. Validation of the final coordinates was based on the criteria of MolProbity [396]. The full particle atomic model (excluding VP4 and the VP1 N-terminal residues 1101-1160) was used as a starting atomic model for model building and refinement of the empty particle structure.

As a further validation of the EM map resolution and of the fitting between the atomic model and the final EM map, a density map was calculated based on the atomic model specifying a resolution of 2.79 Å for the full particle structure and 3.16 Å for the empty particle structure. An FSC was computed between the resultant density map and the final EM map. The resolution determined using 0.5 FSC as a cut-off was 2.85 Å (full particle) and 3.24 Å (empty particle). Oligomers were generated using VIPERdb [399]. Figures were made using Chimera [400] and Pymol (https://www.pymol.org/).

4.4 Results

4.4.1 Production of RV-C15a viruses

Recently, a recombinant RV-C15 virus [437], adapted for tissue culture growth by serial passage in HeLa-E8 cells [432] (a transduced HeLa cell line expressing CDHR3) led to new protocols for enhanced virus yields. The derivative, RV-C15a, represents a cell-adapted, uncloned population. The consensus sequence of this population differs in the capsid region from that of RV-C15, primarily by a single, high-frequency, nucleotide polymorphism. The substitution converts residue 1125 from Thr to Lys. (The numbering convention follows what was described for EV-D68 in Chapter 3.) In this chapter, an RV-C15a sample, purified only by sucrose cushion sedimentation, was used for cryo-EM structure analysis. To obtain a minimum of five to six particles per micrograph, given the high dilution of the sample, data collection was carried out at a low magnification. Specifically, movies of frozen RV-C15a particles within a thin layer of vitreous ice were recorded at a nominal magnification of 14,000x using a Gatan

K2 Summit direct electron detector. However, the trade-off was a low signal-to-noise ratio and a high anisotropic magnification distortion compared to what would be the case were high magnifications used for data collection.

4.4.2 Biochemical characterization of two forms of particles

Cryo-EM micrographs of RV-C15a showed the presence of two major forms of particles. One form lacked density at their centers and another form had density at their centers (Fig. 4.1). When fractionated on sucrose gradients, these types of particles separated from each other. One form was full, infectious virions that contained VP1, VP2, VP3 and VP4 whereas the other form (about 30% of all particles) was native empty particles (NEP) that had VP1, VP3, and uncleaved VP0, as shown by western blot analyses using an antibody against VP2 (Fig. 4.1). Unlike the full virions, NEPs were devoid of viral RNA and had no infectivity to HeLa-E8 cells (Fig. 4.1).

4.4.3 Cryo-EM structure determination

The procedures for cryo-EM structure determination is shown in Fig. 4.2. In essence, images of full and empty particles were separated by reference-free 2D classification using the program Relion [337]. A truly independent procedure of 3D reconstruction was employed to avoid overfitting to noise [339, 446]. Essentially, initial model calculations, low resolution refinements and high resolution refinements were performed independently for each of the two half-data subsets. Parameters of anisotropic magnification distortion, a major resolution limiting factor for large assemblies (e.g., viruses), were estimated using powder diffraction patterns of polycrystalline gold particles [448]. The resultant parameters were used in the program jspr for correcting anisotropic magnification distortion on individual particles [449] (Fig. 4.3). Refinements of particle center, orientation, defocus, astigmatism, scale, and beam tilt resulted in icosahedral reconstructions of 8,973 full particles and 3,614 empty particles at 2.8 Å and 3.2 Å resolution, respectively (Table 4.1 and Fig. 4.4).

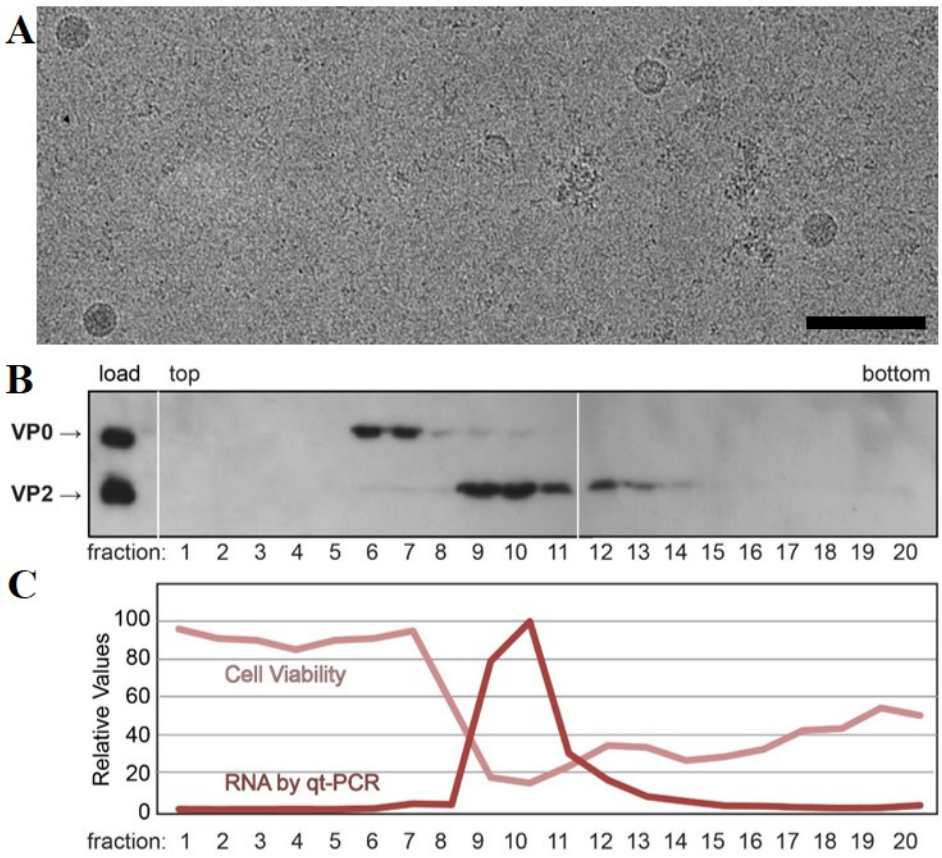

Fig. 4.1. **Characterizations of two forms of RV-C15a particles. A.** A typical region of a cryo-EM micrograph shows the presence of full and empty RV-C15a particles. The micrograph was recorded at a defocus of 3.1 μm. It was four-fold binned and low passed to 15 Å resolution for better visualization. The scale bar indicates 100 nm. A sample of RV-C15a was sedimented through a sucrose gradient. Fractions (1 ml) were collected (from the top) and then probed for VP2/VP0 content by Western blot analyses (**B**) using mouse anti-RV-C15-VP2. These fractions were also tested for infectivity according to cytopathic effect (**C**), and for RNA content by qRT-PCR (**C**)

The resolution of the maps was estimated by calculating the Fourier shell correlation between the two half maps, using 0.143 as a cut-off [452] (Fig. 4.5).

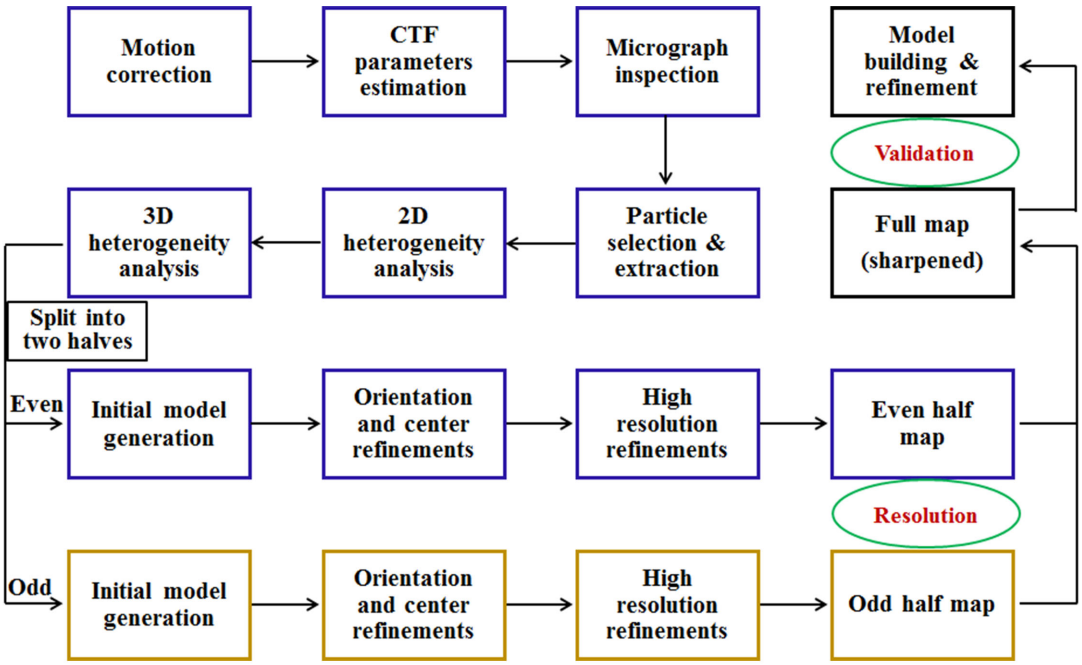

Fig. 4.2. **Workflow of cryo-EM structure determination in the current thesis.** Heterogeneity analysis refers to classification of experimental EM images based on similarity at the level of 2D image or at the level of 3D reconstruction [455]. The assumption is that all datasets show a certain degree of particle heterogeneity. This process allows for "virtual" purification of a heterogeneous particle population to yield homogeneous subpopulations of particles. These subpopulations are then treated as independent particle sets in the following image processing procedures. Included in typical high resolution refinements are parameters for particle center, particle orientation, astigmatism, defocus, scale, and anisotropic magnification distortion.

4.4.4 RV-C15a has a spiky structure

The structure of the RV-C15a full particle has 60 dominant spike-like protrusions, or fingers, on the outer surface of the virion (Fig. 4.6). In contrast, all other EV structures have smoother, spherical surfaces (Fig. 4.6). Each RV-C15a finger, located at the juncture between VP1, VP2 and VP3 that form a protomer, is formed by the VP1 C-terminal residues 1252-1265 as well as residues 2136-2138 and 2160-2165 that

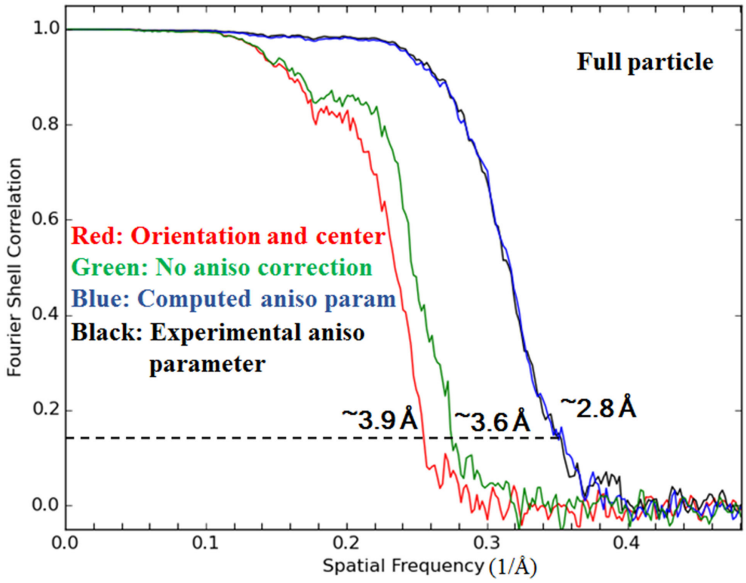

Fig. 4.3. **Anisotropic magnification distortion is a major resolution limiting factor.** Resolution of EM reconstructions was estimated using FSC (0.143 as a cut-off) between two independent half-maps. Shown are FSC curves for reconstructions that were computed by varying parameters during refinement process. All parameters refer to a combination of those for for particle orientation, particle center, defocus, scale, astigmatism, beam tilt, and anisotropic magnification distortion (or aniso in short). Red: only parameters for particle orientation and center were included; green: all parameters but no aniso were included; blue and black: all parameters were included, where aniso was determined computationally by matching projections of a 3D EM reconstruction with experimental particle images (blue) or experimentally (black) using polycrystalline gold particles.

form part of the VP2 EF loop (Fig. 4.6). The quality of the density for the finger is not as good as is typical for the rest of the virus, presumably because this density is on the periphery of the virus. It is noteworthy that residues 2160-2165 are highly variable among alignments of RV-C sequences [439]. This segment corresponds to the neutralizing immunogenic site NIm-II on the RV-B14 structure [13, 439]. The VP1 contribution to the finger, residues 1252-1265, is an RV-C-specific insertion. This region, is also conserved in length but not in sequence among all members of the RV-C (Fig. 4.7).

Table 4.1
Data collection and refinement statistics

	RV-C15a full	RV-C15a empty
Data collection and processing		
Microscope	Titan Krios	Titan Krios
Accelerating voltage (kV)	300	300
Camera	Gatan K2 Summit	Gatan K2 Summit
Pixel size[a] (Å/pixel)	1.04	1.04
Dose rate (e^-/pixel/s)	8	8
Total dose (e^-/Å^2)	25.7	25.7
Particle No. for final reconstruction	8973	3614
Resolution[b] (Å)	2.79	3.16
Map sharpening B factor (Å^2)	-108.6	-122.2
Model Statistics		
Correlation coefficient (around atoms)[c]	0.885	0.88
Number of atoms		
Protein	6221	6007
Water	60	0
Avg. B-factor (Å^2)	24.1	31.7
r.m.s deviations[d]		
Bond lengths (Å)	0.01	0.01
Bond angles (°)	0.96	0.944
Ramachadran plot[d]		
Favored (%)	93.4	92
Allowed (%)	6.5	7.6
Outliers (%)	0.1	0.4

[a] Pixel size in super resolution mode. The physical pixel size is 2.08 Å/pixel
[b] Resolution was determined by Fourier shell correlation between two half-maps using 0.143 as a cut-off.
[c] Real space correlation coefficient (around atoms) between final EM map and a density map calculated based on the coordinates.
[d] Based on the criteria of Molprobity

Because of relatively large deletions (21-35 residues) in parts of the VP1 BC, DE and HI loops, the RV-C15a structure lacks a protruding plateau around each of the 5-fold vertices, a characteristic feature of other EV (Fig. 4.6). Thus the RV-C do not have the analogous surface mass near the 5-fold vertices to form immunogenic sites equivalent to NIm-IA (VP1 BC loop) and NIm-IB (VP1 DE loop) on RV-B14 [13]. Instead, the finger regions, as mentioned above, probably function as the dominant

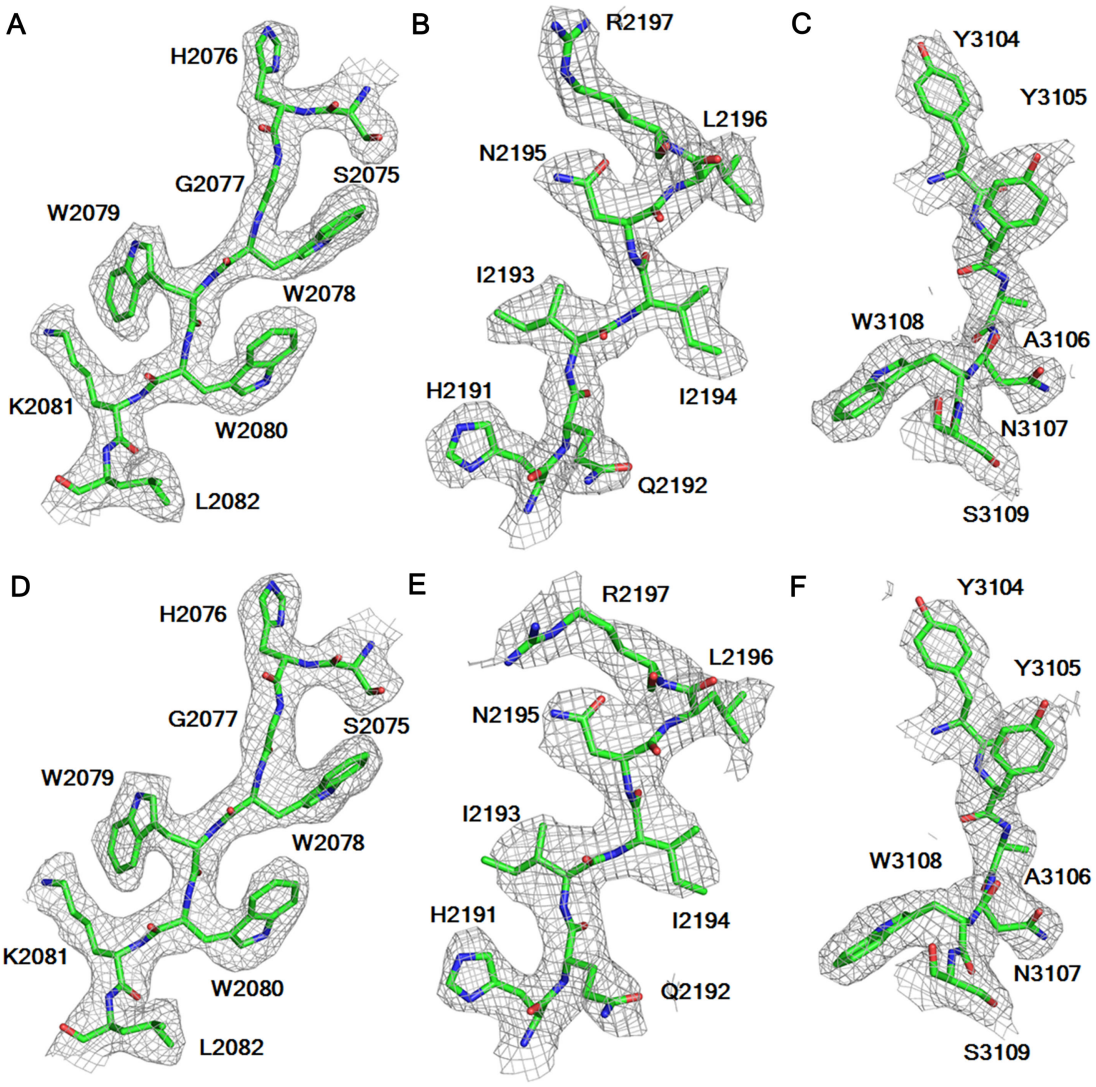

Fig. 4.4. **Typical densities of the full (A-C) and empty (D-F) particle EM maps.**

antigenic sites [439]. As another consequence of these finger regions, the RV-C15a particles have narrow, non-continuous canyons, much like the surface of EV-D68, a virus that also causes respiratory illnesses [2, 456]. In each icosahedral asymmetric unit, the C-proximal, RV-C15a VP1 insertion helps create a wall-like feature blocking the eastern end of the canyon (defined with respect to the usual orientation of picornaviruses used in most figures) (Fig. 4.6).

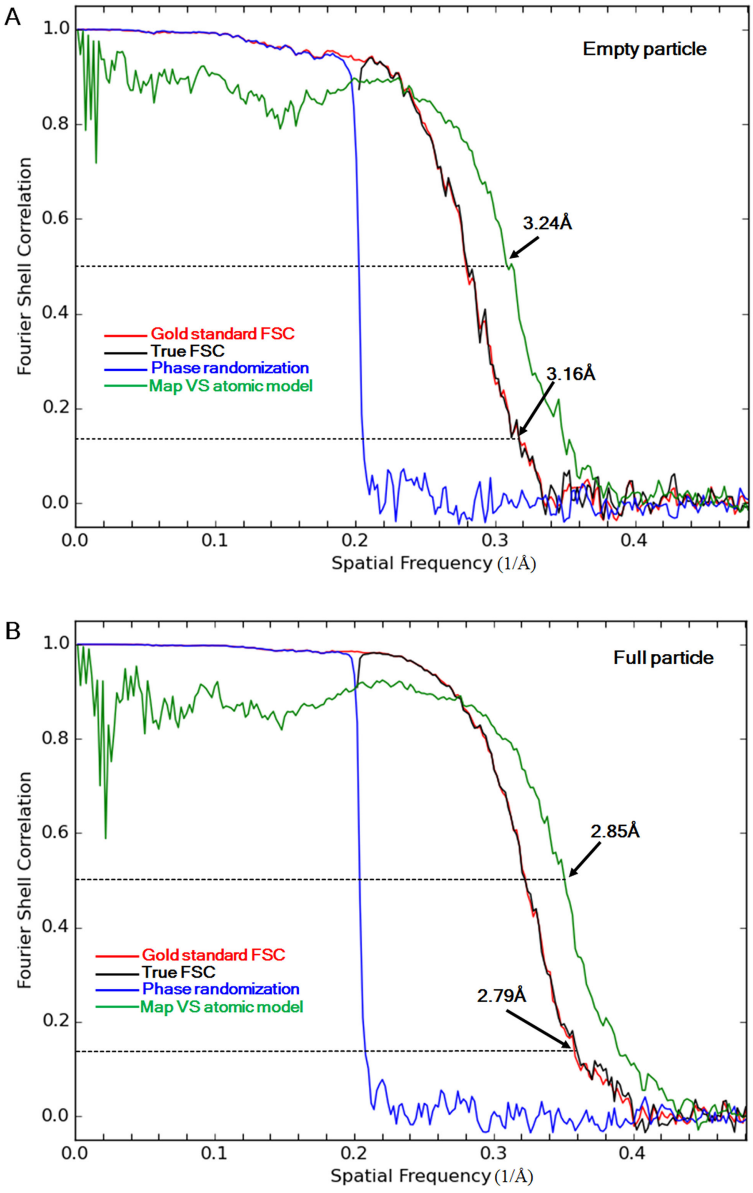

Fig. 4.5. **The resolution of the empty (A) and full (B) particle maps is estimated based on FSC.** The FSC curves between two half subset maps calculated using the original images (Gold standard FSC) and using phase randomized (beyond 5 Å) images (Phase randomization) are colored red and blue. True FSC curves are colored black. The FSC curves between the final EM map and a density map computed based on the modeled atomic coordinates were colored green.

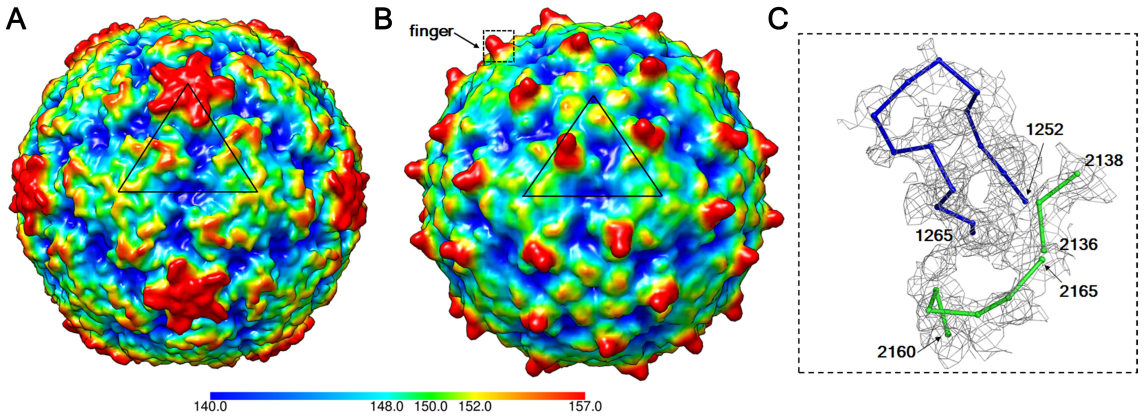

Fig. 4.6. **The spiky structure of RV-C15a.** A 10 Å resolution density map of RV-B14 (PDB 4RHV) (**A**) and RV-C15a (**B**) calculated based on the respective coordinates is colored by radial distance (Å) to the virus center. A black triangle indicates an icosahedral asymmetric unit on each of the two viruses. A rectangle (black dash line) outlines the limit of a close up view of a finger in (**C**). Residues that form the finger region, which are fitted into the EM map densities (grey), are shown as Cα backbones and colored blue (VP1) and green (VP2).

4.4.5 A sequence conserved depression could bind glycosylated CDHR3

Sialic acid is the glycan moiety recognized by EV-D68 when it interacts with its cellular receptor [3]. Superposition of EV-D68 structure complexed with sialic acid (Fig. 4.8) onto the structure of RV-C15a showed that the region near the eastern end of the RV-C15a canyon has a similar surface electrostatic potential as the sialic acid binding site on EV-D68 (Fig. 4.8). In the EV-D68, sialic acid can be bound mainly by the Pro3231 carbonyl group and by the Arg3104 guanidinium group (Fig. 4.8). In RV-C15a, potentially those interactions would be replaced by the structurally equivalent carbonyl group of Pro3226 and by the side chain amino group of Lys1271, respectively (Fig. 4.8). Some of the nearby surface residues contributing to this region are conserved among all RV-C (Fig. 4.7), and it is clear that the overall topography could readily accommodate a sialic acid ligand. Therefore, this region, close to the

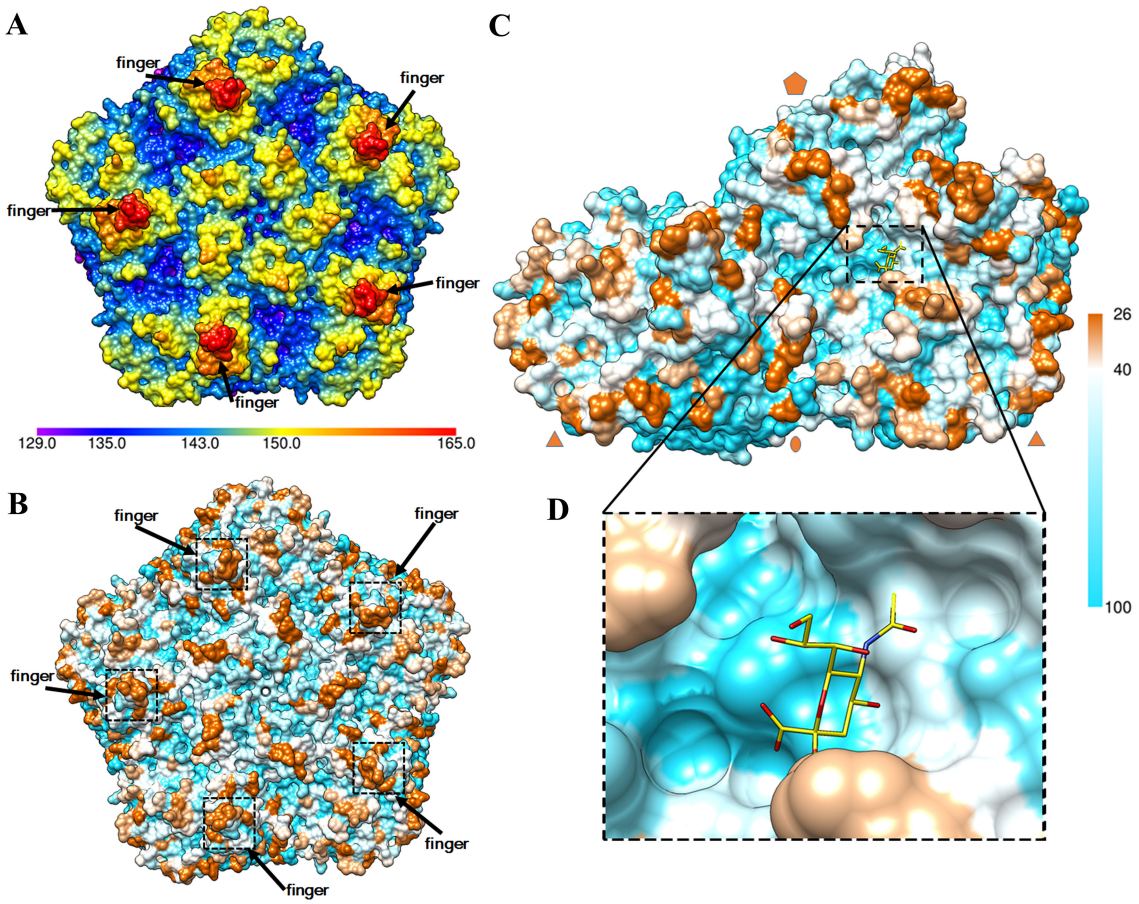

Fig. 4.7. **Sequence conservation of outer surface amino acid residues.** A surface representation of a pentamer of the RV-C15a capsid is colored by radial distance (Å) to the virus center (**A**) or by conservation of amino acid sequences (**B**) among 33 types of RV-C virus. A total of 67 sequences of RV-C viruses for which the complete sequence of P1 region is available are used in sequence alignment. Shown in the color key is the occurrence (%) of the most popular residue at a given alignment position among the 67 sequences. A surface representation of two protomers (**C**) is colored by conservation of amino acid sequences. A black rectangle (dash line) outlines the limit of a close-up view of the potential sialic acid (yellow) binding site shown in (**D**).

base of each finger in the RV-C15a structure, is a likely binding site for a CDHR3 glycan. Consistent with this prediction, mutation of Asn186 a key glycosylation site

on CDHR3, impairs RV-C15 binding to receptor-expressing cells [432]. Therefore, glycans must play an important role in RV-C receptor interactions, as they do also for EV-D68.

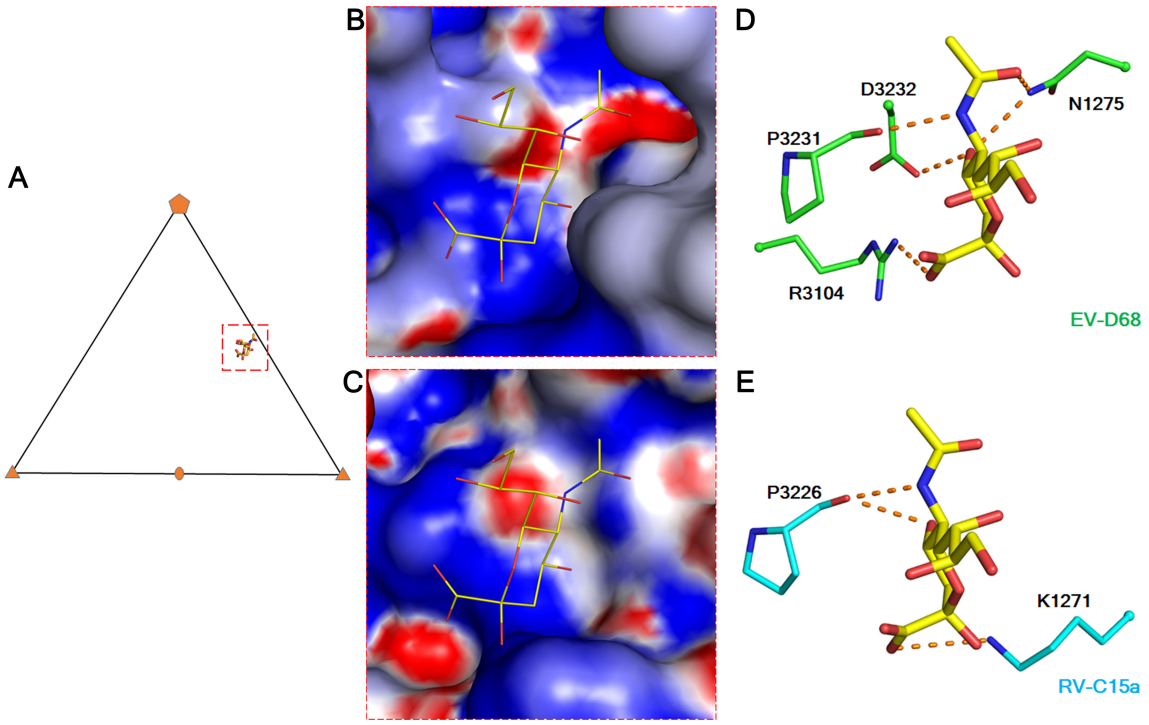

Fig. 4.8. **A potential binding site for glycans on CDHR3. A.** A triangle indicates an icosahedral asymmetric unit. A red rectangle (dash line) outlines the limit of the sialic acid binding site. Surface electrostatic potential of EV-D68 (PDB 5BNO) (**B**) and RV-C15a (**C**) is represented with a scale of -8kT/e (red) to 8kT/e (blue). **D-E.** The sialic acid (yellow) interacts with surrounding residues on EV-D68 (green) and as anticipated on RV-C15a (cyan). Red dash lines indicate (potential) polar interactions. Oxygen and nitrogen atoms are colored red and blue, respectively.

4.4.6 The hydrophobic pocket is unsuitable for capsid binding agents

Capsid-binding reagents that replace the pocket factor within VP1 are effective antiviral therapeutics against many EV [457], but not RV-C [438]. Unlike many

EV structures the hydrophobic pocket within the VP1 jelly roll fold, where a pocket factor is typically bound [2,16,429], is collapsed in RV-C15a (Fig. 4.9). The collapsed structure is similar to the empty pockets found in purified RV-B14 [13] and RV-B3 [20]. None of these three structures have sufficient space to accommodate a fatty-acid pocket factor, because for each, the VP1 GH loop, located at the boundary between the canyon and the entrance to the VP1 pocket, is in a conformation that squeezes the pocket. Nevertheless, in RV-B3 and RV-B14, the flexibility of the VP1 GH loop allows enlargement of the pocket that then can bind antiviral reagents. The RV-B14 pocket is lined with multiple small residues (e.g., Ala, Ser, Val, etc) that can accommodate such compounds. In contrast, the collapsed RV-C15a VP1 pocket is filled with bulky, hydrophobic residues (in particular, Trp1080, Phe1096, Met1116, and Met1180) (Fig. 4.9 and Table 4.2). These amino acids are conserved in almost all RV-C (14). Additionally, Ile1198 and Tyr1246 partially block the entrance to the VP1 pocket. Therefore, as has been observed experimentally [438], no RV-C are likely to be responsive to antiviral therapies based on pocket-binding compounds.

4.4.7 Comparison of the Full and Empty Particle Structures

RV-C15a full and empty particles differed mainly in regions on the inner surfaces of their capsid shells (Fig. 4.10). In particular, the VP1 N-terminal residues 1017-1053 are well-ordered in the full particle map, but disordered in the empty particle map. This is consistent with other EV structures where the VP1 N-terminus is involved in binding to viral RNA [16] and is externalized prior to ejecting the genome during infection [114]. Thus the specific configuration of this internal region is RNA-dependent and is likely to exert strong influence on VP0 cleavage when the RNA is packaged [63]. In the empty particles, VP0 residues 4024-4050 form a hairpin loop positioning the VP0 cleavage site in close proximity to His2191 (Fig. 4.10), a crucial residue in the cleavage mechanism [64]. Nearby VP1 residues 1054-1064 interact with the VP0 hairpin within the same protomer, presumably helping to set up the pending

Table 4.2
Comparison of amino acid residues lining the VP1 hydrophobic pocket among enteroviruses

	Residues[a]	RV-C15a	RV-A16	RV-B14	EV-A71	CVB3	PV1	EV-D68	Mengo	FMDV
head[b]	1096	PHE	LEU	LEU	ILE	PRO	TYR	THR	PRO	LEU
	1106	PHE	PHE	LEU	VAL	LEU	LEU	LEU	-	-
	1114	PHE	PHE	PHE	PHE	PHE	PHE	PHE	CYS	SER
	1178	TYR	TYR	TYR	TYR	TYR	TYR	TYR	LEU	LEU
	1180	MET	MET	CYS	TRP	ASN	HIS	VAL	ALA	THR
	1198	ILE	THR	ILE	ALA	ILE	ALA	ILE	-	-
	1246	TYR	HIS	GLY	ALA	LYS	-	ALA	-	-
middle[b]	1080	TRP	ILE	VAL	VAL	VAL	VAL	VAL	ILE	ILE
	1092	TRP	TRP	TRP	TRP	TRP	TRP	TRP	VAL	HIS
	1094	ILE	ILE	ILE	ILE	ILE	ILE	ILE	LEU	ILE
	1116	MET	SER	SER	ALA	LEU	MET	ALA	LEU	LEU
	1169	ILE	LEU	VAL	VAL	VAL	VAL	ILE	VAL	LEU
	1204	MET	MET	MET	MET	MET	PHE	ILE	PHE	TYR
	1224	VAL	HIS	HIS	MET	PHE	LEU	MET	LEU	VAL
tail[b]	1118	VAL	ILE	TYR	PHE	LEU	LEU	ILE	VAL	ILE
	1120	ILE	MET	ILE	PHE	PHE	PHE	ILE	LEU	VAL
	1130	ILE	TYR	ALA	TYR	ILE	ILE	ALA	VAL	LEU
	1132	PHE	TYR	TYR	PHE	TYR	TYR	PHE	TRP	TRP
	1154	PRO	ALA	PRO	PRO	PRO	PRO	ALA	PRO	PRO
	1156	VAL	VAL	VAL	VAL	VAL	ILE	VAL	VAL	ALA
	1167	PHE	PHE	PHE	VAL	MET	ILE	MET	PHE	LEU
	1207	LEU	LEU	MET	PHE	LEU	LEU	LEU	LEU	ILE
	3024	ILE	ALA	ALA	ILE	ALA	ALA	VAL	ILE	VAL

[a] Numbering based on the amino acid sequence of RV-C15a
[b] These terms refer to residues that are close to the head, the middle part, or the end of the pocket factor.
[c] The PDB accession number from RV-A16 to FMDV are 1AYM, 4RHV, 3ZFE, 1COV, 1ASJ, 4WM8, 2MEV, and 1ZBE

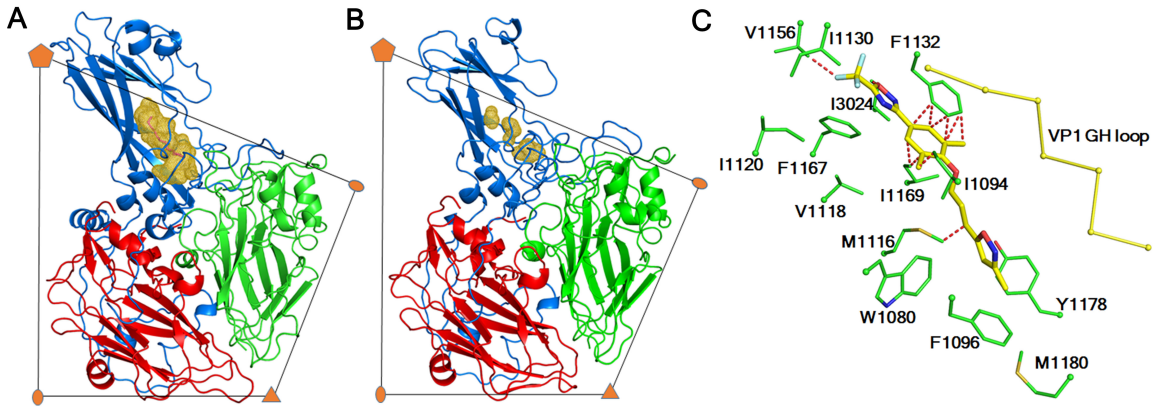

Fig. 4.9. **RV-C15a has a collapsed VP1 hydrophobic pocket.** RV-A16 (**A**) and RV-C15a (**B**) are colored by polypeptides: VP1 (blue), VP2 (green), and VP3 (red). The volume of the VP1 hydrophobic pocket, calculated using Pymol, is colored gold. **C.** Residues lining the VP1 pocket of RV-C15a clash with pleconaril when superimposing the structures of RV-C15a and RV-B14 complexed with pleconaril. The VP1 GH loop (yellow) of RV-B14 is shown as Cα backbones, which adopts a conformation that can accommodate pleconaril. Red dash lines indicate a distance of closer than 2.5 Å between a given atom of a RV-C15 residue (green) and a given atom of pleconaril (yellow). Oxygen, nitrogen and sulfur atoms are colored red, dark blue and dark yellow, respectively.

cleavage reaction. However, in the full particle structure, the VP1 N-terminal residues 1027-1053 (disordered in the empty particles) interact with the C-terminus of VP4 within the same protomer and participates in viral RNA binding (Fig. 4.10).

4.5 Discussion

The cryo-EM structure of RV-C15a showed a collapsed hydrophobic pocket in VP1 that is filled with multiple bulky residues that inhibit the entrance of compounds which inhibit other EV by binding into the VP1 pocket. This is reminiscent of the collapsed pockets of non-EV picornaviruses, such as foot-and-mouth disease virus (genus *Aphthovirus*) [286] and Mengovirus (genus *Cardiovirus*) [458]. Those pockets

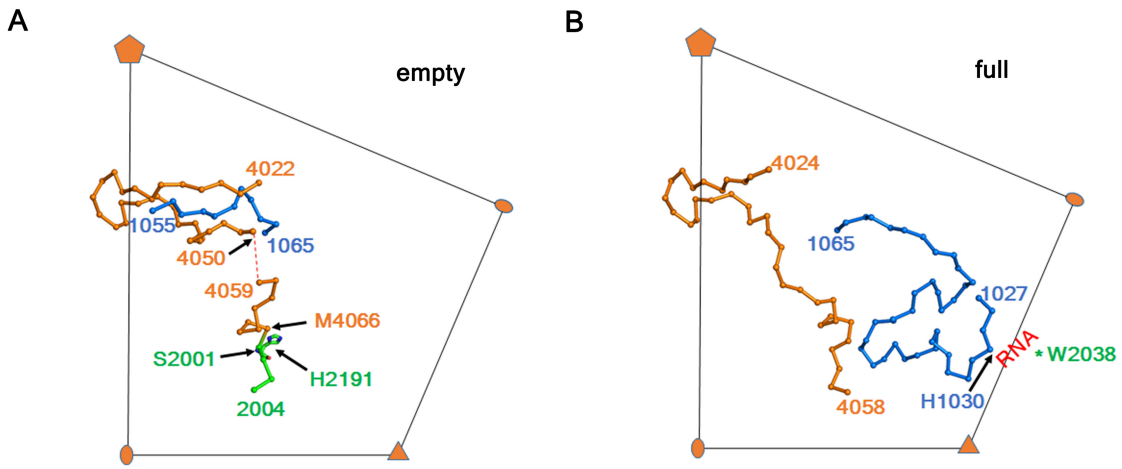

Fig. 4.10. **The full and empty RV-C15a particle structures differ in regions at the capsid interior.** The VP1 N-terminus and VP4 undergo structural rearrangements when the empty particle (**A**) and full particle (**B**) structures are compared. Amino acid residues are shown as Cα backbones. VP4, VP2, and VP1 are colored orange, green and blue, respectively. In the RV-C15a full particle structure, His1030, together with a conserved residue Trp2038 shared by many EV, are involved in forming an RNA binding site [16, 18, 20].

are similarly occupied by multiple bulky, hydrophobic side chains and are unable to serve as drug targets.

Inclusion of large hydrophobic residues into the VP1 pocket of RV-Cs and incorporation of a fatty-acid like pocket factor into the VP1 pocket of many other EVs produce similar hydrophobic effects that favor the folding of the VP1 jelly roll β barrel. On one hand large hydrophobic residues (e.g., Phe, Trp, Met) are more effective than small residues (e.g., Val, Ala) at reducing solvent accessible surface areas in the pocket. Likewise, a pocket factor with a long hydrophobic tail (more than eight carbon atoms) plays a crucial role in expelling water out of the VP1 pocket of many EVs that contain multiple small residues. On the other hand, the presence of large hydrophobic side chains or a pocket factor in a VP1 pocket keeps the two sheets (one with strands C, H, E, F and the other with strands B, I, D, G) in a favorable

distance for forming a barrel and offers hydrophobic interactions that stabilize the jelly roll fold.

Concerning enteroviruses (e.g., EV-A71 and RV-A2) that have a pocket factor bound in the VP1 pocket in the native form, a collapsed VP1 pocket is formed when these viruses are converted into uncoating intermediates, including A(altered)-particle [212] and emptied particle [31,238]. In this process, the VP1 GH loop changes its conformation, whereas other residues lining the pocket remain nearly unchanged. Specifically, the VP1 GH loop moves into and squeezes the pocket, adopting a conformation that resembles that in the RV-C15a, RV-B3, and RV-B14 structures. It is thus probable that the collapsed pocket in RV-C15a, RV-B3 and RV-B14 might facilitate virus uncoating. These viruses might undergo particle expansion to become A-particles where pores are formed in the capsid, as was previously described for other EV [209, 212].

The large interior rearrangements characterizing the full and the native empty particles of RV-C15a, contrast with the conserved external surfaces. Both particle types have the same diameter, and display the same finger protrusions, truncated 5-fold vertices, and putative glycan binding regions. Presently, it is not clear whether the observed high proportion (about 30%) of empty particles is a property of all RV-C, or unique only to RV-C15a. Possibly the RV-C species use these native empty particles as immunogenic molecular decoys during infections, or they are merely byproducts of the assembly process [48].

The published atomic models of RV-C [439, 440] predicted the loss of VP1 mass at the five-fold vertices, relative to the crystal structures of other RV virions. The more rigorous one of these models [438] also predicted steric impediments in the VP1 pockets as the cause of drug binding failures. However, although the overall r.m.s.d. between equivalent Cα atoms of this predicted model and the present cryo-EM structure was about 1.3 Å, none of the bioinformatics-derived information correctly projected the finger-like features which dominate the particle surface. The relative VP1 insertion contributing to each protrusion is unique to the RV-C.

The atomic structures of an RV-C virus, as reported here, show novel molecular targets for designing anti-RV-C therapeutics. Furthermore the non-infectious empty particles may have potential as vaccine candidates. These possibilities have clinical relevance since many RV-C, including RV-C15, are associated with severe, hospitalization-category infections in young children [431, 459], especially those with asthma, and can also lead to significant adult respiratory problems, including chronic obstructive pulmonary disease.

5. ACID INDUCED STRUCTURAL CHANGES OF HUMAN ENTEROVIRUS D68

The data and text in this chapter are part of a manuscript in preparation.

5.1 Chapter Abstract

Enterovirus D68 (EV-D68) mainly causes respiratory infections and is sensitive to acid, much like rhinoviruses. The molecular basis of the acid sensitivity of EV-D68 has not been studied. This chapter presents a 2.3 Å resolution cryo-electron microscopy (cryo-EM) structure of a current strain of EV-D68. The structure shows that the pocket factors is absent and that the VP1 hydrophobic pocket is partially collapsed. This structural feature correlates with a low stability of EV-D68 under acidic conditions, a characteristic that facilitates viral RNA release into host cells for virus replication. Furthermore, the structure of an uncoating intermediate of EV-D68, which was formed at late-endosomal pH (pH 5.5), has been determined to about 3.0 Å resolution. Acid treatment of EV-D68 leads to particle expansion and formation of pores at two-fold axes through which the viral RNA might exit. Finally, as a result of the low stability of the virus, cryo-EM analyses using a single specimen of EV-D68 at neutral pH show six distinct structural states of the capsid. These states differ mainly in particle size and in regions at the capsid interior. Thus these results provide the structural basis for understanding the uncoating process of EV-D68 and related viruses.

5.2 Introduction

Human enterovirus D68 (EV-D68) mainly causes respiratory infections [456]. The optimum growth temperature of EV-D68 is 33°C, which is the temperature of the human upper respiratory tract [401]. Furthermore, EV-D68 is sensitive to acid. These are common biological characteristics shared by rhinoviruses (viruses from the species RV-A , RV-B, and RV-C) but not by viruses from the species EV-A, EV-B and EV-C [4]. Rhinoviruses primarily infect the human upper respiratory tract and are transmitted through respiratory route. However, viruses from the species EV-A, EV-B and EV-C, as exemplified by polioviruses, are transmitted through fecal-oral route and need to be sufficiently stable to thrive in the acidic environment of the human gastrointestinal tract [4].

Acid lability (virus instability at pH <6) has been explored as a potential anti-rhinovirus therapeutic target [460], because acid treatment of rhinoviruses resulted in partial or nearly complete loss of viral infectivity [461]. In the cases of RV-A2, RV-B3, and RV-B14, early studies demonstrated that *in vitro* incubation of the virus at pH 5 led to the production of two different forms of subviral particles that had slower sedimentation rates than native virions (150S) [106, 461]. The two forms exhibited characteristics of what were later known as A-particles (135S) and emptied particles (80S) [204, 205, 219, 229, 238], respectively. In essence, A-particles, which still retain viral genome, are featured by externalization of VP1 N-terminal residues and by loss of VP4 [205, 209, 212, 213]. Emptied particles have similar capsid structure but are void of viral genome [31,205,238]. Crystallographic studies of RV-B14 crystals treated immediately with acidic buffer showed that the VP1 GH loops, residues around the five-fold cation sites, and the VP3 N-terminal regions became disordered [462], as compared to the native virion structure. These acid induced structural changes were proposed to facilitate release of VP4 [462]. Furthermore, *in vitro* treatment of RV-A2 at pH 5.6, which is close to the late endosome pH, led to the formation of A-particles as characterized by X-ray crystallography [205]. This is consistent with the fact

that endosomal acidification is important for successful cell entry of a number of RVs [197, 463]. Comparison of the native RV-A2 structure and the 6.0 Å resolution crystal structure of RV-A2 A-particle showed that the viral RNA loses contacts with the VP1 N-terminus in A-particles and might form an ordered layer beneath the capsid shell [205]. These results suggested a mechanism where global structural changes of the virus are induced by acid. Given the structural similarity of EV-D68 to a number of rhinoviruses, it is hypothesized that acid triggers EV-D68 uncoating.

This chapter characterizes structural changes of EV-D68 that are associated with virus uncoating by cryo-EM analyses. The molecular basis of the acid lability of EV-D68 (as also rhinoviruses) is also discussed.

5.3 Materials and Methods

5.3.1 Viruses and cells

EV-A71 (strain MY104-9-SAR-97, GenBank ABC69262.1) was provided by Jane Cardosa (Universiti Malaysia Sarawak, Malaysia). In addition to the aforementioned EV-D68 strain US/MO/14-18947, another isolate of EV-D68 from the 2014 outbreak in the United States, US/KY/14-18953 (GenBank: AIS73057.1), was provided by M. Steven Oberste through BEI Resources, National Institute of Allergy and Infectious Diseases, National Institute of Health. Procedures for maintaining HeLa and RD cells and for producing virus stocks have been described in earlier chapters.

5.3.2 Virus Growth and Purification

A sample (Prep A) for structure determination of full EV-D68 virion (strain US/MO/14-18947) to 2.3 Å resolution was prepared as described in Chapter 2 with slight modifications. After the crude virus sample was sedimented through a potassium tartrate density gradient, a band in the middle of the tube was extracted and subjected to buffer exchange. The resultant sample was further purified using an

iodixanol (OptiPrep from Sigma) density gradient (10% - 51% (v/v) in 250 mM HEPES, 250 mM NaCl, pH 7.5 (buffer A)) at 175274 x g (SW 41 Ti rotor) for 2h at 4°C. Electron micrographs of the final sample verified the presence of more than 95% full particles. The sample was stored at 4°C.

A virus preparation (Prep B) that contained a heterogeneous population of EV-D68 particles was used for structural studies at both neutral pH and acidic pH. Briefly, RD cells were infected with EV-D68 (strain US/MO/14-18947) at an MOI of about 0.01. Cells and supernantant were harvested at 3 days post infection and were then separated by centrifugation. Cell pellets were subjected to multiple cycles of freeze-and-thaw, and were centrifuged to remove cell debris. Polyethylene glycol 8000 (PEG8000) (40% w/v stock solution) and NaCl (powder) were added into the original supernatants (after infection) to reach a final concentration of 8% PEG8000 and about 500 mM of NaCl. After low speed agitation at 4°C for about 6h, the mixture was spun down. The resultant white pellets were resuspended in buffer A, which was combined with the previous supernantant from the step concerning cell pellets. All supernatant was centrifuged using a Ti 50.2 rotor at 277,937 x g for 2h at 4°C. The resultant pellets were resuspended in buffer A and treated sequentially as follows: 1) add 5 mM (final concentration throughout the treatments) $MgCl_2$; 2) add 10 μg/ml DNAse; 3) add 7.5 mg/ml RNase and leave at room temperature for 30 min; 4) add 0.8 mg/ml trypsin and incubate at 35°C for 10 min; 5) add 15mM EDTA; 6) add stock n-lauryl-Sarcosine (10%, w/v, in buffer A) to reach a final concentration of 1% (w/v). Pellets were resuspended in buffer A and then purified through an iodixanol density gradient mentioned above. The sample was stored at 4°C.

5.3.3 Infectivity Assay

Four different viruses were used, including the acid resistant EV-A71, the acid labile EV-D68 strain Fermon CA62-1, and two EV-D68 isolates (US/MO/14-18947 and US/KY/14-18953) from the 2014 US outbreak. Purified viruses were treated

with phosphate-citrate buffer (100 mM Na_2HPO_4 and 50 mM citric acid) at pH 4, 5, 6, or 7.2 at 33°C for about 40 min. The resultant samples were neutralized back to about 7.2 using phosphate-citrate buffer (400 mM Na_2HPO_4 and 200 mM citric acid, pH 7.3) before being assayed for viral titers using a plaque assay (Chapter 2).

5.3.4 Cryo Electron Microscopy

About 2.8 μl of virus sample was applied onto a 400 mesh continuous carbon grid. Immediately after blotting for about 8s, the grid was vitrified in liquid ethane that was pre-cooled by liquid nitrogen. Frozen particles within a thin layer of vitreous ice were imaged with a Gatan K2 Summit direct electron detector using a Titan Krios TEM (300 kV). All samples for EM data collection were of strain US/MO/14-18947. The dose rate was kept at approximately 8e^-/pixel/s for collecting all data, as will be described below. For structure determination of native full virions using Prep A, data (dataset A_Native) were collected at a nominal magnification of 22,500x in super resolution mode with defocus values ranging from 0.3 to 3.0 μm. A total electron dose of about 36 $e^-/Å^2$ was fractionated into 38 frames (200ms/frame). For initial low pH studies using Prep B, viruses were treated with phosphate-citrate buffer (100 mM Na_2HPO_4 and 50 mM citric acid) to reach a final pH of 5.5 (dataset B_RT_Acid) or a pH of 7.2 (dataset B_RT_Neu), followed by incubation at room temperature for 20 min and subsequently neutralization with 400 mM Na_2HPO_4 and 200 mM citric acid (pH 7.8). Data were collected at a nominal magnification of 22,500x in super resolution mode. The defocus range for datasets B_RT_Acid (144 micrographs) and B_RT_Neu (87 micrographs) were 0.9-4.8 μm and 1.3-3.6 μm, respectively. For dataset B_RT_Acid, a total electron dose of about 28 $e^-/Å^2$ was fractionated into 30 frames (200ms/frame). For dataset B_RT_Neu, a total electron dose of about 25 $e^-/Å^2$ was fractionated into 27 frames (200ms/frame). For low pH studies using Prep B to mimic conditions during virus infection, viruses were treated at pH 5.5 similarly to the aforementioned procedure except that the incubation temperature was at 33°C.

Data (dataset B_33_Acid) were collected at a nominal magnification of 22,500x with defocus values ranging from 0.5 to 3.5 μm. A total electron dose of about 38 $e^-/Å^2$ was fractionated into 40 frames (200ms/frame). For analyzing the heterogeneous particle population of Prep B (stored at 4°C) at neutral pH, data (dataset B_4_Neu) were collected at a nominal magnification of 18,000x in electron counting mode with defocus values ranging from 1.7 to 5.3 μm. A total electron dose of about 45 $e^-/Å^2$ was fractionated into 60 frames (250ms/frame).

5.3.5 Image Processing

Procedures for image processing were similar to what had been described for RV-C15a (Chapter 4). In essence, concerning all datasets, movie frames were subjected to motion correction using a modified version of MOTIONCORR [331] (Wen Jiang). The aligned frames were summed up to produce individual micrographs, which were used to determine parameters of contrast transfer function (CTF) using CTFFIND3 [444]. For some datasets, virus particles were picked up from the micrographs manually using e2boxer.py in the EMAN2 program package [335]. For some datasets, particle selection was performed first manually using e2boxer.py and subsequently automatically using the program DogPicker [445] based on templates derived from manually selected particles. Particles were subsequently boxed and extracted from the micrographs. The process was integrated into the Appion data processing pipeline [443]. The resultant particle images were subjected to two dimensional (2D) classification using the program Relion [337]. which identified and removed some low quality particles and separated images of full particles from those of empty particles.

The following reconstruction procedures were employed for all datasets except for dataset B_4_Neu using the program jspr [339, 446]. In brief, particle images (8x binned, with a pixel size of 5.20 Å/pixel) were divided into two halves. As described in Chapter 4, for each half, a random initial model approach, specifying icosahedral symmetry, was employed to generate multiple initial three dimensional (3D) models,

from which a suitable initial model was selected. The best particle orientation and center of each particle image was searched with respect to projections of the initial reference model. The reference model for the next iteration was reconstructed from particle images employing parameters for orientation and center determined in the current iteration. The refinement procedure was then extended to 4x binned and then 2x binned data. Specifically, for dataset A_Neu_2.3, the procedure was extended to unbinned data. At this point, individual particles images were subjected to correction of anisotropic magnification distortion using the program jspr, which was done with experimentally determined distortion parameters [449]. Subsequently, multiple parameters were then included in the refinement process, which were parameters for particle orientation, particle center, beam tilt, defocus, scale, astigmatism. To achieve 3D reconstructions with the highest possible resolution, particle images were re-extracted from micrographs that were generated by averaging aligned frames 3-16. In this way, frames that underwent large motions and that contained limited high resolution information due to radiation damage were discarded. Frames 3-16 were selected using a trial-and-error approach where different combinations were tested, including frames 3-9, 3-16, 3-23, and 3-30. Fourier shell correlation (FSC) of two interdependently calculated half-maps (after masked with a soft mask) was used to estimate the resolution of the final EM maps [452, 453]. The maps were sharpened using a negative B-factor for better visualization during model building [452].

The following procedures were done for dataset B_4_Neu. After 2D classification of all particle images in the dataset, the resultant full particle images (4x binned, 6.48 Å/pixel) were used to generate initial three dimensional (3D) models, from which a suitable initial model was selected. The refinement process was performed using a projection matching approach as what was described above. After multiple iterative cycles when the process converged, the resultant 3D model was essentially an average of all possible structural states present in the collection of full particle images. The model was low pass filtered to 60 Å resolution and then utilized as a reference model for 3D classification of full particle images (4x binned) using the program Relion [337],

where the number of classes was 4 and where icosahedral symmetry was imposed. Particle images from two of the resultant four classes yielded 3D reconstructions that were nearly identical to each other by visual inspection. Thus, particle images from the two classes were combined into one class. The same process was also applied to images of empty particles. Hence, all particle images in the dataset were classified into a total of six classes (three for full particles and three for empty particles), which represented six different structural states. Procedures for cryo-EM structure determinations were the same when using each class of particle images, as were detailed in the last paragraph.

5.3.6 Model Building and Refinement

Procedures for model building and refinement were essentially the same as what had been done for the RV-C15a structure (Chapter 4). The same procedures were employed for all atomic structures presented in this chapter. In brief, the coordinates of Fermon strain excluding the pocket factor and water molecules (PDB accession number 4WM8) were used as a starting atomic model. It was manually fit into the EM map using Chimera [400]. Then multiple cycles of model rebuilding in Coot [394] followed by real space refinement against the EM map using Phenix [397] yielded an atomic model that fit well into the map density by visual inspection. A mask that contained all grid points within a radius of 5 Å around each atom of the atomic model was used to cut out a map segment from the EM map. The atomic model was subjected to refinement of atomic coordinates, B factors, and occupancy against pseudo crystallographic structure factors (defined as in Chapter 4) that were computed from the map segment using Phenix [397]. In this reciprocal space refinement procedure, R factors were monitored. The resultant atomic model was used for real space refinement with NCS constraints using Phenix [397]. The final atomic model was validated based on the criteria of MolProbity [454].

5.4 Results

5.4.1 The EV-D68 strain MO is acid sensitive

The effect of acid treatment on virus infectivity was tested using a plaque assay. EV-A71 is acid resistant and retained infectivity at low pH (pH 4-6). In contrast, the tested EV-D68 strains are acid labile, including the prototype Fermon strain and two strains (US/MO/14-18947 and US/KY/14-18953) from the 2014 US outbreak. Hereafter, US/MO/14-18947 and US/KY/14-18953 will be referred as MO and KY, respectively. Among these strains, strain MO is most sensitive to acid (Fig. 5.1).

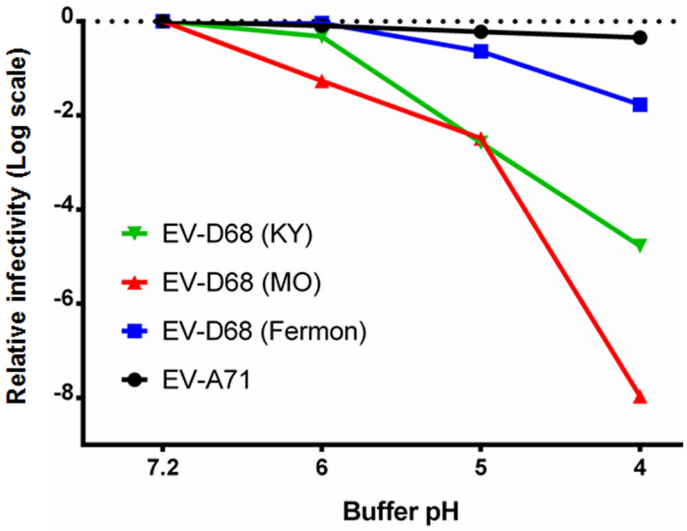

Fig. 5.1. **The EV-D68 strain MO is acid sensitive.** Viruses were treated using buffer with a series of pH values and then assayed for viral titers. Shown is a plot of changes of virus infectivity in logarithm scale as a function of buffer pH.

Cryo-EM analysis of the full virion of EV-D68 strain MO was performed similarly as what was done for RV-C15a (Chapter 4), except that data collection was at a nominal magnification of 22500x that gave a better signal-to-noise ratio and a finer pixel size than in the case of 14000x. Cryo electron micrographs showed that there were more than 95% of full virions in the sample (hereafter referred to as Prep A),

which was prepared using two rounds of density gradient centrifugation. The virus structure (dataset A_Native) was determined to about 2.3 Å resolution using 11,344 particles (Fig. 5.2 and Table 5.1). The pocket factor was found to be absent in the VP1 hydrophobic pocket, which is partially collapsed. This structural feature may explain the low stability of strain MO under acidic conditions, a characteristic that probably allows efficient virus uncoating within host cells.

5.4.2 Acid induces EV-D68 uncoating

In consistent with the low stability of strain MO, a virus sample (hereafter referred to as Prep B) that was not as intensively purified as Prep A yielded a mixture of full virions and empty particles that co-existed within one fraction of about 0.7 ml. To study acid triggered structural changes of the virus, initial structural analysis was performed, where Prep B was treated with either a pH 5.5 buffer (dataset B_RT_Acid) or a neutral pH buffer (dataset B_RT_Neu) at room temperature for 20 min. Two-dimensional (2D) classification of particle images in dataset B_RT_Neu showed the presence of full and empty particles with a particle number ratio of about 1.9:1 (full:empty) (Fig. 5.3). In contrast, 2D class averages of particle images in dataset B_RT_Acid showed the presence of empty particles as well as a particle form that contained genome but exhibited a thinner capsid shell than native full virions. The ratio between the new form of particles and empty particles was about 1.7:1 (Fig. 5.3), suggesting that acid triggered the conversion of native full virions to the new particle form. Icosahedral reconstructions of the new form of particles (3,708 particles) and empty particles (2,150 particles) in dataset B_RT_Acid were calculated to about 3.3 Å and 3.8 Å resolution, respectively. The VP1 N-terminal residues 1001-1041 (numbering based on the amino acid sequence of the Fermon strain) and a majority of VP4 residues are well ordered in the map of native full virion but become disordered (or missing) in the map of the new particle form. This observation demonstrates that the particle form represents A(altered)-particle, an uncoating intermediate known for

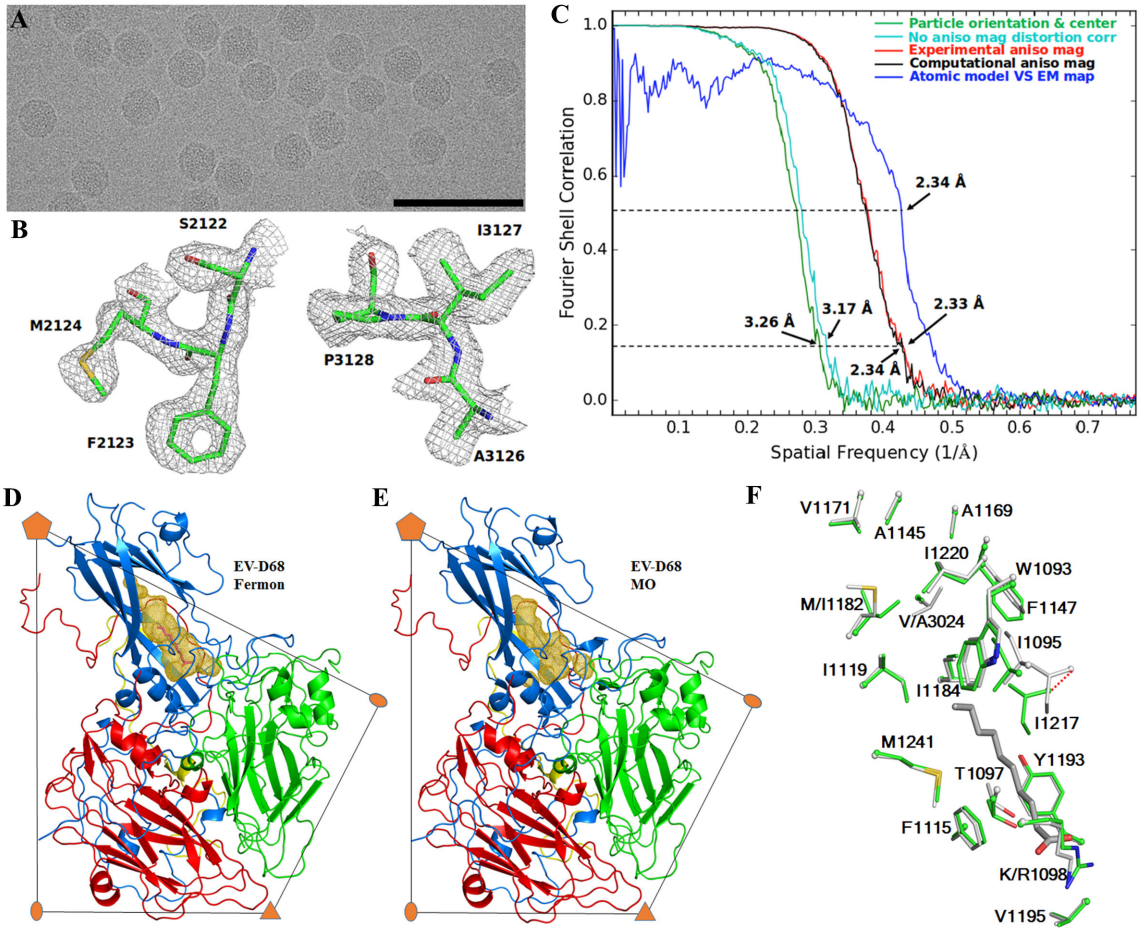

Fig. 5.2. **The cryo-EM structure of EV-D68 strain MO. A.** A typical portion of an electron micrograph (eight times binned) of strain MO. The micrograph was collected at a defocus of 1.3 μm. Scale bar: 100 nm. **B.** Typical cryo-EM map densities. **C.** Resolution estimation based on Fourier shell correlation (FSC) between two independently calculated half-maps. Different kinds of FSC curves are labeled as in Fig. 4.3. A fatty acid-like pocket factor is present in strain Fermon (**D**), but is absent in strain MO (**E**). The volume of the VP1 pocket, calculated using Pymol, is colored gold. **F.** Comparison of Amino acid residues lining the VP1 hydrophobic pocket in the structures of strain Fermon (grey) and strain MO (green). The pocket factor is colored black. Concerning strain MO, residue I1217 moves by 1.9 Å (Cα atom, red dash line) into the pocket that would clash with the pocket factor.

Table 5.1
Data collection and processing statistics

	A_Native	B_33_Acid_A-ptcl	B_33_Acid_emp
Data collection and processing			
Microscope	Titan Krios		
Accelerating voltage (kV)	300		
Camera	Gatan K2 Summit		
No. of micrographs[a]	642	950	950
Pixel size[b] (Å/pixel)	0.65	0.65	0.65
Dose rate (e^-/pixel/s)	8	8	8
Total dose ($e^-/Å^2$)	36	38	38
Frame rate (ms)	200	200	200
Defocus (μm)	0.3-3.0	0.5-3.5	0.5-3.5
No. of ptcls for reconstruction	11344	23151	21132
Resolution[c] (Å)	2.33	2.96	3.08
Map sharpening B-factor ($Å^2$)	-90.4	-150.8	-141.5
Model Statistics			
Correlation coefficient[d]	0.850	0.845	0.862
No. of atoms			
Protein	6264	5398	5149
Water	490	0	0
Avg. B-factor ($Å^2$)	14.1	20.7	27.3
r.m.s deviations[e]			
Bond lengths (Å)	0.009	0.010	0.010
Bond angles (°)	0.998	0.995	0.984
Ramachadran plot[e]			
Favored (%)	97.10	94.98	93.48
Allowed (%)	2.90	4.73	6.52
Outliers (%)	0.00	0.30	0.00

[a] No. of micrograhs where particles were extracted.
[b] Data collection was in electron couting mode. The physical pixel size is 1.62 Å/pixel.
[c] Estimated by Fourier shell correlation between two half-maps using 0.143 as a cut-off.
[d] Real space correlation coefficient (around atoms) between final EM map and a density map calculated based on the coordinates.
[e] Based on the criteria of Molprobity

many EVs (19-21). The capsid structure of empty particles is considerably similar to that of A-particles (with a root mean square deviation (RMSD) of 0.2 Å). The RMSD values of two given structures were calculated based on equivalent Cα atoms

throughout the chapter. This indicates that these empty particles are emptied particles that are formed after native full virions have released the viral genome. Emptied particles are distinct from VP0 containing native empty particles that have nearly the same capsid structure as native full virions.

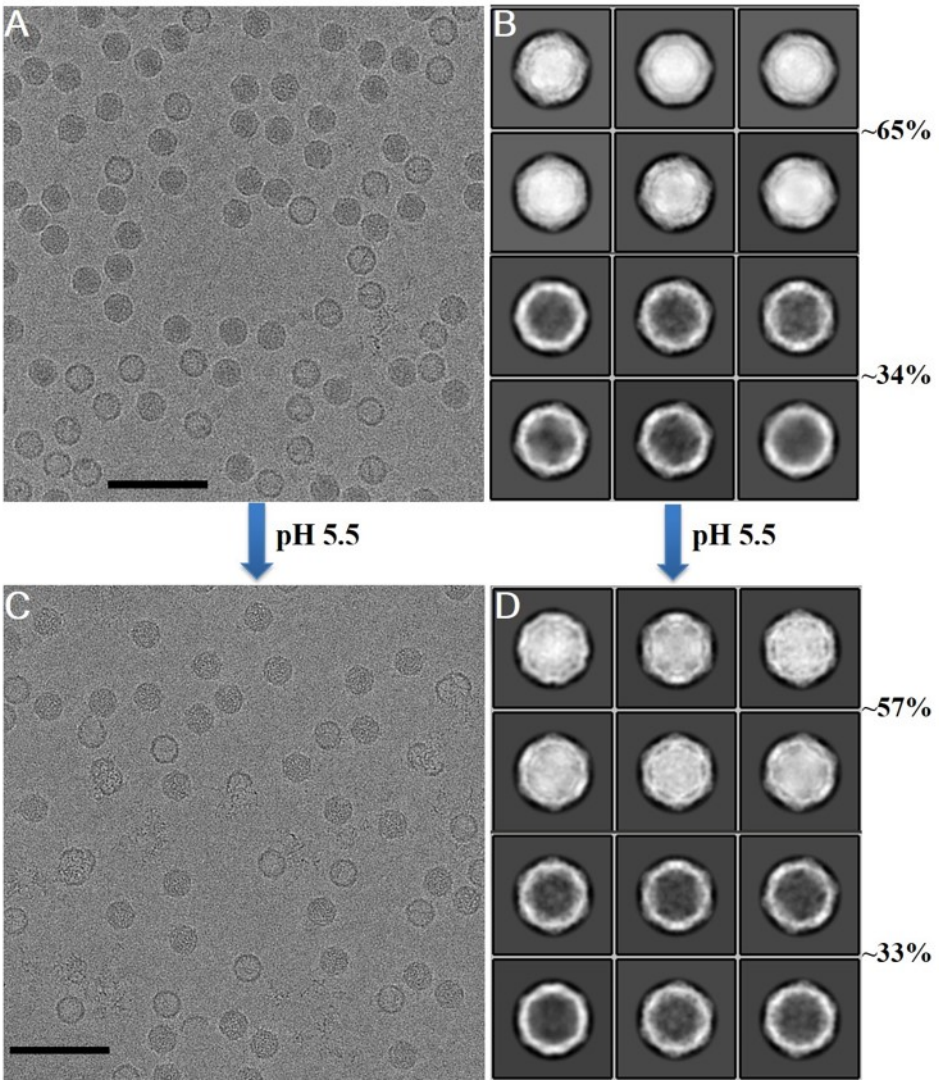

Fig. 5.3. **Acid induces structural changes of strain MO.** Typical electron micrographs (four times binned) show EV-D68 MO particles treated with pH 7.2 buffer (**A**) and with pH 5.5 buffer (**C**). Scale bar: 100 nm. The corresponding 2D class averages of particle images are shown in (**B**) and (**D**), respectively. On the far right, the percentage of particle images that are classified to be full or empty is given.

In order to mimic the environment for virus uncoating in host cells, Prep B was treated with a pH 5.5 (late endosomal pH) buffer at 33°C for 20 min(dataset B_33_Acid). Similar to the aforementioned observation in the case of room temperature incubation, A-particles and emptied particles were present in dataset B_33_Acid. The cryo-EM structures of A-particles (23,151 particles) and emptied particles (21,132 particles) were determined to about 3.0 Å and 3.1 Å resolution, respectively (Table 5.1 and Fig. 5.4). Radial density distribution of spherically averaged EM maps show that A-particles and emptied particles are similarly expanded by about 8Å in diameter relative to native full virions (Fig. 5.4). Moreover, pores are opened up at two-fold axes on A-particles (with a pore size of about 8Å x 14Å) and emptied particles (pore size of about 7Å x 29Å). A VP2 helix (residues 2091-2098) and the equivalent helix from a two-fold related VP2 molecule move away from each other (Fig. 5.4). These pores might function as sites where the genomic RNA exits, partially because a single strand RNA, assuming no secondary structures, has a size of slightly less than 8Å x 10Å (concerning the adenosine residue that is larger than other residues) by looking in the direction normal to the planar aromatic ring of the nucleotide base. More importantly, when native full virions are converted into A-particles, the VP1 N-terminal residues 1042-1051 undergo dramatic conformational changes, causing the movement of residue 1042 and residue 1051 by about 35 Å (Cα) and 8 Å (Cα), respectively. In native full virions, residues 1042-1051 reside in the virus interior. In the A-particles, residues 1044-1051 traverse the capsid shell such that residue 1042 lies on the outer surface (Fig. 5.4). These changes cause the externalization of the VP1 amphiphathic helix (disordered in the A-particle structure) through a pore at the base of the canyon. The VP1 amphipathic helix was previously predicted as a segment of about 25 amino acids at the extreme N-terminus [114]. Thus, acid induced structural changes facilitate EV-D68 uncoating.

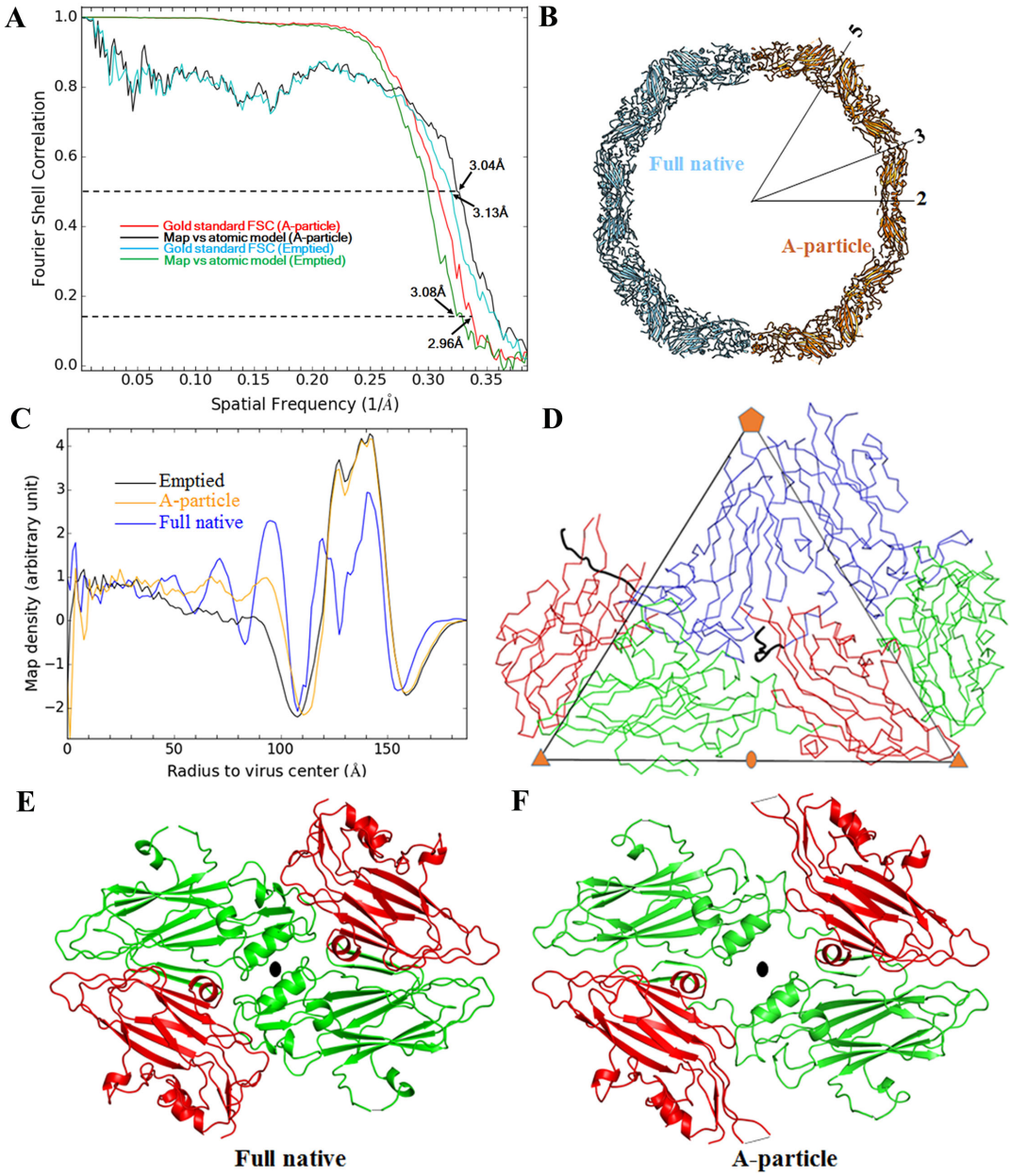

Fig. 5.4. **The structures of EV-D68 uncoating intermediates.** **A.** Resolution estimation of reconstructions using FSC (0.143 as a cut-off) between two half-maps. **B.** Radial density distribution of spherically averaged cryo-EM maps. **C.** For each one of the full native and A-particle atomic structures, a half capsid shell is represented as a slab of about 20 Å. **D.** The Cα backbone representation of two protomers is colored blue (VP1), green (VP2), and red (VP3). VP1 residues 42-52 are highlighted in black. **E-F.** Pores are formed at two-fold axes in A-particles, as compared with native full virions.

5.4.3 Multiple structural intermediates are involved in EV-D68 uncoating

At neutral pH, Prep B is made up of a heterogeneous particle population as mentioned above. To analyze the sample heterogeneity at neutral pH in detail, 2D classification and subsequently three-dimensional (3D) classification of particle images (dataset B_4_Neu) resulted in six different structural states of the virus capsid. These structures were determined to about 3.5-3.6 Å resolution (Table 5.2). These states differ mainly in particle size and in internal regions including the VP1 N-terminal residues 1001-1053 and VP4. The two predominant states are full native virions (accounting for about 50% of all particles) and emptied particles (about 21%) (Fig. 5.5). This observation suggests that a portion of native full virions might have undergone uncoating to produce emptied particles during virus purification. Consistent with this prediction, two uncoating intermediates have also been identified from the whole particle population. One intermediate is A-particles (about 10%), whereas the other one represents a previously undescribed structural state (about 5%), which is termed "expanded 1 particle" (E1 particle) here. The VP1 N-terminal residues 1001-1053 and VP4 residues 4030-4057 are ordered in E1 particles, as is the case for full native virions (Fig. 5.5). Nevertheless, the E1 particle is expanded by about 8 Å in diameter relative to the native full virion as indicated by calculation of radial density distribution. The RMSD between the two structures when aligning icosahedral symmetry axes is about 4.0 Å. There are pores formed at two-fold axes on E1 particles. The size of the pores is about 6 Å in one direction and about 9-23 Å in the orthogonal direction. This uncertainty of pore size is due to an ambiguity in building some amino acid side chains into the EM map at about 3.6 Å resolution. It is probable that virus uncoating is initiated by particle expansion of full native virions to form E1 particles. Subsequent loss of the VP4 molecules and externalization of the VP1 N-termini through pores on the E1 particles result in A-particles. The genomic RNA

is ultimately released to yield emptied particles. These results show that multiple structural intermediates are involved in EV-D68 uncoating (Fig. 5.5).

In addition, two other structural states, each of which accounts for about 7% of all particles, were found to have similar capsid structures to the full native virion (Fig. 5.6). The RMSD between the full virion and each of the two states is slightly less than 1.0 Å when aligning icosahedral symmetry axes. The two states either lack inner densities or show rod-like densities in the particle. They might be abortive products during virus assembly. Nevertheless, further studies are needed to unravel the true identity of these states.

5.5 Discussion

In the present work, acid treatment was found to diminish or abolish EV-D68 infectivity (Fig. 5.1). This is primarily because A-particles, which are formed under acidic conditions, have limited infectivity according to a previous report [217]. The absent of VP4 in A-particles probably prevents pore formation on host cell membranes [234]. Additionally, externalization of the membrane associated region of VP1 N-terminal residues might impair receptor binding of A-particles. These factors would render A-particles poorly infectious.

Differences of amino acid sequences in the P1 capsid region might explain why the two current strains, MO and KY, are more sensitive to acid than the Fermon strain. Strains MO and KY possess six more charged residues (Lys, Arg, Glu, and Asp) on the virus surface than the Fermon strain. More importantly, the two current strains have a His at position 2098, whereas the Fermon strain has a Tyr. There is also a conserved His at position 2099 shared by enteroviruses. Histidine can act as a pH sensor whose pKa is about 6. In particular, residue 2098 is located on the aforementioned helix (residue 2091-2098) that is in close proximity to the icosahedral two-fold axis and that contributes to the opening of pores at two-fold axes in EV-D68 uncoating intermediates. At low pH conditions (pH$\leq$6), histidine residues

Table 5.2
EM Data collection and processing statistics

	Full_1[a]	Full_2[a]	Full_3[a]	Emp_1[a]	Emp_2[a]	Emp_3[a]
Data collection and processing						
(Probable) identity	Native	Expanded 1	A-ptcl	Emptied	Abortive ptcl 1	Abortive ptcl 2
Microscope	Titan Krios (300 kV)					
Camera	Gatan K2 Summit					
No. of micrographs[b]	413	413	413	413	413	413
Defocus (μm)	1.7-5.3	1.7-5.3	1.7-5.3	1.7-5.3	1.7-5.3	1.7-5.3
Pixel size[c] (Å/pixel)	1.62	1.62	1.62	1.62	1.62	1.62
Dose rate (e^-/pixel/s)	8	8	8	8	8	8
Frame rate (ms)	250	250	250	250	250	250
Total dose ($e^-/Å^2$)	45	45	45	45	45	45
No. of ptcls for reconstruction	6000	2532	5291	11912	3962	3758
Resolution[d] (Å)	3.45	3.57	3.63	3.59	3.59	3.53
Map sharpening B-factor ($Å^2$)	-194.8	-162.8	-202.0	-215.8	-178.7	-193.1
Model Statistics						
Correlation coefficient[e]	0.824	0.820	0.817	0.807	0.831	0.829
No. of atoms in protein	6264	6053	5398	5149	5723	5576
Avg. B-factor ($Å^2$)	28.6	37.7	32.0	32.6	40.4	28.7
RMSD Bond lengths (Å)	0.009	0.010	0.010	0.01	0.009	0.010
RMSD Bond angles (°)	0.860	0.906	0.996	0.968	0.843	0.896
Ramachadran plot favored (%)	95.33	94.50	93.35	93.48	95.68	95.30
Ramachadran plot allowed (%)	4.67	5.24	6.35	6.37	4.18	4.56
Ramachadran plot outliers (%)	0.00	0.26	0.30	0.16	0.14	0.14

[a] The Names of structural states determined using Prep B of strain MO at neutral pH which was stored at 4°C.
[b] No. of micrographs where particles were extracted.
[c] Virtual pixel size in super resolution mode. Physical pixel size is 1.30 Å/pixel.
[d] Estimated by Fourier shell correlation between two half-maps using 0.143 as a cut-off.
[e] Real space correlation coefficient (around atoms) between final EM map and a density map calculated based on the coordinates.

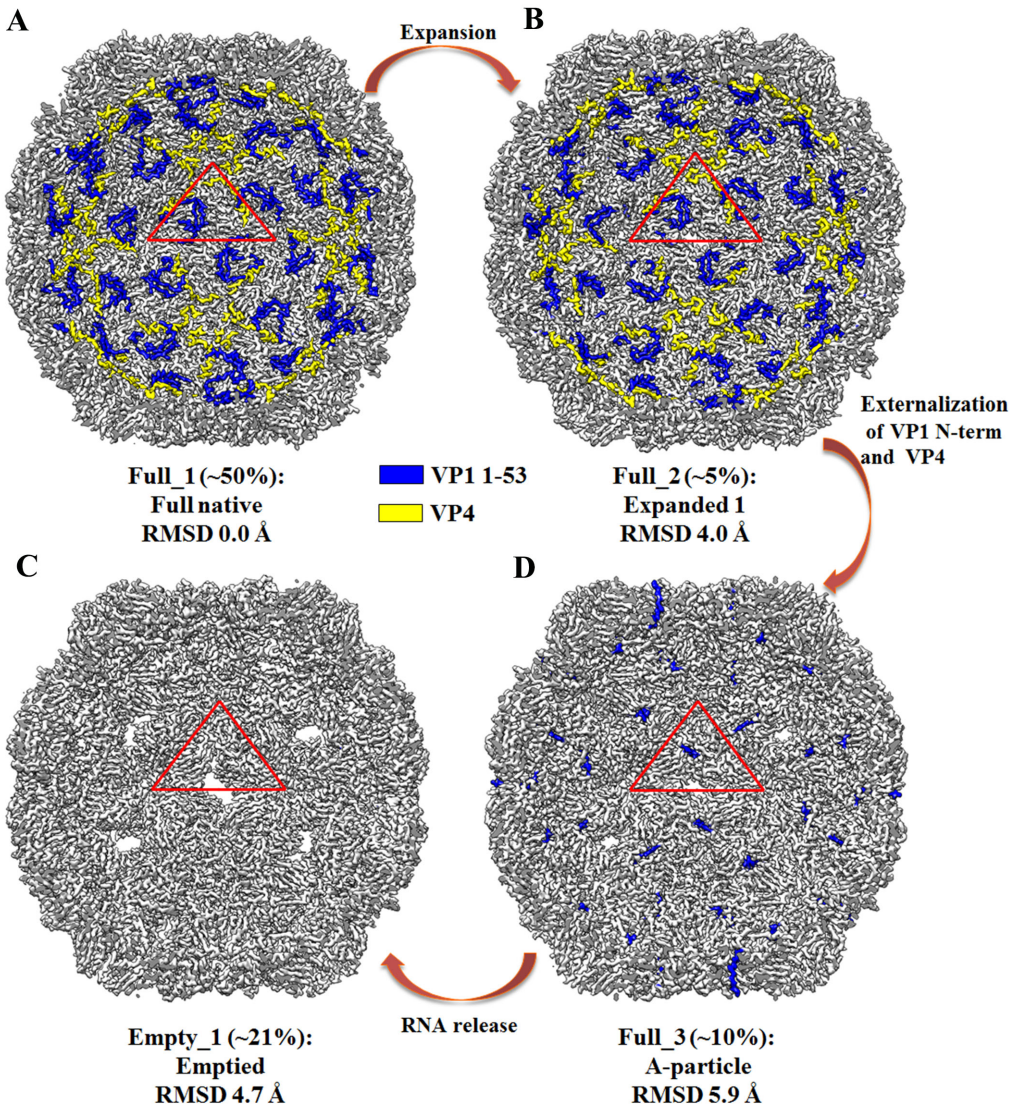

Fig. 5.5. **EV-D68 uncoating entails multiple structural intermediates. A-D.** A cut-way view of each of four different structural states of the EV-D68 (strain MO) capsid by looking down an icosahedral two-fold axis from particle exterior to particle interior. A red triangle indicates an icosahedral asymmetric unit. RMSD values are calculated based on equivalent Cα atoms using the native full virion structure as a reference and by aligning icosahedral symmetry axes. The percentage of particles images that are classified into a given state is shown in parentheses.

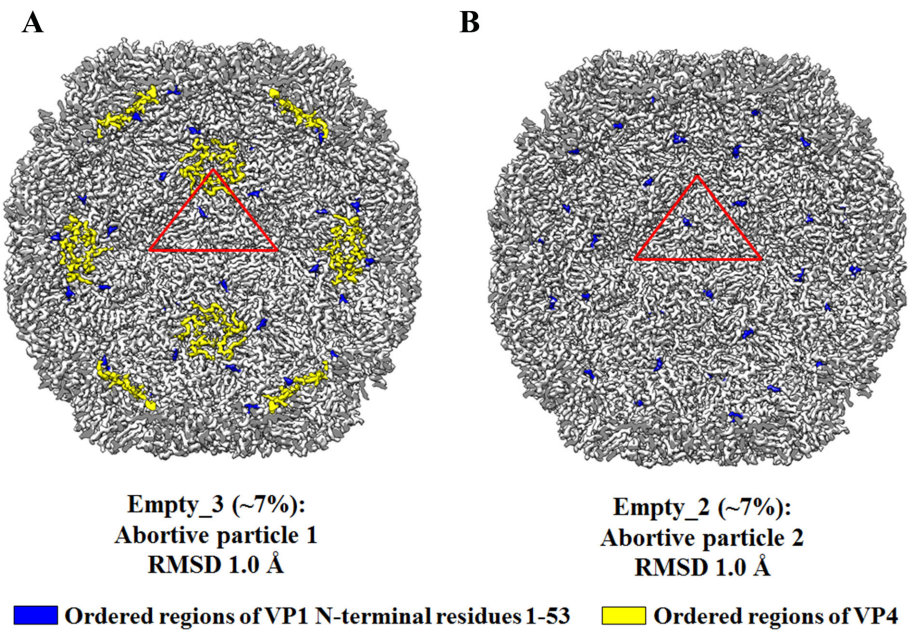

Fig. 5.6. **Multiple structural states are present at neutral pH. A-B.** Two additional structural states represent probable abortive products during virus assembly. Details for making the figure and for labeling are the same as those in Fig. 5.5.

near two fold axes become protonated and might facilitate acid induced structural changes of the virus. A similar mechanism was previously proposed for an animal picornavirus, foot-and-mouth-disease virus (FMDV). The repulsive electrostatic interactions at the pentamer-pentamer interface caused by protonated histidine residues were suggested to trigger the dissociation of FMDV pentamers upon endosomal acidification [286, 464]. Furthermore, 25 out of 297 EV-D68 strains for which the (nearly) complete genome sequence is available (as of October 2016) have a Tyr at position 2098 and were isolated in between 1962 and 2013. This indicates that current EV-D68 strains have evolved to acquire a His at position 2098, which might confer a high acid sensitivity of the virus and the efficiency of virus uncoating.

Amino acid sequence alignments of multiple enteroviruses showed that EV-A71, CVB3, PV, RV-A16, RV-A2, RV-B14, and EV-D68 (Fermon) contain a Tyr/Phe at the equivalent position to position 2098 in EV-D68 [2]. Thus, alternative mechanisms

might exist that account for the acid lability of rhinoviruses and early EV-D68 strains that have a Tyr at position 2098. For instance, previous electrostatic calculations of viral stability postulated a mechanism where a β-sheet at the pentamer-pentamer interface regulates the accessibility of buried histidine residues to acid [465]. The β-sheet appears to be unstable in rhinoviruses but is stable in polioviruses at low pH conditions.

Sialic acid receptor and endosomal acidification probably assist EV-D68 entry into host cells in a synergistic manner. Sialic acid receptor binding to the Fermon strain caused ejection of the pocket factor that destabilizes the virus. The infectivity of the Fermon strain was slighted impaired at pH 5-6, suggesting that endosomal acidification alone would not be sufficient to result in uncoating of the strain. This observation raises the possibility that sialic acid receptor binding increases the pH threshold for triggering virus uncoating. Nevertheless, the synergistic action of receptor and low pH depends on virus strains. Concerning strain MO (as probably also strain KY), because of the absence of a pocket factor in the native structure and of the low stability under acidic conditions, sialic acid receptor binding might not contribute to virus destabilization or to prime virus uncoating.

In summary, cryo-EM studies of the acid sensitive EV-D68 have shown the involvement of multiple structural intermediates in virus uncoating. The identification of expanded 1 particles, a previously unknown intermediate, suggests the conformational fluctuation of enterovirus capsids.

6. INHIBITION OF HUMAN ENTEROVIRUS D68

Part of the data and text in this chapter are taken from [2, 3] and are highlighted by a black, vertical line in the right margin below. Macmillan Publishers Ltd: Nature Communications [3], copyright 2015. Text and data from [2] are reprinted with permission from AAAS.

6.1 Chapter abstract

Effective antiviral treatments are currently not available to combat respiratory diseases and rare neurological diseases associated with EV-D68. Structural similarity between EV-D68 and rhinoviruses opens up the possibility of re-purposing known rhinovirus inhibitors for inhibiting EV-D68 infections. Here, pleconaril, a compound that had been specifically developed for rhinoviruses, has been found to be a nanomolar inhibitor against the prototype strain and two circulating strains of EV-D68. The crystal structure of EV-D68 in complex with pleconaril showed that it replaces the pocket factor in binding the VP1 pocket. Furthermore, pleconaril inhibits EV-D68 attachment onto host cells and prevents virus uncoating. These results suggest that pleconaril represents a candidate antiviral approach for treatments of EV-D68 infections.

6.2 Introduction

Over the last several decades, the hydrophobic pocket of VP1 has been explored as target for a variety of small hydrophobic molecules that are known as capsid-binding inhibitors of enterovirus (EV) infection. They stabilize the virus [188] by filling the pocket with a well-fitting hydrophobic molecule, thereby inhibiting uncoating of the

virus and the release of the genome into the infected cell. These compounds also prevent attachment to cells by altering the surface features of the canyon floor where the virus attaches to a cellular receptor [183, 188]. In addition, it was also shown that capsid-binding compounds impedes virus breathing, which refers to reversible conformational changes of the virus [253, 254].

In most enteroviruses that have been investigated these capsid binding antiviral compounds displace the pocket factor (e,g. PVs and many rhinoviruses (RVs)). RV-B14 [13,243] and RV-B3 [20] do not contain a pocket factor, and they have a collapsed VP1 pocket. Either neither RV-B14 nor RV-B3 bind a pocket factor *in vivo* or it was lost during the purification procedure. Much effort was made between 1985 and 2000 to design a compound that fits into the VP1 pocket and would inhibit the maximum number of rhinoviruses [457]. The final optimal structure was pleconaril which not only had good efficacy but was also stable enough to maintain good bioavailability in clinical tests [466]. For instance, oral pleconaril treatment was effective in reducing the duration of common colds among adults in phase III clinical trials [466]. However, pleconaril was not licensed primarily because it put women using birth control drugs at risk of conception.

Currently, there are two capsid binding anti-EV compounds that are in clinical trials. Pocapavir (or V-073) [81] is now being developed specifically for polioviruses, aiming for usage in the post-eradication era [467]. Vapendavir (or BTA-798) [80] has passed several phase II clinical trials with asthmatic patients. It is in development for treatment of human rhinovirus infections and rhinovirus induced asthma exacerbations that can result in chronic obstructive pulmonary disease.

This chapter describes the discovery of pleconaril as an effective capsid binding inhibitor against EV-D68. Structural and functional analysis also unraveled the mechanism of action of pleconaril. Pleconaril interferes with EV-D68 entry into host cells by inhibiting virus attachment and uncoating.

6.3 Materials and Methods

6.3.1 Co-crystallization and data collection

Highly purified EV-D68 virions (2-3 mg/ml in PBS) were incubated with 0.2 mg/ml (in PBS) pleconaril at room temperature for 6h. 0.6 μl of the resultant solution were then mixed with 0.6 μl of the reservoir solution (0.1 M sodium acetate (pH 4.5) with 3.5 M sodium formate) for crystallization using the hanging drop vapor diffusion technique. Thick plate-like or cubic, shiny crystals were obtained in 2-3 days at room temperature. Crystals were cryo-protected in the same cryo-solution (as in Chapter 2) except that 0.2 mg/ml pleconaril was added. Data collection on single crystals was performed in the same way as mentioned for native EV-D68 crystals (Chapter 2).

6.3.2 Structure determination

The crystals for the EV-D68-pleconaril complex were isomorphous with the native EV-D68 crystals (Chapter 2). Initial phases were calculated using the native EV-D68 structure (without the pocket factor or water) for reflections to 8.0 Å resolution. Phase extensions were performed using a step size of 1/a $Å^{-1}$ until 2.3 Å resolution had been reached similar to the phase determination of the native EV-D68 crystals.

6.3.3 *In silico* docking

In silico docking was performed by Woong-Hee Shin in the Kihara laboratory (Purdue). Pleconaril, pirodavir and BTA-188 were docked into EV-D68 using AutoDock4 [468]. The three-dimensional coordinates of pirodavir and BTA-188 were obtained from the PubChem database [469]. The binding pocket in EV-D68 was defined as a cube-shaped box that ranged 22.5 °C in each direction from the geometrical center of the pleconaril molecule as observed in the crystal structure. Each compound was treated as being fully flexible (all single bonds that are not in a ring structure

or between two double bonds were allowed to rotate) while the surrounding protein structure of the virus was kept rigid. The Lamarckian Genetic Algorithm [470] was used for conformational searches of the compound. The parameters that described the conformation of the compound and its orientation and position in the search box were set to random values to initiate each run. These were then optimized to minimize the calculated binding energy. One thousand runs were made. The resultant one thousand structures were then clustered around the final structures with the lowest calculated binding energy. In each cluster, all structures have an r.m.s.d. value of less than 2.0 Å relative to the lowest energy structure in this cluster. The structure with the lowest calculated binding energy from the largest cluster was finally selected as the most likely structure.

6.3.4 Viral attachment assay

To test the effect of pleconaril on EV-D68 attachment, purified virus (the prototype strain) was incubated with pleconaril in a series of concentrations ranging from 0 14 μM at 33°C for 1h, where 0 μM represents the virus only control in which the virus was incubated with only DMSO. The resultant mixture was cooled down on ice and added to 90% confluent HELF cells in a 24-well plate right after blocking each well with the blocking solution as mentioned above. The MOI was 20. After incubation at 4°C for 1h, the wells were washed three times with cold DMEM to remove unbound virus. Similar results were obtained when the virus was incubated with pleconaril at 4°C overnight. Total RNA in each well was extracted using an RNeasy Mini Kit (Qiagen) per manufacturers protocol (RNA extraction was performed by Ju Sheng). The viral RNA of the bound virus in each sample was quantified a quantitative real-time RT-PCR assay (together with Ju Sheng). All experiments were done in triplicate.

6.3.5 Thermal stability assay

Thermal stability assays were performed similarly as previously described [471, 472] with some modifications. This was done together with Ju Sheng. Briefly, 1.5 μg of EV-D68 virus were incubated with pleconaril (with a final concentration of 10 μg/mL or 50 μg/ml) at 33°C for 1h. The control virus was treated the same way except that no pleconaril was added. 1% DMSO (v/v) was used consistently. Sybr green II dye (Life Technologies) was added to reach a concentration of 6X and RNAseOUT (Life Technologies) at a concentration of 1U/μl. For each sample, a 50 μl reaction was set up and the fluorescence intensity was recorded in triplicate at 1°C intervals between 31°C and 95°C using a real time PCR system (Applied Biosystems 7300). After heating to a given temperature and holding for 20s, the sample temperature was then lowered to 30°C and held for 2 min. This ensured that the fluorescence was recorded at a constant temperature. The fluorescence intensity was plotted as a function of temperature and the data were fitted with a sigmoidal curve.

6.3.6 Plaque reduction assay

Three EV-D68 strains were used for plaque reduction assays, including the prototype strain and two strains (US/MO/14-18947 and US/KY/14-18953) from the 2014 outbreaks in the United States. Experiments were performed together with Ju Sheng. The virus was incubated with a specific inhibitory compound that had been dissolved in DMSO at 33°C for 1h. For each of the three compounds (pleconaril, pirodavir, and BTA-188), a series of concentrations were assayed in at least triplicate. For vehicle control, the same amount of DMSO was added without using a test compound. Confluent HeLa cells in 6-well plates were infected with approximately 150 PFU (plaque-forming unit) EV-D68 with compounds or DMSO per well. An overlay containing 0.8% agarose was added to each well. After 4 days of incubation at 33°C, the plaques were counted in each well. The percent inhibition was calculated

by $(N_{control} - N_{inhibitor}) \times 100/N_{control}$, where $N_{control}$ and $N_{inhibitor}$ are plaque counts for the control and inhibitor wells, respectively.

6.4 Results

6.4.1 Pleconaril inhibits EV-D86 infection

The structural similarity of EV-D68 and many RVs suggested that the EV-D68 VP1 pocket might be targeted by known capsid-binding inhibitors against RVs. The anti-EV-D68 activity of two capsid binding compounds, pirodavir and BTA-188 (Fig. 6.1), that had significant anti-rhinovirus activity were compared with pleconaril using plaque reduction assays in HeLa cells (Fig. 6.2). The half maximal effective concentration, EC50, value of these two compounds were found to be comparable to previous results using cytopathic effect inhibition assays against EV-D68 [473]. However, pleconaril was found to be more potent against EV-D68 than pirodavir and BTA-188 (Fig. 6.2). The inhibitory effect of pleconaril is similar against EV-D68, RV-A16 and RV-B14 but better than against EV-A71. It is, therefore, noteworthy that pleconaril was an effective inhibitor in extensive clinical tests for treatment of common colds [466, 474] .

6.4.2 Pleconaril interferes with virus entry

Furthermore, pleconaril was found to interfere with virus attachment and uncoating during cell entry of EV-D68. As described in Chapter 3, the structures of EV-D68 complexed with sialylated trisaccharides suggest that the receptor molecule and the pocket factor compete to bind the virion in the initial step of EV-D68 entry into host cells. Pleconaril inhibits sialic acid dependent viral attachment to HELF cells (Fig. 6.2) because the bound pleconaril blocks the conformational change of the virus that favors sialic acid binding. In addition, fluorescence-based thermal stability assays indicated that when EV-D68 was incubated with either 10 μg/ml or 50 μg/ml

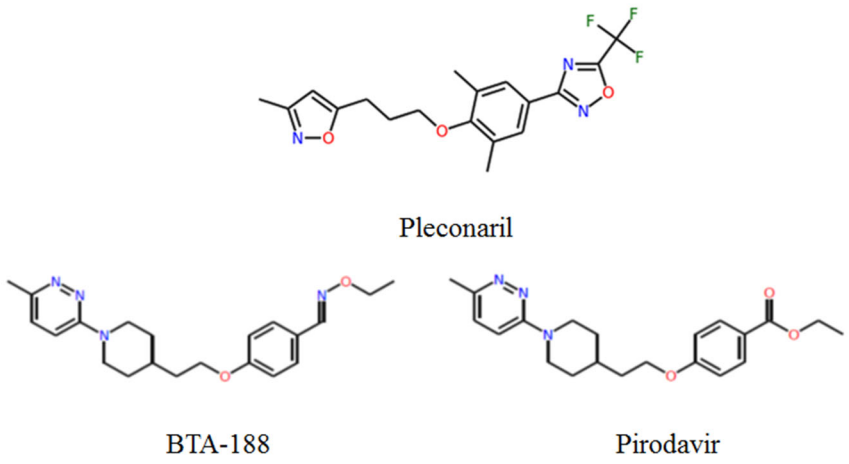

Fig. 6.1. **Chemical structures of pleconaril** [75] **, BTA-188** [475]**, and pirodavir** [476].

pleconaril, 4°C higher temperatures were required to release the RNA genome than when no pleconaril was present (Fig. 6.2). Thus, pleconaril stabilizes EV-D68 capsids and prevents the virus from uncoating during viral entry.

6.4.3 Structure of EV-D68 in complex with pleconaril

The structure of EV-D68 was also determined to 2.3 Å resolution when co-crystalized with pleconaril (Table 6.1). The crystallographic procedure was the same as for the native structure determination. The R factor was 0.243 (Table 6.1). The electron density of the ligand inside the hydrophobic pocket was of the same height but much longer than that of the pocket factor in the native EV-D68 structure (Fig. 6.3) and could be easily fitted with the structure of pleconaril (Fig. 6.3). This demonstrated that the native pocket factor was replaced by pleconaril. However, the density of the ligand and of the pocket factor are slightly lower than that of the polypeptide main chain. In part this is to be expected because the ligand or fatty acid pocket factor are composed primarily of only carbon atoms as opposed to the heavier combination of carbon, nitrogen plus oxygen atoms of the main chain. In part the slightly

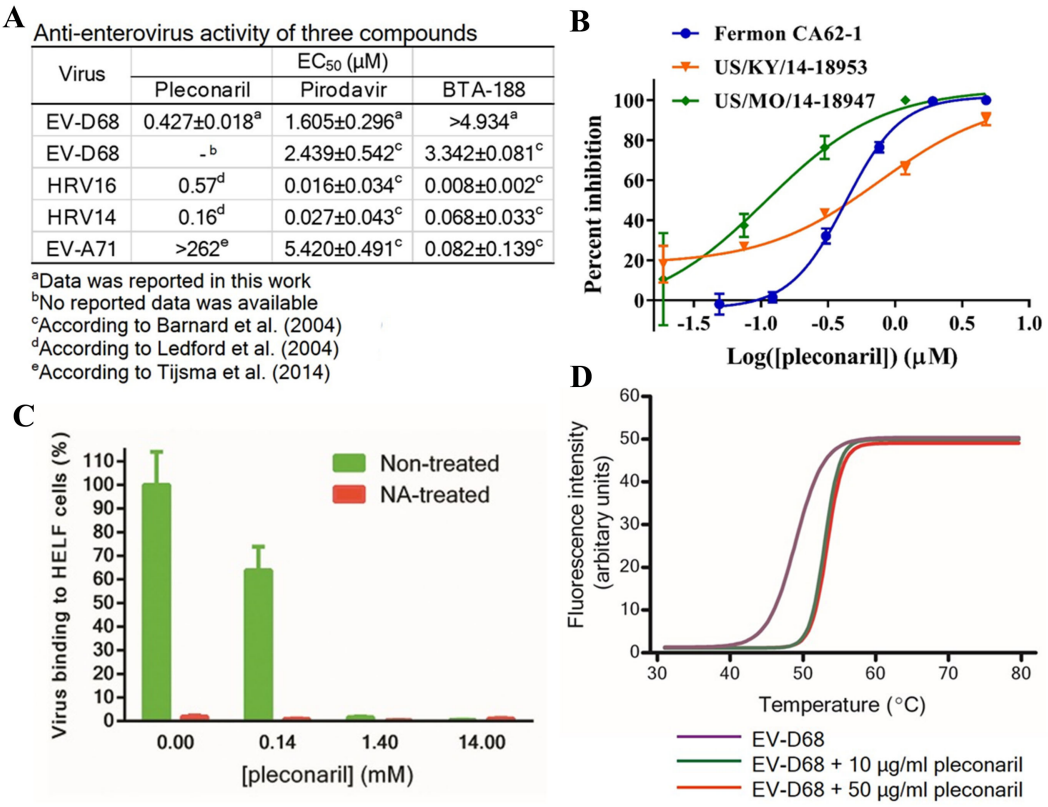

Fig. 6.2. **Pleconaril is effective against EV-D68**. **A.** List of EC50 values. **B.** Plot of % plaque reduction of pleconaril as a function of the log of its concentration. Error bars indicate SD. **C.** Preincubation of EV-D68 (prototype) with pleconaril inhibits viral attachment onto non-treated HELF cells. Data are represented as mean±SD. Experiments were done in triplicate. **D.** Release of EV-D68 genome upon increase in temperature as monitored by Sybr green II. The experiments were done in triplicate. For each data point, the ratio between mean fluorescence intensity and standard deviation is at least 7.6. Shown are curves fitted with a sigmoidal function for the native virus and for the virus after incubation with pleconaril. Panels **A**, **B**, and part of panel **C** from [2]. Reprinted with permission from AAAS.

lower density of the ligand might be due to some variations of conformation within the VP1 binding pocket.

Part of the VP1 GH loop (residues 212-215) that forms the entrance to the VP1 pocket had become less ordered. The Cα atom of residue 211 had moved 1.2 Å

Table 6.1
Data collection and refinement statistics[a]

	EV-D68 with pleconaril
Data collection	
Oscillation angle (°)	0.2
No. of crystals (No. of frames)	2 (232)
Space group	I222
Cell dimensions	
a, b, c ()	323.2, 346.1, 355.5
α, β, γ (°)	90.0, 90.0, 90.0
Resolution ()	50.0-2.32 (2.40-2.32)[b]
No. of unique reflections	399300 (26345)
Completeness (%)	47.2 (31.3)
Redundancy	1.6(1.2)
Rmerge[c]	0.077 (0.185)
$I/\sigma(I)$	6.98 (2.35)
Refinement	
Resolution ()	50.0-2.32 (2.40-2.32)
No. of reflections	399130 (26181)
R factor	0.235 (0.345)
Correlation coefficient	0.876
No. of atoms	
Protein	6260
Ligand	27
Water	121
RMSD bond (Å)	0.006
RMSD angle (°)	1.388
Mean B-factor (Å^2)	17.3
Mean B-factor of ligand (Å^2)	62.5
Ramachandran plot	
Favored (%)	94.5
Allowed (%)	5.5
Outliers (%)	0

[a] From [2]. Reprinted with permission from AAAS
[b] Values in parentheses represent the highest resolution shell
[c] $R_{merge} = \sum_{hkl} \sum_i |I_i(hkl) - < I(hkl) > | / \sum_{hkl} \sum_i I_i(hkl)$

towards the inside of the pocket relative to that of the native structure, possibly blocking the entrance to the pocket once pleconaril had entered (Fig. 6.3). Thus the

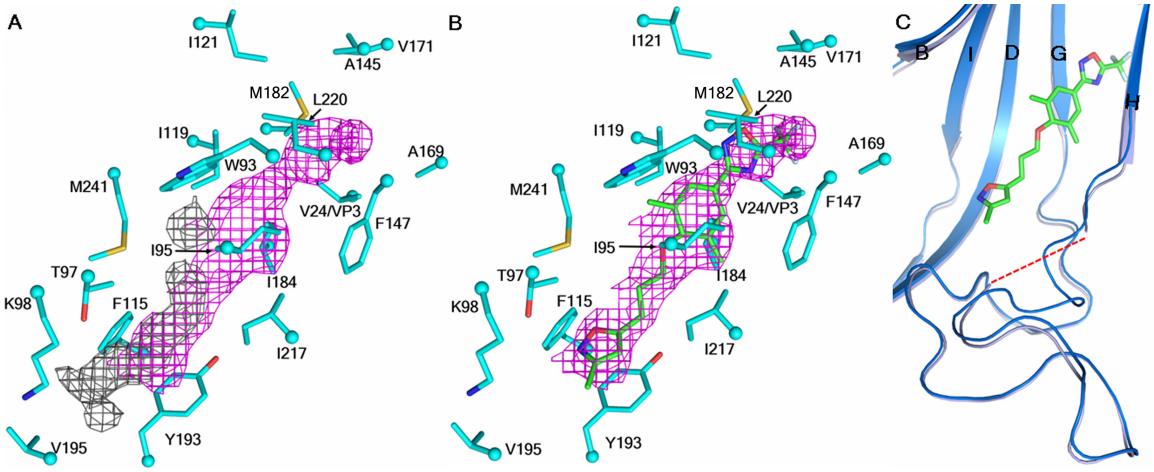

Fig. 6.3. **Structure of pleconaril bound into the VP1 pocket of EV-D68**. **A.** Pocket factor density (grey) compared to the pleconaril density (magenta). **B.** Pleconaril (green) fitted to density in the structure of the complex. **C.** Conformational change of the VP1 GH loop as a consequence of the presence of pleconaril. The native and complex structures are shown in marine blue and baby blue, respectively. Oxygen, nitrogen, sulfur and fluorine atoms are shown in red, dark blue, yellow and light green, respectively. From [2]. Reprinted with permission from AAAS.

dynamics of GH loop might be an important consideration for future structure-based design of EV-D68 capsid-binding inhibitors.

A comparison of the EV-D68-pleconaril, RV-B14-pleconaril and RV-A16-pleconaril structures showed a similar binding mode for pleconaril in the VP1 pocket of these three viruses (Fig. 6.4). This may explain why pleconaril is similarly effective against these three enteroviruses. To investigate why pleconaril is more effective against EV-D68 than pirodavir or BTA-188, in silico docking was performed. The presence of trifluoromethyl substituted oxadiazole moiety in pleconaril, rather than a more hydrophilic group in either pirodavir (ethyl carboxylate group) or BTA-188 (*O*-ethyloxime group) at structurally equivalent positions, likely contributes to more favorable interactions of pleconaril with the hydrophobic residues deep inside the VP1 pocket of EV-D68.

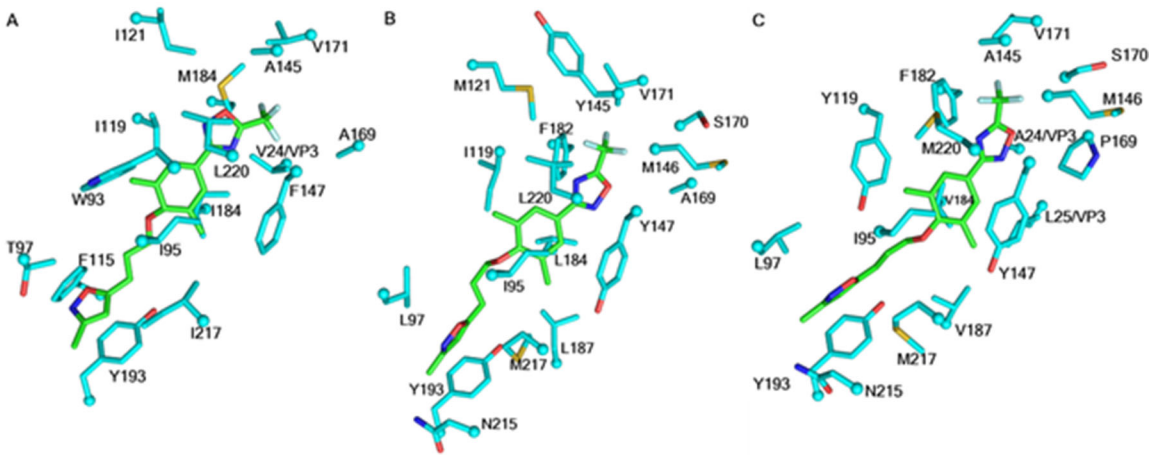

Fig. 6.4. Comparison of (A) RV-A16 complexed with pleconaril (PDB accession number: 1NCR), (B) RV-B14 complexed with pleconaril (PDB accession number: 1NCQ) and (C) EV-D68 complexed with pleconaril. Pleconaril and the protein structure are shown in green and cyan, respectively. Oxygen, nitrogen, sulfur and fluorine atoms are colored red, dark blue, yellow and light green, respectively. Residues in the three structures are all numbered according to EV-D68 numbering. Residues shown are those within 4 Å to any pleconaril atom in the corresponding structure. From [2]. Reprinted with permission from AAAS.

More importantly, in addition to the prototype Fermon strain, pleconaril also inhibited two strains from the 2014 outbreak in the United States. The EC50 values for strains US/KY/14-18953 and US/MO/14-18947 were about 760 nM and 110 nM, respectively (Fig. 6.2). US/KY/14-18953, a phylogenetically minor strain in the 2014 outbreak, has the the same set of pleconaril interacting residues as the Fermon strain strain. US/MO/14-18947, a phylogenetically predominant strain in the outbreak, possesses two substitutions, M182I (VP1) and V24A (VP3), relative to the Fermon strain.

6.5 Discussion

The structure of EV-D68 has considerable similarities to the well-studied RVs for which pleconaril was specifically designed. This chapter shows that pleconaril replaces the pocket factor and is a potent inhibitor of EV-D68 strains. The size and location of the pocket factor lodged in the VP1 pocket is similar to that found in other RVs and different to the pocket factors found in poliovirus 1 and EV-A71. This correlates with the observation that pleconaril is far more active when the natural pocket factor is short as in the RVs and in EV-D68.

Pleconaril was found to be an effective inhibitor against not only the prototype strain (isolated in 1962) but also two circulating strains (isolated in 2014). Furthermore, sequence alignment of 188 EV-D68 strains found between 1962 and 2013 indicates that residues in VP1 which interact with pleconaril, as identified from the complex structure, are completely conserved with one exception. Additionally, the activity of pleconaril to US/MO/14-18947 was not impaired by the presence of two amino acid substitutions in the hydrophobic pocket. These results indicate that pleconaril might be able to inhibit a broad spectrum of EV-D68 strains. In accordance with this prediction, pleconaril recently proved to be effective against a range of EV-D68 clinical isolates that were classified into three different clades [477] .

Consistent with the activity of pleconaril using a plaque assay in HeLa cells presented here, several other recent work reported overall similar results when using cytophatic effect inhibition assays in HeLa cells [477–479]. Furthermore, the clinical efficacy of pleconaril in treatment of common colds was shown to correlate with the susceptibility (to pleconaril) of viruses that infect human subjects. The greatest activity of pleconaril was observed in subjects infected with viruses that showed an EC50 of less than 0.38 μg/ml (or better than about 1 μM) [474]. Thus, it is probable that pleconaril, a nanomolar inhibitor of EV-D68, would be clinically effective in treatment of EV-D68 infections.

Nevertheless, some uncertainties have also been raised over the clinical efficacy of pleconaril against EV-D68. One recent report found that the activity of pleconaril against circulating strains depends on the cell lines used for inhibition assays [478].

This observation makes it more complicated to predict clinical efficacy according to cell-based inhibition data. Moreover, EV-D68 variants resistant to pleconaril were readily selected in the laboratory. The variants shared one common substitution (V1069A) that was proposed to weaken the interactions of pleconaril with the virus [477]. Therefore, resistance of EV-D68 to pleconaril is another factor that would possibly impair the clinical efficacy.

7. SUMMARY

Enterovirus (EV) is an important genus of *Picornaviridae*, a family of non enveloped, icosahedral viruses with a positive-strand RNA genome. The genus includes a number of human pathogens, such as polioviruses, enterovirus A71 and many respiratory viruses, including human enterovirus D68 (EV-D68) and isolates of a newly discovered species rhinovirus C (RV-C). Specifically, EV-D68 was the causative agent of an outbreak of respiratory infections among young children in the United States (US) in 2014. It also occasionally causes neurological diseases. Nevertheless, there are currently no effective antiviral treatments or vaccines available.

The crystal structures have been determined of the prototype strain of EV-D68 by itself and in complex with a capsid-binding inhibitor, pleconaril, which was developed as an anti-rhinovirus inhibitor. Antiviral compound screening shows that pleconaril is an effective inhibitor against the prototype strain and circulating strains of EV-D68. Structural analysis further demonstrates that pleconaril binds to EV-D68 capsids and replaces the pocket factor, a fatty acid-like molecule that stabilizes the virus in its native state. Thus binding of pleconaril enhances the stability of EV-D68 virions, preventing the virus from releasing its genome. These results suggest that pleconaril is a possible drug candidate to alleviate EV-D68 outbreaks.

Receptor dependent cell entry of EV-D68 has been studied through structural and functional analyses. Attachment, infectivity, and inhibition assays show that sialic acid on the cell surface is indispensable for EV-D68 to attach onto and infect host cells. To analyze the interactions of EV-D68 with sialic acid, the crystal structures of the virus have been solved when complexed with three sialylated trisaccharides that are receptor analogues. Binding of sialic acid receptor analogues to a depression, the canyon, on the virus surface causes a cascade of structural rearrangements of EV-

D68 to eject the pocket factor. Thus the sialic acid receptor destabilizes the virus and facilitates cell entry.

Isolates of RV-C are closely linked to childhood asthma exacerbations that can lead to significant adult respiratory problems. The RV-C are difficult to be propagated *in vitro*, representing a challenge for structure determination. Using cryo-electron microscopy (cryo-EM), the atomic structure of a cell adapted rhinovirus C has been determined. The RV-C structure highlights novel immunogenic surfaces, a potential binding site for glycans on the RV-C receptor and antiviral drug resistance properties. Thus structural analysis of an RV-C defines molecular determinants for designing effective antiviral therapeutics and vaccines. More importantly, this study has established a workflow for structure determination of related viruses by cryo-EM.

To characterize structural changes of EV-D68 during virus uncoating, cryo-EM studies were performed using an EV-D68 strain, namely strain MO, from the 2014 US outbreak. A 2.3 Å resolution cryo-EM structure of the virus shows the absence of a pocket factor in the hydrophobic pocket in viral protein 1. This structural feature is consistent with an instability of strain MO under acidic conditions. Acid treatment of strain MO leads to the formation of an uncoating intermediate, A(altered)-particles. Pores are opened up at icosahedral two-fold axes in A-particles, which probably allows for the exiting of viral RNA. Furthermore, cryo-EM structures of six conformational states of the viral capsid have been determined using a single sample of strain MO at neutral pH. These states exhibit differences concerning particle size and internal regions of the capsid. Thus, the process of EV-D68 uncoating might proceed via the involvement of multiple structural intermediates.

In summary, these studies have advanced the knowledge of receptor-mediated EV-D68 entry into host cells and EV-D68 uncoating. The structures presented in this thesis will facilitate the design and development of antiviral therapeutics and vaccines for respiratory enteroviruses including EV-D68 and the RV-C.

LIST OF REFERENCES

LIST OF REFERENCES

[1] Y. Liu and M. G. Rossmann, "The cellular receptor for enterovirus 71," *Protein & cell*, vol. 5, no. 9, p. 655, 2014.

[2] Y. Liu, J. Sheng, A. Fokine, G. Meng, W.-H. H. Shin, F. Long, R. J. Kuhn, D. Kihara, and M. G. Rossmann, "Structure and inhibition of EV-D68, a virus that causes respiratory illness in children," *Science*, vol. 347, no. 6217, pp. 71–74, 2015.

[3] Y. Liu, J. Sheng, J. Baggen, G. Meng, C. Xiao, H. J. Thibaut, F. J. M. van Kuppeveld, and M. G. Rossmann, "Sialic acid-dependent cell entry of human enterovirus D68," *Nature communications*, vol. 6, p. 8865, 2015.

[4] V. R. Racaniello, "Picornaviridae: The Viruses and Their Replication," in *Fields Virology* (D. M. Knipe and P. M. Howley, eds.), vol. 1, pp. 796–839, Philadelphia: Lippincott Williams & Wilkins, 5 ed., 2007.

[5] N. J. Knowles, T. Hovi, T. Hyypiä, A. M. Q. King, A. M. Lindberg, M. A. Pallansch, A. C. Palmenberg, P. Simmonds, T. Skern, G. Stanway, T. Yamashita, and R. Zell, "Picornaviridae," in *Virus Taxonomy: Classification and Nomenclature of Viruses: Ninth Report of the International Committee on Taxonomy of Viruses* (A. M. Q. King, M. J. Adams, E. B. Carstens, and E. J. Lefkowitz, eds.), pp. 855–880, San Diego: Elsevier, 2012.

[6] M. J. Adams, A. M. King, and E. B. Carstens, "Ratification vote on taxonomic proposals to the International Committee on Taxonomy of Viruses (2013)," *Arch. Virol.*, vol. 158, no. 9, pp. 2023–2030, 2013.

[7] Committee on Enteroviruses, "Classification of human enteroviruses," vol. 16, no. 4, pp. 501–504, 1962.

[8] R. M. Conant and V. V. Hamparian, "Rhinoviruses: basis for a numbering system. II. Serologic characterization of prototype strains.," *Journal of immunology (Baltimore, Md. : 1950)*, vol. 100, pp. 114–9, jan 1968.

[9] M. K. Cooney, J. P. Fox, and G. E. Kenny, "Antigenic groupings of 90 rhinovirus serotypes.," *Infection and immunity*, vol. 37, pp. 642–7, aug 1982.

[10] M. S. Oberste, K. Maher, D. R. Kilpatrick, M. R. Flemister, B. A. Brown, and M. A. Pallansch, "Typing of human enteroviruses by partial sequencing of VP1," *J Clin Microbiol*, vol. 37, no. 5, pp. 1288–1293, 1999.

[11] M. A. Pallansch and R. P. Roos, "Enteroviruses: Polioviruses, Coxsackieviruses, Echoviruses, and Newer Enteroviruses," in *Fields Virology* (D. M. Knipe and P. M. Howley, eds.), vol. 1, pp. 840–893, Philadelphia: Lippincott Williams & Wilkins, 2007.

[12] A. C. Palmenberg and J. E. Gern, "Classification and evolution of human rhinoviruses.," *Methods in molecular biology (Clifton, N.J.)*, vol. 1221, pp. 1–10, 2015.

[13] M. G. Rossmann, E. Arnold, J. W. Erickson, E. a. Frankenberger, J. P. Griffith, H. J. Hecht, J. E. Johnson, G. Kamer, M. Luo, A. G. Mosser, E. al., R. R. Rueckert, B. Sherry, and G. Vriend, "Structure of a human common cold virus and functional relationship to other picornaviruses," *Nature*, vol. 317, no. 6033, pp. 145–153, 1985.

[14] J. M. Hogle, M. Chow, and D. J. Filman, "Three-dimensional structure of poliovirus at 2.9 A resolution.," *Science (New York, N.Y.)*, vol. 229, pp. 1358–65, sep 1985.

[15] S. S. Kim, T. J. Smith, M. S. Chapman, M. C. Rossmann, D. C. Pevear, F. J. Dutko, P. J. Felock, G. D. Diana, and M. A. McKinlay, "Crystal structure of human rhinovirus serotype 1A (HRV1A).," *Journal of molecular biology*, vol. 210, pp. 91–111, nov 1989.

[16] D. J. Filman, R. Syed, M. Chow, A. J. Macadam, P. D. Minor, and J. M. Hogle, "Structural factors that control conformational transitions and serotype specificity in type 3 poliovirus," *EMBO J.*, vol. 8, pp. 1567–1579, may 1989.

[17] M. A. Oliveira, R. Zhao, W. Lee, M. J. Kremer, I. Minor, R. R. Rueckert, G. D. Diana, D. C. Pevear, F. J. Dutko, M. A. McKinlay, and M. G. Rossmann, "The structure of human rhinovirus 16," *Structure*, vol. 1, pp. 51–68, 1993.

[18] J. K. Muckelbauer, M. Kremer, I. Minor, G. Diana, F. J. Dutko, J. Groarke, D. C. Pevear, and M. G. Rossmann, "The structure of coxsackievirus B3 at 3.5 Å resolution," *Structure*, vol. 3, pp. 653–667, 1995.

[19] M. Smyth, J. Tate, E. Hoey, C. Lyons, S. Martin, and D. Stuart, "Implications for viral uncoating from the structure of bovine enterovirus.," *Nature structural biology*, vol. 2, pp. 224–31, mar 1995.

[20] R. Zhao, D. C. Pevear, M. J. Kremer, V. L. Giranda, J. A. Kofron, R. J. Kuhn, and M. G. Rossmann, "Human rhinovirus 3 at 3.0 Å resolution," *Structure*, vol. 4, pp. 1205–1220, 1996.

[21] K. N. Lentz, A. D. Smith, S. C. Geisler, S. Cox, P. Buontempo, A. Skelton, J. DeMartino, E. Rozhon, J. Schwartz, V. Girijavallabhan, J. O'Connell, and E. Arnold, "Structure of poliovirus type 2 Lansing complexed with antiviral agent SCH48973: comparison of the structural and biological properties of three poliovirus serotypes," *Structure*, vol. 5, no. 7, pp. 961–978, 1997.

[22] D. J. Filman, M. W. Wien, J. A. Cunningham, J. M. Bergelson, and J. M. Hogle, "Structure determination of echovirus 1.," *Acta crystallographica. Section D, Biological crystallography*, vol. 54, pp. 1261–72, nov 1998.

[23] E. Hendry, H. Hatanaka, E. Fry, M. Smyth, J. Tate, G. Stanway, J. Santti, M. Maaronen, T. Hyypiä, and D. Stuart, "The crystal structure of coxsackievirus A9: new insights into the uncoating mechanisms of enteroviruses.," *Structure (London, England : 1993)*, vol. 7, pp. 1527–38, dec 1999.

[24] N. Verdaguer, D. Blaas, and I. Fita, "Structure of human rhinovirus serotype 2 (HRV2).," *Journal of molecular biology*, vol. 300, pp. 1179–94, jul 2000.

[25] A. D. Stuart, T. A. McKee, P. A. Williams, C. Harley, S. Shen, D. I. Stuart, T. D. K. Brown, and S. M. Lea, "Determination of the structure of a decay accelerating factor-binding clinical isolate of echovirus 11 allows mapping of mutants with altered receptor requirements for infection.," *Journal of virology*, vol. 76, pp. 7694–704, aug 2002.

[26] E. E. Fry, N. J. Knowles, J. W. I. Newman, G. Wilsden, Z. Rao, A. M. Q. King, and D. I. Stuart, "Crystal structure of Swine vesicular disease virus and implications for host adaptation.," *Journal of virology*, vol. 77, pp. 5475–86, may 2003.

[27] N. Verdaguer, M. A. Jimenez-Clavero, I. Fita, and V. Ley, "Structure of swine vesicular disease virus: mapping of changes occurring during adaptation of human coxsackie B5 virus to infect swine.," *Journal of virology*, vol. 77, pp. 9780–9, sep 2003.

[28] C. Xiao, C. M. Bator-Kelly, E. Rieder, P. R. Chipman, A. Craig, R. J. Kuhn, E. Wimmer, and M. G. Rossmann, "The crystal structure of coxsackievirus A21 and its interaction with ICAM-1," *Structure*, vol. 13, pp. 1019–1033, jul 2005.

[29] P. Plevka, S. Hafenstein, K. G. Harris, J. O. Cifuente, Y. Zhang, V. D. Bowman, P. R. Chipman, C. M. Bator, F. Lin, M. E. Medof, and M. G. Rossmann, "Interaction of decay-accelerating factor with echovirus 7.," *Journal of virology*, vol. 84, pp. 12665–74, dec 2010.

[30] P. Plevka, R. Perera, J. Cardosa, R. J. Kuhn, and M. G. Rossmann, "Crystal structure of human enterovirus 71," *Science*, vol. 336, p. 1274, 2012.

[31] X. Wang, W. Peng, J. Ren, Z. Hu, J. Xu, Z. Lou, X. Li, W. Yin, X. Shen, C. Porta, T. S. Walter, G. Evans, D. Axford, R. Owen, D. J. Rowlands, J. Wang, D. I. Stuart, E. E. Fry, and Z. Rao, "A sensor-adaptor mechanism for enterovirus uncoating from structures of EV71," *Nat. Struct. Mol. Biol.*, vol. 19, no. 4, pp. 424–429, 2012.

[32] G. Zocher, N. Mistry, M. Frank, I. Hahnlein-Schick, J. O. Ekstrom, N. Arnberg, and T. Stehle, "A sialic acid binding site in a human picornavirus," *PLoS Pathog.*, vol. 10, no. 10, p. e1004401, 2014.

[33] D. L. Caspar and A. Klug, "Physical principles in the construction of regular viruses," *Cold Spring Harb Symp Quant Biol*, vol. 27, pp. 1–24, 1962.

[34] A. V. Paul, A. Schultz, S. E. Pincus, S. Oroszlan, and E. Wimmer, "Capsid protein VP4 of poliovirus is N-myristoylated.," *Proceedings of the National Academy of Sciences of the United States of America*, vol. 84, pp. 7827–31, nov 1987.

[35] M. Chow, J. F. E. Newman, D. Filman, J. M. Hogle, D. J. Rowlands, and F. Brown, "Myristylation of picornavirus capsid protein VP4 and its structural significance," *Nature*, vol. 327, pp. 482–486, jun 1987.

[36] S. C. Harrison, A. J. Olson, C. E. Schutt, F. K. Winkler, and G. Bricogne, "Tomato bushy stunt virus at 2.9 A resolution.," *Nature*, vol. 276, pp. 368–73, nov 1978.

[37] C. Abad-Zapatero, S. S. Abdel-Meguid, J. E. Johnson, A. G. Leslie, I. Rayment, M. G. Rossmann, D. Suck, and T. Tsukihara, "Structure of southern bean mosaic virus at 2.8 A resolution.," *Nature*, vol. 286, pp. 33–9, jul 1980.

[38] M. G. Rossmann and J. E. Johnson, "Icosahedral RNA virus structure," *Annu Rev Biochem*, vol. 58, pp. 533–573, 1989.

[39] B. V. Prasad and M. F. Schmid, "Principles of virus structural organization," *Adv Exp Med Biol*, vol. 726, pp. 17–47, 2012.

[40] N. Kitamura, B. L. Semler, P. G. Rothberg, G. R. Larsen, C. J. Adler, A. J. Dorner, E. A. Emini, R. Hanecak, J. J. Lee, S. van der Werf, C. W. Anderson, and E. Wimmer, "Primary structure, gene organization and polypeptide expression of poliovirus RNA.," *Nature*, vol. 291, pp. 547–53, jun 1981.

[41] V. R. Racaniello and D. Baltimore, "Molecular cloning of poliovirus cDNA and determination of the complete nucleotide sequence of the viral genome.," *Proceedings of the National Academy of Sciences of the United States of America*, vol. 78, pp. 4887–91, aug 1981.

[42] Y. F. Lee, A. Nomoto, B. M. Detjen, and E. Wimmer, "A protein covalently linked to poliovirus genome RNA.," *Proceedings of the National Academy of Sciences of the United States of America*, vol. 74, pp. 59–63, jan 1977.

[43] A. V. Paul, J. H. van Boom, D. Filippov, and E. Wimmer, "Protein-primed RNA synthesis by purified poliovirus RNA polymerase.," *Nature*, vol. 393, pp. 280–4, may 1998.

[44] J. Pelletier and N. Sonenberg, "Internal initiation of translation of eukaryotic mRNA directed by a sequence derived from poliovirus RNA," *Nature*, vol. 334, pp. 320–325, jul 1988.

[45] S. K. Jang, H. G. Kräusslich, M. J. Nicklin, G. M. Duke, A. C. Palmenberg, and E. Wimmer, "A segment of the 5' nontranslated region of encephalomyocarditis virus RNA directs internal entry of ribosomes during in vitro translation.," *Journal of virology*, vol. 62, pp. 2636–43, aug 1988.

[46] D. F. Summers and J. V. Maizel, "Evidence for large precursor proteins in poliovirus synthesis.," *Proceedings of the National Academy of Sciences of the United States of America*, vol. 59, pp. 966–71, mar 1968.

[47] A. C. Palmenberg, "Proteolytic Processing of Picornaviral Polyprotein," *Annual Review of Microbiology*, vol. 44, pp. 603–623, oct 1990.

[48] P. Jiang, Y. Liu, H.-C. Ma, A. V. Paul, and E. Wimmer, "Picornavirus morphogenesis.," *Microbiology and Molecular Biology Reviews*, vol. 78, pp. 418–37, sep 2014.

[49] D. Egger, R. Gosert, and K. Bienz, "Role of cellular structures in viral RNA replication," in *Molecular biology of picornaviruses* (E. Wimmer and B. Selmer, eds.), pp. 247–253, Washington, D.C.: ASM Press, 2002.

[50] M. F. Ypma-Wong, P. G. Dewalt, V. H. Johnson, J. G. Lamb, and B. L. Semler, "Protein 3CD is the major poliovirus proteinase responsible for cleavage of the P1 capsid precursor.," *Virology*, vol. 166, pp. 265–70, sep 1988.

[51] L. van der Linden, K. C. Wolthers, and F. J. M. van Kuppeveld, "Replication and Inhibitors of Enteroviruses and Parechoviruses.," *Viruses*, vol. 7, pp. 4529–62, aug 2015.

[52] N. Lévêque and B. L. Semler, "A 21st Century Perspective of Poliovirus Replication," *PLOS Pathogens*, vol. 11, p. e1004825, jun 2015.

[53] T. J. Tuthill, E. Groppelli, J. M. Hogle, and D. J. Rowlands, "Picornaviruses," *Curr Top Microbiol Immunol*, vol. 343, pp. 43–89, 2010.

[54] J. M. Bergelson and C. B. Coyne, "Picornavirus entry," *Adv Exp Med Biol*, vol. 790, pp. 24–41, 2013.

[55] L. A. Caliguiri and I. Tamm, "Membranous structures associated with translation and transcription of poliovirus RNA.," *Science (New York, N.Y.)*, vol. 166, pp. 885–6, nov 1969.

[56] R. W. A. L. Limpens, H. M. van der Schaar, D. Kumar, A. J. Koster, E. J. Snijder, F. J. M. van Kuppeveld, and M. Barcena, "The Transformation of Enterovirus Replication Structures: a Three-Dimensional Study of Single- and Double-Membrane Compartments," *mBio*, vol. 2, pp. e00166–11–e00166–11, oct 2011.

[57] G. A. Belov, V. Nair, B. T. Hansen, F. H. Hoyt, E. R. Fischer, and E. Ehrenfeld, "Complex Dynamic Development of Poliovirus Membranous Replication Complexes," *Journal of Virology*, vol. 86, pp. 302–312, jan 2012.

[58] E. Ehrenfeld, J. V. Maizel, and D. F. Summers, "Soluble RNA polymerase complex from poliovirus-infected HeLa cells.," *Virology*, vol. 40, pp. 840–6, apr 1970.

[59] A. A. Thompson and O. B. Peersen, "Structural basis for proteolysis-dependent activation of the poliovirus RNA-dependent RNA polymerase," *The EMBO Journal*, vol. 23, pp. 3462–3471, sep 2004.

[60] M. H. Baron and D. Baltimore, "In vitro copying of viral positive strand RNA by poliovirus replicase. Characterization of the reaction and its products.," *The Journal of biological chemistry*, vol. 257, pp. 12359–66, oct 1982.

[61] M. Girard, "In vitro synthesis of poliovirus ribonucleic acid: role of the replicative intermediate.," *Journal of virology*, vol. 3, pp. 376–84, apr 1969.

[62] D. J. Barton and J. B. Flanegan, "Coupled translation and replication of poliovirus RNA in vitro: synthesis of functional 3D polymerase and infectious virus.," *Journal of virology*, vol. 67, pp. 822–31, feb 1993.

[63] R. Basavappa, R. Syed, O. Flore, J. P. Icenogle, D. J. Filman, and J. M. Hogle, "Role and mechanism of the maturation cleavage of VP0 in poliovirus assembly: structure of the empty capsid assembly intermediate at 2.9 A resolution," *Protein Sci*, vol. 3, pp. 1651–1669, oct 1994.

[64] M. Hindiyeh, Q. H. Li, R. Basavappa, J. M. Hogle, and M. Chow, "Poliovirus mutants at histidine 195 of VP2 do not cleave VP0 into VP2 and VP4.," *Journal of virology*, vol. 73, pp. 9072–9, nov 1999.

[65] Y.-H. Chen, W. Du, M. C. Hagemeijer, P. M. Takvorian, C. Pau, A. Cali, C. A. Brantner, E. S. Stempinski, P. S. Connelly, H.-C. Ma, P. Jiang, E. Wimmer, G. Altan-Bonnet, and N. Altan-Bonnet, "Phosphatidylserine Vesicles Enable Efficient En Bloc Transmission of Enteroviruses," *Cell*, vol. 160, pp. 619–630, feb 2015.

[66] K. Landsteiner and E. Popper, "Mikroscopische präparate von einem menschlichen und zwei affentückermarker," *Wein klin Wschr*, vol. 21, p. 1930, 1908.

[67] J. F. Enders, T. H. Weller, and F. C. Robbins, "Cultivation of the Lansing Strain of Poliomyelitis Virus in Cultures of Various Human Embryonic Tissues," *Science*, vol. 109, no. 2822, 1949.

[68] J. E. Salk, "Studies in human subjects on active immunization against poliomyelitis. I. A preliminary report of experiments in progress.," *Journal of the American Medical Association*, vol. 151, pp. 1081–98, mar 1953.

[69] A. B. Sabin, "Immunization of chimpanzees and human beings with avirulent strains of poliomyelitis virus.," *Annals of the New York Academy of Sciences*, vol. 61, pp. 1050–6, sep 1955.

[70] A. B. Sabin, "Oral, live poliovirus vaccine for elimination of poliomyelitis.," *Archives of internal medicine*, vol. 106, pp. 5–9, jul 1960.

[71] P. Minor, "Vaccine-derived poliovirus (VDPV): Impact on poliomyelitis eradication.," *Vaccine*, vol. 27, pp. 2649–52, may 2009.

[72] F. Zhu, W. Xu, J. Xia, Z. Liang, Y. Liu, X. Zhang, X. Tan, L. Wang, Q. Mao, J. Wu, Y. Y. Hu, T. Ji, L. Song, Q. Liang, B. Zhang, Q. Gao, J. Li, S. Wang, Y. Y. Hu, S. Gu, J. Zhang, G. Yao, J. Gu, X. Wang, Y. Zhou, C. Chen, M. Zhang, M. Cao, J. Wang, H. Wang, and N. Wang, "Efficacy, safety, and immunogenicity of an enterovirus 71 vaccine in China," *N Engl J Med*, vol. 370, no. 9, pp. 818–828, 2014.

[73] R. Li, L. Liu, Z. Mo, X. Wang, J. Xia, Z. Liang, Y. Zhang, Y. Li, Q. Mao, J. J. Wang, L. Jiang, C. Dong, Y. Che, T. Huang, Z. Jiang, Z. Xie, L. Wang, Y. Liao, Y. Liang, Y. Nong, J. Liu, H. Zhao, R. Na, L. Guo, J. Pu, E. Yang, L. Sun, P. Cui, H. Shi, J. J. Wang, and Q. Li, "An inactivated enterovirus 71 vaccine in healthy children," *N Engl J Med*, vol. 370, no. 9, pp. 829–837, 2014.

[74] S. Lee, M. T. Nguyen, M. G. Currier, J. B. Jenkins, E. A. Strobert, A. E. Kajon, R. Madan-Lala, Y. A. Bochkov, J. E. Gern, K. Roy, X. Lu, D. D. Erdman, P. Spearman, and M. L. Moore, "A polyvalent inactivated rhinovirus vaccine is broadly immunogenic in rhesus macaques," *Nature Communications*, vol. 7, p. 12838, sep 2016.

[75] G. D. Diana, P. Rudewicz, D. C. Pevear, T. J. Nitz, S. C. Aldous, D. J. Aldous, D. T. Robinson, T. Draper, F. J. Dutko, and C. Aldi, "Picornavirus inhibitors: trifluoromethyl substitution provides a global protective effect against hepatic metabolism.," *Journal of medicinal chemistry*, vol. 38, pp. 1355–71, apr 1995.

[76] A. M. De Palma, I. Vliegen, E. De Clercq, and J. Neyts, "Selective inhibitors of picornavirus replication," *Med Res Rev*, vol. 28, pp. 823–884, nov 2008.

[77] P. S. Dragovich, T. J. Prins, R. Zhou, S. E. Webber, J. T. Marakovits, S. A. Fuhrman, A. K. Patick, D. A. Matthews, C. A. Lee, C. E. Ford, B. J. Burke, P. A. Rejto, T. F. Hendrickson, T. Tuntland, E. L. Brown, J. W. Meador, R. A. Ferre, J. E. V. Harr, M. B. Kosa, and S. T. Worland, "Structure-Based Design, Synthesis, and Biological Evaluation of Irreversible Human Rhinovirus 3C Protease Inhibitors. 4. Incorporation of P1 Lactam Moieties as L-Glutamine Replacements," *Journal of Medicinal Chemistry*, vol. 42, pp. 1213–1224, apr 1999.

[78] S. L. Binford, P. T. Weady, F. Maldonado, M. A. Brothers, D. A. Matthews, and A. K. Patick, "In vitro resistance study of rupintrivir, a novel inhibitor of human rhinovirus 3C protease.," *Antimicrobial agents and chemotherapy*, vol. 51, pp. 4366–73, dec 2007.

[79] J. R. P. M. Strating, L. van der Linden, L. Albulescu, J. Bigay, M. Arita, L. Delang, P. Leyssen, H. M. van der Schaar, K. H. W. Lanke, H. J. Thibaut, R. Ulferts, G. Drin, N. Schlinck, R. W. Wubbolts, N. Sever, S. A. Head, J. O. Liu, P. A. Beachy, M. A. De Matteis, M. D. Shair, V. M. Olkkonen, J. Neyts, and F. J. M. van Kuppeveld, "Itraconazole inhibits enterovirus replication by targeting the oxysterol-binding protein.," *Cell reports*, vol. 10, pp. 600–15, feb 2015.

[80] S. C. Feil, S. Hamilton, G. Y. Krippner, B. Lin, A. Luttick, D. B. McConnell, R. Nearn, M. W. Parker, J. Ryan, P. C. Stanislawski, S. P. Tucker, K. G. Watson, and C. J. Morton, "An Orally Available 3-Ethoxybenzisoxazole Capsid Binder with Clinical Activity against Human Rhinovirus," *ACS Med Chem Lett*, vol. 3, no. 4, pp. 303–307, 2012.

[81] P. J. Buontempo, S. Cox, J. Wright-Minogue, J. L. DeMartino, A. M. Skelton, E. Ferrari, R. Albin, E. J. Rozhon, V. Girijavallabhan, J. F. Modlin, and J. F. O'Connell, "SCH 48973: a potent, broad-spectrum, antienterovirus compound.," *Antimicrobial agents and chemotherapy*, vol. 41, pp. 1220–5, jun 1997.

[82] C. L. Jolly and Q. J. Sattentau, "Attachment factors.," *Advances in experimental medicine and biology*, vol. 790, pp. 1–23, 2013.

[83] A. Demogines, J. Abraham, H. Choe, M. Farzan, and S. L. Sawyer, "Dual Host-Virus Arms Races Shape an Essential Housekeeping Protein," *PLoS Biology*, vol. 11, p. e1001571, may 2013.

[84] T. Ito and Y. Kawaoka, "Host-range barrier of influenza A viruses," *Veterinary Microbiology*, vol. 74, no. 1, pp. 71–75, 2000.

[85] P. J. Maddon, A. G. Dalgleish, J. S. McDougal, P. R. Clapham, R. A. Weiss, and R. Axel, "The T4 gene encodes the AIDS virus receptor and is expressed in the immune system and the brain.," *Cell*, vol. 47, pp. 333–48, nov 1986.

[86] H. Deng, R. Liu, W. Ellmeier, S. Choe, D. Unutmaz, M. Burkhart, P. D. Marzio, S. Marmon, R. E. Sutton, C. M. Hill, C. B. Davis, S. C. Peiper, T. J. Schall, D. R. Littman, and N. R. Landau, "Identification of a major co-receptor for primary isolates of HIV-1," *Nature*, vol. 381, pp. 661–666, jun 1996.

[87] T. Dragic, V. Litwin, G. P. Allaway, S. R. Martin, Y. Huang, K. A. Nagashima, C. Cayanan, P. J. Maddon, R. A. Koup, J. P. Moore, and W. A. Paxton, "HIV-1 entry into CD4+ cells is mediated by the chemokine receptor CC-CKR-5," *Nature*, vol. 381, pp. 667–673, jun 1996.

[88] L. Wu, N. P. Gerard, R. Wyatt, H. Choe, C. Parolin, N. Ruffing, A. Borsetti, A. A. Cardoso, E. Desjardin, W. Newman, C. Gerard, and J. Sodroski, "CD4-induced interaction of primary HIV-1 gp120 glycoproteins with the chemokine receptor CCR-5," *Nature*, vol. 384, pp. 179–183, nov 1996.

[89] C. C. Huang, S. N. Lam, P. Acharya, M. Tang, S. H. Xiang, S. S. U. Hussan, R. L. Stanfield, J. Robinson, J. Sodroski, I. A. Wilson, R. Wyatt, C. A. Bewley, and P. D. Kwong, "Structures of the CCR5 N Terminus and of a Tyrosine-Sulfated Antibody with HIV-1 gp120 and CD4," *Science*, vol. 317, pp. 1930–1934, sep 2007.

[90] U. F. Greber, "Signalling in viral entry.," *Cellular and molecular life sciences : CMLS*, vol. 59, pp. 608–26, apr 2002.

[91] B. Hu, W. Margolin, I. J. Molineux, and J. Liu, "The bacteriophage t7 virion undergoes extensive structural remodeling during infection.," *Science (New York, N.Y.)*, vol. 339, pp. 576–9, feb 2013.

[92] J. Mercer, M. Schelhaas, and A. Helenius, "Virus Entry by Endocytosis," *Annual Review of Biochemistry*, vol. 79, pp. 803–833, jun 2010.

[93] J. Huotari and A. Helenius, "Endosome maturation," *The EMBO Journal*, vol. 30, pp. 3481–3500, aug 2011.

[94] S. C. Harrison, "Viral membrane fusion," *Nature Structural & Molecular Biology*, vol. 15, pp. 690–698, jul 2008.

[95] R. Sahli, R. Freund, T. Dubensky, R. Garcea, R. Bronson, and T. Benjamin, "Defect in entry and altered pathogenicity of a polyoma virus mutant blocked in VP2 myristylation.," *Virology*, vol. 192, pp. 142–53, jan 1993.

[96] G. A. Farr, L. G. Zhang, and P. Tattersall, "Parvoviral virions deploy a capsid-tethered lipolytic enzyme to breach the endosomal membrane during cell entry," *Proceedings of the National Academy of Sciences*, vol. 102, pp. 17148–17153, nov 2005.

[97] C. M. Wiethoff, H. Wodrich, L. Gerace, and G. R. Nemerow, "Adenovirus protein VI mediates membrane disruption following capsid disassembly.," *Journal of virology*, vol. 79, pp. 1992–2000, feb 2005.

[98] M. Suomalainen and U. F. Greber, "Uncoating of non-enveloped viruses.," *Current opinion in virology*, vol. 3, pp. 27–33, feb 2013.

[99] U. F. Greber and M. Fornerod, "Nuclear import in viral infections.," *Current topics in microbiology and immunology*, vol. 285, pp. 109–38, 2005.

[100] Y. Yamauchi and U. F. Greber, "Principles of Virus Uncoating: Cues and the Snooker Ball," *Traffic*, vol. 17, pp. 569–592, jun 2016.

[101] P. A. Bullough, F. M. Hughson, J. J. Skehel, and D. C. Wiley, "Structure of influenza haemagglutinin at the pH of membrane fusion.," *Nature*, vol. 371, pp. 37–43, sep 1994.

[102] A. Merk and S. Subramaniam, "HIV-1 envelope glycoprotein structure," *Current Opinion in Structural Biology*, vol. 23, no. 2, pp. 268–276, 2013.

[103] K. Schornberg, S. Matsuyama, K. Kabsch, S. Delos, A. Bouton, and J. White, "Role of endosomal cathepsins in entry mediated by the Ebola virus glycoprotein.," *Journal of virology*, vol. 80, pp. 4174–8, apr 2006.

[104] C. Burkard, M. H. Verheije, O. Wicht, S. I. van Kasteren, F. J. van Kuppeveld, B. L. Haagmans, L. Pelkmans, P. J. M. Rottier, B. J. Bosch, and C. A. M. de Haan, "Coronavirus Cell Entry Occurs through the Endo-/Lysosomal Pathway in a Proteolysis-Dependent Manner," *PLoS Pathogens*, vol. 10, p. e1004502, nov 2014.

[105] G. Kaplan, M. S. Freistadt, and V. R. Racaniello, "Neutralization of poliovirus by cell receptors expressed in insect cells.," *Journal of virology*, vol. 64, pp. 4697–702, oct 1990.

[106] H. Hoover-Litty and J. M. Greve, "Formation of rhinovirus-soluble ICAM-1 complexes and conformational changes in the virion.," *J. Virol.*, vol. 67, pp. 390–397, jan 1993.

[107] M. Brabec, G. Baravalle, D. Blaas, and R. Fuchs, "Conformational changes, plasma membrane penetration, and infection by human rhinovirus type 2: role of receptors and low pH.," *Journal of virology*, vol. 77, pp. 5370–7, may 2003.

[108] M. Strauss, D. J. Filman, D. M. Belnap, N. Cheng, R. T. Noel, and J. M. Hogle, "Nectin-like interactions between poliovirus and its receptor trigger conformational changes associated with cell entry.," *Journal of virology*, vol. 89, pp. 4143–57, apr 2015.

[109] U. F. Greber, M. Willetts, P. Webster, and A. Helenius, "Stepwise dismantling of adenovirus 2 during entry into cells.," *Cell*, vol. 75, pp. 477–86, nov 1993.

[110] D. H. Ebert, J. Deussing, C. Peters, and T. S. Dermody, "Cathepsin L and cathepsin B mediate reovirus disassembly in murine fibroblast cells.," *The Journal of biological chemistry*, vol. 277, pp. 24609–17, jul 2002.

[111] R. M. Richards, D. R. Lowy, J. T. Schiller, and P. M. Day, "Cleavage of the papillomavirus minor capsid protein, L2, at a furin consensus site is necessary for infection.," *Proceedings of the National Academy of Sciences of the United States of America*, vol. 103, pp. 1522–7, jan 2006.

[112] M. Schelhaas, J. Malmström, L. Pelkmans, J. Haugstetter, L. Ellgaard, K. Grünewald, and A. Helenius, "Simian Virus 40 depends on ER protein folding and quality control factors for entry into host cells.," *Cell*, vol. 131, pp. 516–29, nov 2007.

[113] A. H. Abdelhakim, E. N. Salgado, X. Fu, M. Pasham, D. Nicastro, T. Kirchhausen, and S. C. Harrison, "Structural Correlates of Rotavirus Cell Entry," *PLoS Pathogens*, vol. 10, p. e1004355, sep 2014.

[114] C. E. Fricks and J. M. Hogle, "Cell-induced conformational change in poliovirus: externalization of the amino terminus of VP1 is responsible for liposome binding," *J. Virol.*, vol. 64, pp. 1934–1945, may 1990.

[115] P. R. Dormitzer, E. B. Nason, B. V. V. Prasad, and S. C. Harrison, "Structural rearrangements in the membrane penetration protein of a non-enveloped virus.," *Nature*, vol. 430, pp. 1053–8, aug 2004.

[116] X. Zhang, A. Patel, C. C. Celma, X. Yu, P. Roy, and Z. H. Zhou, "Atomic model of a nonenveloped virus reveals pH sensors for a coordinated process of cell entry," *Nature Structural & Molecular Biology*, vol. 23, pp. 74–80, dec 2015.

[117] A. Gottschalk and P. E. Lind, "Product of interaction between influenza virus enzyme and ovomucin," *Nature*, vol. 164, p. 232, aug 1949.

[118] E. Klenk, H. Faillard, and H. Lempfrid, "Enzymatic effect of the influenza virus," *Hoppe-Seyler's Zeitschrift fur physiologische Chemie*, vol. 301, pp. 235–46, sep 1955.

[119] D. A. Jackson, R. H. Symons, and P. Berg, "Biochemical method for inserting new genetic information into DNA of Simian Virus 40: circular SV40 DNA molecules containing lambda phage genes and the galactose operon of Escherichia coli.," *Proceedings of the National Academy of Sciences of the United States of America*, vol. 69, pp. 2904–9, oct 1972.

[120] G. Köhler and C. Milstein, "Continuous cultures of fused cells secreting antibody of predefined specificity.," *Nature*, vol. 256, pp. 495–7, aug 1975.

[121] J. D. Fingeroth, J. J. Weis, T. F. Tedder, J. L. Strominger, P. A. Biro, and D. T. Fearon, "Epstein-Barr virus receptor of human B lymphocytes is the C3d receptor CR2.," *Proceedings of the National Academy of Sciences of the United States of America*, vol. 81, pp. 4510–4, jul 1984.

[122] A. G. Dalgleish, P. C. Beverley, P. R. Clapham, D. H. Crawford, M. F. Greaves, and R. A. Weiss, "The CD4 (T4) antigen is an essential component of the receptor for the AIDS retrovirus.," *Nature*, vol. 312, no. 5996, pp. 763–7.

[123] D. Klatzmann, E. Champagne, S. Chamaret, J. Gruest, D. Guetard, T. Hercend, J. C. Gluckman, and L. Montagnier, "T-lymphocyte T4 molecule behaves as the receptor for human retrovirus LAV.," *Nature*, vol. 312, no. 5996, pp. 767–8.

[124] J. M. Greve, G. Davis, A. M. Meyer, C. P. Forte, S. C. Yost, C. W. Marlor, M. E. Kamarck, and A. McClelland, "The major human rhinovirus receptor is ICAM-1.," *Cell*, vol. 56, pp. 839–47, mar 1989.

[125] D. E. Staunton, V. J. Merluzzi, R. Rothlein, R. Barton, S. D. Marlin, and T. A. Springer, "A cell adhesion molecule, ICAM-1, is the major surface receptor for rhinoviruses.," *Cell*, vol. 56, pp. 849–53, mar 1989.

[126] C. L. Mendelsohn, E. Wimmer, and V. R. Racaniello, "Cellular receptor for poliovirus: molecular cloning, nucleotide sequence, and expression of a new member of the immunoglobulin superfamily.," *Cell*, vol. 56, pp. 855–65, mar 1989.

[127] W. Li, M. J. Moore, N. Vasilieva, J. Sui, S. K. Wong, M. A. Berne, M. Somasundaran, J. L. Sullivan, K. Luzuriaga, T. C. Greenough, H. Choe, and M. Farzan, "Angiotensin-converting enzyme 2 is a functional receptor for the SARS coronavirus.," *Nature*, vol. 426, pp. 450–4, nov 2003.

[128] H. Yan, G. Zhong, G. Xu, W. He, Z. Jing, Z. Gao, Y. Huang, Y. Qi, B. Peng, H. Wang, L. Fu, M. Song, P. Chen, W. Gao, B. Ren, Y. Sun, T. Cai, X. Feng, J. Sui, and W. Li, "Sodium taurocholate cotransporting polypeptide is a functional receptor for human hepatitis B and D virus.," *eLife*, vol. 1, p. e00049, nov 2012.

[129] M. D. Mühlebach, M. Mateo, P. L. Sinn, S. Prüfer, K. M. Uhlig, V. H. J. Leonard, C. K. Navaratnarajah, M. Frenzke, X. X. Wong, B. Sawatsky, S. Ramachandran, P. B. McCray, K. Cichutek, V. von Messling, M. Lopez, R. Cattaneo, and R. Cattaneo, "Adherens junction protein nectin-4 is the epithelial receptor for measles virus.," *Nature*, vol. 480, pp. 530–3, dec 2011.

[130] P. P. Rose, S. L. Hanna, A. Spiridigliozzi, N. Wannissorn, D. P. Beiting, S. R. Ross, R. W. Hardy, S. A. Bambina, M. T. Heise, and S. Cherry, "Natural resistance-associated macrophage protein is a cellular receptor for sindbis virus in both insect and mammalian hosts.," *Cell host & microbe*, vol. 10, pp. 97–104, aug 2011.

[131] J. E. Carette, M. Raaben, A. C. Wong, A. S. Herbert, G. Obernosterer, N. Mulherkar, A. I. Kuehne, P. J. Kranzusch, A. M. Griffin, G. Ruthel, P. Dal Cin, J. M. Dye, S. P. Whelan, K. Chandran, and T. R. Brummelkamp, "Ebola virus entry requires the cholesterol transporter Niemann-Pick C1.," *Nature*, vol. 477, pp. 340–3, aug 2011.

[132] R. C. Orchard, C. B. Wilen, J. G. Doench, M. T. Baldridge, B. T. McCune, Y.-C. J. Lee, S. Lee, S. M. Pruett-Miller, C. A. Nelson, D. H. Fremont, and H. W. Virgin, "Discovery of a proteinaceous cellular receptor for a norovirus," *Science*, 2016.

[133] L. T. Jae and T. R. Brummelkamp, "Emerging intracellular receptors for hemorrhagic fever viruses," *Trends in Microbiology*, vol. 23, no. 7, pp. 392–400, 2015.

[134] E. Sun, J. He, and X. Zhuang, "Live cell imaging of viral entry.," *Current opinion in virology*, vol. 3, pp. 34–43, feb 2013.

[135] Á. Vázquez-Calvo, J. C. Saiz, K. C. McCullough, F. Sobrino, and M. A. Martín-Acebes, "Acid-dependent viral entry," *Virus Research*, vol. 167, no. 2, pp. 125–137, 2012.

[136] T. J. Tuthill, D. Bubeck, D. J. Rowlands, and J. M. Hogle, "Characterization of early steps in the poliovirus infection process: receptor-decorated liposomes induce conversion of the virus to membrane-anchored entry-intermediate particles," *J Virol*, vol. 80, pp. 172–180, jan 2006.

[137] M. G. Rossmann, R. Bernal, and S. V. Pletnev, "Combining electron microscopic with x-ray crystallographic structures," *J Struct Biol*, vol. 136, no. 3, pp. 190–200, 2001.

[138] W. Weis, J. H. Brown, S. Cusack, J. C. Paulson, J. J. Skehel, and D. C. Wiley, "Structure of the influenza virus haemagglutinin complexed with its receptor, sialic acid.," *Nature*, vol. 333, pp. 426–31, jun 1988.

[139] D. K. Takemoto, J. J. Skehel, and D. C. Wiley, "A Surface Plasmon Resonance Assay for the Binding of Influenza Virus Hemagglutinin to Its Sialic Acid Receptor," *Virology*, vol. 217, no. 2, pp. 452–458, 1996.

[140] S. Harutyunyan, A. Sedivy, G. Köhler, H. Kowalski, and D. Blaas, "Application of FCS in studies of rhinovirus receptor binding and uncoating.," *Methods in molecular biology (Clifton, N.J.)*, vol. 1221, pp. 83–100, 2015.

[141] C. Uetrecht and A. J. R. Heck, "Modern Biomolecular Mass Spectrometry and its Role in Studying Virus Structure, Dynamics, and Assembly," *Angewandte Chemie International Edition*, vol. 50, pp. 8248–8262, aug 2011.

[142] T. M. Dobrowsky, Y. Zhou, S. X. Sun, R. F. Siliciano, and D. Wirtz, "Monitoring early fusion dynamics of human immunodeficiency virus type 1 at single-molecule resolution.," *Journal of virology*, vol. 82, pp. 7022–33, jul 2008.

[143] T. Ivanovic, J. L. Choi, S. P. Whelan, A. M. van Oijen, and S. C. Harrison, "Influenza-virus membrane fusion by cooperative fold-back of stochastically induced hemagglutinin intermediates.," *eLife*, vol. 2, p. e00333, 2013.

[144] P. Zhang, "Correlative cryo-electron tomography and optical microscopy of cells.," *Current opinion in structural biology*, vol. 23, pp. 763–70, oct 2013.

[145] W. Kukulski, M. Schorb, S. Welsch, A. Picco, M. Kaksonen, and J. A. G. Briggs, "Correlated fluorescence and 3D electron microscopy with high sensitivity and spatial precision," *Journal of Cell Biology*, vol. 192, no. 1, pp. 111–119, 2011.

[146] J. E. Tomassini, D. Graham, C. M. DeWitt, D. W. Lineberger, J. A. Rodkey, and R. J. Colonno, "cDNA cloning reveals that the major group rhinovirus receptor on HeLa cells is intercellular adhesion molecule 1.," *Proceedings of the National Academy of Sciences of the United States of America*, vol. 86, pp. 4907–11, jul 1989.

[147] J. M. Bergelson, M. P. Shepley, B. M. Chan, M. E. Hemler, and R. W. Finberg, "Identification of the integrin VLA-2 as a receptor for echovirus 1.," *Science (New York, N.Y.)*, vol. 255, pp. 1718–20, mar 1992.

[148] F. Hofer, M. Gruenberger, H. Kowalski, H. Machat, M. Huettinger, E. Kuechler, and D. Blaas, "Members of the low density lipoprotein receptor family mediate cell entry of a minor-group common cold virus.," *Proceedings of the National Academy of Sciences of the United States of America*, vol. 91, pp. 1839–42, mar 1994.

[149] M. Roivainen, L. Piirainen, T. Hovi, I. Virtanen, T. Riikonen, J. Heino, and T. Hyypiä, "Entry of coxsackievirus A9 into host cells: specific interactions with alpha v beta 3 integrin, the vitronectin receptor.," *Virology*, vol. 203, pp. 357–65, sep 1994.

[150] J. M. Bergelson, M. Chan, K. R. Solomon, N. F. St John, H. Lin, and R. W. Finberg, "Decay-accelerating factor (CD55), a glycosylphosphatidylinositol-anchored complement regulatory protein, is a receptor for several echoviruses.," *Proceedings of the National Academy of Sciences of the United States of America*, vol. 91, pp. 6245–8, jun 1994.

[151] T. Ward, P. A. Pipkin, N. A. Clarkson, D. M. Stone, P. D. Minor, and J. W. Almond, "Decay-accelerating factor CD55 is identified as the receptor for echovirus 7 using CELICS, a rapid immuno-focal cloning method.," *The EMBO journal*, vol. 13, pp. 5070–4, nov 1994.

[152] J. M. Bergelson, J. G. Mohanty, R. L. Crowell, N. F. St John, D. M. Lublin, and R. W. Finberg, "Coxsackievirus B3 adapted to growth in RD cells binds to decay-accelerating factor (CD55).," *Journal of virology*, vol. 69, pp. 1903–6, mar 1995.

[153] D. R. Shafren, R. C. Bates, M. V. Agrez, R. L. Herd, G. F. Burns, and R. D. Barry, "Coxsackieviruses B1, B3, and B5 use decay accelerating factor as a receptor for cell attachment.," *Journal of virology*, vol. 69, pp. 3873–7, jun 1995.

[154] T. M. Karnauchow, D. L. Tolson, B. A. Harrison, E. Altman, D. M. Lublin, and K. Dimock, "The HeLa cell receptor for enterovirus 70 is decay-accelerating factor (CD55).," *Journal of virology*, vol. 70, pp. 5143–52, aug 1996.

[155] D. R. Shafren, D. J. Dorahy, S. J. Greive, G. F. Burns, and R. D. Barry, "Mouse cells expressing human intercellular adhesion molecule-1 are susceptible to infection by coxsackievirus A21.," *Journal of virology*, vol. 71, pp. 785–9, jan 1997.

[156] D. R. Shafren, D. J. Dorahy, R. A. Ingham, G. F. Burns, and R. D. Barry, "Coxsackievirus A21 binds to decay-accelerating factor but requires intercellular adhesion molecule 1 for cell entry.," *Journal of virology*, vol. 71, pp. 4736–43, jun 1997.

[157] R. P. Tomko, R. Xu, and L. Philipson, "HCAR and MCAR: the human and mouse cellular receptors for subgroup C adenoviruses and group B coxsackieviruses.," *Proceedings of the National Academy of Sciences of the United States of America*, vol. 94, pp. 3352–6, apr 1997.

[158] J. M. Bergelson, J. A. Cunningham, G. Droguett, E. A. Kurt-Jones, A. Krithivas, J. S. Hong, M. S. Horwitz, R. L. Crowell, and R. W. Finberg, "Isolation of a common receptor for Coxsackie B viruses and adenoviruses 2 and 5.," *Science (New York, N.Y.)*, vol. 275, pp. 1320–3, feb 1997.

[159] I. G. Goodfellow, A. B. Sioofy, R. M. Powell, and D. J. Evans, "Echoviruses Bind Heparan Sulfate at the Cell Surface," *Journal of Virology*, vol. 75, pp. 4918–4921, may 2001.

[160] D. A. Alexander and K. Dimock, "Sialic acid functions in enterovirus 70 binding and infection," *J. Virol.*, vol. 76, no. 22, pp. 11265–11272, 2002.

[161] A. E. Zautner, U. Korner, A. Henke, C. Badorff, and M. Schmidtke, "Heparan sulfates and coxsackievirus-adenovirus receptor: each one mediates coxsackievirus B3 PD infection," *J. Virol.*, vol. 77, no. 18, pp. 10071–10077, 2003.

[162] M. Vlasak, I. Goesler, and D. Blaas, "Human rhinovirus type 89 variants use heparan sulfate proteoglycan for cell attachment.," *Journal of virology*, vol. 79, pp. 5963–70, may 2005.

[163] E. C. Nilsson, F. Jamshidi, S. M. Johansson, M. S. Oberste, and N. Arnberg, "Sialic acid is a cellular receptor for coxsackievirus A24 variant, an emerging virus with pandemic potential," *J. Virol.*, vol. 82, no. 6, pp. 3061–3068, 2008.

[164] B. Yang, H. Chuang, and K. D. Yang, "Sialylated glycans as receptor and inhibitor of enterovirus 71 infection to DLD-1 intestinal cells," *Virol. J.*, vol. 6, p. 141, 2009.

[165] S. Yamayoshi, Y. Yamashita, J. Li, N. Hanagata, T. Minowa, T. Takemura, and S. Koike, "Scavenger receptor B2 is a cellular receptor for enterovirus 71.," *Nature medicine*, vol. 15, pp. 798–801, jul 2009.

[166] Y. Nishimura, M. Shimojima, Y. Tano, T. Miyamura, T. Wakita, and H. Shimizu, "Human P-selectin glycoprotein ligand-1 is a functional receptor for enterovirus 71," *Nat Med*, vol. 15, pp. 794–797, jul 2009.

[167] N. Mistry, H. Inoue, F. Jamshidi, R. J. Storm, M. S. Oberste, and N. Arnberg, "Coxsackievirus A24 variant uses sialic acid-containing O-linked glycoconjugates as cellular receptors on human ocular cells.," *Journal of virology*, vol. 85, pp. 11283–90, nov 2011.

[168] P. Y. Su, Y. T. Liu, H. Y. Chang, S. W. Huang, Y. F. Wang, C. K. Yu, J. R. Wang, and C. F. Chang, "Cell surface sialylation affects binding of enterovirus 71 to rhabdomyosarcoma and neuroblastoma cells," *BMC Microbiol.*, vol. 12, p. 162, 2012.

[169] C. W. Tan, C. L. Poh, I. C. Sam, and Y. F. Chan, "Enterovirus 71 uses cell surface heparan sulfate glycosaminoglycan as an attachment receptor," *J. Virol.*, vol. 87, no. 1, pp. 611–620, 2013.

[170] N. H. Olson, P. R. Kolatkar, M. A. Oliveira, R. H. Cheng, J. M. Greve, A. McClelland, T. S. Baker, and M. G. Rossmann, "Structure of a human rhinovirus complexed with its receptor molecule.," *Proceedings of the National Academy of Sciences of the United States of America*, vol. 90, pp. 507–11, jan 1993.

[171] P. R. Kolatkar, J. Bella, N. H. Olson, C. M. Bator, T. S. Baker, and M. G. Rossmann, "Structural studies of two rhinovirus serotypes complexed with fragments of their cellular receptor," *The EMBO Journal*, vol. 18, pp. 6249–6259, nov 1999.

[172] L. Xing, K. Tjarnlund, B. Lindqvist, G. G. Kaplan, D. Feigelstock, R. H. Cheng, and J. M. Casasnovas, "Distinct cellular receptor interactions in poliovirus and rhinoviruses.," *The EMBO journal*, vol. 19, pp. 1207–16, mar 2000.

[173] D. M. Belnap, D. J. Filman, B. L. Trus, N. Cheng, F. P. Booy, J. F. Conway, S. Curry, C. N. Hiremath, S. K. Tsang, A. C. Steven, and J. M. Hogle, "Molecular tectonic model of virus structural transitions: the putative cell entry states of poliovirus.," *Journal of virology*, vol. 74, pp. 1342–54, feb 2000.

[174] Y. He, V. D. Bowman, S. Mueller, C. M. Bator, J. Bella, X. Peng, T. S. Baker, E. Wimmer, R. J. Kuhn, and M. G. Rossmann, "Interaction of the poliovirus receptor with poliovirus," *Proc Natl Acad Sci U S A*, vol. 97, no. 1, pp. 79–84, 2000.

[175] Y. He, P. R. Chipman, J. Howitt, C. M. Bator, M. A. Whitt, T. S. Baker, R. J. Kuhn, C. W. Anderson, P. Freimuth, and M. G. Rossmann, "Interaction of coxsackievirus B3 with the full length coxsackievirus-adenovirus receptor.," *Nature structural biology*, vol. 8, pp. 874–8, oct 2001.

[176] C. Xiao, C. M. Bator, V. D. Bowman, E. Rieder, Y. He, B. Hebert, J. Bella, T. S. Baker, E. Wimmer, R. J. Kuhn, and M. G. Rossmann, "Interaction of Coxsackievirus A21 with Its Cellular Receptor, ICAM-1," *Journal of Virology*, vol. 75, pp. 2444–2451, mar 2001.

[177] Y. He, S. Mueller, P. R. Chipman, C. M. Bator, X. Peng, V. D. Bowman, S. Mukhopadhyay, E. Wimmer, R. J. Kuhn, and M. G. Rossmann, "Complexes of poliovirus serotypes with their common cellular receptor, CD155," *J Virol*, vol. 77, no. 8, pp. 4827–4835, 2003.

[178] L. Xing, J. M. Casasnovas, and R. H. Cheng, "Structural analysis of human rhinovirus complexed with ICAM-1 reveals the dynamics of receptor-mediated virus uncoating," *J Virol*, vol. 77, pp. 6101–6107, jun 2003.

[179] C. Xiao, T. J. Tuthill, C. M. Bator Kelly, L. J. Challinor, P. R. Chipman, R. A. Killington, D. J. Rowlands, A. Craig, and M. G. Rossmann, "Discrimination among Rhinovirus Serotypes for a Variant ICAM-1 Receptor Molecule," *Journal of Virology*, vol. 78, pp. 10034–10044, sep 2004.

[180] D. Bubeck, D. J. Filman, and J. M. Hogle, "Cryo-electron microscopy reconstruction of a poliovirus-receptor-membrane complex," *Nature Structural & Molecular Biology*, vol. 12, pp. 615–618, jul 2005.

[181] P. Zhang, S. Mueller, M. C. Morais, C. M. Bator, V. D. Bowman, S. Hafenstein, E. Wimmer, and M. G. Rossmann, "Crystal structure of CD155 and electron microscopic studies of its complexes with polioviruses," *Proc Natl Acad Sci U S A*, vol. 105, pp. 18284–18289, nov 2008.

[182] L. J. Organtini, A. M. Makhov, J. F. Conway, S. Hafenstein, and S. D. Carson, "Kinetic and structural analysis of coxsackievirus B3 receptor interactions and formation of the A-particle," *J. Virol.*, vol. 88, no. 10, pp. 5755–5765, 2014.

[183] M. G. Rossmann, Y. He, and R. J. Kuhn, "Picornavirus-receptor interactions," *Trends Microbiol.*, vol. 10, pp. 324–331, jul 2002.

[184] M. Smyth, T. Pettitt, A. Symonds, and J. Martin, "Identification of the pocket factors in a picornavirus," *Arch. Virol.*, vol. 148, no. 6, pp. 1225–1233, 2003.

[185] J. M. Casasnovas and T. A. Springer, "Kinetics and thermodynamics of virus binding to receptor. Studies with rhinovirus, intercellular adhesion molecule-1 (ICAM-1), and surface plasmon resonance.," *The Journal of biological chemistry*, vol. 270, pp. 13216–24, jun 1995.

[186] B. M. McDermott, A. H. Rux, R. J. Eisenberg, G. H. Cohen, and V. R. Racaniello, "Two distinct binding affinities of poliovirus for its cellular receptor.," *The Journal of biological chemistry*, vol. 275, pp. 23089–96, jul 2000.

[187] S. D. Carson, "Kinetic models for receptor-catalyzed conversion of coxsackievirus B3 to A-particles.," *Journal of virology*, vol. 88, pp. 11568–75, oct 2014.

[188] M. G. Rossmann, "Viral cell recognition and entry," *Prot. Sci.*, vol. 3, pp. 1712–1725, oct 1994.

[189] Y. He, F. Lin, P. R. Chipman, C. M. Bator, T. S. Baker, M. Shoham, R. J. Kuhn, M. E. Medof, and M. G. Rossmann, "Structure of decay-accelerating factor bound to echovirus 7: A virus-receptor complex," *Proceedings of the National Academy of Sciences*, vol. 99, pp. 10325–10329, aug 2002.

[190] N. Verdaguer, I. Fita, M. Reithmayer, R. Moser, and D. Blaas, "X-ray structure of a minor group human rhinovirus bound to a fragment of its cellular receptor protein," *Nat Struct Mol Biol*, vol. 11, pp. 429–434, may 2004.

[191] S. Shakeel, J. J. T. Seitsonen, T. Kajander, P. Laurinmaki, T. Hyypia, P. Susi, and S. J. Butcher, "Structural and Functional Analysis of Coxsackievirus A9 Integrin v 6 Binding and Uncoating," *Journal of Virology*, vol. 87, pp. 3943–3951, apr 2013.

[192] M. Dang, X. Wang, Q. Wang, Y. Wang, J. Lin, Y. Sun, X. Li, L. Zhang, Z. Lou, J. Wang, Z. Rao, Dang M., Wang X., Wang Q., Wang Y., Lin J., Sun Y., Li X., Zhang L., Lou Z., Wang J., Rao Z., M. Dang, X. Wang, Q. Wang, Y. Wang, J. Lin, Y. Sun, X. Li, L. Zhang, Z. Lou, J. Wang, and Z. Rao, "Molecular mechanism of SCARB2-mediated attachment and uncoating of EV71," *Protein Cell*, vol. 5, pp. 692–703, sep 2014.

[193] P. Chen, Z. Song, Y. Qi, X. Feng, N. Xu, Y. Sun, X. Wu, X. Yao, Q. Mao, X. Li, W. Dong, X. Wan, N. Huang, X. Shen, Z. Liang, and W. Li, "Molecular determinants of enterovirus 71 viral entry: cleft around GLN-172 on VP1 protein interacts with variable region on scavenge receptor B 2," *J Biol Chem*, vol. 287, pp. 6406–6420, feb 2012.

[194] S. Yamayoshi, S. Ohka, K. Fujii, and S. Koike, "Functional comparison of SCARB2 and PSGL1 as receptors for enterovirus 71.," *Journal of virology*, vol. 87, pp. 3335–47, mar 2013.

[195] L. Xing, M. Huhtala, V. Pietiäinen, J. Käpylä, K. Vuorinen, V. Marjomäki, J. Heino, M. S. Johnson, T. Hyypiä, and R. H. Cheng, "Structural and functional analysis of integrin alpha2I domain interaction with echovirus 1.," *The Journal of biological chemistry*, vol. 279, pp. 11632–8, mar 2004.

[196] V. Pietiäinen, V. Marjomäki, P. Upla, L. Pelkmans, A. Helenius, and T. Hyypiä, "Echovirus 1 endocytosis into caveosomes requires lipid rafts, dynamin II, and signaling events.," *Molecular biology of the cell*, vol. 15, pp. 4911–25, nov 2004.

[197] R. Fuchs and D. Blaas, "Productive entry pathways of human rhinoviruses," *Adv Virol*, vol. 2012, p. 826301, 2012.

[198] V. Marjomäki, P. Turkki, and M. Huttunen, "Infectious Entry Pathway of Enterovirus B Species.," *Viruses*, vol. 7, pp. 6387–99, dec 2015.

[199] Y.-W. Lin, H.-Y. Lin, Y.-L. Tsou, E. Chitra, K.-N. Hsiao, H.-Y. Shao, C.-C. Liu, C. Sia, P. Chong, and Y.-H. Chow, "Human SCARB2-mediated entry and endocytosis of EV71.," *PloS one*, vol. 7, no. 1, p. e30507, 2012.

[200] H.-Y. Lin, Y.-T. Yang, S.-L. Yu, K.-N. Hsiao, C.-C. Liu, C. Sia, and Y.-H. Chow, "Caveolar endocytosis is required for human PSGL-1-mediated enterovirus 71 infection.," *Journal of virology*, vol. 87, pp. 9064–76, aug 2013.

[201] B. Brandenburg, L. Y. Lee, M. Lakadamyali, M. J. Rust, X. Zhuang, and J. M. Hogle, "Imaging poliovirus entry in live cells," *PLoS Biol*, vol. 5, p. e183, jul 2007.

[202] C. B. Coyne, K. S. Kim, and J. M. Bergelson, "Poliovirus entry into human brain microvascular cells requires receptor-induced activation of SHP-2," *The EMBO Journal*, vol. 26, pp. 4016–4028, sep 2007.

[203] C. B. Coyne and J. M. Bergelson, "Virus-Induced Abl and Fyn Kinase Signals Permit Coxsackievirus Entry through Epithelial Tight Junctions," *Cell*, vol. 124, pp. 119–131, jan 2006.

[204] G. Nurani, B. Lindqvist, and J. M. Casasnovas, "Receptor priming of major group human rhinoviruses for uncoating and entry at mild low-pH environments.," *Journal of virology*, vol. 77, pp. 11985–91, nov 2003.

[205] A. Pickl-Herk, D. Luque, L. Vives-Adrian, J. Querol-Audi, D. Garriga, B. L. Trus, N. Verdaguer, D. Blaas, J. R. Caston, L. Vives-Adrián, J. Querol-Audí, D. Garriga, B. L. Trus, N. Verdaguer, D. Blaas, and J. R. Castón, "Uncoating of common cold virus is preceded by RNA switching as determined by X-ray and cryo-EM analyses of the subviral A-particle," *Proc Natl Acad Sci U S A*, vol. 110, pp. 20063–20068, dec 2013.

[206] K. Wetz and T. Kucinski, "Influence of different ionic and pH environments on structural alterations of poliovirus and their possible relation to virus uncoating.," *The Journal of general virology*, pp. 2541–4, oct 1991.

[207] D. Bubeck, D. J. Filman, N. Cheng, A. C. Steven, J. M. Hogle, and D. M. Belnap, "The structure of the poliovirus 135S cell entry intermediate at 10-angstrom resolution reveals the location of an externalized polypeptide that binds to membranes.," *Journal of virology*, vol. 79, pp. 7745–55, jun 2005.

[208] K. L. Shingler, J. L. Yoder, M. S. Carnegie, R. E. Ashley, A. M. Makhov, J. F. Conway, and S. Hafenstein, "The enterovirus 71 A-particle forms a gateway to allow genome release: a cryoEM study of picornavirus uncoating," *PLoS Pathog*, vol. 9, no. 3, p. e1003240, 2013.

[209] C. Butan, D. J. Filman, and J. M. Hogle, "Cryo-electron microscopy reconstruction shows poliovirus 135S particles poised for membrane interaction and RNA release.," *Journal of virology*, vol. 88, pp. 1758–70, feb 2014.

[210] J. M. Greve, C. P. Forte, C. W. Marlor, A. M. Meyer, H. Hoover-Litty, D. Wunderlich, and A. McClelland, "Mechanisms of receptor-mediated rhinovirus neutralization defined by two soluble forms of ICAM-1.," *Journal of virology*, vol. 65, pp. 6015–23, nov 1991.

[211] J. Lin, N. Cheng, M. Chow, D. J. Filman, A. C. Steven, J. M. Hogle, and D. M. Belnap, "An externalized polypeptide partitions between two distinct sites on genome-released poliovirus particles," *J Virol*, vol. 85, pp. 9974–9983, oct 2011.

[212] J. Ren, X. Wang, Z. Hu, Q. Gao, Y. Sun, X. Li, C. Porta, T. S. Walter, R. J. Gilbert, Y. Zhao, D. Axford, M. Williams, K. McAuley, D. J. Rowlands, W. Yin, J. Wang, D. I. Stuart, Z. Rao, and E. E. Fry, "Picornavirus uncoating intermediate captured in atomic detail," *Nat. Commun.*, vol. 4, p. 1929, 2013.

[213] H. Lee, K. L. Shingler, L. J. Organtini, R. E. Ashley, A. M. Makhov, J. F. Conway, and S. Hafenstein, "The novel asymmetric entry intermediate of a picornavirus captured with nanodiscs," *Science Advances*, vol. 2, pp. e1501929–e1501929, aug 2016.

[214] M. L. Fenwick and P. D. Cooper, "Early interactions between poliovirus and ERK cells: Some observations on the nature and significance of the rejected particles," *Virology*, vol. 18, no. 2, pp. 212–223, 1962.

[215] R. L. Crowell and L. Philipson, "Specific alterations of coxsackievirus B3 eluted from HeLa cells.," *Journal of virology*, vol. 8, pp. 509–15, oct 1971.

[216] J. de Sena and B. Mandel, "Studies on the in vitro uncoating of poliovirus II. Characteristics of the membrane-modified particle," *Virology*, vol. 78, no. 2, pp. 554–566, 1977.

[217] S. Curry, M. Chow, and J. M. Hogle, "The poliovirus 135S particle is infectious.," *Journal of virology*, vol. 70, pp. 7125–31, oct 1996.

[218] Y. Huang, J. M. Hogle, and M. Chow, "Is the 135S poliovirus particle an intermediate during cell entry?," *J Virol*, vol. 74, pp. 8757–8761, sep 2000.

[219] E. Prchla, E. Kuechler, D. Blaas, and R. Fuchs, "Uncoating of human rhinovirus serotype 2 from late endosomes.," *Journal of virology*, vol. 68, no. 6, pp. 3713–3723, 1994.

[220] R. A. Grant, C. N. Hiremath, D. J. Filman, R. Syed, K. Andries, and J. M. Hogle, "Structures of poliovirus complexes with anti-viral drugs: implications for viral stability and drug design.," *Current biology : CB*, vol. 4, pp. 784–97, sep 1994.

[221] M. T. Tosteson and M. Chow, "Characterization of the ion channels formed by poliovirus in planar lipid membranes.," *Journal of virology*, vol. 71, pp. 507–11, jan 1997.

[222] M. Brabec, D. Schober, E. Wagner, N. Bayer, R. F. Murphy, D. Blaas, and R. Fuchs, "Opening of size-selective pores in endosomes during human rhinovirus serotype 2 in vivo uncoating monitored by single-organelle flow analysis.," *Journal of virology*, vol. 79, pp. 1008–16, jan 2005.

[223] G. Bilek, N. M. Matscheko, A. Pickl-Herk, V. U. Weiss, X. Subirats, E. Kenndler, and D. Blaas, "Liposomal nanocontainers as models for viral infection: monitoring viral genomic RNA transfer through lipid membranes," *J Virol*, vol. 85, pp. 8368–8375, aug 2011.

[224] D. Schober, P. Kronenberger, E. Prchla, D. Blaas, and R. Fuchs, "Major and minor receptor group human rhinoviruses penetrate from endosomes by different mechanisms.," *Journal of virology*, vol. 72, no. 2, pp. 1354–1364, 1998.

[225] J. Lin, L. Y. Lee, M. Roivainen, D. J. Filman, J. M. Hogle, and D. M. Belnap, "Structure of the Fab-labeled "breathing" state of native poliovirus.," *Journal of virology*, vol. 86, pp. 5959–62, may 2012.

[226] M. Strauss, H. C. Levy, M. Bostina, D. J. Filman, and J. M. Hogle, "RNA transfer from poliovirus 135S particles across membranes is mediated by long umbilical connectors," *J Virol*, vol. 87, pp. 3903–3914, apr 2013.

[227] M. Kumar and D. Blaas, "Human rhinovirus subviral a particle binds to lipid membranes over a twofold axis of icosahedral symmetry," *J Virol*, vol. 87, pp. 11309–11312, oct 2013.

[228] U. Katpally, T.-M. Fu, D. C. Freed, D. R. Casimiro, and T. J. Smith, "Antibodies to the buried N terminus of rhinovirus VP4 exhibit cross-serotypic neutralization.," *Journal of virology*, vol. 83, pp. 7040–8, jul 2009.

[229] E. A. Hewat and D. Blaas, "Cryoelectron microscopy analysis of the structural changes associated with human rhinovirus type 14 uncoating," *J Virol*, vol. 78, pp. 2935–2942, mar 2004.

[230] M. P. Davis, G. Bottley, L. P. Beales, R. A. Killington, D. J. Rowlands, and T. J. Tuthill, "Recombinant VP4 of human rhinovirus induces permeability in model membranes.," *Journal of virology*, vol. 82, pp. 4169–74, apr 2008.

[231] A. Panjwani, M. Strauss, S. Gold, H. Wenham, T. Jackson, J. J. Chou, D. J. D. D. J. Rowlands, N. J. Stonehouse, J. M. J. J. M. Hogle, and T. J. Tuthill, "Capsid protein VP4 of human rhinovirus induces membrane permeability by the formation of a size-selective multimeric pore.," *PLoS pathogens*, vol. 10, p. e1004294, aug 2014.

[232] N. Moscufo, A. G. Yafal, A. Rogove, J. Hogle, and M. Chow, "A mutation in VP4 defines a new step in the late stages of cell entry by poliovirus.," *Journal of virology*, vol. 67, pp. 5075–8, aug 1993.

[233] P. Danthi, M. Tosteson, Q.-H. Li, and M. Chow, "Genome delivery and ion channel properties are altered in VP4 mutants of poliovirus.," *Journal of virology*, vol. 77, pp. 5266–74, may 2003.

[234] M. T. Tosteson, H. Wang, A. Naumov, and M. Chow, "Poliovirus binding to its receptor in lipid bilayers results in particle-specific, temperature-sensitive channels.," *The Journal of general virology*, vol. 85, pp. 1581–9, jun 2004.

[235] E. A. Hewat, E. Neumann, and D. Blaas, "The concerted conformational changes during human rhinovirus 2 uncoating," *Mol Cell*, vol. 10, pp. 317–326, aug 2002.

[236] H. C. Levy, M. Bostina, D. J. Filman, and J. M. Hogle, "Catching a virus in the act of RNA release: a novel poliovirus uncoating intermediate characterized by cryo-electron microscopy.," *Journal of virology*, vol. 84, pp. 4426–41, may 2010.

[237] J. J. T. Seitsonen, S. Shakeel, P. Susi, A. P. Pandurangan, R. S. Sinkovits, H. Hyvonen, P. Laurinmaki, J. Yla-Pelto, M. Topf, T. Hyypia, and S. J. Butcher, "Structural Analysis of Coxsackievirus A7 Reveals Conformational Changes Associated with Uncoating," *Journal of Virology*, vol. 86, pp. 7207–7215, jul 2012.

[238] D. Garriga, A. Pickl-Herk, D. Luque, J. Wruss, J. R. Castón, D. Blaas, N. Verdaguer, J. R. Caston, D. Blaas, and N. Verdaguer, "Insights into minor group rhinovirus uncoating: the X-ray structure of the HRV2 empty capsid," *PLoS Pathog*, vol. 8, p. e1002473, jan 2012.

[239] M. Bostina, H. Levy, D. J. Filman, and J. M. Hogle, "Poliovirus RNA is released from the capsid near a twofold symmetry axis.," *Journal of virology*, vol. 85, no. 2, pp. 776–783, 2011.

[240] S. Harutyunyan, M. Kumar, A. Sedivy, X. Subirats, H. Kowalski, G. Köhler, D. Blaas, G. Kohler, D. Blaas, G. Köhler, and D. Blaas, "Viral uncoating is directional: exit of the genomic RNA in a common cold virus starts with the poly-(A) tail at the 3'-end," *PLoS Pathog*, vol. 9, no. 4, p. e1003270, 2013.

[241] S. Harutyunyan, H. Kowalski, and D. Blaas, "The rhinovirus subviral a-particle exposes 3'-terminal sequences of its genomic RNA," *J Virol*, vol. 88, pp. 6307–6317, jun 2014.

[242] M. Brabec-Zaruba, B. Pfanzagl, D. Blaas, and R. Fuchs, "Site of human rhinovirus RNA uncoating revealed by fluorescent in situ hybridization.," *Journal of virology*, vol. 83, pp. 3770–7, apr 2009.

[243] T. J. Smith, M. J. Kremer, M. Luo, G. Vriend, E. Arnold, G. Kamer, M. G. Rossmann, M. A. McKinlay, G. D. Diana, and M. J. Otto, "The site of attachment in human rhinovirus 14 for antiviral agents that inhibit uncoating," *Science*, vol. 233, pp. 1286–1293, sep 1986.

[244] J. Badger, I. Minor, M. J. Kremer, M. A. Oliveira, T. J. Smith, J. P. Griffith, D. M. A. Guerin, S. Krishnaswamy, M. Luo, M. G. Rossmann, M. A. McKinlay, G. D. Diana, F. J. Dutko, M. Fancher, R. R. Rueckert, and B. A. Heinz, "Structural analysis of a series of antiviral agents complexed with human rhinovirus 14," *Proc. Natl. Acad. Sci. U.S.A.*, vol. 85, pp. 3304–3308, 1988.

[245] P. Plevka, R. Perera, M. L. Yap, J. Cardosa, R. J. Kuhn, and M. G. Rossmann, "Structure of human enterovirus 71 in complex with a capsid-binding inhibitor.," *Proceedings of the National Academy of Sciences of the United States of America*, vol. 110, pp. 5463–7, apr 2013.

[246] L. De Colibus, X. Wang, J. A. B. Spyrou, J. Kelly, J. Ren, J. Grimes, G. Puerstinger, N. Stonehouse, T. S. Walter, Z. Hu, J. Wang, X. Li, W. Peng, D. J. Rowlands, E. E. Fry, Z. Rao, and D. I. Stuart, "More-powerful virus inhibitors from structure-based analysis of HEV71 capsid-binding molecules.," *Nature structural & molecular biology*, vol. 21, pp. 282–8, mar 2014.

[247] M. P. Fox, M. J. Otto, and M. A. McKinlay, "Prevention of rhinovirus and poliovirus uncoating by WIN 51711, a new antiviral drug," *Antimicrob Agents Chemother*, vol. 30, no. 1, pp. 110–116, 1986.

[248] H. Zeichhardt, M. J. Otto, M. A. McKinlay, P. Willingmann, and K. O. Habermehl, "Inhibition of poliovirus uncoating by disoxaril (WIN 51711).," *Virology*, vol. 160, pp. 281–5, sep 1987.

[249] D. A. Shepard, B. A. Heinz, and R. R. Rueckert, "WIN 52035-2 inhibits both attachment and eclipse of human rhinovirus 14.," *Journal of virology*, vol. 67, pp. 2245–54, apr 1993.

[250] D. C. Pevear, M. J. Fancher, P. J. Felock, M. G. Rossmann, M. S. Miller, G. Diana, A. M. Treasurywala, M. A. McKinlay, and F. J. Dutko, "Conformational change in the floor of the human rhinovirus canyon blocks adsorption to HeLa cell receptors," *J Virol*, vol. 63, no. 5, pp. 2002–2007, 1989.

[251] B. Dewindt, K. van Eemeren, and K. Andries, "Antiviral capsid-binding compounds can inhibit the adsorption of minor receptor rhinoviruses.," *Antiviral research*, vol. 25, pp. 67–72, sep 1994.

[252] A. W. Dove and V. R. Racaniello, "An antiviral compound that blocks structural transitions of poliovirus prevents receptor binding at low temperatures.," *Journal of virology*, vol. 74, pp. 3929–31, apr 2000.

[253] Q. Li, A. G. Yafal, Y. M. Lee, J. Hogle, and M. Chow, "Poliovirus neutralization by antibodies to internal epitopes of VP4 and VP1 results from reversible exposure of these sequences at physiological temperature.," *Journal of virology*, vol. 68, pp. 3965–70, jun 1994.

[254] J. K. Lewis, B. Bothner, T. J. Smith, and G. Siuzdak, "Antiviral agent blocks breathing of the common cold virus.," *Proceedings of the National Academy of Sciences of the United States of America*, vol. 95, pp. 6774–8, jun 1998.

[255] A. Roy and C. B. Post, "Long-distance correlations of rhinovirus capsid dynamics contribute to uncoating and antiviral activity.," *Proceedings of the National Academy of Sciences of the United States of America*, vol. 109, pp. 5271–6, apr 2012.

[256] J. D. Watson and F. H. Crick, "Molecular structure of nucleic acids; a structure for deoxyribose nucleic acid.," *Nature*, vol. 171, pp. 737–8, apr 1953.

[257] J. C. Kendrew, R. E. Dickerson, B. E. Strangberg, R. G. Hart, D. R. Davies, D. C. Phillips, and V. C. Shore, "Structure of myoglobin: A three-dimensional Fourier synthesis at 2 A. resolution.," *Nature*, vol. 185, pp. 422–7, feb 1960.

[258] M. F. Perutz, M. G. Rossmann, A. F. Cullis, H. Muirhead, G. Will, and A. C. North, "Structure of haemoglobin: a three-dimensional Fourier synthesis at 5.5-A. resolution, obtained by X-ray analysis.," *Nature*, vol. 185, pp. 416–22, feb 1960.

[259] W. Friedrich, P. Knipping, and M. Laue, "Interferenzerscheinungen bei Röntgenstrahlen," *Annalen der Physik*, vol. 346, no. 10, pp. 971–988, 1913.

[260] W. L. Bragg, "The diffraction of short electromagnetic waves by a crystal," in *Proceedings of the Cambridge Philosophical Society*, vol. 17, pp. 43–57, 1913.

[261] W. T. Astbury, R. Lomax, J. D. Bernal, and D. Crowfoot, "X-ray photographs of crystalline pepsin," *Nature*, vol. 133, no. 3369, p. 795, 1934.

[262] D. W. Green, V. M. Ingram, and M. F. Perutz, "The Structure of Haemoglobin. IV. Sign Determination by the Isomorphous Replacement Method," *Proceedings of the Royal Society of London A: Mathematical, Physical and Engineering Sciences*, vol. 225, no. 1162, 1954.

[263] B. W. Matthews, "Heavy-atom location and phase determination with single-wavelength diffraction data," in *International Tables for Crystallography*, pp. 293–298, Chester, England: International Union of Crystallography, oct 2006.

[264] M. G. Rossmann, "The accurate determination of the position and shape of heavy-atom replacement groups in proteins," *Acta Crystallographica*, vol. 13, pp. 221–226, mar 1960.

[265] A. L. Patterson, "A Fourier Series Method for the Determination of the Components of Interatomic Distances in Crystals," *Physical Review*, vol. 46, pp. 372–376, sep 1934.

[266] D. Harker, "The determination of the phases of the structure factors of non-centrosymmetric crystals by the method of double isomorphous replacement," *Acta Crystallographica*, vol. 9, pp. 1–9, jan 1956.

[267] D. M. Blow and M. G. Rossmann, "The single isomorphous replacement method," *Acta Crystallographica*, vol. 14, pp. 1195–1202, nov 1961.

[268] D. M. Blow and F. H. C. Crick, "The treatment of errors in the isomorphous replacement method," *Acta Crystallographica*, vol. 12, pp. 794–802, oct 1959.

[269] W. Hendrickson, "Determination of macromolecular structures from anomalous diffraction of synchrotron radiation," *Science*, vol. 254, no. 5028, 1991.

[270] D. M. Blow, "The Structure of Haemoglobin. VII. Determination of Phase Angles in the Non-Centrosymmetric [100] Zone," *Proceedings of the Royal Society of London A: Mathematical, Physical and Engineering Sciences*, vol. 247, no. 1250, 1958.

[271] A. C. T. North, "The combination of isomorphous replacement and anomalous scattering data in phase determination of non-centrosymmetric reflexions," *Acta Crystallographica*, vol. 18, pp. 212–216, feb 1965.

[272] B. W. Matthews, "The extension of the isomorphous replacement method to include anomalous scattering measurements," *Acta Crystallographica*, vol. 20, pp. 82–86, jan 1966.

[273] W. A. Hendrickson, J. R. Horton, and D. M. LeMaster, "Selenomethionyl proteins produced for analysis by multiwavelength anomalous diffraction (MAD): a vehicle for direct determination of three-dimensional structure.," *The EMBO journal*, vol. 9, pp. 1665–72, may 1990.

[274] M. G. Rossmann, "The position of anomalous scatterers in protein crystals," *Acta Crystallographica*, vol. 14, pp. 383–388, apr 1961.

[275] Q. Liu, T. Dahmane, Z. Zhang, Z. Assur, J. Brasch, L. Shapiro, F. Mancia, and W. A. Hendrickson, "Structures from Anomalous Diffraction of Native Biological Macromolecules," *Science*, vol. 336, pp. 1033–1037, may 2012.

[276] M. G. Rossmann, "The molecular replacement method," *Acta Crystallographica Section A*, vol. 46, pp. 73–82, feb 1990.

[277] M. G. Rossmann and D. M. Blow, "The detection of sub-units within the crystallographic asymmetric unit," *Acta Crystallographica*, vol. 15, pp. 24–31, jan 1962.

[278] L. Tong, "Translation functions," in *International Tables for Crystallography*, pp. 275–278, Chester, England: International Union of Crystallography, oct 2006.

[279] R. A. Crowther and D. M. Blow, "A method of positioning a known molecule in an unknown crystal structure," *Acta Crystallographica*, vol. 23, pp. 544–548, oct 1967.

[280] H. Muirhead, J. M. Cox, L. Mazzarella, and M. Perutz, "Structure and function of haemoglobin: III. A three-dimensional fourier synthesis of human deoxyhaemoglbin at 5·5 Å resolution," *Journal of Molecular Biology*, vol. 28, no. 1, pp. 117–150, 1967.

[281] M. Buehner, G. C. Ford, D. Moras, K. W. Olsen, and M. G. Rossmann, "Structure determination of crystalline lobster d-glyceraldehyde-3-phosphate dehydrogenase," *Journal of Molecular Biology*, vol. 82, no. 4, pp. 563–585, 1974.

[282] P. Argos, G. C. Ford, and M. G. Rossmann, "An application of the molecular replacement technique in direct space to a known protein structure," *Acta Crystallographica Section A*, vol. 31, pp. 499–506, jul 1975.

[283] W. P. Gaykema, A. Volbeda, and W. G. Hol, "Structure determination of Panulirus interruptus haemocyanin at 3.2 Å resolution: Successful phase extension by sixfold density averaging," *Journal of Molecular Biology*, vol. 187, no. 2, pp. 255–275, 1986.

[284] E. Arnold, G. Vriend, M. Luo, J. P. Griffith, G. Kamer, J. W. Erickson, J. E. Johnson, and M. G. Rossmann, "The structure determination of a common cold virus, human rhinovirus 14," *Acta Crystallographica Section A*, vol. 43, pp. 346–361, may 1987.

[285] M. Luo, G. Vriend, G. Kamer, and M. G. Rossmann, "Structure determination of Mengo virus.," *Acta crystallographica. Section B, Structural science*, vol. 45 (Pt 1), pp. 85–92, feb 1989.

[286] R. Acharya, E. Fry, D. Stuart, G. Fox, D. Rowlands, and F. Brown, "The three-dimensional structure of foot-and-mouth disease virus at 2.9 A resolution," *Nature*, vol. 337, no. 6209, pp. 709–716, 1989.

[287] R. McKenna, D. Xia, P. Willingmann, L. L. Ilag, and M. G. Rossmann, "Structure determination of the bacteriophage phiX174.," *Acta crystallographica. Section B, Structural science*, vol. 48 (Pt 4), pp. 499–511, aug 1992.

[288] J. Tsao, M. S. Chapman, H. Wu, M. Agbandje, W. Keller, and M. G. Rossmann, "Structure determination of monoclinic canine parvovirus," *Acta Crystallogr B*, vol. 48 (Pt 1), pp. 75–88, 1992.

[289] J. K. Muckelbauer, M. Kremer, I. Minor, L. Tong, A. Zlotnick, J. E. Johnson, and M. G. Rossmann, "Structure determination of coxsackievirus B3 to 3.5 A resolution," *Acta Crystallogr D Biol Crystallogr*, vol. 51, no. Pt 6, pp. 871–887, 1995.

[290] P. Plevka, R. Perera, J. Cardosa, R. J. Kuhn, and M. G. Rossmann, "Structure determination of enterovirus 71," *Acta Crystallographica Section D Biological Crystallography*, vol. 68, pp. 1217–1222, sep 2012.

[291] B.-C. Wang, "Resolution of phase ambiguity in macromolecular crystallography," *Methods in Enzymology*, vol. 115, pp. 90–112, 1985.

[292] P. Main and M. G. Rossmann, "Relationship among structure factors due to identical molecules in different crystallographic environments," *Acta Crystallographica*, vol. 21, pp. 67–72, jul 1966.

[293] M. G. Rossmann and E. Arnold, "Noncrystallographic symmetry averaging of electron density for molecular-replacement phase refinement and extension," in *International Tables for Crystallography*, pp. 279–292, Chester, England: International Union of Crystallography, oct 2006.

[294] M. Knoll and E. Ruska, "Das elektronenmikroskop," *Zeitschrift für Physik*, vol. 78, no. 5-6, pp. 318–339, 1932.

[295] R. Henderson, "The potential and limitations of neutrons, electrons and X-rays for atomic resolution microscopy of unstained biological molecules.," *Quarterly reviews of biophysics*, vol. 28, pp. 171–93, may 1995.

[296] S. Brenner and R. W. Horne, "A negative staining method for high resolution electron microscopy of viruses.," *Biochimica et biophysica acta*, vol. 34, pp. 103–110, 1959.

[297] D. J. De Rosier and A. Klug, "Reconstruction of three dimensional structures from electron micrographs.," *Nature*, vol. 217, pp. 130–4, jan 1968.

[298] H. P. Erickson and A. Klug, "Measurement and Compensation of Defocusing and Aberrations by Fourier Processing of Electron Micrographs," *Philosophical Transactions of the Royal Society of London B: Biological Sciences*, vol. 261, no. 837, 1971.

[299] M. Ohi, Y. Li, Y. Cheng, and T. Walz, "Negative Staining and Image Classification - Powerful Tools in Modern Electron Microscopy.," *Biological procedures online*, vol. 6, pp. 23–34, 2004.

[300] K. A. Taylor and R. M. Glaeser, "Electron Diffraction of Frozen, Hydrated Protein Crystals," *Science*, vol. 186, pp. 1036–1037, dec 1974.

[301] M. Adrian, J. Dubochet, J. Lepault, and A. W. McDowall, "Cryo-electron microscopy of viruses.," *Nature*, vol. 308, no. 5954, pp. 32–6.

[302] J. Chang, X. Liu, R. H. Rochat, M. L. Baker, and W. Chiu, "Reconstructing virus structures from nanometer to near-atomic resolutions with cryo-electron microscopy and tomography.," *Advances in experimental medicine and biology*, vol. 726, pp. 49–90, 2012.

[303] R. Henderson, J. Baldwin, T. Ceska, F. Zemlin, E. Beckmann, and K. Downing, "Model for the structure of bacteriorhodopsin based on high-resolution electron cryo-microscopy," *Journal of Molecular Biology*, vol. 213, pp. 899–929, jun 1990.

[304] A. Miyazawa, Y. Fujiyoshi, and N. Unwin, "Structure and gating mechanism of acetylcholine receptor pore," *Nature*, vol. 423, jun 2003.

[305] K. Yonekura, S. Maki-Yonekura, and K. Namba, "Complete atomic model of the bacterial flagellar filament by electron cryomicroscopy," *Nature*, vol. 424, pp. 643–650, aug 2003.

[306] R. Henderson and P. N. Unwin, "Three-dimensional model of purple membrane obtained by electron microscopy.," *Nature*, vol. 257, pp. 28–32, sep 1975.

[307] T. Gonen, Y. Cheng, P. Sliz, Y. Hiroaki, Y. Fujiyoshi, S. C. Harrison, and T. Walz, "Lipid-protein interactions in double-layered two-dimensional AQP0 crystals.," *Nature*, vol. 438, pp. 633–8, dec 2005.

[308] B. Böttcher, S. A. Wynne, and R. A. Crowther, "Determination of the fold of the core protein of hepatitis B virus by electron cryomicroscopy," 1997.

[309] J. F. Conway, N. Cheng, A. Zlotnick, P. T. Wingfield, S. J. Stahl, and A. C. Steven, "Visualization of a 4-helix bundle in the hepatitis B virus capsid by cryo-electron microscopy," *Nature*, vol. 386, pp. 91–94, mar 1997.

[310] X. Yu, L. Jin, and Z. H. Zhou, "3.88Å structure of cytoplasmic polyhedrosis virus by cryo-electron microscopy," *Nature*, vol. 453, pp. 415–419, may 2008.

[311] X. Zhang, E. Settembre, C. Xu, P. R. Dormitzer, R. Bellamy, S. C. Harrison, and N. Grigorieff, "Near-atomic resolution using electron cryomicroscopy and single-particle reconstruction.," *Proceedings of the National Academy of Sciences of the United States of America*, vol. 105, pp. 1867–72, feb 2008.

[312] J.-P. Armache, A. Jarasch, A. M. Anger, E. Villa, T. Becker, S. Bhushan, F. Jossinet, M. Habeck, G. Dindar, S. Franckenberg, V. Marquez, T. Mielke, M. Thomm, O. Berninghausen, B. Beatrix, J. Söding, E. Westhof, D. N. Wilson, and R. Beckmann, "Localization of eukaryote-specific ribosomal proteins in a 5.5-Å cryo-EM map of the 80S eukaryotic ribosome.," *Proceedings of the National Academy of Sciences of the United States of America*, vol. 107, pp. 19754–9, nov 2010.

[313] K. H. Downing and R. M. Glaeser, "Restoration of weak phase-contrast images recorded with a high degree of defocus: The twin image problem associated with CTF correction," *Ultramicroscopy*, vol. 108, pp. 921–928, aug 2008.

[314] R. A. Crowther, "Procedures for Three-Dimensional Reconstruction of Spherical Viruses by Fourier Synthesis from Electron Micrographs," *Philosophical Transactions of the Royal Society of London B: Biological Sciences*, vol. 261, no. 837, 1971.

[315] S. Fuller, S. Butcher, R. Cheng, and T. Baker, "Three-Dimensional Reconstruction of Icosahedral ParticlesThe Uncommon Line," *Journal of Structural Biology*, vol. 116, pp. 48–55, jan 1996.

[316] X. Liu, W. Jiang, J. Jakana, and W. Chiu, "Averaging tens to hundreds of icosahedral particle images to resolve protein secondary structure elements using a Multi-Path Simulated Annealing optimization algorithm.," *Journal of Structural Biology*, vol. 160, pp. 11–27, oct 2007.

[317] M. Van Heel, "Angular reconstitution: A posteriori assignment of projection directions for 3D reconstruction," *Ultramicroscopy*, vol. 21, no. 2, pp. 111–123, 1987.

[318] P. Dube, P. Tavares, R. Lurz, and M. van Heel, "The portal protein of bacteriophage SPP1: a DNA pump with 13-fold symmetry.," *The EMBO journal*, vol. 12, pp. 1303–9, apr 1993.

[319] P. A. Penczek, R. A. Grassucci, and J. Frank, "The ribosome at improved resolution: new techniques for merging and orientation refinement in 3D cryo-electron microscopy of biological particles.," *Ultramicroscopy*, vol. 53, pp. 251–70, mar 1994.

[320] M. Radermacher, T. Wagenknecht, A. Verschoor, and J. Frank, "Three-dimensional reconstruction from a single-exposure, random conical tilt series applied to the 50S ribosomal subunit of Escherichia coli.," *Journal of microscopy*, vol. 146, pp. 113–36, may 1987.

[321] T. S. Baker and R. H. Cheng, "A model-based approach for determining orientations of biological macromolecules imaged by cryoelectron microscopy.," *Journal of structural biology*, vol. 116, no. 1, pp. 120–30, 1996.

[322] R. M. Glaeser and R. J. Hall, "Reaching the information limit in cryo-EM of biological macromolecules: experimental aspects.," *Biophysical journal*, vol. 100, pp. 2331–7, may 2011.

[323] J. Brink, M. B. Sherman, J. Berriman, and W. Chiu, "Evaluation of charging on macromolecules in electron cryomicroscopy.," *Ultramicroscopy*, vol. 72, pp. 41–52, apr 1998.

[324] R. M. Glaeser, "Specimen Behavior in the Electron Beam.," *Methods in enzymology*, vol. 579, pp. 19–50, 2016.

[325] R. M. Glaeser, G. McMullan, A. R. Faruqi, and R. Henderson, "Images of paraffin monolayer crystals with perfect contrast: minimization of beam-induced specimen motion.," *Ultramicroscopy*, vol. 111, pp. 90–100, jan 2011.

[326] A. R. Faruqi and S. Subramaniam, "CCD detectors in high-resolution biological electron microscopy," *Quarterly Reviews of Biophysics*, vol. 33, no. 1, pp. 1–27, 2000.

[327] A.-C. Milazzo, P. Leblanc, F. Duttweiler, L. Jin, J. C. Bouwer, S. Peltier, M. Ellisman, F. Bieser, H. S. Matis, H. Wieman, P. Denes, S. Kleinfelder, and N.-H. Xuong, "Active pixel sensor array as a detector for electron microscopy," *Ultramicroscopy*, vol. 104, no. 2, pp. 152–159, 2005.

[328] A. F. Brilot, J. Z. Chen, A. Cheng, J. Pan, S. C. Harrison, C. S. Potter, B. Carragher, R. Henderson, and N. Grigorieff, "Beam-induced motion of vitrified specimen on holey carbon film," *Journal of Structural Biology*, vol. 177, no. 3, pp. 630–637, 2012.

[329] G. McMullan, A. R. Faruqi, and R. Henderson, "Direct Electron Detectors.," *Methods in enzymology*, vol. 579, pp. 1–17, 2016.

[330] G. McMullan, A. R. Faruqi, D. Clare, and R. Henderson, "Comparison of optimal performance at 300keV of three direct electron detectors for use in low dose electron microscopy.," *Ultramicroscopy*, vol. 147, pp. 156–63, dec 2014.

[331] X. Li, P. Mooney, S. Zheng, C. R. Booth, M. B. Braunfeld, S. Gubbens, D. A. Agard, and Y. Cheng, "Electron counting and beam-induced motion correction enable near-atomic-resolution single-particle cryo-EM.," *Nature methods*, vol. 10, no. 6, pp. 584–90, 2013.

[332] S. Zheng, E. Palovcak, J.-P. Armache, Y. Cheng, and D. Agard, "Anisotropic Correction of Beam-induced Motion for Improved Single-particle Electron Cryomicroscopy," *bioRxiv*, 2016.

[333] T. Grant and N. Grigorieff, "Measuring the optimal exposure for single particle cryo-EM using a 2.6 Å reconstruction of rotavirus VP6," *Elife*, vol. 4, p. e06980, 2015.

[334] X.-C. Bai, I. S. Fernandez, G. McMullan, and S. H. Scheres, "Ribosome structures to near-atomic resolution from thirty thousand cryo-EM particles," *eLife*, vol. 2, feb 2013.

[335] G. Tang, L. Peng, P. R. Baldwin, D. S. Mann, W. Jiang, I. Rees, and S. J. Ludtke, "EMAN2: an extensible image processing suite for electron microscopy," *J Struct Biol*, vol. 157, no. 1, pp. 38–46, 2007.

[336] N. Grigorieff, "FREALIGN: high-resolution refinement of single particle structures.," *Journal of structural biology*, vol. 157, pp. 117–25, jan 2007.

[337] S. H. W. Scheres, "RELION: implementation of a Bayesian approach to cryo-EM structure determination.," *Journal of structural biology*, vol. 180, pp. 519–30, dec 2012.

[338] H. Elmlund, D. Elmlund, and S. Bengio, "PRIME: Probabilistic initial 3D model generation for single-particle cryo-electron microscopy," *Structure*, vol. 21, no. 8, pp. 1299–1306, 2013.

[339] F. Guo and W. Jiang, "Single particle cryo-electron microscopy and 3-D reconstruction of viruses," *Methods Mol Biol*, vol. 1117, pp. 401–443, 2014.

[340] C. Suloway, J. Pulokas, D. Fellmann, A. Cheng, F. Guerra, J. Quispe, S. Stagg, C. S. Potter, and B. Carragher, "Automated molecular microscopy: the new Leginon system," *J Struct Biol*, vol. 151, no. 1, pp. 41–60, 2005.

[341] F. Sigworth, "A Maximum-Likelihood Approach to Single-Particle Image Refinement," *Journal of Structural Biology*, vol. 122, no. 3, pp. 328–339, 1998.

[342] A. Bartesaghi, A. Merk, S. Banerjee, D. Matthies, X. Wu, J. L. S. Milne, and S. Subramaniam, "2.2 Å resolution cryo-EM structure of β-galactosidase in complex with a cell-permeant inhibitor.," *Science (New York, N.Y.)*, vol. 348, pp. 1147–51, jun 2015.

[343] M. G. Campbell, D. Veesler, A. Cheng, C. S. Potter, and B. Carragher, "2.8 Å resolution reconstruction of the Thermoplasma acidophilum 20S proteasome using cryo-electron microscopy," *eLife*, vol. 4, mar 2015.

[344] J. Jiang, B. L. Pentelute, R. J. Collier, and Z. H. Zhou, "Atomic structure of anthrax protective antigen pore elucidates toxin translocation," *Nature*, vol. 521, pp. 545–549, mar 2015.

[345] S. Banerjee, A. Bartesaghi, A. Merk, P. Rao, S. L. Bulfer, Y. Yan, N. Green, B. Mroczkowski, R. J. Neitz, P. Wipf, V. Falconieri, R. J. Deshaies, J. L. S. Milne, D. Huryn, M. Arkin, and S. Subramaniam, "2.3 Å resolution cryo-EM structure of human p97 and mechanism of allosteric inhibition.," *Science (New York, N.Y.)*, vol. 351, pp. 871–5, feb 2016.

[346] M. Shalev-Benami, Y. Zhang, D. Matzov, Y. Halfon, A. Zackay, H. Rozenberg, E. Zimmerman, A. Bashan, C. L. Jaffe, A. Yonath, and G. Skiniotis, "2.8-Å Cryo-EM Structure of the Large Ribosomal Subunit from the Eukaryotic Parasite Leishmania.," *Cell reports*, vol. 16, pp. 288–94, jul 2016.

[347] A. Merk, A. Bartesaghi, S. Banerjee, V. Falconieri, P. Rao, M. I. Davis, R. Pragani, M. B. Boxer, L. A. Earl, J. L. S. Milne, and S. Subramaniam, "Breaking Cryo-EM Resolution Barriers to Facilitate Drug Discovery.," *Cell*, vol. 165, pp. 1698–707, jun 2016.

[348] M. Liao, E. Cao, D. Julius, and Y. Cheng, "Structure of the TRPV1 ion channel determined by electron cryo-microscopy," *Nature*, vol. 504, pp. 107–112, dec 2013.

[349] G. Fan, M. L. Baker, Z. Wang, M. R. Baker, P. A. Sinyagovskiy, W. Chiu, S. J. Ludtke, and I. I. Serysheva, "Gating machinery of InsP3R channels revealed by electron cryomicroscopy," *Nature*, vol. 527, pp. 336–341, oct 2015.

[350] A. Dashti, P. Schwander, R. Langlois, R. Fung, W. Li, A. Hosseinizadeh, H. Y. Liao, J. Pallesen, G. Sharma, V. A. Stupina, A. E. Simon, J. D. Dinman, J. Frank, and A. Ourmazd, "Trajectories of the ribosome as a Brownian nanomachine.," *Proceedings of the National Academy of Sciences of the United States of America*, vol. 111, pp. 17492–7, dec 2014.

[351] R. Zalk, O. B. Clarke, A. des Georges, R. A. Grassucci, S. Reiken, F. Mancia, W. A. Hendrickson, J. Frank, and A. R. Marks, "Structure of a mammalian ryanodine receptor," *Nature*, vol. 517, pp. 44–49, dec 2014.

[352] A. Zhou, A. Rohou, D. G. Schep, J. V. Bason, M. G. Montgomery, J. E. Walker, N. Grigorieff, and J. L. Rubinstein, "Structure and conformational states of the bovine mitochondrial ATP synthase by cryo-EM," *eLife*, vol. 4, oct 2015.

[353] Y. He, J. Fang, D. J. Taatjes, and E. Nogales, "Structural visualization of key steps in human transcription initiation," *Nature*, vol. 495, pp. 481–486, feb 2013.

[354] J. A. Letts, K. Fiedorczuk, and L. A. Sazanov, "The architecture of respiratory supercomplexes," *Nature*, vol. 537, pp. 644–648, sep 2016.

[355] X. Wei, X. Su, P. Cao, X. Liu, W. Chang, M. Li, X. Zhang, and Z. Liu, "Structure of spinach photosystem IILHCII supercomplex at 3.2Å resolution," *Nature*, vol. 534, pp. 69–74, may 2016.

[356] Y. Tao, N. H. Olson, W. Xu, D. L. Anderson, M. G. Rossmann, and T. S. Baker, "Assembly of a tailed bacterial virus and its genome release studied in three dimensions.," *Cell*, vol. 95, pp. 431–7, oct 1998.

[357] F. Guo, Z. Liu, F. Vago, Y. Ren, W. Wu, E. T. Wright, P. Serwer, and W. Jiang, "Visualization of uncorrelated, tandem symmetry mismatches in the internal genome packaging apparatus of bacteriophage T7.," *Proceedings of the National Academy of Sciences of the United States of America*, vol. 110, pp. 6811–6, apr 2013.

[358] X. Zhang, K. Ding, X. Yu, W. Chang, J. Sun, and Z. Hong Zhou, "In situ structures of the segmented genome and RNA polymerase complex inside a dsRNA virus," *Nature*, vol. 527, pp. 531–534, oct 2015.

[359] I. S. Fernandez, X.-C. Bai, T. Hussain, A. C. Kelley, J. R. Lorsch, V. Ramakrishnan, and S. H. W. Scheres, "Molecular Architecture of a Eukaryotic Translational Initiation Complex," *Science*, vol. 342, pp. 1240585–1240585, nov 2013.

[360] A. des Georges, V. Dhote, L. Kuhn, C. U. T. Hellen, T. V. Pestova, J. Frank, and Y. Hashem, "Structure of mammalian eIF3 in the context of the 43S preinitiation complex," *Nature*, vol. 525, pp. 491–495, sep 2015.

[361] P. J. Robinson, M. J. Trnka, D. A. Bushnell, R. E. Davis, P.-J. Mattei, A. L. Burlingame, and R. D. Kornberg, "Structure of a Complete Mediator-RNA Polymerase II Pre-Initiation Complex," *Cell*, vol. 166, pp. 1411–1422.e16, sep 2016.

[362] A. Singharoy, I. Teo, R. McGreevy, J. E. Stone, J. Zhao, and K. Schulten, "Molecular dynamics-based refinement and validation for sub-5 Å cryo-electron microscopy maps," *eLife*, vol. 5, jul 2016.

[363] J. P. Erzberger, F. Stengel, R. Pellarin, S. Zhang, T. Schaefer, C. H. Aylett, P. Cimermančič, D. Boehringer, A. Sali, R. Aebersold, and N. Ban, "Molecular Architecture of the 40SeIF1eIF3 Translation Initiation Complex," *Cell*, vol. 158, pp. 1123–1135, aug 2014.

[364] B. J. Greber, P. Bieri, M. Leibundgut, A. Leitner, R. Aebersold, D. Boehringer, and N. Ban, "The complete structure of the 55S mammalian mitochondrial ribosome," *Science*, vol. 348, pp. 303–308, apr 2015.

[365] R. Danev and K. Nagayama, "Phase Plates for Transmission Electron Microscopy," pp. 343–369, 2010.

[366] R. Danev, B. Buijsse, M. Khoshouei, J. M. Plitzko, and W. Baumeister, "Volta potential phase plate for in-focus phase contrast transmission electron microscopy.," *Proceedings of the National Academy of Sciences of the United States of America*, vol. 111, pp. 15635–40, nov 2014.

[367] M. Khoshouei, M. Radjainia, A. J. Phillips, J. A. Gerrard, A. K. Mitra, J. M. Plitzko, W. Baumeister, and R. Danev, "Volta phase plate cryo-EM of the small protein complex Prx3," *Nature Communications*, vol. 7, p. 10534, jan 2016.

[368] C. J. Russo and L. A. Passmore, "Controlling protein adsorption on graphene for cryo-EM using low-energy hydrogen plasmas," *Nature Methods*, vol. 11, pp. 649–652, apr 2014.

[369] J. A. Berriman and P. B. Rosenthal, "Paraxial charge compensator for electron cryomicroscopy.," *Ultramicroscopy*, vol. 116, pp. 106–14, may 2012.

[370] I. Razinkov, V. P. Dandey, H. Wei, Z. Zhang, D. Melnekoff, W. J. Rice, C. Wigge, C. S. Potter, and B. Carragher, "A new method for vitrifying samples for cryoEM.," *Journal of structural biology*, vol. 195, pp. 190–8, aug 2016.

[371] V. Lučić, F. Förster, and W. Baumeister, "Structural studies by electron tomography: from cells to molecules.," vol. 74, pp. 833–865, jun 2005.

[372] W. Wan and J. Briggs, "Cryo-Electron Tomography and Subtomogram Averaging," in *Methods in Enzymology*, vol. 579, pp. 329–367, 2016.

[373] F. K. M. Schur, M. Obr, W. J. H. Hagen, W. Wan, A. J. Jakobi, J. M. Kirkpatrick, C. Sachse, H.-G. Krausslich, and J. A. G. Briggs, "An atomic model of HIV-1 capsid-SP1 reveals structures regulating assembly and maturation," *Science*, vol. 353, pp. 506–508, jul 2016.

[374] C. Xiao, Y. G. Kuznetsov, S. Sun, S. L. Hafenstein, V. A. Kostyuchenko, P. R. Chipman, M. Suzan-Monti, D. Raoult, A. McPherson, and M. G. Rossmann, "Structural Studies of the Giant Mimivirus," *PLoS Biology*, vol. 7, p. e1000092, apr 2009.

[375] C. Hagen, K. C. Dent, T. Zeev-Ben-Mordehai, M. Grange, J. B. Bosse, C. Whittle, B. G. Klupp, C. A. Siebert, D. Vasishtan, F. J. Bäuerlein, J. Cheleski, S. Werner, P. Guttmann, S. Rehbein, K. Henzler, J. Demmerle, B. Adler, U. Koszinowski, L. Schermelleh, G. Schneider, L. W. Enquist, J. M. Plitzko, T. C. Mettenleiter, and K. Grünewald, "Structural Basis of Vesicle Formation at the Inner Nuclear Membrane," *Cell*, vol. 163, pp. 1692–1701, dec 2015.

[376] J. Mahamid, S. Pfeffer, M. Schaffer, E. Villa, R. Danev, L. Kuhn Cuellar, F. Förster, A. A. Hyman, J. M. Plitzko, and W. Baumeister, "Visualizing the molecular sociology at the HeLa cell nuclear periphery," *Science*, vol. 351, no. 6276, 2016.

[377] R. Grimm, M. Bärmann, W. Häckl, D. Typke, E. Sackmann, and W. Baumeister, "Energy filtered electron tomography of ice-embedded actin and vesicles," *Biophysical Journal*, vol. 72, pp. 482–489, jan 1997.

[378] M. Marko, C. Hsieh, R. Schalek, J. Frank, and C. Mannella, "Focused-ion-beam thinning of frozen-hydrated biological specimens for cryo-electron microscopy," *Nature Methods*, vol. 4, pp. 215–217, mar 2007.

[379] A. Rigort, F. J. B. Bauerlein, E. Villa, M. Eibauer, T. Laugks, W. Baumeister, and J. M. Plitzko, "Focused ion beam micromachining of eukaryotic cells for cryoelectron tomography," *Proceedings of the National Academy of Sciences*, vol. 109, pp. 4449–4454, mar 2012.

[380] S. Asano, Y. Fukuda, F. Beck, A. Aufderheide, F. Forster, R. Danev, and W. Baumeister, "A molecular census of 26S proteasomes in intact neurons," *Science*, vol. 347, pp. 439–442, jan 2015.

[381] J. H. Schieble, V. L. Fox, and E. H. Lennette, "A probable new human picornavirus associated with respiratory diseases," *Am. J. Epidemiol.*, vol. 85, no. 2, pp. 297–310, 1967.

[382] N. Khetsuriani, A. Lamonte-Fowlkes, S. Oberst, M. A. Pallansch, and Centers for Disease Control and Prevention, "Enterovirus surveillance–United States, 1970-2005.," *Morbidity and mortality weekly report. Surveillance summaries (Washington, D.C. : 2002)*, vol. 55, pp. 1–20, sep 2006.

[383] R. Tokarz, C. Firth, S. A. Madhi, S. R. Howie, W. Wu, A. A. Sall, S. Haq, T. Briese, and W. I. Lipkin, "Worldwide emergence of multiple clades of enterovirus 68," *J. Gen. Virol.*, vol. 93, no. Pt 9, pp. 1952–1958, 2012.

[384] C. M. Midgley, M. A. Jackson, R. Selvarangan, G. Turabelidze, E. Obringer, D. Johnson, B. L. Giles, A. Patel, F. Echols, M. S. Oberste, W. A. Nix, J. T. Watson, and S. I. Gerber, "Severe respiratory illness associated with enterovirus D68 - Missouri and Illinois, 2014," *MMWR Morb. Mortal. Wkly. Rep.*, vol. 63, no. 36, pp. 798–799, 2014.

[385] S. Esposito, S. Bosis, H. Niesters, and N. Principi, "Enterovirus D68 Infection.," *Viruses*, vol. 7, pp. 6043–50, nov 2015.

[386] J. J. Farrell, O. Ikladios, K. M. Wylie, L. M. O'Rourke, K. S. Lowery, J. S. Cromwell, T. N. Wylie, E. L. V. Melendez, Y. Makhoul, R. Sampath, R. A. Bonomo, and G. A. Storch, "Enterovirus D68 Associated Acute Respiratory Distress Syndrome in Adult, United States, 2014," *Emerging Infectious Diseases*, vol. 21, pp. 914–916, may 2015.

[387] J. D. Kreuter, A. Barnes, J. E. McCarthy, J. D. Schwartzman, M. S. Oberste, C. H. Rhodes, J. F. Modlin, and P. F. Wright, "A fatal central nervous system enterovirus 68 infection," *Arch. Pathol. Lab. Med.*, vol. 135, no. 6, pp. 793–796, 2011.

[388] P. Ayscue, K. Van Haren, H. Sheriff, E. Waubant, P. Waldron, S. Yagi, C. Yen, A. Clayton, T. Padilla, C. Pan, J. Reichel, K. Harriman, J. Watt, J. Sejvar, W. A. Nix, D. Feikin, C. Glaser, and Centers for Disease Control and Prevention (CDC), "Acute flaccid paralysis with anterior myelitis - California, June 2012-June 2014.," *MMWR. Morbidity and mortality weekly report*, vol. 63, pp. 903–6, oct 2014.

[389] K. Lyu, J. Ding, J.-F. Han, Y. Zhang, X.-Y. Wu, Y.-L. He, C.-F. Qin, and R. Chen, "Human enterovirus 71 uncoating captured at atomic resolution.," *Journal of virology*, vol. 88, pp. 3114–26, mar 2014.

[390] Z. Otwinowski and W. Minor, "Processing of X-ray Diffraction Data Collected in Oscillation Mode," in *Methods in Enzymology* (C. W. Carter and R. M. Sweet, eds.), vol. 276, pp. 307–326, New York: Academic Press, 1997.

[391] L. Tong and M. G. Rossmann, "Rotation function calculations with GLRF program," *Methods Enzymol*, vol. 276, pp. 594–611, 1997.

[392] G. J. Kleywegt and R. J. Read, "Not your average density," *Structure*, vol. 5, pp. 1557–1569, 1997.

[393] G. J. Kleywegt and T. A. Jones, "Software for handling macromolecular envelopes," *Acta Crystallogr. D Biol. Crystallogr.*, vol. 55, pp. 941–944, 1999.

[394] P. Emsley, B. Lohkamp, W. G. Scott, and K. Cowtan, "Features and development of Coot," *Acta Crystallogr. D Biol. Crystallogr.*, vol. 66, no. Pt 4, pp. 486–501, 2010.

[395] A. T. Brünger, P. D. Adams, G. M. Clore, W. L. DeLano, P. Gros, R. W. Grosse-Kunstleve, J. S. Jiang, J. Kuszewski, M. Nilges, N. S. Pannu, R. J. Read, L. M. Rice, T. Simonson, G. L. Warren, A. T. Brunger, P. D. Adams, G. M. Clore, W. L. DeLano, P. Gros, R. W. Grosse-Kunstleve, J. S. Jiang, J. Kuszewski, M. Nilges, N. S. Pannu, R. J. Read, L. M. Rice, T. Simonson, and G. L. Warren, "Crystallography & NMR system: A new software suite for macromolecular structure determination," *Acta Crystallogr. D Biol. Crystallogr.*, vol. 54, no. Pt 5, pp. 905–921, 1998.

[396] V. B. Chen, W. B. Arendall 3rd, J. J. Headd, D. A. Keedy, R. M. Immormino, G. J. Kapral, L. W. Murray, J. S. Richardson, and D. C. Richardson, "MolProbity: all-atom structure validation for macromolecular crystallography," *Acta Crystallogr. D Biol. Crystallogr.*, vol. 66, no. Pt 1, pp. 12–21, 2010.

[397] P. D. Adams, P. V. Afonine, G. Bunkoczi, V. B. Chen, I. W. Davis, N. Echols, J. J. Headd, L. W. Hung, G. J. Kapral, R. W. Grosse-Kunstleve, A. J. McCoy, N. W. Moriarty, R. Oeffner, R. J. Read, D. C. Richardson, J. S. Richardson, T. C. Terwilliger, and P. H. Zwart, "PHENIX: a comprehensive Python-based system for macromolecular structure solution," *Acta Crystallogr. D Biol. Crystallogr.*, vol. 66, pp. 213–221, 2010.

[398] Collaborative Computational Project Number 4, "The CCP4 suite: programs for protein crystallography," *Acta Crystallogr D Biol Crystallogr*, vol. 50, no. Pt 5, pp. 760–763, 1994.

[399] M. Carrillo-Tripp, C. M. Shepherd, I. A. Borelli, S. Venkataraman, G. Lander, P. Natarajan, J. E. Johnson, C. L. Brooks 3rd, and V. S. Reddy, "VIPERdb2: an enhanced and web API enabled relational database for structural virology," *Nucleic Acids Res.*, vol. 37, no. Database issue, pp. D436–42, 2009.

[400] E. F. Pettersen, T. D. Goddard, C. C. Huang, G. S. Couch, D. M. Greenblatt, E. C. Meng, and T. E. Ferrin, "UCSF Chimera–a visualization system for exploratory research and analysis," *J Comput Chem*, vol. 25, no. 13, pp. 1605–1612, 2004.

[401] M. S. Oberste, K. Maher, D. Schnurr, M. R. Flemister, J. C. Lovchik, H. Peters, W. Sessions, C. Kirk, N. Chatterjee, S. Fuller, J. M. Hanauer, and M. A. Pallansch, "Enterovirus 68 is associated with respiratory illness and shares biological features with both the enteroviruses and the rhinoviruses," *J. Gen. Virol.*, vol. 85, no. Pt 9, pp. 2577–2584, 2004.

[402] X. Robert and P. Gouet, "Deciphering key features in protein structures with the new ENDscript server," *Nucleic Acids Research*, vol. 42, pp. W320–W324, jul 2014.

[403] T. Imamura and H. Oshitani, "Global reemergence of enterovirus D68 as an important pathogen for acute respiratory infections," *Reviews in Medical Virology*, vol. 25, pp. 102–114, mar 2015.

[404] M. R. Nokhbeh, S. Hazra, D. a. Alexander, A. Khan, M. McAllister, E. J. Suuronen, M. Griffith, and K. Dimock, "Enterovirus 70 binds to different glycoconjugates containing a2,3-linked sialic acid on different cell lines," *J. Virol.*, vol. 79, no. 11, pp. 7087–7094, 2005.

[405] C. R. Uncapher, C. M. Dewitt, and R. J. Colonno, "The major and minor group receptor families contain all but one human rhinovirus serotype," *Virology*, vol. 180, no. 2, pp. 814–817, 1991.

[406] T. Imamura, M. Okamoto, S.-i. Nakakita, A. Suzuki, M. Saito, R. Tamaki, S. Lupisan, C. N. Roy, H. Hiramatsu, K.-e. E. Sugawara, K. Mizuta, Y. Matsuzaki, Y. Suzuki, and H. Oshitani, "Antigenic and receptor binding properties of enterovirus 68," *J. Virol.*, vol. 88, no. 5, pp. 2374–2384, 2014.

[407] T. Walther, R. Karamanska, R. W. Y. Chan, M. C. W. Chan, N. Jia, G. Air, C. Hopton, M. P. Wong, A. Dell, J. S. Malik Peiris, S. M. Haslam, and J. M. Nicholls, "Glycomic analysis of human respiratory tract tissues and correlation with influenza virus infection," *PLoS Pathog.*, vol. 9, no. 3, p. e1003223, 2013.

[408] C. Xiao and M. G. Rossmann, "Interpretation of electron density with stereographic roadmap projections," *J. Struct. Biol.*, vol. 158, no. 2, pp. 182–187, 2007.

[409] A. M. De Palma, W. Heggermont, P. Leyssen, G. Purstinger, E. Wimmer, E. De Clercq, A. Rao, A. M. Monforte, A. Chimirri, and J. Neyts, "Anti-enterovirus activity and structure-activity relationship of a series of 2,6-dihalophenyl-substituted 1H,3H-thiazolo[3,4-a]benzimidazoles," *Biochem. Biophys. Res. Commun.*, vol. 353, no. 3, pp. 628–632, 2007.

[410] U. Dierssen, F. Rehren, C. Henke-Gendo, G. Harste, and A. Heim, "Rapid routine detection of enterovirus RNA in cerebrospinal fluid by a one-step real-time RT-PCR assay," *J. Clin. Virol.*, vol. 42, no. 1, pp. 58–64, 2008.

[411] K. J. Livak and T. D. Schmittgen, "Analysis of relative gene expression data using real-time quantitative PCR and the 2-DDCT method," *Methods*, vol. 25, no. 4, pp. 402–408, 2001.

[412] J. E. Carette, C. P. Guimaraes, M. Varadarajan, A. S. Park, I. Wuethrich, A. Godarova, M. Kotecki, B. H. Cochran, E. Spooner, H. L. Ploegh, and T. R. Brummelkamp, "Haploid genetic screens in human cells identify host factors used by pathogens," *Science*, vol. 326, no. 5957, pp. 1231–1235, 2009.

[413] U. Neu, J. Bauer, and T. Stehle, "Viruses and sialic acids: rules of engagement," *Curr. Opin. Struct. Biol.*, vol. 21, no. 5, pp. 610–618, 2011.

[414] A. Meijer, K. S. Benschop, G. A. Donker, and H. G. van der Avoort, "Continued seasonal circulation of enterovirus D68 in the Netherlands, 2011-2014.," *Euro surveillance : bulletin Europeen sur les maladies transmissibles = European communicable disease bulletin*, vol. 19, oct 2014.

[415] E. E. Fry, S. M. Lea, T. Jackson, J. W. I. Newman, F. M. Ellard, W. E. Blakemore, R. Abu-Ghazaleh, A. Samuel, A. M. Q. King, and D. I. Stuart, "The structure and function of a foot-and-mouth disease virus-oligosaccharide receptor complex," *EMBO J.*, vol. 18, pp. 543–554, 1999.

[416] L. Zhou, Y. Luo, Y. Wu, J. Tsao, and M. Luo, "Sialylation of the host receptor may modulate entry of demyelinating persistent Theiler's virus," *J. Virol.*, vol. 74, no. 3, pp. 1477–1485, 2000.

[417] E. E. Fry, T. J. Tuthill, K. Harlos, T. S. Walter, D. J. Rowlands, and D. I. Stuart, "Crystal structure of equine rhinitis A virus in complex with its sialic acid receptor," *Journal of General Virology*, vol. 91, pp. 1971–1977, aug 2010.

[418] M. S. Kim and V. R. Racaniello, "Enterovirus 70 receptor utilization is controlled by capsid residues that also regulate host range and cytopathogenicity," *J. Virol.*, vol. 81, no. 16, pp. 8648–8655, 2007.

[419] T. Smura, P. Ylipaasto, P. Klemola, S. Kaijalainen, L. Kyllonen, V. Sordi, L. Piemonti, and M. Roivainen, "Cellular tropism of human enterovirus D species serotypes EV-94, EV-70, and EV-68 in vitro: implications for pathogenesis," *J. Med. Virol.*, vol. 82, no. 11, pp. 1940–1949, 2010.

[420] H. C. Pfeiffer, K. Bragstad, M. K. Skram, H. Dahl, P. K. Knudsen, M. S. Chawla, M. Holberg-Petersen, K. Vainio, S. G. Dudman, A. M. Kran, and A. E. Rojahn, "Two cases of acute severe flaccid myelitis associated with enterovirus D68 infection in children, Norway, autumn 2014," *Euro Surveill.*, vol. 20, no. 10, p. 21062, 2015.

[421] A. L. Greninger, S. N. Naccache, K. Messacar, A. Clayton, G. Yu, S. Somasekar, S. Federman, D. Stryke, C. Anderson, S. Yagi, S. Messenger, D. Wadford, D. Xia, J. P. Watt, K. Van Haren, S. R. Dominguez, C. Glaser, G. Aldrovandi, and C. Y. Chiu, "A novel outbreak enterovirus D68 strain associated with acute flaccid myelitis cases in the USA (2012-14): a retrospective cohort study.," *The Lancet. Infectious diseases*, vol. 15, pp. 671–82, jun 2015.

[422] K. Messacar, T. L. Schreiner, J. A. Maloney, A. Wallace, J. Ludke, M. S. Oberste, W. A. Nix, C. C. Robinson, M. P. Glode, M. J. Abzug, and S. R. Dominguez, "A cluster of acute flaccid paralysis and cranial nerve dysfunction temporally associated with an outbreak of enterovirus D68 in children in Colorado, USA," *Lancet*, vol. 385, no. 9978, pp. 1662–1671, 2015.

[423] M. Lang, A. Mirand, N. Savy, C. Henquell, S. Maridet, R. Perignon, A. Labbe, and H. Peigue-Lafeuille, "Acute flaccid paralysis following enterovirus D68 associated pneumonia, France, 2014.," *Euro Surveillance*, vol. 19, nov 2014.

[424] N. Aliabadi, K. Messacar, D. M. Pastula, C. C. Robinson, E. Leshem, J. J. Sejvar, W. A. Nix, M. S. Oberste, D. R. Feikin, and S. R. Dominguez, "Enterovirus D68 Infection in Children with Acute Flaccid Myelitis, Colorado, USA, 2014," *Emerging Infectious Diseases*, vol. 22, pp. 1387–1394, aug 2016.

[425] J. J. Sejvar, A. S. Lopez, M. M. Cortese, E. Leshem, D. M. Pastula, L. Miller, C. Glaser, A. Kambhampati, K. Shioda, N. Aliabadi, M. Fischer, N. Gregoricus, R. Lanciotti, W. A. Nix, S. K. Sakthivel, D. S. Schmid, J. F. Seward, S. Tong, M. S. Oberste, M. Pallansch, and D. Feikin, "Acute Flaccid Myelitis in the United States, August-December 2014: Results of Nationwide Surveillance.," *Clinical Infectious Diseases*, vol. 63, pp. 737–45, sep 2016.

[426] J. Baggen, H. J. Thibaut, J. Staring, L. T. Jae, Y. Liu, H. Guo, J. J. Slager, J. W. de Bruin, A. L. W. van Vliet, V. A. Blomen, P. Overduin, J. Sheng, C. A. M. de Haan, E. de Vries, A. Meijer, M. G. Rossmann, T. R. Brummelkamp, and F. J. M. van Kuppeveld, "Enterovirus D68 receptor requirements unveiled by haploid genetics," *Proceedings of the National Academy of Sciences*, vol. 113, pp. 1399–1404, feb 2016.

[427] W. Wei, H. Guo, J. Chang, Y. Yu, G. Liu, N. Zhang, S. H. Willard, S. Zheng, and X.-F. Yu, "ICAM-5/Telencephalin Is a Functional Entry Receptor for Enterovirus D68," *Cell Host & Microbe*, vol. 0, pp. 1399–1404, oct 2016.

[428] Y. Liu, M. G. Hill, T. Klose, Z. Chen, K. Watters, Y. A. Bochkov, W. Jiang, A. C. Palmenberg, and M. G. Rossmann, "Atomic structure of a rhinovirus C, a virus species linked to severe childhood asthma," *Proceedings of the National Academy of Sciences*, vol. 113, pp. 8997–9002, aug 2016.

[429] J. M. Hogle, "A 3D framework for understanding enterovirus 71," *Nat Struct Mol Biol*, vol. 19, no. 4, pp. 367–368, 2012.

[430] E. K. Miller, N. Khuri-Bulos, J. V. Williams, A. A. Shehabi, S. Faouri, I. Al Jundi, Q. Chen, L. Heil, Y. Mohamed, L. L. Morin, A. Ali, and N. B. Halasa, "Human rhinovirus C associated with wheezing in hospitalised children in the Middle East," *J Clin Virol*, vol. 46, no. 1, pp. 85–89, 2009.

[431] J. Bizzintino, W.-M. Lee, I. A. Laing, F. Vang, T. Pappas, G. Zhang, A. C. Martin, S.-K. Khoo, D. W. Cox, G. C. Geelhoed, P. C. McMinn, J. Goldblatt, J. E. Gern, and P. N. Le Souef, "Association between human rhinovirus C and severity of acute asthma in children.," *The European respiratory journal*, vol. 37, pp. 1037–1042, may 2011.

[432] Y. A. Bochkov, K. Watters, S. Ashraf, T. F. Griggs, M. K. Devries, D. J. Jackson, A. C. Palmenberg, and J. E. Gern, "Cadherin-related family member 3, a childhood asthma susceptibility gene product, mediates rhinovirus C binding and replication," *Proc Natl Acad Sci U S A*, vol. 112, pp. 5485–5490, apr 2015.

[433] K. Bonnelykke, P. Sleiman, K. Nielsen, E. Kreiner-Moller, J. M. Mercader, D. Belgrave, H. T. den Dekker, A. Husby, A. Sevelsted, G. Faura-Tellez, L. J. Mortensen, L. Paternoster, R. Flaaten, A. Molgaard, D. E. Smart, P. F. Thomsen, M. A. Rasmussen, S. Bonas-Guarch, C. Holst, E. A. Nohr, R. Yadav, M. E. March, T. Blicher, P. M. Lackie, V. W. Jaddoe, A. Simpson, J. W. Holloway, L. Duijts, A. Custovic, D. E. Davies, D. Torrents, R. Gupta, M. V. Hollegaard, D. M. Hougaard, H. Hakonarson, and H. Bisgaard, "A genome-wide association study identifies CDHR3 as a susceptibility locus for early childhood asthma with severe exacerbations," *Nat Genet*, vol. 46, no. 1, pp. 51–55, 2014.

[434] A. Piralla, F. Rovida, G. Campanini, V. Rognoni, A. Marchi, F. Locatelli, and G. Gerna, "Clinical severity and molecular typing of human rhinovirus C strains during a fall outbreak affecting hospitalized patients," *J Clin Virol*, vol. 45, no. 4, pp. 311–317, 2009.

[435] L. Royston and C. Tapparel, "Rhinoviruses and Respiratory Enteroviruses: Not as Simple as ABC," *Viruses*, vol. 8, p. 16, jan 2016.

[436] K. E. Arden, P. McErlean, M. D. Nissen, T. P. Sloots, and I. M. Mackay, "Frequent detection of human rhinoviruses, paramyxoviruses, coronaviruses, and bocavirus during acute respiratory tract infections," *J Med Virol*, vol. 78, no. 9, pp. 1232–1240, 2006.

[437] Y. A. Bochkov, A. C. Palmenberg, W. M. Lee, J. A. Rathe, S. P. Amineva, X. Sun, T. R. Pasic, N. N. Jarjour, S. B. Liggett, and J. E. Gern, "Molecular modeling, organ culture and reverse genetics for a newly identified human rhinovirus C," *Nat Med*, vol. 17, no. 5, pp. 627–632, 2011.

[438] H. A. Basta, S. Ashraf, J.-Y. Y. Sgro, Y. A. Bochkov, J. E. Gern, and A. C. Palmenberg, "Modeling of the human rhinovirus C capsid suggests possible causes for antiviral drug resistance," *Virology*, vol. 448, pp. 82–90, jan 2014.

[439] H. A. Basta, J. Y. Sgro, and A. C. Palmenberg, "Modeling of the human rhinovirus C capsid suggests a novel topography with insights on receptor preference and immunogenicity," *Virology*, vol. 448, pp. 176–184, 2014.

[440] P. McErlean, L. A. Shackelton, E. Andrews, D. R. Webster, S. B. Lambert, M. D. Nissen, T. P. Sloots, and I. M. Mackay, "Distinguishing molecular features and clinical characteristics of a putative new rhinovirus species, human rhinovirus C (HRV C).," *PloS one*, vol. 3, p. e1847, apr 2008.

[441] E. Nogales, "The development of cryo-EM into a mainstream structural biology technique," *Nature Methods*, vol. 13, pp. 24–27, dec 2015.

[442] T. F. Griggs, Y. A. Bochkov, K. Nakagome, A. C. Palmenberg, and J. E. Gern, "Production, purification, and capsid stability of rhinovirus C types.," *Journal of virological methods*, vol. 217, pp. 18–23, jun 2015.

[443] G. C. Lander, S. M. Stagg, N. R. Voss, A. Cheng, D. Fellmann, J. Pulokas, C. Yoshioka, C. Irving, A. Mulder, P. W. Lau, D. Lyumkis, C. S. Potter, and B. Carragher, "Appion: an integrated, database-driven pipeline to facilitate EM image processing," *J Struct Biol*, vol. 166, no. 1, pp. 95–102, 2009.

[444] J. A. Mindell and N. Grigorieff, "Accurate determination of local defocus and specimen tilt in electron microscopy," *J Struct Biol*, vol. 142, no. 3, pp. 334–347, 2003.

[445] N. R. Voss, C. K. Yoshioka, M. Radermacher, C. S. Potter, and B. Carragher, "DoG Picker and TiltPicker: software tools to facilitate particle selection in single particle electron microscopy," *J Struct Biol*, vol. 166, no. 2, pp. 205–213, 2009.

[446] Z. Liu, F. Guo, F. Wang, T.-C. Li, and W. Jiang, "2.9 Å Resolution Cryo-EM 3D Reconstruction of Close-Packed Virus Particles.," *Structure (London, England : 1993)*, vol. 24, pp. 319–28, feb 2016.

[447] W. Jiang, F. Guo, and Z. Liu, "A graph theory method for determination of cryo-EM image focuses," *J Struct Biol*, vol. 180, no. 2, pp. 343–351, 2012.

[448] T. Grant and N. Grigorieff, "Automatic estimation and correction of anisotropic magnification distortion in electron microscopes," *J Struct Biol*, vol. 192, no. 2, pp. 204–208, 2015.

[449] G. Yu, K. Li, Y. Liu, Z. Chen, Z. Wang, R. Yan, T. Klose, L. Tang, and W. Jiang, "An algorithm for estimation and correction of anisotropic magnification distortion of cryo-EM images without need of pre-calibration," *Journal of structural biology*, 2016.

[450] W. O. Saxton and W. Baumeister, "The correlation averaging of a regularly arranged bacterial cell envelope protein," *Journal of Microscopy*, vol. 127, pp. 127–138, aug 1982.

[451] M. van Heel and M. Stöffler-Meilicke, "Characteristic views of E. coli and B. stearothermophilus 30S ribosomal subunits in the electron microscope.," *The EMBO journal*, vol. 4, pp. 2389–95, sep 1985.

[452] P. B. Rosenthal and R. Henderson, "Optimal determination of particle orientation, absolute hand, and contrast loss in single-particle electron cryomicroscopy," *Journal of Molecular Biology*, vol. 333, no. 4, pp. 721–745, 2003.

[453] S. H. W. Scheres and S. Chen, "Prevention of overfitting in cryo-EM structure determination," *Nature Methods*, vol. 9, no. 9, pp. 853–854, 2012.

[454] S. Chen, G. McMullan, A. R. Faruqi, G. N. Murshudov, J. M. Short, S. H. Scheres, and R. Henderson, "High-resolution noise substitution to measure overfitting and validate resolution in 3D structure determination by single particle electron cryomicroscopy," *Ultramicroscopy*, vol. 135, pp. 24–35, 2013.

[455] S. Jonić, "Cryo-electron Microscopy Analysis of Structurally Heterogeneous Macromolecular Complexes," *Computational and Structural Biotechnology Journal*, vol. 14, pp. 385–390, 2016.

[456] C. C. Holm-Hansen, S. E. Midgley, and T. K. Fischer, "Global emergence of enterovirus D68: a systematic review," *The Lancet Infectious Diseases*, vol. 16, pp. e64–e75, may 2016.

[457] J. M. Rogers, G. D. Diana, and M. A. McKinlay, "Pleconaril. A broad spectrum antipicornaviral agent," *Adv. Exp. Med. Biol.*, vol. 458, pp. 69–76, 1999.

[458] M. Luo, G. Vriend, G. Kamer, I. Minor, E. Arnold, M. G. Rossmann, U. Boege, D. G. Scraba, G. M. Duke, and A. C. Palmenberg, "The atomic structure of Mengo virus at 3.0 A resolution," *Science*, vol. 235, no. 4785, pp. 182–191, 1987.

[459] J. E. Gern, "How rhinovirus infections cause exacerbations of asthma," *Clinical & Experimental Allergy*, vol. 45, pp. 32–42, jan 2015.

[460] J. E. Gern, A. G. Mosser, C. A. Swenson, P. J. Rennie, R. J. England, J. Shaffer, and H. Mizoguchi, "Inhibition of rhinovirus replication in vitro and in vivo by acid-buffered saline," *J Infect Dis*, vol. 195, no. 8, pp. 1137–1143, 2007.

[461] B. D. Korant, K. Lonberg-Holm, J. Noble, and J. T. Stasny, "Naturally occurring and artificially produced components of three rhinoviruses," *Virology*, vol. 48, no. 1, pp. 71–86, 1972.

[462] V. L. Giranda, B. A. Heinz, M. A. Oliveira, I. Minor, K. H. Kim, P. R. Kolatkar, M. G. Rossmann, and R. R. Rueckert, "Acid-induced structural changes in human rhinovirus 14: possible role in uncoating," *Proc Natl Acad Sci U S A*, vol. 89, no. 21, pp. 10213–10217, 1992.

[463] R. Fuchs and D. Blaas, "Uncoating of human rhinoviruses," *Rev Med Virol*, vol. 20, pp. 281–297, sep 2010.

[464] F. M. Ellard, J. Drew, W. E. Blakemore, D. I. Stuart, and A. M. King, "Evidence for the role of His-142 of protein 1C in the acid-induced disassembly of foot-and-mouth disease virus capsids.," *The Journal of general virology*, vol. 80 (Pt 8), pp. 1911–8, aug 1999.

[465] J. Warwicker, "Model for the differential stabilities of rhinovirus and poliovirus to mild acidic pH, based on electrostatics calculations.," *Journal of molecular biology*, vol. 223, pp. 247–57, jan 1992.

[466] F. G. Hayden, D. T. Herrington, T. L. Coats, K. Kim, E. C. Cooper, S. A. Villano, S. Liu, S. Hudson, D. C. Pevear, M. Collett, and M. McKinlay, "Efficacy and Safety of Oral Pleconaril for Treatment of Colds Due to Picornaviruses in Adults: Results of 2 Double-Blind, Randomized, Placebo-Controlled Trials," *Clinical Infectious Diseases*, vol. 36, pp. 1523–1532, jun 2003.

[467] M. S. Oberste, D. Moore, B. Anderson, M. A. Pallansch, D. C. Pevear, and M. S. Collett, "In vitro antiviral activity of V-073 against polioviruses," *Antimicrob Agents Chemother*, vol. 53, no. 10, pp. 4501–4503, 2009.

[468] G. M. Morris, R. Huey, W. Lindstrom, M. F. Sanner, R. K. Belew, D. S. Goodsell, and A. J. Olson, "AutoDock4 and AutoDockTools4: Automated docking with selective receptor flexibility.," *Journal of computational chemistry*, vol. 30, pp. 2785–91, dec 2009.

[469] E. E. Bolton, Y. Wang, P. A. Thiessen, and S. H. Bryant, "Chapter 12 PubChem: Integrated Platform of Small Molecules and Biological Activities," in *Annual Reports in Computational Chemistry*, vol. 4, pp. 217–241, 2008.

[470] G. M. Morris, D. S. Goodsell, R. S. Halliday, R. Huey, W. E. Hart, R. K. Belew, and A. J. Olson, "Automated docking using a Lamarckian genetic algorithm and an empirical binding free energy function," *Journal of Computational Chemistry*, vol. 19, pp. 1639–1662, nov 1998.

[471] T. S. Walter, J. Ren, T. J. Tuthill, D. J. Rowlands, D. I. Stuart, and E. E. Fry, "A plate-based high-throughput assay for virus stability and vaccine formulation.," *Journal of virological methods*, vol. 185, pp. 166–70, oct 2012.

[472] P. Plevka, P.-Y. Lim, R. Perera, J. Cardosa, A. Suksatu, R. J. Kuhn, and M. G. Rossmann, "Neutralizing antibodies can initiate genome release from human enterovirus 71.," *Proceedings of the National Academy of Sciences of the United States of America*, vol. 111, pp. 2134–9, feb 2014.

[473] D. L. Barnard, V. D. Hubbard, D. F. Smee, R. W. Sidwell, K. G. Watson, S. P. Tucker, and P. A. Reece, "In vitro activity of expanded-spectrum pyridazinyl oxime ethers related to pirodavir: novel capsid-binding inhibitors with potent antipicornavirus activity," *Antimicrob. Agents Chemother.*, vol. 48, no. 5, pp. 1766–1772, 2004.

[474] D. C. Pevear, F. G. Hayden, T. M. Demenczuk, L. R. Barone, M. A. McKinlay, and M. S. Collett, "Relationship of pleconaril susceptibility and clinical outcomes in treatment of common colds caused by rhinoviruses.," *Antimicrobial agents and chemotherapy*, vol. 49, pp. 4492–9, nov 2005.

[475] K. G. Watson, R. N. Brown, R. Cameron, D. K. Chalmers, S. Hamilton, B. Jin, G. Y. Krippner, A. Luttick, D. B. McConnell, P. A. Reece, J. Ryan, P. C. Stanislawski, S. P. Tucker, W.-Y. Wu, D. L. Barnard, and R. W. Sidwell, "An orally bioavailable oxime ether capsid binder with potent activity against human rhinovirus.," *Journal of medicinal chemistry*, vol. 46, pp. 3181–4, jul 2003.

[476] K. Andries, B. Dewindt, J. Snoeks, R. Willebrords, K. van Eemeren, R. Stokbroekx, and P. A. Janssen, "In vitro activity of pirodavir (R 77975), a substituted phenoxy-pyridazinamine with broad-spectrum antipicornaviral activity.," *Antimicrobial agents and chemotherapy*, vol. 36, pp. 100–7, jan 1992.

[477] L. Sun, A. Meijer, M. Froeyen, L. Zhang, H. J. Thibaut, J. Baggen, S. George, J. Vernachio, F. J. M. van Kuppeveld, P. Leyssen, R. Hilgenfeld, J. Neyts, and L. Delang, "Antiviral Activity of Broad-Spectrum and Enterovirus-Specific Inhibitors against Clinical Isolates of Enterovirus D68," *Antimicrobial Agents and Chemotherapy*, vol. 59, pp. 7782–7785, dec 2015.

[478] E. Rhoden, M. Zhang, W. A. Nix, and M. S. Oberste, "In Vitro Efficacy of Antiviral Compounds against Enterovirus D68," *Antimicrobial Agents and Chemotherapy*, vol. 59, pp. 7779–7781, dec 2015.

[479] D. F. Smee, W. J. Evans, K. Nicolaou, E. B. Tarbet, and C. W. Day, "Susceptibilities of enterovirus D68, enterovirus 71, and rhinovirus 87 strains to various antiviral compounds," *Antiviral Research*, vol. 131, pp. 61–65, jul 2016.

[480] N. J. Schmidt, E. H. Lennette, and H. H. Ho, "An apparently new enterovirus isolated from patients with disease of the central nervous system.," *The Journal of infectious diseases*, vol. 129, pp. 304–9, mar 1974.

[481] C. C. Y. Yip, S. K. P. Lau, P. C. Y. Woo, and K.-Y. Y. Yuen, "Human enterovirus 71 epidemics: what's next?," *Emerg Health Threats J*, vol. 6, p. 19780, 2013.

[482] S.-L. Yang, Y.-T. Chou, C.-N. Wu, and M.-S. Ho, "Annexin II binds to capsid protein VP1 of enterovirus 71 and enhances viral infectivity.," *Journal of virology*, vol. 85, pp. 11809–20, nov 2011.

[483] N. Du, H. Cong, H. Tian, H. Zhang, W. Zhang, L. Song, and P. Tien, "Cell surface vimentin is an attachment receptor for enterovirus 71," *J Virol*, vol. 88, no. 10, pp. 5816–5833, 2014.

[484] P.-Y. Su, Y.-F. Wang, S.-W. Huang, Y.-C. Lo, Y.-H. Wang, S.-R. Wu, D.-B. Shieh, S.-H. Chen, J.-R. Wang, M.-D. Lai, and C.-F. Chang, "Cell surface nucleolin facilitates enterovirus 71 binding and infection.," *Journal of virology*, vol. 89, pp. 4527–38, apr 2015.

[485] S. Yamayoshi, S. Iizuka, T. Yamashita, H. Minagawa, K. Mizuta, M. Okamoto, H. Nishimura, K. Sanjoh, N. Katsushima, T. Itagaki, Y. Nagai, K. Fujii, and S. Koike, "Human SCARB2-dependent infection by coxsackievirus A7, A14, and A16 and enterovirus 71," *J Virol*, vol. 86, pp. 5686–5696, may 2012.

[486] P. Yu, Z. Gao, Y. Zong, L. Bao, L. Xu, W. Deng, F. Li, Q. Lv, Z. Gao, Y. Xu, Y. Yao, and C. Qin, "Histopathological features and distribution of EV71 antigens and SCARB2 in human fatal cases and a mouse model of enterovirus 71 infection," *Virus Research*, vol. 189, pp. 121–132, 2014.

[487] D. Neculai, M. Schwake, M. Ravichandran, F. Zunke, R. F. Collins, J. Peters, M. Neculai, J. Plumb, P. Loppnau, J. C. Pizarro, A. Seitova, W. S. Trimble, P. Saftig, S. Grinstein, and S. Dhe-Paganon, "Structure of LIMP-2 provides functional insights with implications for SR-BI and CD36.," *Nature*, vol. 504, pp. 172–6, dec 2013.

[488] Y. Zhao, J. Ren, S. Padilla-Parra, E. E. Fry, and D. I. Stuart, "Lysosome sorting of β-glucocerebrosidase by LIMP-2 is targeted by the mannose 6-phosphate receptor," *Nature Communications*, vol. 5, jul 2014.

[489] S. Yamayoshi and S. Koike, "Identification of a human SCARB2 region that is important for enterovirus 71 binding and infection," *J Virol*, vol. 85, pp. 4937–4946, may 2011.

[490] A. R. Aricescu, W. Lu, and E. Y. Jones, "A time- and cost-efficient system for high-level protein production in mammalian cells.," *Acta crystallographica. Section D, Biological crystallography*, vol. 62, pp. 1243–50, oct 2006.

[491] D. F. Kelly, D. Dukovski, and T. Walz, "Strategy for the use of affinity grids to prepare non-his-tagged macromolecular complexes for single-particle electron microscopy," *Journal of Molecular Biology*, vol. 400, no. 4, pp. 675–681, 2010.

[492] G. Yu, F. Vago, D. Zhang, J. E. Snyder, R. Yan, C. Zhang, C. Benjamin, X. Jiang, R. J. Kuhn, P. Serwer, D. H. Thompson, and W. Jiang, "Single-step antibody-based affinity cryo-electron microscopy for imaging and structural analysis of macromolecular assemblies," *J Struct Biol*, vol. 187, no. 1, pp. 1–9, 2014.

APPENDIX

A. INTERACTIONS OF ENTEROVIRUS A71 WITH HUMAN SCAVENGER RECEPTOR B2

Part of the text in this chapter is taken verbatim from [1] and is highlighted by a black, vertical line in the right margin below.

A.1 Introduction

Enterovirus A71 (EV-A71) was first isolated from patients with neurological diseases in California in 1969 [480]. It is one of the major causative agents of hand, foot and mouth disease (HFMD) in infants and young children. It is also notable for severe neurological complications, such as acute flaccid paralysis, aseptic meningitis and encephalitis [481]. It also occasionally leads to fatal cases [481]. Recently, frequent outbreaks have been reported particularly in Asia-Pacific region, raising significant public health concerns [481]. Although there is no antiviral intervention available, two vaccines using heat-inactivated whole virions have been approved for prevention of EV-A71 infections among children in China [72, 73].

Over the last few years, a number of cellular receptors and attachment factors have been identified for EV-A71, including hSCARB2 (human scavenger receptor B2), PSGL-1 (P-selectin glycoprotein ligand 1), heparan sulfate, sialylated glycans, annexin II, vimentin, and nucleolin [164–166, 168, 169, 482–484]. These cell surface molecules were shown to be indispensable for or only enhance EV71 infection in cell culture. Specifically, hSCARB2 is a functional receptor for a broad range of EV-A71 strains [485]. It is expressed in a variety of human tissues, including neurons in the central nervous system [486]. In addition, EV-A71 can not use mouse SCARB2 as a receptor [165]. Thus, SCARB2 is a host factor that impacts the host range, tissue tropism, and pathogenesis of EV-A71. More importantly, hSCARB2 plays crucial

roles in virus attachment onto host cell surface, internalization through clathrin-dependent endocytosis, and virus uncoating [193, 194, 199, 485]. In contrast, other receptors or attachment factors have not been shown to induce EV-A71 uncoating [194].

hSCARB2 is a glycoprotein also known as lysosomal integral membrane protein II, which is an abundant protein in lysosomes [487]. It normally functions as a trafficking receptor of beta-glucocerebrosidase, an important enzyme for glycolipid metabolism. hSCARB2 is a type-III transmembrane protein with both termini spanning across the membrane. It contains a large ectodomain (about 400 amino acids) when being present on the plasma membrane (or a large lumenal domain when residing on the lysosome membrane). The crystal structure of the hSCARB2 ectodomain showed a twisted beta barrel core with an internal tunnel traversing the whole length of the molecule [192, 487, 488]. Thus, hSCARB2 is structurally different from many known EV receptors that possess repeated Ig-like domains [183]. Nevertheless, similar to the interactions of Ig-like receptors with respective EVs, hSCARB2 was suggested to bind into the canyon region of EV-A71, despite that the EV-A71 canyon is shallower than many other EVs [30, 31]. Moreover, hSCARB2 triggers EV-A71 uncoating at low-pH conditions [192–194].

Mutagenesis studies showed that residues 144-151 of a three-helix bundle at the head region of hSCARB2 are directly involved in EV71 binding according to two independent studies [193, 489]. Nevertheless, there is some uncertainty whether there are also other residues involved in virus attachment. It is also not known how glycans on hSCARB2 contribute to virus-receptor binding. Moreover, the three-helix bundle undergoes a pH-dependent conformational change and possibly regulates the accessibility of the entrance to the aforementioned internal tunnel, which was proposed to function as a lipid-transfer tunnel [192]. However, it remains obscure how such structural changes influence hSCARB2 induced EV-A71 uncoating at acidic conditions.

This chapter describes current progress towards a structural study of EV-A71 in complex with hSCARB2. A major challenge of this study is that aggregates were

formed when purified EV-A71 were incubated with purified hSCARB2. This was shown by two former members of the Rossmann laboratory, Dr. Pavel Plevka and Dr. Steffanie Becker. Therefore, the major focuses of this chapter are analyzing the interactions of purified EV-A71 with recombinant hSCARB2 proteins and forming a virus-receptor complex *in vitro* that is suitable for cryo-EM structure determination.

A.2 Materials and Methods

A.2.1 Cells and viruses

SF9 cells (*Spodoptera frugiperda*) were kindly provided by Jue Chen (Rockefeller University, US). These cells were maintained in Sf-900 III serum free medium (Gibco) and incubated in a shaker at 27°C with a speed of 125 rpm. Human embryonic kidney (HEK) 293T cells (ATCC CRL-11268) were maintained in DMEM supplemented with 10% FBS and NEAA. These cells were grown at 37°C with 5% CO_2. Stock recommbinant baculoviruses for hSCARB2-Fc-His expression and for His-hSCARB2 expression were supplied by Ian Jones (University of Reading, UK) and by Sergio Grinstein (University of Toronto, Canada), receptively. To amplify recombinant baculoviruses for one more passage from the stock virus, SF9 cells (at 1.5-2.0 million cells/ml) were inoculated with stock virus. At about 3 days post infection, supernatants were harvested after spinning down the culture and stored at 4°C.

A.2.2 Virus growth and purification

Growth and purification of EV-A71 was performed using a similar protocol described for EV-D68 in Chapter 2. The only modification was that EV-A71 (strain MY104-9-SAR-97) infect RD cells at 37°C rather than at 33°C.

A.2.3 Cloning

To produce the construct hSCARB2-His-Monomer, the ectodomain of hSCARB2 (residues 28-431) was cloned from the template pCAGGS-hSCARB2-F into the pHLsec vector [490]. pCAGGS-hSCARB2-F is a construct that encodes full length hSCARB2 with a C-terminal FLAG-tag. It was kindly supplied by Satoshi Koike (Tokyo Metropolitan Institute of Medical Science, Japan). The pHLsec vector was kindly provided by Yuguang Zhao (Oxford University, UK). Briefly, the cloning procedure included the following steps. DNA that encodes the ectodomain of hSCARB2 was obtained by PCR using the plasmid pCAGGS-hSCARB2-F as a template. The two primers were 5'-ATACCGGTGTCTTCCAGAAGGCTGTAG-3'(forward) and 5'-ATAGGTACCAGTGTTAATCATAGACTTC-3'(reverse). The DNA fragment and pHLsec vector were independently digested using restriction enzymes *Age*I and *Kpn*I. The resultant insert and linearized vector were ligated. The ligation product was then transformed into NovaBlue Singles competent cells (Novagen). Single colonies were picked up, and cell culture was scaled up for plasmid extraction. The plasmid was used for sequencing which confirmed the correctness of inserted sequences.

A.2.4 Protein expression and purification

For expression of hSCARB2-Fc-His or His-hSCARB2, SF9 cells (at 2.5-3.0 million cells/ml) were inoculated with their respective recombinant baculoviruses. At about 3 days post infection, cell viability dropped down from more than 98% (before infection) to about 50%. Supernantants were harvested after spinning down the culture. About 80 ml of 10X buffer A was added to 1000 ml of supernatant. 1X buffer A refers to 50 mM HEPES, 500 mM NaCl, 1 mM imidazole (pH 7.5), where HEPES is short for 4-(2-hydroxyethyl)-1-piperazineethanesulfonic acid. The adjusted supernatant was then incubated with about 5 ml of Ni-NTA (nickel-nitrilotriacetic acid) agarose beads (Qiagen) in a shaker at 80 rpm and 4°C, where the beads had been pre-equilibrated with 1X buffer A. Beads were collected into a gravity flow column and washed with

1X buffer A and then 20 mM imidazole in 1X buffer A. The proteins were eluted with 400 mM imidazole in 1X buffer A. After concentration, the proteins were loaded onto a size exclusion chromatographic column, Hiload 16/600 Superdex 200 pg or Superdex 200 10/300 GL (GE Health), for further purification. The resultant fractions were analyzed by SDS-PAGE.

hSCARB2-His-Monomer was expressed using a transient mammalian cell expression system. Protein expression level was first monitored for a small scale test by western blot analysis, which allowed for optimization of the protein production yield. The primary and secondary antibodies were Mouse Anti-6X His (Genescript) and Goat Anti-Mouse antibody conjugated with an infrared fluorescent dye (hereafter, the secondary antibody is named as GαM800) that has an emission peak at close to 800 nm (LI-COR), respectively. Fluorescent intensities were recorded using an Odyssey imaging system. For large scale expression, about 60% confluent 293T cells were transfected with the plasmid DNA that was pre-complexed with the transfection reagent PEI (polyethylenimine). For each 150mm dish, about 15μg plasmid was used, and the ratio of plasmid to PEI was about 1:5. Supernatants were harvested at about 4 days post transfection. Purification procedures were similar to those for the two recombinant hSCARB2 forms mentioned above. Essentially, immobilized nickel affinity chromatography and size exclusion chromatography were employed. The yield was about 10-15 mg purified proteins per 500 ml culture.

For expression of hSCARB2-F, 297T cells were similarly transfected with the plasmid DNA using PEI as the transfection reagent. At about 48h post transfection, all cells became detached. Proteins were purified per protocol offered by Satoshi Koike. Briefly, after the culture was spun down, cell pellets were lysed in NTE buffer (20 mM Tris, 120 mM NaCl, 1 mM EDTA, pH 8.0) with 1% (v/v) Triton X-100 (Sigma), where Tris stands for tris(hydroxymethyl)aminomethane and EDTA stands for ethylenediaminetetraacetic acid. The resultant mixture was spun down, and the supernatant was used for immunoaffinity chromatography. Essentially, the supernatant was incubated Anti-FLAG M1 beads (Sigma) in the presence of calcium cations (10 mM).

After centrifugation and subsequently washing the beads, the proteins were eluted from the beads using FLAG peptides (Sigma) in NTE buffer with 0.05% (v/v) NP-40 (Sigma). NP-40 interferes with the UV absorbance of protein at the wavelength of 280 nm. Thus protein concentration was assayed using Coomassie brilliant blue R-250 dye that detects the presence of proteins and using BSA as a reference protein.

A.2.5 Enzyme-linked immunosorbent assay

Purified EV-A71 virions (with concentrations ranging from 0-9 μg/ml) in PBS were coated onto a NUNC MaxiSorp 96-well plate (NUNC Inc.) at 4°C for overnight. After washing with PBS and then blocking with blocking solution (2% (w/v) BSA in PBS), wells were incubated at 4°C] for 1h with His-hSCARB2, PSGL-1-Fc, hSCARB2-Fc-His, or hSCARB2-His-Monomer, all of which had a concentration of 20 μg/ml and were in PBS with 1% (w/v) BSA. PSGL-1-Fc, a recombinant PSGL-1, had been shown to bind EV-A71 and was kindly provided by Ian Jones. Then the plate was washed with PBS for multiple times. The bound receptors were detected by the primary antibody Mouse Anti-6X His (at a dilution of 1:750) and then by the secondary antibody Goat Anti-Mouse conjugated with alkaline phosphatase (Promega) (at a dilution of 1:6000). After washing out unbound secondary antibodies, the activity of bound secondary antibodies were assayed using the substrate para-nitrophenyl phosphate in 1M ethanolamine and 0.5 mM $MgCl_2$ (pH 9.8). The absorbance of the product para-nitrophenol in each well was recorded at a wavelength of 405 nm using a SpectraMax M5 Microplate Reader (Molecular Devices). Experiments were performed in triplicates. Non-specific binding of either the primary antibody or the secondary antibody to coated virions was also assessed by including a series of negative controls. Coating of different concentrations of virions onto the plate was verified by using Mouse Anti-EV-A71-VP1 (2 μg/mL, antibodies-online Inc.).

A.2.6 Electron microscopy of negatively stained particles

Purified EV-A71 virions were incubated with or without hSCARB2-Fc-His (molar ratio of receptor to virus was around 120:1) under in 20 mM citrate-phosphate buffer with 150 mM NaCl (pH 4.5) at 4°C for 1h, subsequently at 37°C for 1.5h and sonication (using an ultrasonic bath) for 3 min. For EM sample preparation, about 2.5 μl of sample was applied onto a thin layer of continuous carbon film supported by an EM grid and incubated for about 2 min at room temperature. Excessive sample was washed away with a large drop (about 8 μl) of 2% (w/v) uranyl acetate (pH about 4.5), followed by blotting. The grid was air dried and subsequently examined with a Phillips CM200 microscope (FEI) operated at an accelerating voltage of 200 kV. Electron micrographs were recorded at a nominal magnification of 38,000x using a 1K x 1K CCD camera.

A.3 Results and Discussion

Initial screening using electron microscopy of negatively stained particles was performed with three forms of recombinant hSCARB2. These were hSCARB2-F (full length hSCARB2 residues 1-478 with a C-terminal FLAG-tag), hSCARB2-Fc-His (hSCARB2 ectodomain residues 30-434 with a C-terminal human IgG1 Fc-tag followed by a 6X His-tag), and His-SCARB2 (hSCARB2 ectodomain residues 35-430 with an N-terminal 6 X His-tag). Electron micrographs showed that hSCARB2-Fc-His induced EV-A71 uncoating under an acidic condition (pH 4.5) (Fig. A.1). This observation suggested that hSCARB2-Fc-His is capable of binding EV-A71. hSCARB2-Fc-His was predicted to be a dimeric protein based on gel filtration profile (Fig. A.1). Nevertheless, His-hSCARB2 was not able cause aggregation of EV-A71. Cryo-EM analysis of EV-A71 after incubation with His-hSCARB2 at 4°C for 2 min showed no significant densities of bound His-hSCARB2 on the virus surface in the reconstruction. These results suggested that His-hSCARB2 failed to bind EV-A71. Furthermore, the production of hSCARB2-F, a membrane protein, had a low yield.

Preliminary test with different kinds of detergents, including NP-40 and Tween-20, indicated that they either impaired virus-receptor interactions or deteriorated the contrast of cryo-EM images.

The dimeric hSCARB2-Fc-His proteins probably cross link EV-A71 particles, resulting in the observed aggregation of the virus. Additionally, glycans on hSCARB2-Fc-His (derived from insect cells) might not be favorable for virus-receptor binding [192, 489]. Thus, a new construct, hSCARB2-His-Monomer, was designed, which included the SCARB2 ectodomain (residues 28-431) and a C-terminal 6 x His-tag. The protein was expressed in mammalian cells and purified to yield monomeric hSCARB2, as was predicted based on gel filtration profile (Fig. A.2). ELISA analysis showed that hSCARB2-His-Monomer (as also PSGL-1-Fc) can bind to EV-A71, whereas binding of hSCARB2-Fc-His with EV-A71 appeared to be fairly weak (Fig. A.2). In contrast, His-hSCARB2 can not bind EV-A71, which is consistent with the aforementioned cryo-EM analysis. Thus, hSCARB2-His-Monomer is a candidate recombinant receptor that may alleviate the aggregation problem.

An early study reported that EV-A71 viruses tend to form aggregates [480]. Receptor triggered confromational change of the virus is probably also a reason that explains hSCARB2 induced EV-A71 aggregation. Furthermore, the usual molar ratio of hSCARB2 to EV-A71 in solution is more than 60:1. It is also probable that excessive receptor is a factor that accounts for aggregation. Thus, there exist a few potential approaches to work around the aggregation issue. Addition of sodium deoxycholate, a reagent known for clearing EV-A71 aggregation [480], might be helpful. Alternatively, inclusion of capsid binding inhibitors (e.g., pirodavir [476]), may prevent unnecessary conformational changes but still maintain virus-receptor interactions. Another potential method is to take advantage of the recently developed antibody-based affinity grid [491, 492]. The idea is to fix individual EV71 virions with EV-A71 antibodies prior to complexing the virus with recombinant hSCARB2. Finally, hSCARB2 might be incorporated into artificial membrane systems such as

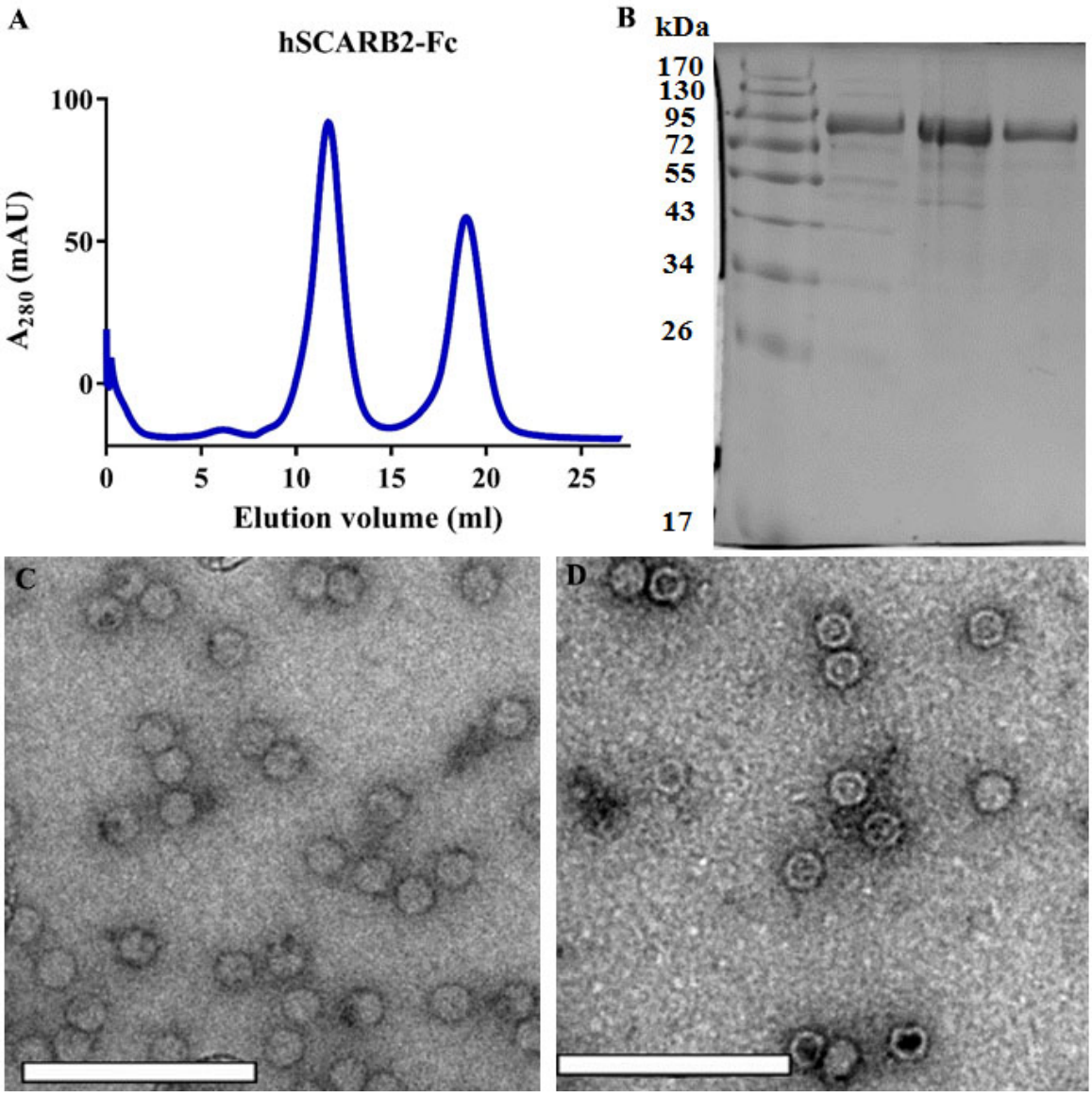

Fig. A.1. **hSCARB2-Fc induces EV-A71 uncoating at low pH.** **A.** Size exclusion chromatographic profile of hSCARB2-Fc-His using a Superdex 200 column shows an estimated dimeric form of the protein. **B.** SDS-PAGE analysis of hSCARB2-Fc-His. Fractions of the left peak (at 11.7 ml) on the gel filtration profile was pooled up and concentrated to yield the final protein (lane 4 from the left). Lanes 2-3 represent samples before gel filtration. **C-D.** Electron micrographs of negative stained EV-A71 particles. **C.** EV-A71 alone was incubated under pH 4.5 at 4°C for 1 h and then at 37°C for 1.5 h. **D.** EV-A71 and hSCARB2-Fc-His were incubated under pH 4.5 at 4°C for 1 h and then at 37 °C for 1.5 h. Scale bar: 200 nm.

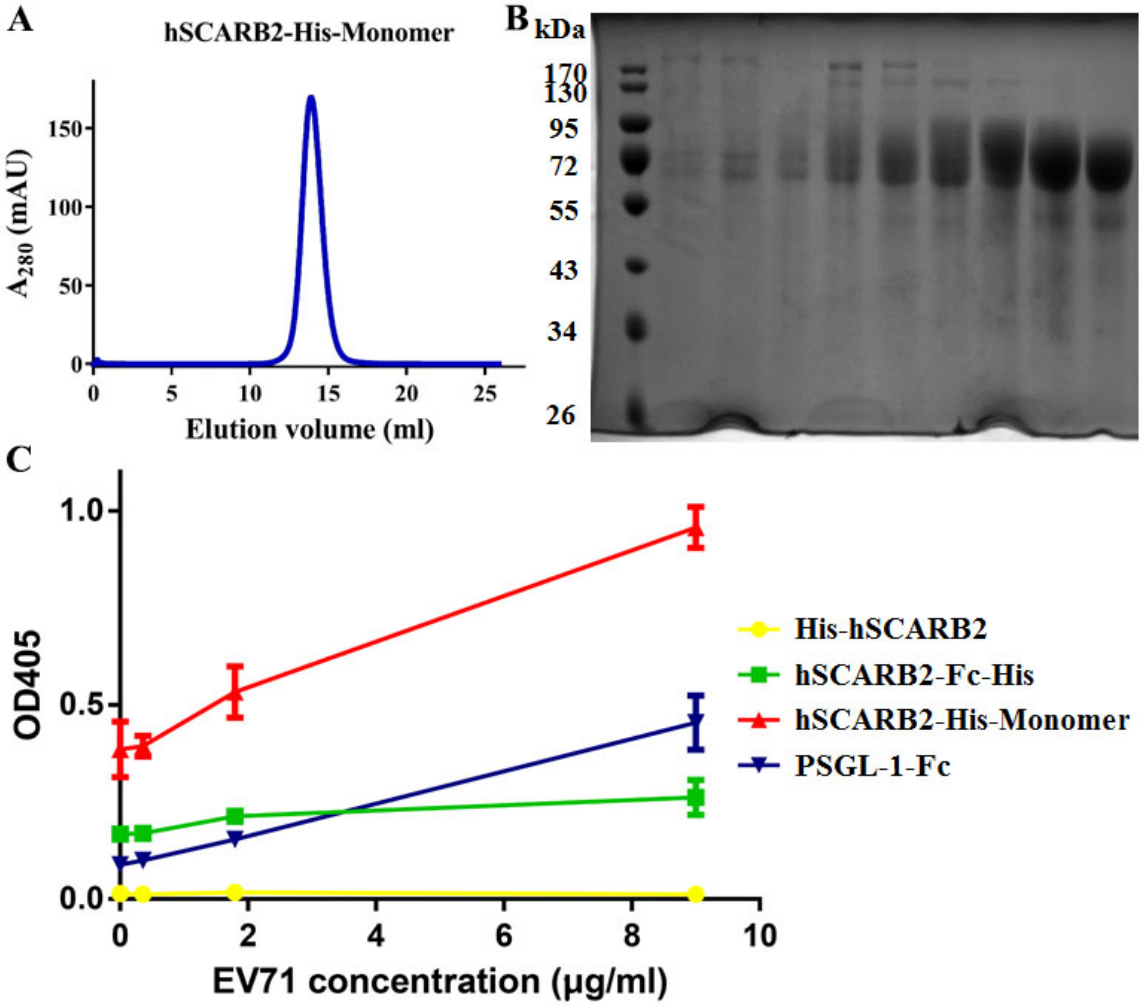

Fig. A.2. **A mammalian cell derived monomeric hSCARB2 binds EV-A71. A.** Gel filtration profile of hSCARB2-His-Monomer shows a predicted monomeric form of the protein. **B.** SDS-PAGE analysis of hSCARB2-His-Monomer. The far right lane represents a sample that was pooled up from the fractions of the peak (at 13.9 ml) shown in **A**. Other lanes correspond to fractions collected from a previous run of gel filtration. **C.** Binding of SCARB2 to EV71 was analyzed by ELISA. Wells were coated with different concentrations of purified virus, followed by addition of hSCARB2. The bound hSCARB2 was detected by using mouse anti-6X Histag and subsequently anti-mouse conjugated with alkaline phosphatase. Experiments were done in triplicates. Data are shown as mean±SD.

liposomes [136] and nanodiscs [213]. This approach would bring the virus-receptor molar ratio from at least 60:1 down to a ratio as low as 1:1.

VITA

VITA

I was born in Hubei province of China in September 1987. I studied applied chemistry for both my bachelor and master of engineering degrees at Beijing Institute of Technology, China. At that stage, my research centered around organic synthesis and mechanism of organic chemical reactions. I then became interested in antiviral therapeutics against virus infections and was fascinated by the fact that these tiny objects can cause considerable morbidity and mortality among humans. It subsequently led to my decision of joining Dr. Michael Rossmann's laboratory at Purdue University, where I investigated how viruses enter into host cells using X-ray crystallography and cryo-electron microscopy since March 2013.